Michael Knap

Collective Modes and Dynamics in Strongly Correlated Manybody Systems: the Variational Cluster Approach

DOCTORAL THESIS

For obtaining the academic degree of
Doktor der technischen Wissenschaften

Doctoral Program of Technical Sciences
Technical Physics

Graz University of Technology

Supervisor:

Univ.-Prof. Dipl.-Phys. Dr.rer.nat. Wolfgang von der Linden

Institute of Theoretical and Computational Physics

Graz, September 2012

to Sabrina

Abstract

Collective behavior in strongly correlated many particle systems can give rise to a rich variety of emergent phenomena, which cannot be predicted from the single particle perspective alone. Understanding their physics is a formidable task. One possible route to gain insight in these systems is by numerical simulations. In this thesis we focus on the variational cluster approach, a numerical technique which is capable to treat symmetry broken states emerging from the collective behavior of many particles.

We study strongly correlated bosonic systems experimentally realized by ultracold atoms in optical lattices and by light-matter systems. In these synthetic manybody systems quantum mechanical interference effects, manifesting for instance in the quantum phase transition from the localized Mott to the delocalized superfluid phase, are observable on a macroscopic scale. We calculate momentum distributions and dynamical spectral functions, which in ultracold atom experiments are accessible by time-of-flight images and Bragg spectroscopy, respectively. From these quantities we deduce the boundary of the quantum phase transition. In the normal phase we also study the excitation characteristics in disordered optical lattices for disorder distributions, which are relevant to ultracold atom experiments. One important technical aspect is the extension of the variational cluster approach to the $U(1)$ symmetry broken, superfluid phase of lattice bosons within the pseudoparticle and the self-energy functional approach adopting Nambu notation.

Moreover, we introduce a variational cluster approach that allows to compute nonequilibrium steady state properties of strongly correlated manybody systems. The method is embedded in the Keldysh Green's function formalism. We introduce a variational principle which allows for a suitable self-consistent optimization of the initial state to the nonequilibrium target state. We apply the presented approach to the nonlinear transport across a strongly correlated quantum wire and calculate the current-voltage characteristics. We also illustrate how the approach bridges to nonequilibrium cellular dynamical mean field theory upon coupling two baths with infinitely many bath degrees of freedom.

Understanding the fundamental properties of strongly correlated manybody systems if of great importance, as on the one hand strongly correlated materials quite generally exhibit peculiar electronic and magnetic properties, which renders them interesting for technological applications, and as on the other hand strongly correlated synthetic manybody systems might pave the way for general purpose quantum information processing.

Kurzfassung

Kollektives Verhalten in stark korrelierten Vielteilchensystemen kann zu Phänomenen führen, die allein von einer Einteilchenbetrachtung nicht vorhergesagt werden können. Daher ist es eine Herausforderung ihre Physik zu verstehen. Numerische Simulationen bieten einen möglichen Zugang, um Einblicke in diese Systeme zu erhalten. Diese Arbeit befasst sich mit der variationellen Clustermethode, eine numerische Methode, die symmetriegebrochene Zustände behandeln kann, welche durch das kollektive Verhalten von vielen Teilchen entstehen.

Wir untersuchen stark korrelierte bosonische Systeme, die experimentell durch ultrakalte Atome in optischen Gittern und durch Licht-Materiesysteme realisiert werden können. In diesen synthetischen Vielteilchensystemen sind quantenmechanische Interferenzeffekte, die sich beispielsweise in dem Quantenphasenübergang von der lokalisierten Mott zur delokalisierten suprafluiden Phase manifestieren, auf makroskopischer Skala beobachtbar. Wir berechnen Impulsverteilungen und dynamische Spektralfunktionen, die in Experimenten mit ultrakalten Atomen durch Flugzeitaufnahmen beziehungsweise Braggspektroskopie zugänglich sind. Aus diesen Observablen berechnen wir die Position des Quantenphasenübergangs. In der lokalisierten Phase untersuchen wir auch die Anregungscharakteristik von ungeordneten optischen Gittern für Unordnungsverteilungen, die für Experimente mit ultrakalten Atomen relevant sind. Ein wichtiger technischer Aspekt ist die Erweiterung der variationellen Clustermethode auf die $U(1)$ symmetriegebrochene, suprafluide Phase von Gitterbosonen. Dazu verwenden wir den Pseudoteilchen-Zugang und den Selbstenergiefunktional-Zugang mit Nambu-Notation.

Darüberhinaus führen wir eine variationelle Clustermethode ein, die die Berechnung von stationären Zuständen von stark korrelierten Vielteilchensystemen im Nichtgleichgewicht ermöglicht. Die Methode ist im Formalismus der Green'schen Funktionen im Keldysh Raum eingebettet. Wir führen ein Variationsprinzip ein, das eine geeignete, selbstkonsistente Optimierung des Anfangszustands auf den Zielzustand im Nichtgleichgewicht ermöglicht. Die neue Methode wenden wir auf den nichtlinearen Transport über einen stark korrelierten Quantendraht an und berechnen Strom-Spannungs-Charakteristiken. Wir illustrieren auch die Zusammenhänge zwischen diesem Zugang und der zellulären dynamischen Molekularfeldtheorie.

Das Verständnis der fundamentalen Eigenschaften von stark korrelierten Vielteilchensystemen ist von großer Wichtigkeit, da einerseits stark korrelierte Materialien im Allgemeinen besondere elektronische und magnetische Eigenschaften aufweisen, die sie für technologische Anwendungen interessant machen, und da andererseits stark korrelierte synthetische Vielteilchensysteme den Weg für universelle Quanteninformationsverarbeitung ebnen könnten.

Contents

1. Introduction

Collective behavior in many particle systems can give rise to a rich variety of emergent phenomena, which cannot be predicted from the single particle perspective alone [1]. However, universality put forward by Ginzburg-Landau theory [2] and Wilson's renormalization group [3] can help to understand the complex collective behavior of many particles.

Often the physics of manybody systems can still be understood from the single particle picture, where however the particle is not the original electron but rather a quasi particle which is dressed by many body interactions. In particular this is the case for weakly interacting particles in higher dimension where Fermi liquid theory [4] is the universal fixed point of the renormalization group flow. Extremely interesting are cases where the Fermi liquid approach breaks down, which is the case for strong interactions and in low dimensions. The break down of the quasi particle picture implies that there is no direct connection of the elementary particles and the dressed particles. One of the most prominent examples might be one-dimensional metallic systems, where excitations are collective density oscillations of bosonic nature [5]. For one-dimensional metallic systems the fixed point of the renormalization group flow is of the universality class of the Tomonaga-Luttinger model [6, 7].

Quite generally systems where strong correlations play a crucial role exhibit unusual electronic and magnetic properties, which also renders them highly relevant for technological applications possibly rooted in energy sciences, health sciences, and information sciences. Examples for these unusual properties include the metal to insulator transition (also known as Mott transition) occurring when ambient parameters such as pressure and doping are changed [8], the colossal magnetoresistance with extraordinarily high sensitivity to applied magnetic fields [9], the Kondo effect where a localized spin is entangled with itinerant fermions in its environment [10, 11], and unconventional superconductivity, where as compared to the electron-ion interaction, which is at the heart of conventional superconductivity, a different mechanism is responsible for superconductivity [12]. Unconventional superconductors are characterized by unconventional electron pairing other than s-wave pairing. In that sense the first discovered unconventional "superconductor" is the superfluid ^{3}He [13]. The neutral ^{3}He atoms can be considered as hard core objects which thus suppress s-wave pairing. But there are also many electronic systems, which exhibit unconventional superconductivity. Probably, the most prominent among them are the cuprates, where copper-oxide layers are believed to be responsible for superconductivity [14]. A very intriguing property of the cuprates is that they exhibit extremely high transition temperatures to the superfluid phase, which are well above liquid nitrogen temperature. There exist also unconventional organic superconductors [15], heavy fermion systems with strongly enhanced

quasi particle mass as compared to the bare electron mass [16], and the recently discovered iron-based superconductors [17].

Understanding the physics of strongly correlated systems is a formidable task. One possible route to gain insight into these systems is to describe their main physical properties by a minimal theoretical model, which contains only a few relevant parameters, yet considers correlations between the particles. For high temperature superconductors the paradigm example is the Hubbard model [18], describing the interplay between the delocalization driven by the kinetic energy and the localization driven by the interaction of electrons in copper oxide planes. The comparison with real materials is often challenging, as real materials have a complicated band structure, model parameters are often unknown, and disorder, which is always present in real samples, can dramatically alter physical properties [19]. Therefore it is of great interest to experimentally realize strongly correlated manybody systems in a clean and controlled way.

In the recent years, the enormous progress in controlling quantum optical and atomic systems lead to the advent of "synthetic" manybody systems, whose microscopic parameters are extremely well known and also controllable. While one of the most elaborate synthetic manybody systems consists of ensembles of ultracold atoms [20, 21, 22], other systems including light-matter systems [23, 24], Josephson junction arrays [25, 26], and optomechanical systems [27] are also actively explored. All these different realizations of synthetic manybody systems have the high controllability and clean realization in common, which renders them as ideal candidates for quantum simulators of strongly correlated manybody systems and also poses new challenges for theory since vastly different energy and time scales are present as compared to condensed matter systems. Additionally, different experimental probes are available to characterize manybody states.

Numerical simulations can provide profound theoretical insight into the physics of strongly correlated manybody systems. In this thesis, we focus on a particular numerical technique—the variational cluster approach (VCA)—which is able to treat symmetry broken states emerging from the collective behavior of many particles. Originally, VCA has been introduced for fermionic systems in equilibrium [28]. One principle goal of this thesis is to extend VCA in the following two directions: First, we consider bosonic lattice systems and extend VCA to the $U(1)$ symmetry broken superfluid phase. Second, we introduce a VCA to calculate the nonequilibrium steady state of strongly correlated manybody systems and explore transport properties including the current density at finite bias voltage.

Strongly correlated bosonic systems can be realized by synthetic manybody systems. In this thesis we focus on ultracold atoms trapped in optical lattices [20, 21, 22] and light matter systems [23, 24]. Optical lattices are created by counter propagating laser beams which form a standing wave. Due to the dipolar interactions the ultracold gas of atoms experiences the periodic potential whose depth can be controlled by the laser light intensity, see Fig. 1.1 (a). Such an experimental realization renders quantum mechanical interference effects observable on a macroscopic scale. Important as well as fundamental is the quantum phase transition [29] of strongly correlated lattice bosons

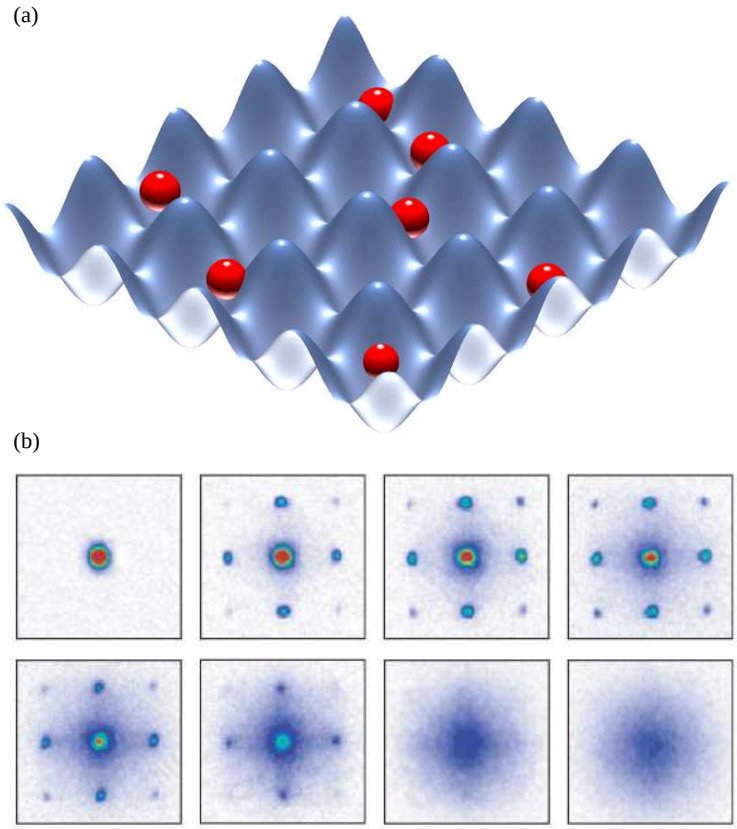

Figure 1.1.: (a) Schematic of a two-dimensional optical lattice created by four counter propagating laser beams. Bosonic particles (red spheres) feel the lattice potential due to the dipole force [22]. (b) Experimental observation of the quantum phase transition from the superfluid phase to the Mott insulating phase from top left to bottom right for increasing optical lattice depth [21].

from the localized Mott phase to the delocalized superfluid phase [30]. This phase transition directly manifests in the momentum distribution, shown in Fig. 1.1 (b), which due to Heisenberg's uncertainty relation is dual to the picture in real space: In the Mott insulating phase a smeared background is observable whereas in the superfluid phase the condensate peak and Bragg reflection peaks are observable; figure is taken over from [21].

In light-matter systems [23, 24], strong interactions can be achieved by optical nonlinearities, which appear due to the dipole coupling of cavity photons to matter in the form of atoms or atomic-like structures such as single atoms trapped in optical dipole traps or quantum dots, see Fig. 1.2. Usually, the interaction between photons and atoms is relatively weak, since the interaction time is small. However, the interaction time can be increased by confining the photons in an optical circuit [33] or cavity [34]. Due to dipolar

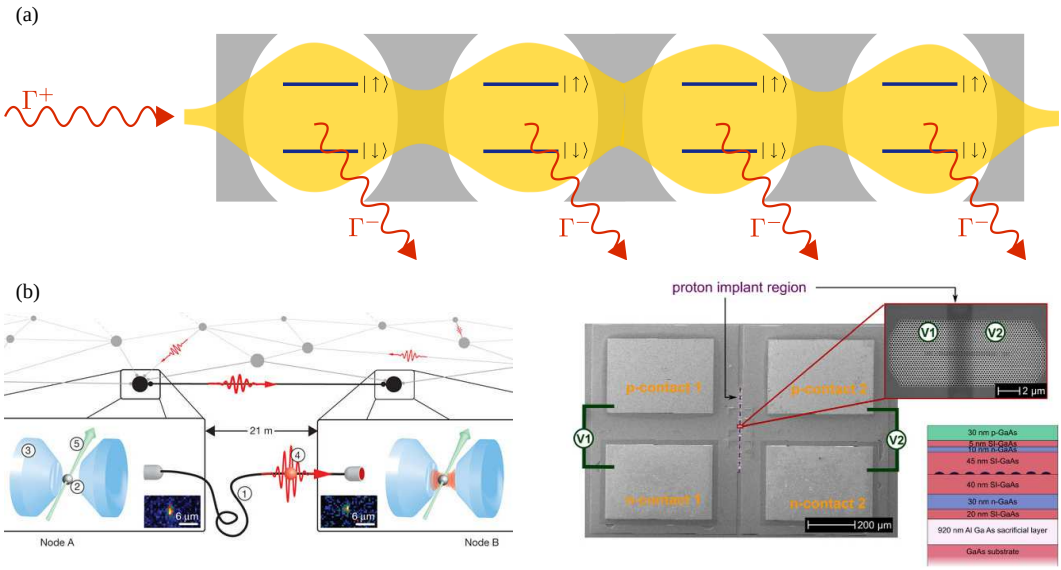

Figure 1.2.: (a) Illustration of laser driven and dissipative coupled quantum electrodynamics cavities. The yellow shaded region depicts the cavity modes, whereas the atomic excitations are indicated by two level systems. Red wavy arrows indicate photon pumping (Γ^+) and photon decay (Γ^-). (b) Two experimental realizations of coupled quantum electrodynamics cavities where nonlinearities are realized by atoms trapped in a dipole trap (left) [31] and quantum dots grown in photonic crystal cavities (right) [32].

interactions, composite particles of atomic excitations and photons are formed, which exhibit mutual repulsive interactions and are termed polaritons. A synthetic manybody system is then realized, when coupling multiple cavities, which can be achieved by engineering a finite overlap of the photonic wave functions [32]. A major advantage of these synthetic realizations of strongly correlated systems is that they are of mesoscopic scale, which allows for a single-site addressability and thus gives access to local quantities and spatially extended correlation functions. Importantly, in experiments these systems inherently operate out of equilibrium as they are laser driven and susceptible to photon loss.

New insight into the fundamental manybody physics can be obtained from a fruitful interplay between theory and experiments on strongly correlated systems. In ultracold atom experiments a rich experimental toolbox exists to characterize manybody states: Time of flight images provide the momentum distribution of trapped atoms [35, 21] and in-situ imaging of the atomic cloud gives access to the particle distribution in real space [36, 37]. Dynamical response functions can be obtained from lattice modulation [38, 39], RF-spectroscopy [40, 41], and Bragg spectroscopy [42, 43, 44]. Also well established quantum optics experiments of Rabi or Ramsey type can be used to char-

acterize manybody states [45, 46, 47]. Information about correlation functions can also be obtained from the analysis of shot-to-shot noise [48]. In VCA we have direct access to the single particle Green's function, and thus to all single particle quantities. In this thesis, we calculate momentum distributions measurable with time of flight images and the dynamical and wave-vector resolved single-particle spectral function accessible by Bragg spectroscopy. We also map out phase diagrams, which can be derived from the above discussed quantities. In the study of the nonequilibrium steady state of a strongly correlated manybody system, we focus on transport properties, such as the current voltage characteristics, which are the natural observables in experiments with mesoscopic systems.

This thesis is mainly based on the following publications:

[1] **Michael Knap**, Enrico Arrigoni, Wolfgang von der Linden, Spectral properties of strongly correlated bosons in two-dimensional optical lattices. *Phys. Rev. B* **81**, 024301 (2010).
Selected for the Virtual Journal of Quantum Fluids, January 2010, edited by Prof. Wolfgang Ketterle (MIT), Prof. Markus Greiner (Harvard), and Prof. Peter Zoller (Innsbruck).

[2] **Michael Knap**, Enrico Arrigoni, Wolfgang von der Linden, Spectral properties of coupled cavity arrays in one dimension. *Phys. Rev. B* **81**, 104303 (2010).

[3] **Michael Knap**, Enrico Arrigoni, Wolfgang von der Linden, Quantum phase transition and excitations of the Tavis-Cummings lattice model. *Phys. Rev. B* **82**, 045126 (2010).
Selected for the Virtual Journal of Quantum Fluids, August 2010, edited by Prof. Wolfgang Ketterle (MIT), Prof. Markus Greiner (Harvard), and Prof. Peter Zoller (Innsbruck).

[4] **Michael Knap**, Enrico Arrigoni, Wolfgang von der Linden, Excitations in disordered bosonic optical lattices. *Phys. Rev. A* **82**, 053628 (2010).

[5] **Michael Knap**, Enrico Arrigoni, Wolfgang von der Linden, Variational cluster approach for strongly-correlated lattice bosons in the superfluid phase. *Phys. Rev. B* **83**, 134507 (2011).

[6] Enrico Arrigoni, **Michael Knap**, Wolfgang von der Linden, Extended self-energy functional approach for strongly correlated lattice bosons in the superfluid phase. *Phys. Rev. B* **84**, 014535 (2011).

[7] **Michael Knap**, Enrico Arrigoni, Wolfgang von der Linden, Nonequilibrium steady state for strongly-correlated many-body systems: Variational cluster approach. *Phys. Rev. B* **84**, 115145 (2011).

A complete list of our publications can be found following the bibliography.

The author of this thesis made substantial contributions to the above stated publications, consisting of an extensive literature research, analytical calculations, design, development, implementation, and test of the numerical approaches, their application to physical problems, evaluation, interpretation and discussions of the results, and writing of the papers. Throughout this thesis we indicate text which is taken over from the above stated publications by a specific font also used to format this sentence. In order to provide a coherent presentation, the methodology and the results of the individual papers are separated. The connection to the original literature can be drawn from the presentation of the structure of this thesis in the following paragraphs.

This thesis is organized as follows: In Ch. 2 we present our extensions and developments of VCA. In particular, in Sec. 2.1 we begin the discussions with a formulation of VCA applicable to the normal Mott phase of strongly correlated bosons. Here, we start with a concise introduction to the self-energy functional approach [49, 50], which is the basis of VCA [28], formulated for the normal phase of lattice bosons, which has been originally introduced by Koller and Dupuis [51]. For technical details and tricks on the numerical techniques I refer to the original work [28, 52, 53, 54] and to my master thesis [55]. Following this short introduction we discuss the accurate calculation of the moments of the spectral function and the extension to disordered lattice bosons [56]. Next, we formulate VCA within a pseudoparticle approach [57], which is less rigorous than the self-energy functional approach, yet allows for a very intuitive understanding of VCA. Using the pseudoparticle approach we extend VCA in Sec. 2.2 to the symmetry broken superfluid phase [57] and put it within a self-energy functional approach on rigorous grounds [58]. The extension of VCA to the nonequilibrium steady state of strongly correlated manybody systems [59] is presented in Sec. 2.3.

In Ch. 3 we discuss equilibrium properties of bosonic manybody systems. In Sec. 3.1 we first focus on the normal Mott insulating phase without [54] and with disorder [56] and subsequently study the superfluid phase [57, 58]. In the following we study in detail two different light-matter systems: In Sec. 3.2 we explore coupled cavities with Jaynes-Cummings nonlinearities provided by a single two-level system [60]. In Sec. 3.3 we extend this study to the Tavis-Cummings model containing multiple two level systems per cavity [61].

Chapter 4 focuses on the nonequilibrium steady state of a strongly correlated quantum wire transversely attached to noninteracting leads [59]. In particular we calculate transport properties such as the steady state current density for a finite applied bias voltage.

Finally, we conclude and summarize our findings in Ch. 5 and give an outlook for further interesting questions. The appendices are devoted to technical details: In App. A and App. B we provide details on the pseudoparticle approach and the self-energy functional approach in the symmetry broken, superfluid phase. Appendix C contributes details to the nonequilibrium VCA and App. D contains supplementary information on the treatment of light-matter systems.

2. Variational cluster approach

Cluster approaches have been proven to be very useful for the numerical investigation of strongly correlated many-body systems. These approaches consist in embedding finite size clusters, for which a numerical exact solution is available, within a lattice of infinite size. The embedding is done by introducing additional fields to the cluster Hamiltonian, in order to take into account the coupling to the rest of the lattice in some appropriate dynamical mean-field way. We will term these fields Weiss fields, since they play an analogous role as in Weiss mean-field theory of ferromagnetism (*cf.* Ref. [62]). Different cluster embedding techniques, such as cluster perturbation theory (CPT) [63, 64, 65], variational cluster approach (VCA) [49, 28, 66], cellular dynamical mean field theory (C-DMFT) [67], and dynamical cluster approximation [68], differ by the nature of the Weiss fields and of the mean-field treatment which fixes their optimal value.

In this chapter, we provide an introduction to VCA and describe in a coherent way the extensions and generalizations, which have been developed in the course of this thesis in our group.

First, we introduce VCA for equilibrium properties of strongly correlated lattice bosons in the normal phase without symmetry breaking [51, 69, 54]. VCA for equilibrium many-body systems, can be understood in a general framework called self-energy functional approach (SFA) [49, 50], in which the grand potential of the physical system of interest is expressed as the stationary point of a particular functional of the self energy. We also present an alternative approach to VCA in which single-particle excitations are expressed in terms of "pseudoparticles," which are similar to Hubbard operators [70], and external fields are "added" to the cluster Hamiltonian and "subtracted perturbatively" [52]. Additionally, we provide a detailed introduction to the Q-matrix formalism which facilitates an accurate calculation of observables and present, how the moments of the spectral function can be evaluated within VCA. Finally, we formulate VCA for disordered lattice bosons and adopt the Q-matrix formalism accordingly.

The next section deals with the extension of VCA to the $U(1)$ symmetry broken, superfluid phase [57, 58]. This theoretical framework, is applicable to a large class of lattice boson systems in the Mott insulating as well as in the superfluid phase. In particular, besides the widely studied Bose-Hubbard model [30, 20], the method can straight forwardly be extended to include disordered systems or multiple components, including fermion-boson mixtures. The extended VCA theory can be applied even to the $U(1)$ broken, superfluid phase of light-matter systems, where photons are confined in coupled, nonlinear quantum-electrodynamics cavities [23, 24]. In order to achieve the extension to the $U(1)$ broken, superfluid phase, it proves convenient to reformulate VCA in terms of the pseudoparticle approach, whereby single-particle excitations within a cluster are approximately mapped onto particlelike excitations. We show that this

approach quite naturally suggests the extension to the superfluid case. In the following section, we demonstrate that the results obtained from the pseudoparticle formalism in the superfluid phase can be equivalently obtained within an appropriate extension of SFA taking into account condensed bosons.

In the last section we present a numerical approach approach that allows to compute nonequilibrium steady state properties of strongly correlated quantum many-body systems [59]. This method is embedded in the Keldysh Green's function formalism and is based upon the idea of the variational cluster approach as far as the treatment of strong correlations is concerned. It turns out that the variational aspect is crucial as it allows for a suitable optimization of a "reference" system to the nonequilibrium target state. The approach is neither perturbative in the many-body interaction nor in the field, that drives the system out of equilibrium, and it allows to study strong perturbations and nonlinear responses of systems in which also the correlated region is spatially extended. We also illustrate how the method bridges to C-DMFT upon coupling two baths containing and increasing number of uncorrelated sites.

2.1. Correlated lattice bosons in the normal phase

2.1.1. Self-energy functional approach

The SFA is based on the fact that Dyson's equation for the exact Green's function is recovered at the stationary point of the grand potential $\Omega[\Sigma]$ considered as a functional of the self-energy Σ. Thus Σ corresponds, at the stationary point, to the real physical self-energy. The self-energy functional $\Omega[\Sigma]$ cannot be evaluated directly as it contains the Legendre transform $F[\Sigma]$ of the Luttinger-Ward functional [71, 49]. However, the functional $F[\Sigma]$ just depends on the interaction term of the Hamiltonian, and is thus equivalent for all Hamiltonians which share a common interaction part. Due to this property $F[\Sigma]$ can be eliminated from the expression of the self-energy functional $\Omega[\Sigma]$. For this purpose an exactly solvable, so-called "reference," system $\hat{H}'$ is constructed, which must be defined on the same lattice and must have the same interaction part as the original system $\hat{H}$. Thus both the self-energy functional of the original system $\Omega[\Sigma]$ and the one of the reference system $\Omega'[\Sigma]$ contain the same $F[\Sigma]$, which can be eliminated by comparison from the expressions of the two self-energy functionals. This yields for bosonic systems [51]

$$\begin{aligned}\Omega[\Sigma] = \Omega'[\Sigma] &- \mathrm{Tr}\,\ln(-(G_0'^{-1} - \Sigma)) \\ &+ \mathrm{Tr}\,\ln(-(G_0^{-1} - \Sigma))\,, \end{aligned} \tag{2.1}$$

where quantities with prime correspond to the reference system and G_0 is the free Green's function. The free Green's function is defined as $G_0^{-1} \equiv (\omega + \mu)\hat{\mathbb{1}} - T$, where T contains the hopping matrix and all other one-particle parameters of the Hamiltonian except for the chemical potential μ, which is already treated separately in the definition. The symbol Tr denotes a summation over bosonic Matsubara frequencies and a trace over site indices. The self-energy functional $\Omega[\Sigma]$ given by Eq. (2.1) is exact. In order to

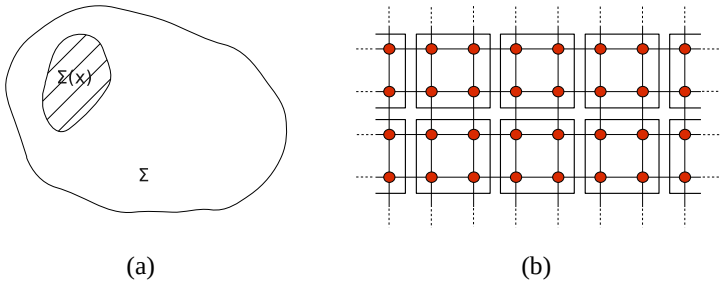

Figure 2.1.: (a) The search space for the self-energy Σ is restricted to self-energies $\Sigma(x)$ which are accessible via the reference system $\hat{H}'$. (b) Lattice decomposition of a square lattice into 2×2 site clusters.

be able to evaluate the functional, the search space of the self-energy Σ has to be restricted [49], which consists in an approximation. More precisely, the functional $\Omega[\Sigma]$ is evaluated for the subset of self-energies available to the reference system $\hat{H}'$, see Fig. 2.1 (a). Practically, this is achieved by varying the single-particle parameters of the reference Hamiltonian in order to find the stationary point of the grand potential. Thus the functional $\Omega[\Sigma]$ becomes a function of the set x of single-particle parameters of $\hat{H}'$

$$\begin{aligned}\Omega(x) &= \Omega'(x) - \mathrm{Tr}\,\ln(-(G_0'^{-1} - \Sigma(x))) \\ &\quad + \mathrm{Tr}\,\ln(-(G_0^{-1} - \Sigma(x))) \\ &= \Omega'(x) + \mathrm{Tr}\,\ln(-G'(x)) - \mathrm{Tr}\,\ln(-G(x))\end{aligned} \tag{2.2}$$

leading to the stationary condition

$$\frac{\partial\,\Omega(x)}{\partial\,x} = 0\ . \tag{2.3}$$

In VCA the reference system is given by the decomposition of the total system into identical clusters, see Fig. 2.1 (b). We evaluate the single particle Green's function of each cluster exactly by means of the band Lanczos method [72, 53]. The Green's function of the total system is obtained via the relation

$$G^{-1}(\omega) = G'^{-1}(\omega) - V\ , \tag{2.4}$$

which can be deduced from the Dyson equation of the total system $G^{-1} = G_0^{-1} - \Sigma(x)$ and the reference system $G'^{-1} = G_0'^{-1} - \Sigma(x)$. The self-energy can be eliminated and it follows that

$$G^{-1} = G'^{-1} - (G_0'^{-1} - G_0^{-1})\ .$$

The expression in parenthesis defines the matrix

$$\begin{aligned}V &\equiv G_0'^{-1} - G_0^{-1} = ((\omega + \mu')\hat{\mathbb{1}} - T') - ((\omega + \mu)\hat{\mathbb{1}} - T) \\ &= -(\mu - \mu')\hat{\mathbb{1}} + (T - T')\ .\end{aligned} \tag{2.5}$$

With Eq. (2.4) the grand potential $\Omega(x)$ can be rewritten as

$$\Omega(x) = \Omega'(x) + \mathrm{Tr}\ln(\hat{\mathbb{1}} - VG') \ . \tag{2.6}$$

The decomposition of the N-site lattice into clusters of L sites can be described by a superlattice. The original lattice is obtained by attaching a cluster to each site of the superlattice [73, 55]. A partial Fourier transform from superlattice indices to wave vectors $\tilde{\mathbf{k}}$, which belong to the first Brillouin zone of the superlattice, yields the total Green's function

$$G^{-1}(\tilde{\mathbf{k}}, \omega) = G'^{-1}(\omega) - V(\tilde{\mathbf{k}}) \ . \tag{2.7}$$

Due to the diagonality of G' in the superlattice indices its partial Fourier transform does not depend on $\tilde{\mathbf{k}}$. The matrices in Eq. (2.7) are now defined in the space of cluster-site indices and are thus of size $L \times L$. The N wave vectors $\mathbf{k}$ from the Brillouin zone of the total lattice can be expressed as

$$\mathbf{k} = \tilde{\mathbf{k}} + \mathbf{K} \ , \tag{2.8}$$

where $\mathbf{K}$ belongs to both the reciprocal superlattice and the first Brillouin zone of the total lattice [73, 55].

2.1.2. Q-matrix formalism for bosonic systems

The frequency integration implicit in the expression for the grand potential, given in Eq. (2.6), can be carried out analytically, yielding at zero temperature [51, 50, 73]

$$\Omega(x) = \Omega'(x) + \sum_{\lambda'_r<0} \lambda'_r - \frac{1}{N_c} \sum_{\tilde{\mathbf{k}}} \sum_{\lambda_r(\tilde{\mathbf{k}})<0} \lambda_r(\tilde{\mathbf{k}}) \ , \tag{2.9}$$

where λ'_r and $\lambda_r(\tilde{\mathbf{k}})$ are the poles of the cluster Green's function and total Green's function, respectively. The number of clusters N/L is denoted as N_c. The poles λ'_r of the cluster Green's function can be readily obtained from the Lanczos method, whereas the poles of the total Green's function $\lambda_r(\tilde{\mathbf{k}})$ can be evaluated with the so-called Q-matrix formalism, which was originally proposed for fermionic Green's functions [53, 52]. Here, we extend this formalism to the generic case, i. e., we include bosonic Green's functions. As we will see, this extension is nontrivial, since it involves non-unitary transformations.

For zero temperature, the cluster Green's function reads [74]

$$\begin{aligned} G'_{ij}(\omega) = &\langle\psi_0| a_i \frac{1}{\omega - (\hat{H}' - \omega_0)} a_j^\dagger |\psi_0\rangle \\ &- \epsilon \langle\psi_0| a_j^\dagger \frac{1}{\omega + (\hat{H}' - \omega_0)} a_i |\psi_0\rangle \ , \end{aligned} \tag{2.10}$$

where $|\psi_0\rangle$ is the ground state of the N_p particle system, ω_0 is its (grand-canonical) energy, and $\epsilon = 1$ ($\epsilon = -1$) for bosonic (fermionic) Green's functions. The first term on the right-hand side of Eq. (2.10) describes single-particle excitations from the N_p particle ground state and can thus be referred to as particle term, whereas the second

part corresponds to single-hole excitations and can be called hole term. Inserting the identity $\hat{\mathbb{1}} = \sum_\gamma |\gamma\rangle \langle\gamma|$ into each part of Eq. (2.10), where $|\gamma\rangle$ are the eigenvectors of the reference Hamiltonian with corresponding eigenvalues ω'_γ, yields the Lehmann representation of the Green's function

$$\begin{aligned} G'_{ij}(\omega) = &\sum_\alpha \frac{\langle\psi_0| a_i |\alpha\rangle \langle\alpha| a_j^\dagger |\psi_0\rangle}{\omega - (\omega'_\alpha - \omega_0)} \\ &- \epsilon \sum_\beta \frac{\langle\psi_0| a_j^\dagger |\beta\rangle \langle\beta| a_i |\psi_0\rangle}{\omega + \left(\omega'_\beta - \omega_0\right)} , \end{aligned} \tag{2.11}$$

which can be cast into the form

$$G'_{ij}(\omega) = \sum_\gamma Q_{i\gamma} \frac{1}{\omega - \lambda'_\gamma} S_{\gamma\gamma} Q^\dagger_{\gamma j} . \tag{2.12}$$

In Eq. (2.12), we have introduced the following notation:

$$Q^\dagger_{\gamma j} \equiv \begin{cases} \langle\gamma| a_j^\dagger |\psi_0\rangle & |\gamma\rangle \in \mathcal{H}_{N_p+1} \\ \langle\psi_0| a_j^\dagger |\gamma\rangle & |\gamma\rangle \in \mathcal{H}_{N_p-1} \end{cases} , \tag{2.13}$$

$$\lambda'_\gamma \equiv \begin{cases} \omega'_\gamma - \omega_0 & |\gamma\rangle \in \mathcal{H}_{N_p+1} \\ \omega_0 - \omega'_\gamma & |\gamma\rangle \in \mathcal{H}_{N_p-1} \end{cases} \tag{2.14}$$

and

$$S_{\gamma\gamma'} \equiv \begin{cases} \delta_{\gamma\gamma'} & |\gamma\rangle \in \mathcal{H}_{N_p+1} \\ -\epsilon\, \delta_{\gamma\gamma'} & |\gamma\rangle \in \mathcal{H}_{N_p-1} \end{cases} , \tag{2.15}$$

where $\mathcal{H}_M$ is the Hilbert space of an M particle system. With

$$g'_{\gamma\gamma'}(\omega) \equiv \frac{\delta_{\gamma\gamma'}}{\omega - \lambda'_\gamma} \tag{2.16}$$

the cluster Green's function can be written in matrix notation

$$G' \equiv Q\, g'(\omega)\; S\, Q^\dagger . \tag{2.17}$$

With the help of this expression the VCA Green's function Eq. (2.7) can be rewritten as

$$\begin{aligned} G &= G' \frac{1}{1 - V\, G'} = Q\, g'\, S\, Q^\dagger \frac{1}{1 - V\, Q\, g'\, S\, Q^\dagger} \\ &= Q\, g'\, S\, Q^\dagger \left\{1 + V\, Q\, g'\, S\, Q^\dagger + \ldots\right\} \\ &= Q\, g' \left[1 - S\, Q^\dagger\, V\, Q\, g'\right]^{-1} S\, Q^\dagger \\ &= Q \frac{1}{g'^{-1} - S\, Q^\dagger\, V\, Q} S\, Q^\dagger , \end{aligned} \tag{2.18}$$

where in the third step we expanded the fraction in a Taylor series. The matrix g' is diagonal and contains the poles of the cluster Green's function G', see Eq. (2.16). It can be written as ${g'}^{-1} = \omega - \Lambda$ with $\Lambda_{\gamma\gamma'} = \lambda'_\gamma \, \delta_{\gamma\gamma'}$. Plugging this into Eq. (2.18) yields

$$G = Q \frac{1}{\omega - (\Lambda + S\, Q^\dagger\, V\, Q)} S\, Q^\dagger \; . \tag{2.19}$$

We introduce the matrix $M \equiv \Lambda + S\, Q^\dagger\, V\, Q$. This matrix can be diagonalized as $MX = XD$, where D is a diagonal matrix containing the eigenvalues of M and X is the matrix of the eigenvectors of M. The eigenvalue equation of the matrix M can be rewritten as $M = XDX^{-1}$, where X^{-1} is the inverse of X and not its transpose as M is a non-symmetric matrix. From that we obtain

$$(\omega - M)^{-1} = X(\omega - D)^{-1} X^{-1} \; . \tag{2.20}$$

Therefore, the poles of the total Green's function G in Eq. (2.19) are the eigenvalues of the matrix M. The matrices G and V are defined on the space of cluster-site indices. Thus G and V are of size $L \times L$ and depend on the wave vector $\tilde{\mathbf{k}}$, see Eq. (2.7). The matrix Q is of size $L \times K$, where K is the dimension of the Krylov space generated in the band Lanczos method. Due to the dependence of V on $\tilde{\mathbf{k}}$ the diagonalization of the matrix M yields K eigenvalues $D_{rr'} = \lambda_r(\tilde{\mathbf{k}})\, \delta_{rr'}$, which are used in Eq. (2.9). The diagonalization has to be repeated for all wave vectors $\tilde{\mathbf{k}}$. With that the grand potential $\Omega(x)$ can be evaluated. The crucial point is that for bosonic Green's functions, the entries of the diagonal matrix S can be both 1 as well as -1, see Eq. (2.15). Therefore, the eigenvalue problem is not symmetric. It can happen that some of the poles of the total Green function Eq. (2.7) become complex. This is due to the fact that the matrix M in Eq. (2.20) is not symmetric. For this reason, this anomaly can occur in the bosonic case only. With complex poles, the bosonic Green function is no longer causal and, therefore, the variational solution is unphysical and must be discarded. This situation quite generally signals an instability towards another phase, such as superfluidity, see Sec. 2.2.

The factorization of the total lattice into clusters breaks the translational symmetry of the lattice. Hence the total Green's function would depend on two wave vectors $\mathbf{k}$ and $\mathbf{k}'$, which is certainly not correct for a periodic lattice. This has to be circumvented by a periodization prescription that provides a total Green's function $G(\mathbf{k}, \omega)$ depending only on one wave vector $\mathbf{k}$. The periodization prescription proposed in Ref. [64] (Green's-function periodization) reads as follows:

$$G(\mathbf{k}, \omega) = \frac{1}{L} \sum_{\alpha\beta} e^{-i\, \mathbf{k}\, (\mathbf{r}_\alpha - \mathbf{r}_\beta)} G_{\alpha\beta}(\tilde{\mathbf{k}}, \omega) \; , \tag{2.21}$$

where $\mathbf{k}$ is a wave vector of the total lattice and $\mathbf{r}_\alpha$ refers to lattice sites α of the cluster. The wave vectors $\tilde{\mathbf{k}}$ in Eq. (2.21) can be replaced by the total wave vectors $\mathbf{k}$ as they just differ by a reciprocal superlattice wave vector, see Eq. (2.8). With Eqs. (2.19) and (2.20) the periodized Green's function can be rewritten in matrix notation

$$G(\mathbf{k}, \omega) = \mathbf{v}_\mathbf{k}^\dagger \, Q \, X \, (\omega - D)^{-1} \, X^{-1} \, S \, Q^\dagger \, \mathbf{v}_\mathbf{k} \; , \tag{2.22}$$

where the vector $\mathbf{v_k}$ and its adjoint $\mathbf{v_k^\dagger}$ contain L plane waves

$$\mathbf{v_k^\dagger} \equiv \frac{1}{\sqrt{L}} \left(e^{-i\,\mathbf{k}\,\mathbf{r}_0},\, e^{-i\,\mathbf{k}\,\mathbf{r}_1},\, \ldots\, e^{-i\,\mathbf{k}\,\mathbf{r}_{L-1}} \right) .$$

There exists as well an alternative periodization prescription where the self-energy Σ is periodized [51]. This self-energy periodization should prevent spurious gaps, which arise in the spectral function. However, at least for fermion systems, this procedure yields spurious metallic bands in the Mott phase for arbitrarily large U. Since we do not observe any spurious gaps in the spectral function of the 2D BH model we use the periodization on the Green's function defined in Eq. (2.21).

With the wave-vector resolved Green's function of the total system $G(\mathbf{k},\, \omega)$ we are able to calculate the single-particle spectral function

$$A(\mathbf{k},\, \omega) \equiv -\frac{1}{\pi} \mathrm{Im}\, G(\mathbf{k},\, \omega) \;, \tag{2.23}$$

the density of states

$$N(\omega) \equiv \int A(\mathbf{k},\, \omega)\, d\mathbf{k} = \frac{1}{N} \sum_{\mathbf{k}} A(\mathbf{k},\, \omega) \tag{2.24}$$

and the momentum distribution

$$n(\mathbf{k}) \equiv - \int_{-\infty}^{0} A(\mathbf{k},\, \omega)\, d\omega \;.$$

The frequency integration can be evaluated directly by means of the Q-matrix formalism, which yields a sum of the residues of the Green's function, see Eq. (2.22), corresponding to negative poles $\lambda_r(\mathbf{k}) < 0$,

$$n(\mathbf{k}) = \sum_{\lambda_r(\mathbf{k})<0} (\mathbf{v_k^\dagger}\, Q\, X)_r\, (X^{-1}\, S\, Q^\dagger\, \mathbf{v_k})_r \;. \tag{2.25}$$

2.1.3. Moments of the spectral function

Here, it is described how the moments of the spectral function can be attained within the variational cluster approach (VCA) in a very accurate way. A direct summation over the spectral function weighted with powers of ω is not very accurate since for the numerical evaluation a small but finite artificial broadening $i0^+$ has to be chosen. As the poles are Lorentzians, i. e., distributed over a wide energy range, the artificial broadening will always limit accuracy. However, within the Q-matrix framework we have direct access to the energies and strength of the poles.

The spectral moment of order n is defined as

$$M^n(\mathbf{k}) = \int_{-\infty}^{\infty} d\omega\, \omega^n\; A(\mathbf{k},\, \omega) \;.$$

With Eq. (2.22), we have

$$\begin{aligned} M^n(\mathbf{k}) &= -\frac{1}{\pi}\mathrm{Im}\int_{-\infty}^{\infty} d\omega\,\omega^n\ \mathbf{v}_\mathbf{k}^\dagger Q\, g\,(\omega)\ S\, Q^\dagger \mathbf{v}_\mathbf{k} \\ &= \mathbf{v}_\mathbf{k}^\dagger Q\,[-\frac{1}{\pi}\mathrm{Im}\int_{-\infty}^{\infty} d\omega\omega^n\, g\,(\omega)]\, S\, Q^\dagger \mathbf{v}_\mathbf{k} \\ &= \sum_{ij\gamma} v_{\mathbf{k},i}^\dagger Q_{i\gamma}\,[-\frac{1}{\pi}\mathrm{Im}\int_{-\infty}^{\infty} d\omega\omega^n\,(\omega-\lambda_\gamma+i0^+)^{-1}]\, S_{\gamma\gamma}\, Q_{\gamma j}^\dagger v_{j,\mathbf{k}} \\ &= \sum_{ij\gamma} v_{\mathbf{k},i}^\dagger Q_{i\gamma}\,(\lambda_\gamma)^n\, S_{\gamma\gamma}\, Q_{\gamma j}^\dagger v_{j,\mathbf{k}}\ , \end{aligned}$$

With that we are able to evaluate the moments with extremely high accuracy.

2.1.4. Disordered manybody systems

Disorder is treated by introducing a reference system which shares, in addition to the interaction part, the disorder distribution with the physical system. The expression for the averaged grand-potential within VCA then reads [75]:

$$\Omega_p = \Omega'_p + \mathrm{Tr}\ln[-G_p^{-1}] - \mathrm{Tr}\ln[-G_p'^{-1}]\ , \tag{2.26}$$

where Ω'_p and G'_p are the exact disorder averaged grand potential and Green's function of the reference system, respectively, which can be easily evaluated numerically with high accuracy. The averaged Green's function of the physical system reads $G_p = \left(G_p'^{-1} - V\right)^{-1}$, where $V \equiv G_0'^{-1} - G_0^{-1}$, and G_0 and G'_0 are the noninteracting Green's functions of the pure physical and reference systems, respectively.

In Sec. 2.1.2 it has been discussed for a pure system that it is expedient for the evaluation of the traces in Eq. (2.26) to use the Q-matrix formalism. Here, we extend the Q-matrix formalism to the case of disorder. For a specific disorder configuration η we have

$$G'_\eta = Q_\eta\, g'_\eta\, S\, Q_\eta^\dagger\ , \tag{2.27}$$

where ${g'_\eta}^{-1} = \omega - \Lambda_\eta$ and $(\Lambda_\eta)_{rr'} = \lambda_r^\eta\,\delta_{rr'}$ are the poles of the reference Green's function, see Sec. 2.1.2 for details. In praxis a specific number M of disorder configurations η (each consisting of L disorder realizations ϵ_i) has to be sampled to compute the average of a quantity X_η leading to $X_p \equiv \langle X\rangle_p \approx 1/M\sum_\alpha X_{\eta_\alpha}$. The averaged Green's function G'_p thus reads

$$G'_p = \frac{1}{M}\sum_\alpha G'_{\eta_\alpha} = \frac{1}{M}\sum_\alpha Q_{\eta_\alpha} g'_{\eta_\alpha}\, S\, Q_{\eta_\alpha}^\dagger\ .$$

To exploit the Q-matrix formalism we write the averaged Green's function in a form similar to Eq. (2.27) and define

$$G'_p \equiv \tilde{Q}\,\tilde{g}'\,\tilde{S}\,\tilde{Q}^\dagger\ ,$$

where $\tilde{Q} \equiv (Q_{\eta_1}/\sqrt{M}, Q_{\eta_2}/\sqrt{M} \ldots)$, $\tilde{S} \equiv \mathrm{diag}(S, S, \ldots)$ and $\tilde{g}' \equiv \mathrm{diag}(g'_{\eta_1}, g'_{\eta_2}, \ldots)$. With that we can proceed in the same way as for pure systems and write the averaged Green's function of the physical system as

$$G_p = \tilde{Q} \frac{1}{\omega - (\tilde{\Lambda} - \tilde{S}\,\tilde{Q}^\dagger\, V\, \tilde{Q})}\, \tilde{S}\, \tilde{Q}^\dagger \ ,$$

where $\tilde{\Lambda} \equiv \mathrm{diag}(\Lambda_{\eta_1}, \Lambda_{\eta_2} \ldots)$. By diagonalizing the matrix $M \equiv \tilde{\Lambda} - \tilde{S}\,\tilde{Q}^\dagger\, V\, \tilde{Q} = X\, D\, X^{-1}$ we obtain the poles D of the physical Green's function and are thus able to evaluate the grand potential $\Omega_p(x)$.

2.1.5. Pseudoparticle approach

We reformulate CPT/VCA within the pseudoparticle approach for bosonic systems. In principle, one may argue that the formulation of CPT/VCA using pseudoparticles is complicated and in the case of the normal phase (i. e., Mott phase) CPT/VCA can be obtained from simpler approaches, as, for example, from Dyson's equation (see, e.g. Ref. [65]) and the SFA. The reason why we present this alternative formulation here is that this approach, while not as rigorous as SFA, provides useful hints on how to deal with more complicated situations, like the superfluid phase discussed in Sec. 2.2. In addition, it gives insight on other properties. For example, in the case of normal bosons the pseudoparticle approach is useful in order to understand the occurrence of noncausality of the Green's function in cases, where the chosen reference system is not suitable to describe the phase of the physical system, as we point out below. Thus the aim of this section is to derive the principal theoretical framework of the pseudoparticle approach, for the normal phase, reproducing the known result for the grand potential Ω, which has to be optimized.

The pseudoparticle formalism is in some aspects related to the standard basis matrix operator method developed by Haley and Erdös in Ref. [76] and to the Hubbard-operator approach, see for instance Ref. [70]. The idea is to introduce pseudoparticle operators b_μ and $b_\mu^\dagger$, which connect the ground state $|\psi_0\rangle$ with single-particle excited states $|\psi_\nu\rangle$ of a Hamiltonian describing disconnected clusters in the lattice. In the VCA language the cluster Hamiltonian is termed reference system $\hat{H}'$. Of course, the b_μ and $b_\mu^\dagger$ do not have the properties of ordinary single-particle creation and annihilation operators. The crucial point is that by treating them as such, one recovers the very same results as obtained from CPT and from VCA, as has been shown for fermionic systems in Ref. [52] (see appendix therein). Here, we prove the same result for the bosonic (normal) case, which is somewhat more subtle, as it requires a multimode Bogoliubov transformation. In this picture, excited states $|\psi_\mu\rangle$ are treated as pseudoparticle excitations with the properties

$$|\psi_\mu\rangle = b_\mu^\dagger\, |\psi_0\rangle \qquad b_\mu\, |\psi_\nu\rangle = \delta_{\mu\nu}\, |\psi_0\rangle \ .$$

Within the VCA approximation, pseudoparticles are regarded as noninteracting particles. We stress that, while this may seem a rather crude approximation, it is equivalent

to CPT and VCA. Furthermore, with appropriate extensions it becomes equivalent to C-DMFT.

Within this approach the original bosonic operators a_i and $a_i^\dagger$ can be expressed as linear combinations of the pseudoparticle operators b_μ. This makes it possible to write the coupling of the cluster to the rest of the lattice, which in VCA consists of intercluster hopping terms, as a quadratic form in the b_μ. In combination with the fact that the cluster Hamiltonian is by construction quadratic in these operators as well, one finally obtains a Hamiltonian which is completely quadratic in the pseudoparticle operators, and can, thus, be solved exactly.

The physical system of interacting particles is described by a grand-canonical Hamiltonian $\hat{H}$, which is related to the canonical Hamiltonian in the usual way by the additional single-particle term $-\mu\hat{N}$. The Hamiltonians, which can be treated by the extended VCA theory, generally have the form $\hat{H} = \hat{H}_t + \hat{H}_U$, where $\hat{H}_t$ consists of arbitrary one-particle terms and $\hat{H}_U$ of local two-particle terms. The physical system is defined on a large or even infinite lattice with periodic boundary conditions. The underlying lattice is now tiled into N_c clusters each one containing L orbitals (sites). We split the Hamiltonian into a cluster part $\hat{H}_{cl}$, which only describes processes within the various clusters, and the residual part $\hat{T}$, containing the intercluster processes, which consist of single-particle terms only, so that

$$\hat{H} = \hat{H}_{cl} + \hat{T} \,. \tag{2.28}$$

CPT amounts to first solving for the Hamiltonian $\hat{H}_{cl}$ and then carrying out a perturbation expansion in the intercluster Hamiltonian $\hat{T}$. Of course, within CPT one is free to add an arbitrary single-particle Hamiltonian $-\hat{\Delta}$ to the cluster Hamiltonian $\hat{H}_{cl}$ provided it is then subtracted from $\hat{T}$ so that $\hat{H}$ remains unchanged. This defines a new cluster Hamiltonian $\hat{H}'$

$$\hat{H}' \equiv \hat{H}_{cl} - \hat{\Delta} \,. \tag{2.29}$$

The physical Hamiltonian $\hat{H}$, given in Eq. (2.28), can now be expressed in terms of the new cluster Hamiltonian

$$\hat{H} = \hat{H}' + \hat{\Delta} + \hat{T} \equiv \hat{H}' + \hat{\tilde{T}} \,, \tag{2.30}$$

leading to a new "perturbation" $\hat{\tilde{T}} \equiv \hat{\Delta} + \hat{T}$. The CPT expansion is now carried out in this new "perturbation". While ideal exact results should not depend on $\hat{\Delta}$ (this occurs, for example, in the noninteracting case), in practice results do depend on $\hat{\Delta}$ due to the approximate nature of the expansion. The idea is to fix the parameters $\hat{\Delta}$ by an optimization prescription, which amounts to finding the stationary point of the grand potential Ω obtained from the perturbative expansion. The optimization prescription is put on a rigorous framework within the SFA [50]. It is straightforward to show that this procedure is equivalent to the standard VCA prescription, whereby $\hat{H}'$ is the corresponding *reference system* [77].

In the following, we consider N_c identical disconnected clusters, and denote the sites (orbitals) within a cluster by i. The position of each cluster on the large, physical lattice is specified by a lattice vector $\mathbf{R}$. Accordingly, we denote by $a_{i,\mathbf{R}}$ the annihilation operator for a boson on site i of cluster $\mathbf{R}$, and similarly for creation operators $a^\dagger_{i,\mathbf{R}}$.

In order to keep a compact notation we combine the annihilation operators of a given cluster $\mathbf{R}$ into a column vector of operators

$$\mathbf{a_R} = (a_{1,\mathbf{R}},\, a_{2,\mathbf{R}}, \ldots\, a_{L,\mathbf{R}})^T \;,$$

and correspondingly, the creation operators are row vectors $\mathbf{a}^\dagger_\mathbf{R} = (\mathbf{a_R})^\dagger$. Using these expressions we rewrite the intercluster Hamiltonian as

$$\hat{T} = \sum_{\mathbf{R}\,\mathbf{R}'} \mathbf{a}^\dagger_\mathbf{R} t(\mathbf{R}-\mathbf{R}') \mathbf{a}_{\mathbf{R}'} \;, \tag{2.31}$$

where $t(\mathbf{R}-\mathbf{R}')$ is a matrix describing the hopping terms from cluster $\mathbf{R}'$ to cluster $\mathbf{R}$, with the property $t(\mathbf{R}-\mathbf{R}') = t(\mathbf{R}'-\mathbf{R})^\dagger$. Here we have assumed translation invariance by a cluster translation vector. Similarly, we can express $\hat{\Delta}$ in terms of an intracluster hopping matrix h

$$\hat{\Delta} = \sum_{\mathbf{R}} \mathbf{a}^\dagger_\mathbf{R} h\; \mathbf{a_R} \;,$$

such that $\hat{\bar{T}}$, defined in Eq. (2.30), can be written as Eq. (2.31) with the replacement

$$t(\mathbf{R}-\mathbf{R}') \to \bar{t}(\mathbf{R}-\mathbf{R}') = t(\mathbf{R}-\mathbf{R}') + \delta_{\mathbf{R},\mathbf{R}'} h \;.$$

As explained above, the reference system consists of a sum of Hamiltonians acting on independent clusters $\mathbf{R}$

$$\hat{H}' = \sum_{\mathbf{R}} \hat{H}'(\mathbf{R}) \;.$$

Again considering translation invariance, all $\hat{H}'(\mathbf{R})$ are identical. Thus it suffices to determine numerically the ground state $|\psi_0, \mathbf{R}\rangle$, as well as single particle or single-hole excited states $|\psi_\mu, \mathbf{R}\rangle$ of a single cluster Hamiltonian $\hat{H}'(\mathbf{R})$, with corresponding eigenenergies E'_0 and E'_μ, respectively. The key idea of the approach, to be presented here, is to introduce pseudoparticle operators $b^\dagger_{\mu,\mathbf{R}}$ and $b_{\mu,\mathbf{R}} \equiv (b^\dagger_{\mu,\mathbf{R}})^\dagger$, which are defined by their matrix elements

$$\langle \psi_\mu, \mathbf{R}|\, b^\dagger_{\nu,\mathbf{R}}\, |\psi_0, \mathbf{R}\rangle = \delta_{\mu,\nu} \;. \tag{2.32}$$

In other words, the pseudoparticle operator $b^\dagger_{\mu,\mathbf{R}}$ applied to the exact many-body ground-state $|\psi_0, \mathbf{R}\rangle$ of a cluster creates the exact excited many-body state $|\psi_\mu, \mathbf{R}\rangle$. In this respect, it is of course forbidden to apply a second pseudoparticle creation operator on the excited state. This leads to the supplementary hard-core constraints $b^\dagger_{\nu,\mathbf{R}} b^\dagger_{\mu,\mathbf{R}} |\psi_0, \mathbf{R}\rangle = 0$. To neglect this hard-core constraint and to restrict to single-particle and single-hole excitations within each cluster is the approximation made here. We show below that this approximation, combined with the variational procedure discussed above, gives the same results as VCA. In particular, we obtain the same expression for the grand potential Ω, and for the Green's function. It should be mentioned, however, that within the pseudoparticle approach there is no known rigorous variational principle for Ω. One can simply heuristically state that the "best" solution is the one that "minimizes" the

energy, although, as we know from VCA, the variational solution is not always a minimum. Also for parameters, such as the chemical potential, for which Ω turns out to be a maximum, one can argue that the stationary condition is a kind of "constraint" fixing the consistency of thermodynamic quantities [78], and the corresponding parameter is a kind of "Lagrange multiplier." Nevertheless, it is not the goal of the present work to discuss this issue. Here, we want simply use this tool in order to formulate an extension of the theory to address the bosonic superfluid phase, see Sec. 2.2. The knowledge of the correction to the order parameter and of the grand-potential Ω can then guide and facilitate a rigorous extension of SFA to deal with the superfluid phase.

With the help of these operators, it is straightforward to write down a Hamiltonian which has the same energies and eigenvectors as the reference system, restricted within the subspace of single-particle and single-hole excitations from the ground state

$$\hat{H}' = N_c\ \Omega' + \sum_{\mathbf{R}} \sum_{\nu} \Delta E'_\nu\, b^\dagger_{\nu,\mathbf{R}}\, b_{\nu,\mathbf{R}}, \tag{2.33}$$

with the (positive) excitation energies $\Delta E'_\nu \equiv E'_\nu - E'_0$. Since we are interested in zero temperature $T = 0$, the grand potential of the reference system is $\Omega' \equiv E'_0$.

To proceed further, we need an expression for $\hat{\tilde{T}}$, and, thus, of the original bosonic operators $a_{i,\mathbf{R}}$, in terms of the pseudoparticle operators. For simplicity, we drop the $\mathbf{R}$ index and concentrate on a given cluster. Within the pseudoparticle approximation the operators must coincide only within the constrained subspace. We thus approximate each a_i by an operator $\hat{O}_i\,(b_\mu, b^\dagger_\mu)$ which shares the same matrix elements $\langle\psi_0| \cdot |\psi_0\rangle$, $\langle\psi_0| \cdot |\psi_\nu\rangle$, and $\langle\psi_\nu| \cdot |\psi_0\rangle$. We express $\hat{O}_i$ by means of the *ansatz*

$$\hat{O}_i\,(b_\mu, b^\dagger_\mu) = \sum_{\mu=1}^{n_p} R_{i,\mu} b_\mu + \sum_{\mu=n_p+1}^{n_s} Z_{i,\mu} b^\dagger_\mu + \gamma_i\, \mathbb{1}\ , \tag{2.34}$$

where the first sum contains the n_p indices associated with the single-particle excitations, and the second sum contains the n_h indices for the single-hole excitations. The total number of excitations taken into account is $n_s = n_p + n_h$. Here we have exploited particle-number conservation. Next, we use this expression to evaluate the following matrix elements

$$\langle\psi_0|\, \hat{O}_i\,(b_\mu, b^\dagger_\mu)\, |\psi_0\rangle = \gamma_i \stackrel{!}{=} \langle\psi_0|\, a_i\, |\psi_0\rangle \tag{2.35a}$$

$$\langle\psi_\nu|\, \hat{O}_i\,(b_\mu, b^\dagger_\mu)\, |\psi_0\rangle = Z_{i,\nu} \stackrel{!}{=} \langle\psi_\nu|\, a_i\, |\psi_0\rangle \tag{2.35b}$$

$$\langle\psi_0|\, \hat{O}_i\,(b_\mu, b^\dagger_\mu)\, |\psi_\nu\rangle = R_{i,\nu} \stackrel{!}{=} \langle\psi_0|\, a_i\, |\psi_\nu\rangle\ , \tag{2.35c}$$

where the coefficients γ_i are zero so far, since the reference system conserves the particle number. We now introduce the compact notation

$$B \equiv (b_1, \ldots, b_{n_p}, b^\dagger_{n_p+1} \ldots b^\dagger_{n_s})^T \qquad B^\dagger = (B)^\dagger\ ,$$

i. e., the first part of the vector acts on particle states, and the second part on hole states. Notice that in this form $B^\dagger$ (B) changes the number of particles by $+1$ (-1). We also introduce the Q matrix (which is the same as introduced previously) as

$$Q_{i,\nu} \equiv \begin{cases} R_{i,\nu} & \text{for } 1 \leq \nu \leq n_p \\ Z_{i,\nu} & \text{for } n_p < \nu \leq n_s \end{cases} .$$

The Q matrix can be used to express the original operators $\mathbf{a}$ and $\mathbf{a}^\dagger$ in terms of B operators [*cf.* Eq. (2.34)] in a compact form:

$$\mathbf{a} = QB \tag{2.36a}$$

$$\mathbf{a}^\dagger = B^\dagger Q^\dagger . \tag{2.36b}$$

Using the compact vector notation for B and $B^\dagger$, the reference Hamiltonian [Eq. (2.33)] can be written as

$$\hat{H}' = N_c \Omega' + \sum_{\mathbf{R}} B^\dagger_{\mathbf{R}} S \Lambda B_{\mathbf{R}} - N_c \Delta E'_h , \tag{2.37}$$

where we reintroduced the $\mathbf{R}$ dependence. Here we introduced the diagonal matrices

$$S \equiv \mathrm{diag}(\underbrace{1, \ldots, 1}_{1,\ldots,n_p}, \underbrace{-1, \ldots, -1}_{n_p+1,\ldots,n_s})$$

and

$$\Lambda = S\, \mathrm{diag}(\Delta E'_1, \ldots, \Delta E'_{n_p}, \Delta E'_{n_p+1} \ldots, \Delta E'_{n_s}) .$$

Notice that $S^2 = 1$, while Λ contains the poles of the Green's function for the reference system. The constant

$$\Delta E'_h \equiv \sum_{\mu=n_p+1}^{n_s} \Delta E'_\mu = -\,\mathrm{tr}\, g(\Lambda) ,$$

with the function

$$g(\epsilon) \equiv \epsilon \Theta(-\epsilon)$$

takes into account that some of the boson operators have been rearranged in order to obtain Eq. (2.37). The physical Hamiltonian introduced in Eq. (2.30) reads

$$\hat{H} = \hat{H}' + \sum_{\mathbf{R},\mathbf{R}'} \mathbf{a}^\dagger_{\mathbf{R}} \bar{t}(\mathbf{R} - \mathbf{R}') \mathbf{a}_{\mathbf{R}'} .$$

Using Eqs. (2.36) and (2.37) yields a quadratic expression in the B operators:

$$\hat{H} = N_c \Omega' + N_c\, \mathrm{tr}\, g(\Lambda) + \sum_{\mathbf{R}} B^\dagger_{\mathbf{R}} S \Lambda B_{\mathbf{R}} + \sum_{\mathbf{R},\mathbf{R}'} B^\dagger_{\mathbf{R}}\; Q^\dagger\; \bar{t}(\mathbf{R} - \mathbf{R}')\; Q\; B_{\mathbf{R}'} .$$

We can now introduce a Fourier transform in the cluster vectors $\mathbf{R}$

$$\begin{aligned} B_{\mathbf{q}} &= \frac{1}{\sqrt{N_c}} \sum_{\mathbf{R}} e^{i\mathbf{R}\cdot\mathbf{q}} B_{\mathbf{R}} \\ &= (b_{1,\mathbf{q}}, \ldots, b_{n_p,\mathbf{q}}, b^\dagger_{n_p+1,-\mathbf{q}}, \ldots, b^\dagger_{n_s,-\mathbf{q}})^T \ , \end{aligned} \tag{2.38}$$

leading to

$$\hat{H} = N_c \Omega' + N_c \,\mathrm{tr}\, g(\Lambda) + \sum_{\mathbf{q}} \hat{H}_{\mathbf{q}} \tag{2.39}$$

with

$$\hat{H}_{\mathbf{q}} \equiv B^\dagger_{\mathbf{q}} S M_{\mathbf{q}} B_{\mathbf{q}} \ . \tag{2.40}$$

Here, we have introduced the matrix

$$M_{\mathbf{q}} \equiv \Lambda + S \ Q^\dagger \ \bar{t}_{\mathbf{q}} \ Q \ ,$$

where

$$\bar{t}_{\mathbf{q}} \equiv \sum_{\mathbf{R}} e^{i \ \mathbf{q}\cdot\mathbf{R}} \ \bar{t}(\mathbf{R})$$

is the Fourier transform of $\bar{t}(\mathbf{R} - \mathbf{R}')$. The non-Hermitian matrix $M_{\mathbf{q}}$ is identically defined as previously.

Being quadratic in the B operators, $H_{\mathbf{q}}$ can be quite generally put into diagonal form by a multimode Bogoliubov transformation. To achieve this, we look for "normal-mode" pseudoparticles described by the vector P with the same structure as B (in the following considerations we omit the $\mathbf{q}$ dependence for simplicity)

$$P^\dagger \equiv (p_1^{s'_1}, \ldots \, p_{n_s}^{s'_{n_s}}) \qquad P = (P^\dagger)^\dagger \ ,$$

where $s'_i = \pm 1$ so that $p_i^{+1} \equiv p_i^\dagger$ is a creation and $p_i^{-1} \equiv p_i$ is an annihilation operator. The new P operator shall be connected with B via

$$B = V \, P \ ,$$

where V is a nonsingular but in general nonunitary matrix. From a physical viewpoint the nonsingularity of V corresponds to a pseudoparticle conservation, meaning that there are as many pseudoparticles B as normal-mode pseudoparticles P. The transformation V must satisfy two conditions. First it must be chosen such that P has appropriate bosonic commutation relations, i. e.,

$$[P, P^\dagger] = S' \equiv \mathrm{diag}(s'_1, \ldots, s'_{n_s}) \ .$$

This gives

$$S' \stackrel{!}{=} [P, P^\dagger] = V^{-1} [B, B^\dagger] (V^{-1})^\dagger = V^{-1} S (V^{-1})^\dagger \ ,$$

which in turn yields

$$V\ S'\ V^\dagger\ S = I \tag{2.41a}$$
$$S'\ V^\dagger\ S = V^{-1} \tag{2.41b}$$
$$V^\dagger\ S\ V = \ S' \ . \tag{2.41c}$$

The second requirement on V is

$$V^\dagger S\ M\ V \equiv E \equiv \mathrm{diag}(e_1, \ldots, e_{n_s}) \ , \tag{2.42}$$

since after the transformation from B particles to P particles the Hamiltonian in Eq. (2.40) has to be diagonal. Multiplying Eq. (2.42) from the left by VS' and using Eq. (2.41a) yields the eigenvalue equation

$$MV = VD \ ,$$

where $D \equiv \mathrm{diag}(d_1, \ldots, d_{n_s}) = S'E$ contains the eigenvalues of the non-Hermitian matrix M. From Eq. (2.43) below, where we express the Hamiltonian in terms of the normal-mode pseudoparticles, it can be seen that the diagonal elements e_i correspond to the excitation energies of the physical system. Since the energy of the physical system must be bounded from below, all e_i have to be positive and real, leading to

$$e_i = d_i s'_i > 0 \quad \forall i \ .$$

It will turn out that this stability condition is the only point, where the variables s'_i of the auxiliary operators $p_i^{s'_i}$ show up. In App. A.1 we show that, if M is completely diagonalizable with real eigenvalues and linear independent eigenvectors, which is of course not generally guaranteed for a non-Hermitian matrix M but necessary from the physical viewpoint, then V can be constructed so that both requirements of Eqs. (2.41) and (2.42) are fulfilled, and we can proceed with our analysis. If M is not completely diagonalizable or does not have real eigenvalues, the system is unstable, and it favors a different phase, which cannot be addressed by the reference system in this form. This instability toward a different phase, such as superfluidity, has to be cured by extending the reference system by proper additional variational parameters.

In terms of the P operators we obtain for the Hamiltonian

$$\begin{aligned}
\hat{H}_\mathbf{q} &= B_\mathbf{q}^\dagger\, S M_\mathbf{q}\, B_\mathbf{q} = P_\mathbf{q}^\dagger\, V_\mathbf{q}^\dagger\, S M_\mathbf{q}\, V_\mathbf{q}\, P_\mathbf{q} = P_\mathbf{q}^\dagger S' D_\mathbf{q}\, P_\mathbf{q} \\
&= \sum_\nu e_\nu (\, p_{\nu,\mathbf{q}}^\dagger\, p_{\nu,\mathbf{q}}\ \Theta(S'_{\nu,\nu}) + p_{\nu,\mathbf{q}}\, p_{\nu,\mathbf{q}}^\dagger\ \Theta(-S'_{\nu,\nu})) \\
&= \sum_\nu e_\nu\, p_{\nu,\mathbf{q}}^\dagger\, p_{\nu,\mathbf{q}} + \sum_\nu e_\nu \Theta(-S'_{\nu,\nu}) \\
&= \sum_\nu e_\nu\, p_{\nu,\mathbf{q}}^\dagger\, p_{\nu,\mathbf{q}} - \mathrm{tr}\, g(D_\mathbf{q}) \ .
\end{aligned} \tag{2.43}$$

In the last line we have exploited the fact that in order for the system to be stable, i. e., the energy be bounded from below, all e_ν must be positive.

Inserting this expression in Eq. (2.39) yields the Hamiltonian in terms of diagonal normal modes. From this result one obtains immediately the grand-canonical ground-state energy per cluster

$$\Omega = \Omega' + \operatorname{tr} g(\Lambda) - \frac{1}{N_c} \sum_{\mathbf{q}} \operatorname{tr} g(D_{\mathbf{q}}) \; .$$

As discussed, Λ and $D_{\mathbf{q}}$ are diagonal matrices containing the poles of the reference Green's function and physical Green's function, respectively. Therefore, this expression being equivalent to Eq. (2.9) (see also Refs. [54, 51, 73, 50]) is equivalent to the zero-temperature VCA grand potential.

By using the expression for the Green's function of the noninteracting normal modes

$$\ll p_\alpha; p_\beta^\dagger \gg = \frac{\delta_{\alpha,\beta}}{\omega - e_\alpha} \; ,$$

we readily obtained the Green's function for the physical system

$$\begin{aligned} G_{\mathbf{q}}(\omega) \equiv & \ll a_{\mathbf{q}}; \, a_{\mathbf{q}}^\dagger \gg = Q \ll B_{\mathbf{q}}; \, B_{\mathbf{q}}^\dagger \gg Q^\dagger \\ & = Q V_{\mathbf{q}} \ll P_{\mathbf{q}}; \, P_{\mathbf{q}}^\dagger \gg V_{\mathbf{q}}^\dagger Q^\dagger \\ & = Q V_{\mathbf{q}} (S' \omega - S' D_{\mathbf{q}} \,)^{-1} V_{\mathbf{q}}^\dagger Q^\dagger \\ & = Q V_{\mathbf{q}} (\omega - D_{\mathbf{q}})^{-1} S' V_{\mathbf{q}}^\dagger Q^\dagger \; . \end{aligned}$$

By simple algebra this expression can be rewritten such that it is independent of the auxiliary quantities S' and V and thus equivalent to Eq. (2.19)

$$\begin{aligned} G_{\mathbf{q}}(\omega) &= Q V_{\mathbf{q}} (\omega - V_{\mathbf{q}}^{-1} M_{\mathbf{q}} V_{\mathbf{q}})^{-1} V_{\mathbf{q}}^{-1} S Q^\dagger \\ &= Q (\omega - M_{\mathbf{q}})^{-1} S Q^\dagger \; , \end{aligned} \tag{2.44}$$

where we have used Eqs. (2.41) and (2.42).

We, therefore, succeeded in proving that, for normal bosons, the pseudoparticle approach yields the same Green's function and grand potential as VCA. For fermions, this was shown in Ref. [52], see appendix therein. This result holds for $T = 0$, although extension to $T > 0$ is straightforward.

2.2. Correlated lattice bosons in the superfluid phase

In this section, we extend VCA to the symmetry broken, superfluid phase of lattice bosons. To achieve this, we first adopt the pseudoparticle approach to the symmetry broken phase. While the pseudoparticle formalism is equivalent to VCA in the normal phase of both bosonic and fermionic systems, it lacks the rigorous theoretical framework provided by SFA. In particular, there is no genuine variational principle explaining why one should look for a saddle point in the grand potential. Therefore, we subsequently put the results obtained within the pseudoparticle approach into a rigorous framework

by developing an extended SFA, which is capable to deal with the bosonic superfluid phase.

Within our extension of VCA to the superfluid phase we obtain for the grand potential

$$\begin{aligned}\Omega = \Omega' - \frac{1}{2N_c}\operatorname{Tr}\ln(-G) + \frac{1}{2N_c}\operatorname{Tr}\ln(-G') - \frac{1}{2}\operatorname{tr} h \\ + \frac{1}{2}\langle A^\dagger\rangle G^{-1}_{(0)}\langle A\rangle - \frac{1}{2}\langle A^\dagger\rangle' G'^{-1}_{(0)}\langle A\rangle' \ .\end{aligned} \tag{2.45}$$

The first three terms on the right hand side are essentially identical to those which are also present in standard VCA expressions. Particularly, Ω' is the grand potential (per cluster) of the reference system, and G' and G are the connected Green's functions of the reference and of the physical system, respectively. However, they are expressed in the Nambu representation, which explains the additional factor $1/2$ and the fourth term in comparison with previous results [51, 69, 54]. The suffix (0) used in the second line of Eq. (2.45) means that the corresponding Green's functions are calculated for $\mathbf{q} = \mathbf{0}$ and $\omega = 0$, where $\mathbf{q}$ is the superlattice vector associated to the cluster tiling, and ω is the Matsubara frequency. As usual within VCA theory, the two Green's functions share the same self-energy. The expectation values $\langle A\rangle'$ and $\langle A\rangle$ are the corresponding condensate densities, again in Nambu (vector) notation. The latter are connected by the relation

$$G^{-1}_{(0)}\langle A\rangle = F + G'^{-1}_{(0)}\langle A\rangle' \ , \tag{2.46}$$

where the vector F describes the strength of the source-and-drain term which is introduced in the reference system in order to explicitly break $U(1)$ symmetry. The value of F [see Eq. (2.50)] has to be determined from the variational principle. In addition to the formula for the grand potential Ω, we evaluate expressions for other quantities, which are useful for describing the superfluid phase. In particular, we derive expressions for the normal and anomalous Green's functions, the particle density, and the condensate density.

2.2.1. Pseudoparticle approach

When trying to apply VCA to bosonic lattice systems in regions of the phase diagram outside the Mott phase, one encounters instabilities which manifest in the form of non-causal Green's functions, i. e., in spectral functions with negative (positive) spectral weight for positive (negative) frequencies ω, or in complex poles. Within the pseudoparticle approach these instabilities show up as complex eigenvalues or negative diagonal elements of the matrix E. This kind of instability is well known in approaches based on the bosonic Bogoliubov approximation, such as the spin-wave approximation.

Quite generally, such an instability signals the occurrence of a phase transition toward a new phase. In the case of lattice bosons, this new phase can be the superfluid phase, which is accompanied by a Bose-Einstein condensation. Bose-Einstein condensation is described by a finite value of the order parameter $\langle a_{\mathbf{R}}\rangle$. This suggests to include a source-and-drain term in the reference system, which breaks the $U(1)$ symmetry of the

reference system, leading to the "perturbation" $\hat{\bar{T}}$ [see Eq. (2.30)],

$$\hat{\bar{T}} = \sum_{\mathbf{R},\mathbf{R}'} \mathbf{a}_{\mathbf{R}}^{\dagger}\, \bar{t}(\mathbf{R}-\mathbf{R}')\, \mathbf{a}_{\mathbf{R}'} + \sum_{\mathbf{R}} (\mathbf{a}_{\mathbf{R}}^{\dagger}\mathbf{f}_{\mathbf{R}} + \mathbf{f}_{\mathbf{R}}^{\dagger}\mathbf{a}_{\mathbf{R}}) \;, \tag{2.47}$$

where $\mathbf{f}_{\mathbf{R}} \equiv (f_1,\, f_2 \,\ldots\, f_L)^T$ is a vector of size L and is identical for all clusters. The index $\mathbf{R}$, however, will be kept for notational reasons. In this section, we often adopt symbols already defined for the normal phase, which have a similar meaning but a sometimes a slightly different definition.

Due to these terms, the reference system Hamiltonian does not conserve particle number anymore. Its eigenstates will thus consist of superpositions of states with different particle numbers. Numerically, a cutoff in the maximum number of boson is necessary in order to solve the reference system on the cluster level exactly. We again introduce pseudoparticle operators $\mathbf{b}_{\mathbf{R}}$ connecting the ground state with excited states. Note that we cannot distinguish between particle or hole states anymore. The pseudoparticles are defined by Eq. (2.32) and are connected to the original boson operators $\mathbf{a}_{\mathbf{R}}$ by means of Eq. (2.34). Now, all matrix elements in Eq. (2.35) are nonzero in general. Therefore, the two sums over μ in Eq. (2.34) are extended to $\mu = 1, \ldots, n_s$, where n_s is the number of excited states considered in each cluster.

For the following considerations it is convenient to express the boson operators within a Nambu notation. For the particle operators we introduce in real space

$$A_{\mathbf{R}} = \begin{pmatrix} \mathbf{a}_{\mathbf{R}} \\ \mathbf{a}_{\mathbf{R}}^{\dagger T} \end{pmatrix} \;,$$

which after a Fourier transformation in the cluster vectors, see Eq. (2.38), becomes

$$A_{\mathbf{q}} = \begin{pmatrix} \mathbf{a}_{\mathbf{q}} \\ \mathbf{a}_{-\mathbf{q}}^{\dagger T} \end{pmatrix} \;.$$

For pseudoparticle operators we have in real space

$$B_{\mathbf{R}} \equiv (b_{1,\mathbf{R}},\, b_{2,\mathbf{R}},\, \ldots, b_{n_s,\mathbf{R}},\, b_{1,\mathbf{R}}^{\dagger},\, \ldots, b_{n_s,\mathbf{R}}^{\dagger})^T$$

and in $\mathbf{q}$ space

$$B_{\mathbf{q}} \equiv (b_{1,\mathbf{q}},\, b_{2,\mathbf{q}},\, \ldots, b_{n_s,\mathbf{q}},\, b_{1,-\mathbf{q}}^{\dagger},\, \ldots, b_{n_s,-\mathbf{q}}^{\dagger})^T \;.$$

Similarly to Sec. 2.1.5, we have an approximate linear relation between the A operators and the B operators of the form

$$A_{\mathbf{R}} = Q B_{\mathbf{R}} + \Gamma \;.$$

After the Fourier transformation in the cluster vectors it reads

$$A_{\mathbf{q}} = Q B_{\mathbf{q}} + \Gamma_{\mathbf{q}} \;. \tag{2.48}$$

Here,

$$\Gamma_{\mathbf{q}} = \sqrt{N_c}\delta_{\mathbf{q}}\Gamma \ ,$$

with

$$\Gamma = (\gamma_1,\, \gamma_2 \,\ldots\, \gamma_L,\, \gamma_1^*,\, \gamma_2^* \,\ldots\, \gamma_L^* \,)^T \ ,$$

and the $(2L) \times (2n_s)$ matrix

$$Q = \begin{pmatrix} R & Z \\ Z^* & R^* \end{pmatrix} \ .$$

The constants $\gamma_i \equiv \langle\psi_0|\, a_i \,|\psi_0\rangle$, will be nonzero as the reference system does not conserve the particle number.

In terms of pseudoparticle operators we can again write the reference Hamiltonian for a cluster $\mathbf{R}$, similarly to Eq. (2.37) as

$$\hat{H}'_{\mathbf{R}} = \Omega' + \frac{1}{2} B^\dagger_{\mathbf{R}} S \Lambda B_{\mathbf{R}} + \frac{1}{2} \operatorname{tr} g(\Lambda) \ . \tag{2.49}$$

Here, the matrices S and Λ have a slightly different definition

$$S \equiv \operatorname{diag}(\underbrace{1, \ldots, 1}_{1,\ldots,n_s}, \underbrace{-1, \ldots, -1}_{n_s+1,\ldots,2n_s}) \ ,$$

and

$$\Lambda = S \ \operatorname{diag}(\Delta E'_1,\, \Delta E'_2 \,\ldots\, \Delta E'_{n_s},\, \Delta E'_1,\, \Delta E'_2 \,\ldots\, \Delta E'_{n_s}) \ .$$

To express the "perturbation" $\hat{\bar{T}}$ of Eq. (2.47), we need to introduce a similar Nambu notation for the source-and-drain terms, which, being $\mathbf{R}$ independent, become in $\mathbf{q}$ space

$$\begin{aligned} F_{\mathbf{q}} &= \sqrt{N_c}\delta_{\mathbf{q}} F \\ F &\equiv \begin{pmatrix} \mathbf{f} \\ \mathbf{f}^{\dagger T} \end{pmatrix} \ . \end{aligned} \tag{2.50}$$

After the Fourier transformation in the cluster vectors, we can rewrite

$$\begin{aligned} \hat{\bar{T}} = \hat{T} + \hat{\Delta} = \sum_{\mathbf{q}} \Big(& \frac{1}{2} A^\dagger_{\mathbf{q}} \bar{T}_{\mathbf{q}} A_{\mathbf{q}} - \frac{1}{2} \operatorname{tr} \bar{t}_{\mathbf{q}} \\ & + \frac{1}{2} \left[F^\dagger_{\mathbf{q}} A_{\mathbf{q}} + A^\dagger_{\mathbf{q}} F_{\mathbf{q}} \right] \Big) \ , \end{aligned}$$

where $\bar{T}_{\mathbf{q}} = \operatorname{diag}(\bar{t}_{\mathbf{q}},\, \bar{t}^T_{-\mathbf{q}})$.

Replacing the A operators in terms of the B operators with the help of Eq. (2.48), and combining Eq. (2.49) with the expression above for $\hat{\bar{T}}$, we finally obtain the complete

Hamiltonian, defined in Eq. (2.30), in terms of pseudoparticles

$$\begin{aligned}\hat{H} = N_c\Omega' + \frac{N_c}{2}\operatorname{tr} g(\Lambda) + \sum_{\mathbf{q}}\Big\{ -\frac{1}{2}\operatorname{tr}\bar{t}_{\mathbf{q}} \\ + \frac{1}{2}\Gamma_{\mathbf{q}}^\dagger \bar{T}_{\mathbf{q}}\Gamma_{\mathbf{q}} + \frac{1}{2}B_{\mathbf{q}}^\dagger \underbrace{\Big[S\Lambda + Q^\dagger \bar{T}_{\mathbf{q}} Q\Big]}_{SM_{\mathbf{q}}} B_{\mathbf{q}} \\ + \frac{1}{2}\big[(\Gamma_{\mathbf{q}}^\dagger \bar{T}_{\mathbf{q}} + F_{\mathbf{q}}^\dagger)QB_{\mathbf{q}} + F_{\mathbf{q}}^\dagger\Gamma_{\mathbf{q}} + h.c.\big]\Big\} .\end{aligned}$$

The expression can be further simplified by using the fact that F and Γ are equal in all clusters, and thus have only $\mathbf{q} = \mathbf{0}$ components. In addition we take advantage of

$$\sum_{\mathbf{q}} \operatorname{tr}\bar{t}_{\mathbf{q}} = N_c \operatorname{tr}\bar{t}(\mathbf{R} - \mathbf{R}' = 0) = N_c \operatorname{tr} h \,, \tag{2.51}$$

since $t(\mathbf{R} - \mathbf{R}' = 0) = 0$ is a pure intercluster term. For notational convenience we introduce

$$\tilde{F}^\dagger = F^\dagger + \Gamma^\dagger \bar{T}_{\mathbf{0}} \,. \tag{2.52}$$

This gives

$$\begin{aligned}\hat{H} \quad &= N_c\Omega' + \frac{N_c}{2}\operatorname{tr} g(\Lambda) - \frac{N_c}{2}\operatorname{tr} h + \frac{N_c}{2}\Gamma^\dagger \bar{T}_{\mathbf{0}}\Gamma \\ &+ \frac{N_c}{2}(F^\dagger\Gamma + h.c.) + \frac{\sqrt{N_c}}{2}(\tilde{F}^\dagger Q B_{\mathbf{0}} + h.c.) \\ &+ \frac{1}{2}\sum_{\mathbf{q}} B_{\mathbf{q}}^\dagger SM_{\mathbf{q}} B_{\mathbf{q}} \,.\end{aligned} \tag{2.53}$$

The term linear in B can be eliminated by a shift

$$\tilde{B}_{\mathbf{q}} \equiv B_{\mathbf{q}} + X_{\mathbf{q}} \,,$$

where clearly only the $\mathbf{q} = \mathbf{0}$ term of $X_{\mathbf{q}}$ is nonzero. Considering only the $\mathbf{q} = \mathbf{0}$ part of Eq. (2.53), which we term $Y_{\mathbf{0}}$, and plugging in the shifted operators, we obtain

$$\begin{aligned}Y_{\mathbf{0}} \equiv \frac{1}{2}(\tilde{B}_{\mathbf{0}} - X_{\mathbf{0}})^\dagger SM_{\mathbf{0}}(\tilde{B}_{\mathbf{0}} - X_{\mathbf{0}}) \\ + \frac{\sqrt{N_c}}{2}(\tilde{F}^\dagger Q(\tilde{B}_{\mathbf{0}} - X_{\mathbf{0}}) + h.c.) \,.\end{aligned}$$

The linear term is eliminated by setting

$$X_{\mathbf{0}} = \sqrt{N_c} M_{\mathbf{0}}^{-1} S\, Q^\dagger \tilde{F} \,, \tag{2.54}$$

yielding for the $\mathbf{q} = \mathbf{0}$ term above

$$Y_{\mathbf{0}} = \frac{1}{2}\tilde{B}_{\mathbf{0}}^\dagger SM_{\mathbf{0}}\tilde{B}_{\mathbf{0}} + \frac{N_c}{2}\tilde{F}^\dagger G_{(0)}\tilde{F} \,,$$

where

$$G_{(0)} \equiv G_{\mathbf{q}=\mathbf{0}}(\omega = 0) = -Q\ M_{\mathbf{0}}^{-1} S Q^{\dagger}\ , \tag{2.55}$$

which is the Green's function defined in (2.60) but evaluated for $\mathbf{q} = 0$ and $\omega = 0$. In total we have

$$\hat{H} = N_c\ C + \sum_{\mathbf{q}\in \mathrm{BZ}/2} \tilde{B}_{\mathbf{q}}^{\dagger} S M_{\mathbf{q}} \tilde{B}_{\mathbf{q}} \tag{2.56}$$

with the constant terms

$$\begin{aligned} C = \Omega' &+ \frac{1}{2}\,\mathrm{tr}\, g(\Lambda) - \frac{1}{2}\,\mathrm{tr}\, h + \frac{1}{2}(F^{\dagger}\Gamma + h.c.) \\ &+ \frac{1}{2}\Gamma^{\dagger}\bar{T}_{\mathbf{0}}\Gamma + \frac{1}{2}\tilde{F}^{\dagger} G_{(0)} \tilde{F}\ . \end{aligned}$$

In the last term of Eq. (2.56), we restrict the summation over half of the Brillouin zone, which we denote by $\mathbf{q} \in \mathrm{BZ}/2$, and thus removed the factor $1/2$ in front of the sum. Due to Nambu representation, two summands with $+\mathbf{q}$ and $-\mathbf{q}$ are identical and therefore the restriction to half of the Brillouin zone is convenient. In our convention, the $\mathbf{q} = \mathbf{0}$ term is included in the sum and retains the factor $1/2$.

Condensate density

Before turning to the diagonalization of the Hamiltonian in Eq. (2.56), let us evaluate the condensate density. Since there are no terms linear in $\tilde{B}$, its expectation value $\langle \tilde{B} \rangle$ vanishes. Therefore, we can immediately calculate the condensate density

$$\begin{aligned} \langle A_{\mathbf{q}} \rangle &= \sqrt{N_c}\, \delta_{\mathbf{q}}\ \langle A \rangle \\ &= Q\, \langle B_{\mathbf{q}} \rangle + \Gamma_{\mathbf{q}} = -Q X_{\mathbf{q}} + \Gamma_{\mathbf{q}} \\ &= \sqrt{N_c}\, \delta_{\mathbf{q}}\, [\Gamma + G_{(0)}(F + \bar{T}_{\mathbf{0}}\Gamma)]\ , \end{aligned} \tag{2.57}$$

where we used Eqs. (2.50), (2.52), (2.54) and (2.55). We now exploit the fact that

$$\Gamma = \langle A \rangle'$$

is the condensate density in the reference system. From the Dyson equation for the Green's function of the physical and the reference system we have

$$G_{\mathbf{q}}(\omega)^{-1} = G'(\omega)^{-1} - \bar{T}_{\mathbf{q}}\ .$$

By multiplying (2.57) with $G_{(0)}^{-1}$ we obtain

$$\begin{aligned} G_{(0)}^{-1}\, \langle A \rangle &= G_{(0)}'^{-1}\, \langle A \rangle' - \bar{T}_{\mathbf{0}}\, \langle A \rangle' + F + \bar{T}_{\mathbf{0}}\, \langle A \rangle' \\ &= G_{(0)}'^{-1}\, \langle A \rangle' + F\ , \end{aligned}$$

which corresponds to Eq. (2.46).

Diagonalization of the Hamiltonian

The Hamiltonian of Eq. (2.56) is finally quadratic and its diagonalization proceeds in the same way as in Sec. 2.1.5. Again we introduce P operators

$$\tilde{B}_{\mathbf{q}} = V_{\mathbf{q}} P_{\mathbf{q}} \ ,$$

and find the solution of the non-Hermitian eigenvalue equation

$$M_{\mathbf{q}} V_{\mathbf{q}} = V_{\mathbf{q}} D_{\mathbf{q}} \ ,$$

where $V_{\mathbf{q}}$ satisfies the relation

$$V_{\mathbf{q}} S' V_{\mathbf{q}}^{\dagger} S = I \ .$$

The diagonal matrix S', which is in principle $\mathbf{q}$-dependent as well, consists of $+1$ or -1 terms. It is chosen according to the prescription derived in App. A.1. The stability condition is again that the pseudoparticle eigenenergies

$$S' D_{\mathbf{q}} = \mathrm{diag}(e_{1\mathbf{q}}, \ldots, e_{2n_s\mathbf{q}})$$

are all positive. The physical Hamiltonian in terms of P-particles now reads

$$\begin{aligned} \hat{H} &= \sum_{\mathbf{q}\in \mathrm{BZ}/2} P_{\mathbf{q}}^{\dagger} S' D_{\mathbf{q}} P_{\mathbf{q}} + N_c \, C \\ &= \sum_{\mathbf{q}\in \mathrm{BZ}/2} \sum_{\nu} e_{\nu,\mathbf{q}} p_{\nu,\mathbf{q}}^{\dagger} p_{\nu,\mathbf{q}} - \sum_{\mathbf{q}\in \mathrm{BZ}/2} g(D_{\mathbf{q}}) + N_c \, C \ . \end{aligned} \tag{2.58}$$

From that we readily obtain (see App. A.2) the grand potential per cluster of the physical system Ω, which is the ground state expectation value $\langle \hat{H} \rangle / N_c$

$$\begin{aligned} \Omega = \Omega' &+ \frac{1}{2} \, \mathrm{tr} \, g(\Lambda) - \frac{1}{N_c} \sum_{\mathbf{q}\in \mathrm{BZ}/2} g(D_{\mathbf{q}}) - \frac{1}{2} \, \mathrm{tr} \, h \\ &+ \frac{1}{2} \, \langle A^{\dagger} \rangle \, G_{(0)}^{-1} \, \langle A \rangle - \frac{1}{2} \, \langle A^{\dagger} \rangle' \, G_{(0)}'^{-1} \, \langle A \rangle' \ . \end{aligned} \tag{2.59}$$

By considering the fact that Λ and $D_{\mathbf{q}}$ contain the poles of G' and G, respectively, we conclude that, in the $T \to 0$ limit

$$\begin{aligned} \lim_{T\to 0} &\left[\frac{1}{2} \, \mathrm{Tr} \ln(-G') - \frac{1}{2} \, \mathrm{Tr} \ln(-G) \right] \\ &= \frac{N_c}{2} \, \mathrm{tr} \, g(\Lambda) - \sum_{\mathbf{q}\in \mathrm{BZ}/2} g(D_{\mathbf{q}}) \ . \end{aligned}$$

Thus, Eq. (2.59) is equivalent to Eq. (2.45) in the introduction in the $T = 0$ limit. An extension to $T > 0$ is straight forward.

The *connected* Green's function now contains anomalous contributions, but formally is obtained as in Eq. (2.44),

$$\begin{aligned} G_{\mathbf{q}}(\omega) &\equiv \ll A_{\mathbf{q}};\, A_{\mathbf{q}}^{\dagger} \gg_c = Q \ll \tilde{B}_{\mathbf{q}};\, \tilde{B}_{\mathbf{q}}^{\dagger} \gg Q^{\dagger} \\ &= QV_{\mathbf{q}} \ll P_{\mathbf{q}};\, P_{\mathbf{q}}^{\dagger} \gg V_{\mathbf{q}}^{\dagger} Q^{\dagger} \\ &= QV_{\mathbf{q}} (S'\omega - S'D_{\mathbf{q}})^{-1} V_{\mathbf{q}}^{\dagger} Q^{\dagger} \\ &= QV_{\mathbf{q}} (\omega - D_{\mathbf{q}})^{-1} V_{\mathbf{q}}^{-1} S Q^{\dagger} \\ &= Q(\omega - M_{\mathbf{q}})^{-1} S Q^{\dagger} \,, \end{aligned} \tag{2.60}$$

where we have neglected the shifts Γ and $X_{\mathbf{0}}$ since they only contribute to disconnected parts. Notice that Eq. (2.60) is a $2L \times 2L$ matrix in Nambu and cluster-site space. The $\mathbf{q}$ vectors above refer to the reduced Brillouin zone originating from the cluster tiling, therefore G is expressed in a mixed representation. In translation-invariant systems, the Green's function is expected to be diagonal in the wave vectors $\mathbf{k}$ of the full Brillouin zone. This symmetry is notoriously broken in cluster methods such as VCA or C-DMFT. In order to obtain a $\mathbf{k}$-diagonal 2×2 Nambu Green's function $G(\mathbf{k}, \omega)$ we need to apply a periodization prescription [64]. This gives

$$G(\mathbf{k}, \omega) = \mathbf{v}_{\mathbf{k}}^{\dagger} G_{\mathbf{k}}(\omega) \mathbf{v}_{\mathbf{k}} \,,$$

where

$$\mathbf{v}_{\mathbf{k}}^{\dagger} \equiv \frac{1}{\sqrt{L}} \begin{pmatrix} e^{-i\mathbf{k}\mathbf{r}_1} & \dots & e^{-i\mathbf{k}\mathbf{r}_L} & 0 & \dots & 0 \\ 0 & \dots & 0 & e^{-i\mathbf{k}\mathbf{r}_1} & \dots & e^{-i\mathbf{k}\mathbf{r}_L} \end{pmatrix} , \tag{2.61}$$

and $\mathbf{r}_i$ is the position of site i within the cluster.

A nontrivial test for VCA is the noninteracting limit, for which this approximation becomes exact. In Appendix A.3 we carry out this check for the noninteracting BH model, i. e., we set $U = 0$, and for a reference system consisting of single-site clusters. In this test case the grand potential Ω of the physical system can be evaluated analytically both using the VCA prescription as well as directly from the Hamiltonian of noninteracting lattice bosons.

Particle density and momentum distribution

The total particle density is defined as

$$n = \frac{1}{N} \sum_{\mathbf{q}} \sum_{i} \langle a_{i,\mathbf{q}}^{\dagger} a_{i,\mathbf{q}} \rangle \,,$$

where $N = N_c\, L$ is the total number of lattice sites present in the physical system. The particle density can be easily expressed in Nambu formalism

$$\begin{aligned} n &= \frac{1}{2N}\sum_{\mathbf{q}}\sum_{i}(\langle a^\dagger_{i,\mathbf{q}} a_{i,\mathbf{q}}\rangle + \langle a_{i,-\mathbf{q}} a^\dagger_{i,-\mathbf{q}}\rangle) - \frac{1}{2} \\ &= -\frac{1}{2} + \frac{1}{2N}\sum_{\mathbf{q}}\langle A^\dagger_{\mathbf{q}} A_{\mathbf{q}}\rangle \\ &= -\frac{1}{2} + \frac{1}{2N}\sum_{\mathbf{q}}(\langle P^\dagger_{\mathbf{q}} V^\dagger_{\mathbf{q}} Q^\dagger Q V_{\mathbf{q}} P_{\mathbf{q}}\rangle + \langle A_{\mathbf{q}}\rangle^\dagger \langle A_{\mathbf{q}}\rangle) \\ &= -\frac{1}{2} + \frac{1}{2N}\sum_{\mathbf{q}}\mathrm{tr}[\Theta(-D_{\mathbf{q}}) V^\dagger_{\mathbf{q}} Q^\dagger\ Q V_{\mathbf{q}}] + \frac{1}{2L}\langle A^\dagger\rangle \langle A\rangle\ , \end{aligned} \tag{2.62}$$

where the last term describes the contribution from the condensate, which can be deduced from Eq. (2.57). The term with the sum over $\mathbf{q}$ can be rewritten to obtain the known form of the particle density [54]

$$\begin{aligned} n &= -\frac{1}{2} - \frac{1}{2N}\sum_{\mathbf{q}}\mathrm{tr}[\Theta(-D_{\mathbf{q}}) S' V^\dagger_{\mathbf{q}} Q^\dagger Q V_{\mathbf{q}}] + \frac{1}{2L}\langle A^\dagger\rangle \langle A\rangle \\ &= -\frac{1}{2} - \frac{1}{2N}\sum_{\mathbf{q}}\mathrm{tr}[\Theta(-D_{\mathbf{q}}) V^{-1}_{\mathbf{q}} S Q^\dagger Q V_{\mathbf{q}}] + \frac{1}{2L}\langle A^\dagger\rangle \langle A\rangle\ . \end{aligned}$$

The momentum distribution $n(\mathbf{k})$ can be extracted by the Fourier transform within the cluster leading to

$$\begin{aligned} n(\mathbf{k}) = &-\frac{1}{2N} + \frac{\delta_{\mathbf{k}}}{2L}\langle A^\dagger\rangle \langle A\rangle \\ &+ \frac{1}{2N}\mathrm{tr}[\mathbf{v}^\dagger_{\mathbf{k}} Q V_{\mathbf{k}}\, \Theta(-D_{\mathbf{k}}) V^\dagger_{\mathbf{k}} Q^\dagger \mathbf{v}_{\mathbf{k}}]\ , \end{aligned}$$

where $\mathbf{v}^\dagger_{\mathbf{k}}$ is given by Eq. (2.61).

2.2.2. Self-energy functional approach

Let us summarize the key idea of SFA due to M. Potthoff [49]. The starting point is an appropriate functional

$$\hat{\Omega}[\Sigma, G_0^{-1}, H_U] \equiv \hat{\mathcal{F}}[\Sigma, H_U] + \hat{\mathcal{E}}[\Sigma, G_0^{-1}]\ ,$$

which consists of a functional $\hat{\mathcal{F}}$ of the self-energy, the Legendre transform of the Luttinger-Ward functional, which is universal in the sense that it depends on the interaction part (H_U) of the Hamiltonian but not on the single particle part. The latter enters via the free Green's function G_0^{-1} in the second functional, which is explicitly known

$$\hat{\mathcal{E}}[\Sigma, G_0^{-1}] \equiv -\beta\,\mathrm{tr}\ln(\Sigma - G_0^{-1})$$

The functional $\hat{\Omega}[\Sigma, G_0^{-1}, H_U]$ has three key features, which are crucial for VCA.

a) The non-universal part $\hat{\mathcal{E}}$ enters additively in form of a known functional and the many-body aspects are described by a universal functional independent of the single particle Hamiltonian, or, equivalently, independent of G_0^{-1}.

b) The self-energy of the physical system, characterized by H_U and G_0^{-1} is a stationary point of the functional $\hat{\Omega}$ with respect to Σ.

c) The value of $\hat{\Omega}$ at the stationary point is equal to the thermodynamic grand potential.

Our goal is to generalize this approach to the superfluid phase. Besides the self-energy, which is the interaction correction of the inverse Green's function, we need the corresponding companion that describes the interaction correction to the order parameter, which we call D.

Once the appropriate form of D has been determined, we need a functional

$$\hat{\Omega}_s[\Sigma, D, F, G_0^{-1}, H_U] \equiv \hat{\mathcal{F}}[\Sigma, D, H_U] + \hat{\mathcal{E}}[\Sigma, D, G_0^{-1}, F] \ ,$$

in the self-energy Σ and D with the following features.

a) $\hat{\mathcal{F}}$ is again a universal functional, now in Σ and D. The non-universal part $\hat{\mathcal{E}}$ is explicitly known and carries the dependence on G_0^{-1} and the symmetry breaking source-field F.

b) The functional is again stationary at the exact self-energy Σ and the exact D of the physical system, characterized by H_U, G_0^{-1} and F.

c) The value of $\hat{\Omega}_s$ at the stationary point is equal to the thermodynamic grand potential.

The sought-for functional $\hat{\Omega}_s$, to be derived in this section, will turn out to be (see below for a definition of the quantities)

$$2\beta\hat{\Omega}_s[\Sigma,\, D, G_0^{-1}, F] = \hat{\mathcal{F}}[\Sigma, D] + \hat{\mathcal{E}}[\Sigma,\, D, G_0^{-1}, F] \tag{2.63}$$

$$\hat{\mathcal{E}}[\Sigma,\, D, G_0^{-1}, F] \equiv \beta \,\mathrm{Tr}\ln[(G_0^{-1} - \Sigma)\; G_\infty] + (\bar{D} - \bar{F})(G_0^{-1} - \Sigma)^{-1}(D - F) \ . \tag{2.64}$$

In the normal phase, it is identical to the functional introduced by M. Potthoff. The additional factor 2 is due to the Nambu Green's functions. Moreover, the expression for the grand potential obtained with the help of a so-called reference system, see Eq. (2.91) below, is identical to the one obtained within the pseudoparticle approach, see Sec. 2.2.1.

We start out from the partition function Z of a bosonic many-body system, which in a functional integral representation reads

$$Z = \int \mathcal{D}A \; e^{-S} \ , \tag{2.65}$$

where S is the action, which in general can be written as, see App. B.2

$$S = -\frac{1}{2}\int d\tau \int d\tau'\, \bar{A}(\tau')\, G_0^{-1}(\tau', \tau)\, A(\tau) \\ - \int d\tau \left[\bar{F}(\tau)\, A(\tau) - H_U(A(\tau))\right] . \tag{2.66}$$

In view of treating the superfluid phase we have adopted a Nambu notation in which the bosonic fields are expressed in a vector representation

$$A(\tau) \equiv \begin{pmatrix} a_1(\tau) \\ \vdots \\ a_N(\tau) \\ \bar{a}_1(\tau) \\ \vdots \\ \bar{a}_N(\tau) \end{pmatrix} . \tag{2.67}$$

The indices 1 through N denote the corresponding single-particle orbitals (for example, lattice sites) where the boson operators act, and $a_i(\tau)$ ($\bar{a}_i(\tau)$) are the fields associated with the annihilation (creation) of a boson in the orbital i. The adjoint field is defined as

$$\bar{A}(\tau) \equiv (\bar{a}_1(\tau), \cdots, \bar{a}_N(\tau), a_1(\tau), \cdots, a_N(\tau)) . \tag{2.68}$$

It can be expressed in terms of $A(\tau)$ with the help of the matrix $\mathcal{T}$, which exchanges the first N entries of a vector with the last N ones:

$$\bar{A}(\tau) = A(\tau)^T \mathcal{T} . \tag{2.69}$$

The operator $\mathcal{T}$ has the properties $\mathcal{T}^2 = \mathbb{1}$, and $\mathcal{T} = \mathcal{T}^T$. The action in Eq. (2.66) also contains the source fields

$$\bar{F} \equiv \left(f_1, \cdots f_N, \bar{f}_1, \cdots, \bar{f}_N\right) \quad \text{and} \quad F = \mathcal{T}\bar{F}^T ,$$

which are zero for the physical system of interest, the boson interaction described by H_U, as well as the $2N \times 2N$ noninteracting Green's function matrix $G_0(\tau', \tau)$. Eq. (2.65) with Eq. (2.66) defines the corresponding grand potential as a functional of G_0^{-1} and F

$$\hat{\tilde{\Omega}}_s[G_0^{-1}, F] \equiv -\frac{1}{\beta} \ln \hat{Z} , \tag{2.70}$$

where β is the inverse temperature. Here and in the following, we mark functionals with a hat " ˆ ", and omit their arguments whenever they are obvious. The noninteracting Green's function has the matrix structure (see App. B.3)

$$G_0^{-1}(\tau', \tau) = -\delta(\tau - \tau') \begin{pmatrix} \partial_\tau + \mathbf{t} & 0 \\ 0 & -\partial_\tau + \mathbf{t} \end{pmatrix} , \tag{2.71}$$

where $\mathbf{t}$ is the single-particle Hamiltonian matrix.

In the following, we carry out a sequence of Legendre transformations starting from $\hat{\tilde{\Omega}}_s$, ultimately leading to a universal functional $\hat{\mathcal{F}}[\Sigma, D]$ of the self-energy Σ and of a suitable quantity D defined in Eq. (2.82a). The functional $\hat{\mathcal{F}}$ is the generalization of the self-energy functional [49, 50, 51] to the superfluid phase, where a nonvanishing expectation value $\mathcal{A}(\tau) \equiv \langle A(\tau) \rangle$ of the boson operators A exists. The functional $\hat{\mathcal{F}}$ has the properties, see Eq. (2.84), that its functional derivatives with respect to Σ and D yield the disconnected Green's function, and the expectation value $\mathcal{A}$, respectively. This procedure is inspired by Ref. [79] and extends that approach to the treatment of the superfluid phase.

We first determine the conjugate variables to G_0^{-1} and to the source fields F. The functional derivative of $\hat{\tilde{\Omega}}_s$ with respect to the noninteracting Green's function yields (see App. B.1 and App. B.2)

$$\begin{aligned}
2\beta \frac{\delta \hat{\tilde{\Omega}}_s}{\delta G_{0\,ji}^{-1}(\tau', \tau)} &= -\frac{2}{\hat{Z}} \frac{\delta}{\delta G_{0\,ji}^{-1}(\tau', \tau)} \int \mathcal{D}A \times \\
&\quad \times \exp\Big\{ \frac{1}{2} \int d\tilde{\tau} \int d\tilde{\tau}' \, \bar{A}_l(\tilde{\tau}) \, G_{0\,ll'}^{-1}(\tilde{\tau}, \tilde{\tau}') \, A_{l'}(\tilde{\tau}') \\
&\quad + \int d\tilde{\tau} [\bar{F}_l(\tilde{\tau}) \, A_l(\tilde{\tau}) - H_U(\bar{a}, a)] \Big\} \\
&= -\frac{1}{\hat{Z}} \int \mathcal{D}A \, \bar{A}_j(\tau') \, A_i(\tau) \exp[-S] \\
&\equiv \hat{\mathrm{G}}_{\mathrm{disc},ij}(\tau, \tau') \, .
\end{aligned}$$

Here $\hat{\mathrm{G}}_{\mathrm{disc},ij}(\tau, \tau')$ is the disconnected interacting time-ordered Green's function. Along with the definition of the connected Green's function $\hat{G}[G_0^{-1}, F]$ we obtain

$$2\beta \frac{\delta \hat{\tilde{\Omega}}_s[G_0^{-1}, F]}{\delta G_0^{-1}} = \hat{\mathrm{G}}_{\mathrm{disc}} \equiv \hat{G} - \hat{\mathcal{A}} \hat{\bar{\mathcal{A}}} \, . \tag{2.72a}$$

For the functional derivative with respect to F we obtain similarly

$$2\beta \frac{\delta \hat{\tilde{\Omega}}_s[G_0^{-1}, F]}{\delta \bar{F}} = -2\hat{\mathcal{A}}[G_0^{-1}, F] \, . \tag{2.72b}$$

The two functionals $\hat{G}[G_0^{-1}, F]$ and $\hat{A}[G_0^{-1}, F]$ defined in Eq. (2.72) provide the exact Green's function G and order parameter A for a given noninteracting Green's function G_0^{-1} and source field F of the system. The first step toward the universal functional consists in a Legendre transformation replacing the variables F with $\mathcal{A}$. To this end, we

invert[1] the relation Eq. (2.72) making F a functional $\hat{F}[G_0^{-1}, \mathcal{A}]$ and introduce

$$\hat{\Xi}[G_0^{-1},\, \mathcal{A}] = 2\beta\hat{\tilde{\Omega}}_s + 2\hat{\bar{F}}\mathcal{A}\ , \tag{2.73}$$

where, as usually in Legendre transformations, the functional dependence on F has been eliminated in favor of $\mathcal{A}$ by using the inverse function. It is straightforward to show that the corresponding functional derivatives give

$$\frac{\delta\hat{\Xi}}{\delta 2\mathcal{A}} = \hat{\bar{F}}[G_0^{-1}, A]\ , \quad \frac{\delta\hat{\Xi}}{\delta G_0^{-1}} = \hat{\mathrm{G}}_{\mathrm{disc}}[G_0^{-1}, A]\ .$$

Next, we modify the functional in the following way

$$\hat{\tilde{\Xi}}[G_0^{-1},\, \mathcal{A}] = \hat{\Xi} + \bar{\mathcal{A}}G_0^{-1}\mathcal{A}\ , \tag{2.74}$$

such that we obtain the connected Green's function from the functional derivative with respect to G_0^{-1}. In total we have

$$\frac{\delta\hat{\tilde{\Xi}}}{\delta 2\mathcal{A}} = \hat{\bar{F}}[G_0^{-1}, A] + \bar{\mathcal{A}}G_0^{-1}\ , \tag{2.75}$$

$$\frac{\delta\hat{\tilde{\Xi}}}{\delta G_0^{-1}} = \hat{\mathrm{G}}_{\mathrm{disc}} + \mathcal{A}\bar{\mathcal{A}} = \hat{G}[G_0^{-1}, A]\ . \tag{2.76}$$

The second step is a Legendre transformation replacing the variable G_0^{-1} with G

$$\hat{\Pi}[G,\, \mathcal{A}] = \hat{\tilde{\Xi}} - \beta\,\mathrm{Tr}(G\,\hat{G}_0^{-1} - \mathbb{1})\ , \tag{2.77}$$

where we have expressed $\hat{G}_0^{-1}$ as a functional of G and $\mathcal{A}$, by inverting Eq. (2.76). We subtract an "infinite" constant $\beta\,\mathrm{Tr}\,\mathbb{1}$ in order to keep $\hat{\Pi}[G,\, \mathcal{A}]$ finite. The functional derivatives of the new functional are

$$\frac{\delta\hat{\Pi}}{\delta 2\mathcal{A}} = \hat{\bar{F}} + \bar{\mathcal{A}}\hat{G}_0^{-1}\ , \quad \frac{\delta\hat{\Pi}}{\delta G} = -\hat{G}_0^{-1}\ .$$

Now, we modify the functional such that we get the self-energy from the functional derivative (see App. B.1.3)

$$\hat{\tilde{\Pi}}[G,\, \mathcal{A}] = \hat{\Pi} + \beta\,\mathrm{Tr}\ln\left(G/G_\infty\right)\ . \tag{2.78}$$

This gives

$$\frac{\delta\hat{\tilde{\Pi}}}{\delta 2\mathcal{A}} = \hat{\bar{F}} + \bar{\mathcal{A}}\hat{G}_0^{-1}\ , \quad \frac{\delta\hat{\tilde{\Pi}}}{\delta G} = \hat{\Sigma} \tag{2.79a}$$

$$\hat{\Sigma} \equiv G^{-1} - \hat{G}_0^{-1}\ . \tag{2.79b}$$

[1] Here, and below we assume that the relations between conjugate variables are invertible, at least locally, see also App. B.2

Here we have used the Dyson equation as defining equation for the self-energy. Furthermore, we carry out a third Legendre transformation replacing G with Σ in the usual way. Thus we introduce

$$\hat{P}[\Sigma, \mathcal{A}] = \hat{\tilde{\Pi}} + \beta \operatorname{Tr} \Sigma \hat{G} \tag{2.80}$$

with the properties

$$\frac{\delta \hat{P}}{\delta 2\mathcal{A}} = \hat{\bar{F}} + \bar{\mathcal{A}} \hat{G}_0^{-1} , \quad \frac{\delta \hat{P}}{\delta \Sigma} = \hat{G} .$$

We modify this functional once more so that its derivative yields a new function D, which will be the companion of the self-energy in our extended self-energy approach

$$\hat{\tilde{P}}[\Sigma, \mathcal{A}] = \hat{P} - \bar{\mathcal{A}} \Sigma \mathcal{A} . \tag{2.81}$$

The functional derivatives yield

$$\frac{\delta \hat{\tilde{P}}}{\delta 2\mathcal{A}} = \hat{\bar{F}} + \bar{\mathcal{A}} \hat{G}_0^{-1} - \bar{\mathcal{A}} \Sigma = \hat{\bar{F}} + \bar{\mathcal{A}} \hat{G}^{-1} \equiv \hat{\bar{D}} , \tag{2.82a}$$

$$\frac{\delta \hat{\tilde{P}}}{\delta \Sigma} = \hat{G} - \mathcal{A} \bar{\mathcal{A}} = \hat{G}_{\text{disc}} . \tag{2.82b}$$

Before proceeding, let us discuss the meaning of the function D introduced in Eq. (2.82a). When extending SFA to the superfluid phase one is looking for a quantity, which is related to the condensed order parameter and which plays a similar role as the self-energy, in that it describes the deviation between the interacting and non-interacting case. Thus, this quantity should vanish in the noninteracting case ($H_U = 0$). The reason is that SFA will eventually amount to an approximation for Σ and D, and we require this approximation to become exact for $H_U = 0$. Finally, D must obviously vanish in the normal phase. The expression in Eq. (2.82a) has precisely these features, since $\bar{\mathcal{A}}_0 = -\bar{F} G_0$, which is straightforwardly determined from the Gaussian integral for $H_U = 0$ in Eq. (2.66). Interestingly, the pseudoparticle approach, presented in Ref. [57], and which is based on an intuitive, yet heuristic approximation, provides the same form of D as given in Eq. (2.82a).

The final Legendre transformation replacing $\mathcal{A}$ with D yields the desired functional of the self-energy and D. It represents the generalization of the self-energy functional ($F[\Sigma]$ of Refs. [49] and [51]) to the superfluid phase

$$\hat{\mathcal{F}}[\Sigma, D] = \hat{\tilde{P}} - 2\bar{D}\hat{\mathcal{A}} \tag{2.83}$$

and has the properties

$$\frac{\delta \hat{\mathcal{F}}}{\delta \bar{D}} = -2\hat{\mathcal{A}}[\Sigma, D] , \quad \frac{\delta \hat{\mathcal{F}}}{\delta \Sigma} = \hat{\mathrm{G}}_{\text{disc}}[\Sigma, D] . \tag{2.84}$$

Similarly to $F[\Sigma]$ from Refs. [49] and [51], $\hat{\mathcal{F}}$ is (for fixed H_U) a *universal* functional of Σ and D only, from which the disconnected Green's function and the order parameter are obtained by functional derivative, see Eq. (2.84).

Given Σ and D we can compute by Eq. (2.84) the corresponding values for A and $\mathrm{G}_{\mathrm{disc}}$. On the other hand, for a specific physical system, uniquely defined by G_0^{-1}, F and H_U, the definitions of the self-energy Σ, Eq. (2.79b), and the modified order parameter D, Eq. (2.82a), provide another set of equations, which uniquely fix Σ and D via the equations

$$\begin{aligned}\hat{\mathrm{G}}_{\mathrm{disc}}[\Sigma, D] \stackrel{!}{=} (G_0^{-1} - \Sigma)^{-1} + \\ (G_0^{-1} - \Sigma)^{-1}(D - F)(\bar{D} - \bar{F})(G_0^{-1} - \Sigma)^{-1} \,,\end{aligned} \tag{2.85a}$$

and

$$-2\bar{\mathcal{A}}[\Sigma, D] \stackrel{!}{=} -2(\bar{D} - \bar{F})(G_0^{-1} - \Sigma)^{-1} \,. \tag{2.85b}$$

As for the (original) self-energy functional approach, we seek now a functional, which becomes stationary at the exact Σ and D for specific G_0^{-1} and F, and which consists of the universal functional $\hat{\mathcal{F}}$ plus a non-universal explicit functional of the form

$$2\beta\hat{\Omega}_s[\Sigma, D, G_0^{-1}, F, H_U] = \hat{\mathcal{F}}[\Sigma, D, H_U] + \hat{\mathcal{E}}[\Sigma, D, G_0^{-1}, F] \,.$$

In order to yield the correct stationary point, the functional $\hat{\mathcal{E}}$ has to fulfill according to Eq. (2.85) the equations

$$\begin{aligned}\frac{\delta\hat{\mathcal{E}}}{\delta\Sigma} = &- (G_0^{-1} - \Sigma)^{-1} \\ &- (G_0^{-1} - \Sigma)^{-1}(D - F)(\bar{D} - \bar{F})(G_0^{-1} - \Sigma)^{-1} \,,\end{aligned} \tag{2.86a}$$

$$\frac{\delta\hat{\mathcal{E}}}{\delta D} = 2(\bar{D} - \bar{F})(G_0^{-1} - \Sigma)^{-1} \,. \tag{2.86b}$$

With these ingredients we can now express the sought-for functional $\hat{\Omega}_s$ as

$$\begin{aligned}2\beta\hat{\Omega}_s[\Sigma,\, D, G_0^{-1}, F] = \hat{\mathcal{F}}[\Sigma, D] + \beta\,\mathrm{Tr}\ln[(G_0^{-1} - \Sigma)\; G_\infty] \\ + (\bar{D} - \bar{F})(G_0^{-1} - \Sigma)^{-1}(D - F) \,,\end{aligned} \tag{2.87}$$

which obviously fulfills Eq. (2.86). It remains to show that, whenever evaluated at the exact Σ and D the functional $\hat{\Omega}_s$ corresponds, possibly apart from a constant, to the thermodynamic grand potential $\widetilde{\Omega}_s$ of the system. To this end we add up all the terms used to construct the functional. At the exact values of Σ and D we have

$$\begin{aligned}2\beta\hat{\Omega}_s\big|_{exact} &= 2\beta\widetilde{\Omega}_s + 2\bar{F}\mathcal{A} + \bar{\mathcal{A}}G_0^{-1}\mathcal{A} - \beta\,\mathrm{Tr}\left(GG_0^{-1} - \mathbb{1}\right) \\ &\quad + \beta\,\mathrm{Tr}\ln\left(G/G_\infty\right) + \beta\,\mathrm{Tr}\,\Sigma G - \bar{\mathcal{A}}\Sigma\mathcal{A} - 2\bar{D}\mathcal{A} \\ &\quad - \beta\,\mathrm{Tr}\ln\left(G/G_\infty\right) + \bar{\mathcal{A}}G^{-1}\mathcal{A} \\ &= 2\beta\widetilde{\Omega}_s - 2\underbrace{(\bar{D} - \bar{F})}_{\bar{\mathcal{A}}G^{-1}}\mathcal{A} + 2\bar{\mathcal{A}}G^{-1}\mathcal{A} \\ &= 2\beta\widetilde{\Omega}_s\end{aligned}$$

We can now proceed as in Refs. [49] and [28] and construct a reference system, which can be solved (almost) exactly. The reference system is described by a Hamiltonian H', which shares the same interaction H_U as the physical system, but consists of different noninteracting Green's function G_0' and source fields F'. The point is the following: Due to the fact that $\mathcal{F}$ is a universal functional, it cancels out from the difference between $\hat{\Omega}_s$ for the physical and the reference system, *with the same values of* Σ *and* D. In particular, this gives

$$\begin{aligned} 2\beta\hat{\Omega}_s[\Sigma, D, G_0^{-1}, F] - 2\beta\hat{\Omega}_s[\Sigma, D, G_0'^{-1}, F'] \\ = \beta \operatorname{Tr}\ln\left((G_0^{-1} - \Sigma)G_\infty\right) - \beta \operatorname{Tr}\ln\left((G_0'^{-1} - \Sigma)G_\infty\right) \\ + (\bar{D} - \bar{F})(G_0^{-1} - \Sigma)^{-1}(D - F) \\ - (\bar{D} - \bar{F}')(G_0'^{-1} - \Sigma)^{-1}(D - F')\,, \end{aligned} \tag{2.88}$$

which allows to evaluate the functional $\hat{\Omega}_s$ exactly for the physical system as well, however, in a restricted subspace of Σ and D, representable by the parametric family of reference systems. By construction, the optimal values for Σ and D for the physical system are those of the reference system for the set of optimal variational parameters.

The variational procedure then follows and generalizes Ref. [49]: First a class of exactly solvable reference systems $\hat{H}'$ with the same interaction as the physical system characterized by a continuum of single-particle parameters $\mathbf{t}'$ and source fields F' is identified. In VCA this class is obtained by dividing the original lattice into disconnected clusters with varying single-particle energies and hopping strengths. A larger subspace can be reached by adding bath sites [50]. Then the (connected) Green's function G', the order parameter $\mathcal{A}'$, and the grand potential Ω_s' of the reference system is evaluated. With the help of Dyson's equation Eq. (2.79b) the self-energy Σ', and with the help of Eq. (2.82a) D' is determined. By varying $\mathbf{t}'$ and F' the subspace of self-energies and Ds is spanned, which is accessible to the reference system and to which these objects for the physical system are restricted. Within this subspace the functional $\hat{\Omega}_s$ can be evaluated exactly for arbitrary G_0 and F of the physical system. For the relevant case $F = 0$ we obtain from Eq. (2.88)

$$\begin{aligned} 2\beta\Omega_s = 2\beta\Omega_s' + \beta \operatorname{Tr}\ln\left(-(G_0^{-1} - \Sigma')\right) \\ - \beta \operatorname{Tr}\ln\left(-(G_0'^{-1} - \Sigma')\right) + \bar{D}(G_0^{-1} - \Sigma')^{-1}D \\ - \bar{\mathcal{A}}' G'^{-1}\mathcal{A}\,, \end{aligned} \tag{2.89}$$

where the term with G_∞ cancels out, see App. B.3. Eq. (2.89) is now a *function* of $\mathbf{t}'$ and F'. The infinite physical system can break the symmetry spontaneously, while in the reference systems of disconnected finite clusters, a non-vanishing order parameter can only be achieved by an additional source field F'. This explains, why a finite F' is required although $F = 0$ in the physical system. The SFA approximation consists in finding a stationary point of $\hat{\Omega}_s$ within this subspace of self-energies and D-s. This corresponds, quite generally, to finding a stationary point with respect to $\mathbf{t}'$ and F' of

Eq. (2.89), i. e. to the equations

$$\frac{\partial\Omega}{\partial\mathbf{t}'} = 0 \qquad \frac{\partial\Omega}{\partial F'} = 0 \; . \tag{2.90}$$

Here, we have replaced Ω_s with $\Omega \equiv \Omega_s - \frac{1}{2}\operatorname{tr}\mathbf{t}$ which differs just by a $\mathbf{t}'$- and F'-independent constant and thus does not change the saddle-point equations. The quantity Ω is the grand potential obtained from the normal-ordered Hamiltonian (see App. B.3). We also introduce the grand-potential of the normal-ordered reference system $\Omega' \equiv \Omega'_s - \frac{1}{2}\operatorname{tr}\mathbf{t}'$. This term is also present in the pseudoparticle approach [57], where its origin is easily seen. Moreover, for τ-independent fields and Hamiltonian, the expectation values $\mathcal{A}(\tau)$ are τ-independent as well, and the Green's functions depend on the time difference only. In this way, we can rewrite Eq. (2.89) as

$$\begin{aligned}\Omega = \Omega' - \frac{1}{2}\operatorname{tr}(\mathbf{t}-\mathbf{t}') - \frac{1}{2}\operatorname{Tr}\ln\left(-G\right) + \frac{1}{2}\operatorname{Tr}\ln\left(-G'\right) \\ + \frac{1}{2}\bar{\mathcal{A}}G^{-1}(\omega_n=0)\mathcal{A} - \frac{1}{2}\bar{\mathcal{A}}'G'^{-1}(\omega_n=0)\mathcal{A}' \; ,\end{aligned} \tag{2.91}$$

where $G(\omega_n) \equiv \int d\ \tau\ G(\tau,0)e^{i\tau\omega_n}$ is the Green's function in Matsubara space. The expression for Ω given in Eq. (2.91) is our main result. As can be seen, this expression is the same as Eq. (1) in Ref. [57], except for a different normalization factor, which is the number of clusters N_c. Notice that $N_c h$ in the previous section is equal to $\mathbf{t}-\mathbf{t}'$ in here. We thus proved that the result obtained within the pseudoparticle approach in Ref. [57] can be equivalently obtained within a more rigorous "generalized" self-energy functional approach. While the pseudoparticle approach is quite intuitive, the present self-energy approach provides a rigorous variational principle, explaining why the grand-potential Ω has to be optimized with respect to the cluster parameters $\mathbf{t}'$ and F'. In addition, as in SFA for the normal phase, it suggests more general approximations in which bath sites are used to enlarge the space of possible self-energies [50, 80, 81].

Conclusions: In the present section, we extend the self-energy functional approach to the $U(1)$ symmetry broken, superfluid phase of correlated lattice bosons. A crucial point of this extension is the identification of a quantity, termed D, which is the companion of the self-energy Σ in the superfluid phase. We also identify the appropriate (nonuniversal) functional $\hat{\Omega}_s$ which is stationary at the physical values of the self-energy Σ and of D. In analogy to the self-energy, which is the difference of the interacting and non-interacting Green's function, the quantity D is related to the difference of the order parameter of the interacting and non-interacting systems. Thus, D is zero in the normal phase and for $U = 0$. From these relations also follows that both Σ as well as D vanish in the non-interacting case. Importantly, when the functional $\hat{\Omega}_s$ is evaluated at the exact values of Σ and D it corresponds to the grand potential of the physical Hamiltonian. To evaluate the functional, we proceed as in the original self-energy functional approach [49], and introduce a reference system, which is a cluster decomposition of the physical system. Importantly, the reference system shares its two-particle interaction with the

physical system, and can be exactly solved by numerical methods. By comparison of the functionals, the universal part of $\hat{\Omega}_s$, denoted as $\hat{\mathcal{F}}$, can be eliminated, which allows to evaluate $\hat{\Omega}_s$ exactly on the subspace of Σ and D, spanned by the possible sets of reference systems. The results presented are shown to be equivalent to the ones obtained by a more heuristic method, the pseudoparticle approach introduced in Ref. [57], and thus provide rigorous variational grounds for that approach. In addition, the extended self-energy functional approach introduced here allows to envision more general reference systems, in which bath sites are incorporated to enlarge the space of possible self-energies Σ, and possibly bridge over to (C)-DMFT [49, 62]. For future research it would be interesting to verify whether in the limit of an infinite number of bath sites and for a single correlated site as a reference system, our superfluid SFA becomes equivalent to DMFT for superfluid bosons [82, 83], as it is the case in the normal phase [49]. For a finite number of bath sites this is certainly not the case, since the order parameter in the reference system differs from the physical one.

2.3. Nonequilibrium steady state of correlated manybody systems

The theoretical understanding of the nonequilibrium behavior of strongly correlated quantum many-body systems is a long standing challenge, which has become increasingly relevant with the progress made in the fields of quantum optics and quantum simulation, semiconductor, and magnetic heterostructures, nanotechnology, or spintronics.

A typical nonequilibrium situation in all these systems is conveniently described theoretically by switching on a perturbation at a certain time $\tau = \tau_0$, for example, a bias voltage, which is then kept constant after a short switching time. For this problem one may, on the one hand be interested in transient properties at short times after switching on the perturbation, for example in ultrafast pump-probe spectroscopy [84, 85]. In this case, the properties of the system depend on the initial state, as well as on the line shape of the switch-on pulse. For longer times away from τ_0, quite generally one expects the system to reach a steady state, whose properties do not depend on details of the initial state. Nonequilibrium steady states are relevant, for example, in quantum electronic transport across heterostructures, quantum dots, molecules (see, e. g., Refs. [86, 87, 88, 89, 90, 91]) or in driven-dissipative ultracold atomic systems [92, 93, 94, 95, 96, 97]. Intriguingly, it was shown in Ref. [98] that nonequilibrium noise, which is present for instance in Josephson junctions, trapped ultracold polar molecules or trapped ions, to first order preserves the critical nonequilibrium steady states thus being a marginal perturbation as opposed to the temperature. Among the methods to treat strongly correlated systems out of equilibrium, one should mention density-matrix renormalization group and related matrix-product state methods [99, 100, 101, 102, 103], continuum-time quantum Monte-Carlo [104], different numerical and semi-analytical renormalization-group approaches [105, 106, 91], equation-of-motion methods [86, 89], dynamical mean-field theory [107, 108, 109, 110], scattering Bethe Ansatz [111, 112], and the dual-fermion approach [113]. Recently, Balzer and Potthoff [114] have presented a generalization of

cluster-perturbation theory (CPT) to the Keldysh contour, which allows for the treatment of time-dependent phenomena. Their results show that CPT describes quite accurately the short and medium-time dynamics of a Hubbard chain. A detailed study of the short-time dynamics of weakly correlated electrons in quantum transport based on the time evolution of the nonequilibrium Kadanoff-Baym equations, where correlations are treated in Hartree-Fock-, second Born-, and GW-approximation has been given in Ref. [115]. These approximations are restricted to moderate correlations but on the other hand they allow to study rather complex models and geometries. As far as the steady-state behavior is concerned, the nonequilibrium (Keldysh) Green's function approach has been widely used on an ab-initio or tight-binding level, where correlations are treated in mean-field approximation. Since the effective particles are non-interacting, the Meir-Wingreen expression [88] for the current can be applied, which relates the current to the retarded Green's functions of the scattering with a self-energy that is renormalized due to the presence of the leads. Representative applications for nano-structured materials and molecular devices are given in Refs. [116, 117, 118] and in the review article Ref. [90].

Here we aim at strongly correlated many-body systems, and we propose a variational cluster method, that allows to study steady-state properties.

In order to study steady-state nonequilibrium properties of strongly correlated systems one typically considers a model consisting of two leads with uncorrelated particles, and a central correlated region. The three regions are initially decoupled. At a certain time τ_0 a coupling V between the three regions is switched on. A natural approach is to treat V via strong-coupling perturbation theory, which at the lowest order essentially corresponds to cluster-perturbation theory (CPT). In Ref. [114] it has been shown that the short time behavior can be well described within CPT. This can be understood from the observation that switching on the inter-cluster hopping V for a certain time $\Delta\tau$ produces a perturbation of order $V\,\Delta\tau$, which is accounted for at first order in CPT. Therefore, we expect the result to be accurate for small $\Delta\tau$. When addressing the steady state it is, thus, essential to improve the long-time behavior. Here, we suggest that nonequilibrium CPT can be systematically improved by minimizing some suitable "difference" between the unperturbed ("reference") state which enters CPT and the target steady state.

The strategy presented here to achieve this goal consists in exploiting the fact that the decomposition of the Hamiltonian into an "unperturbed part" and a "perturbation" is not unique. Prompted by the variational cluster approach (VCA), one can actually add "auxiliary" single particle terms to the unperturbed Hamiltonian and subtract them again within CPT. This freedom can be exploited in order to "optimize" the results of the perturbative calculation. As discussed in detail in Refs. [66, 57], in equilibrium this is an alternative way to motivate the introduction of variational parameters in VCA. The idea discussed here, thus, provides the natural extension of VCA to treat a nonequilibrium steady state. There remains to define a criterion for the "difference" between initial and final state. (Cellular) Dynamical Mean-Field Theory [119, 62, 67, 110] (DMFT) provides a natural solution, requiring the cluster-projected Green's functions of the initial

and final state to coincide. Of course, this self-consistency condition requires an infinite number of variational parameters, as well as the solution of a (cluster) impurity problem, which is computationally very expensive and whose accuracy is limited, especially in real time. In equilibrium, the self-energy functional approach [49, 50] (SFA) provides one possible generalization of DMFT if one wants to restrict to a finite number of variational parameters. In this case, the requirement for the "difference" is provided by the Euler equation. While originally derived from the equilibrium grand potential (see, e. g., Ref. [49]) the Euler equation allows for a straight forward extension to nonequilibrium:

$$\frac{\delta\Omega}{\delta t'} = \mathrm{Tr}\left(-G' + (G_0^{-1} - \Sigma)^{-1}\right)\frac{\delta\Sigma(t')}{\delta t'} ,$$

where we used $\Omega = F[\Sigma] + \mathrm{Tr}\ln[-(G_0^{-1} - \Sigma)^{-1}]$ and employed the Luttinger-Ward identity $\delta F[\Sigma]/\delta\Sigma(t') = -G'$.

In this section, we explore an alternative criterion, represented by (2.104), which, upon including an infinite number of bath sites, becomes equivalent to C-DMFT (see App. C.1), similarly to SFA [49]. Without bath sites this corresponds to requiring that, for a given set of variational parameters $\mathbf{p}$, their conjugate operators, i. e., $dh/d\mathbf{p}$, h being the Hamiltonian, have the same expectation value in the unperturbed and in the final target state. This criterion is numerically easier to implement than the SFA, since in this case it is not necessary to search for a saddle point, which is well known to be numerically expensive [120]. In addition, inclusion of bath sites provides self consistency conditions for dynamic correlation functions as well.

The freedom discussed above can be additionally exploited by including the hybridization between correlated regions and the leads as well as part of the leads themselves into the unperturbed Hamiltonian which is solved exactly by Lanczos exact diagonalization. In this way, CPT is then used to treat hopping terms further away from the correlated region.[2] This partly accounts for the influence of the leads onto the self-energy of the correlated region.

Finally, let us mention that the method is probably most suited to deal with models for which the correlated region is spatially extended (see Fig. 2.2). In this case, this region must be partitioned into clusters which can be solved exactly, while the intercluster terms are included into the perturbative part.

2.3.1. Variational cluster approach for nonequilibrium steady state

The physical model of interest consists of a "left" and "right" noninteracting lead, as well as a correlated region described by the Hamiltonians $\bar{h}_l$, $\bar{h}_r$, and $\bar{h}_c$, respectively, see Fig. 2.2. $\bar{h}_c$ contains local (Hubbard-type) interactions, as well as arbitrary single-particle terms. For $\tau < \tau_0$, the three regions are in equilibrium with three reservoirs at different chemical potentials, μ_l, μ_r, and μ_c respectively. The correlated region is much

[2] To avoid confusion, we denote as "correlated region" the "physical" one containing interacting sites, bounded by the hoppings V. On the other hand, the "central region" is the one containing the clusters, and is bounded by t_{bic}. (See Fig. 2.2)

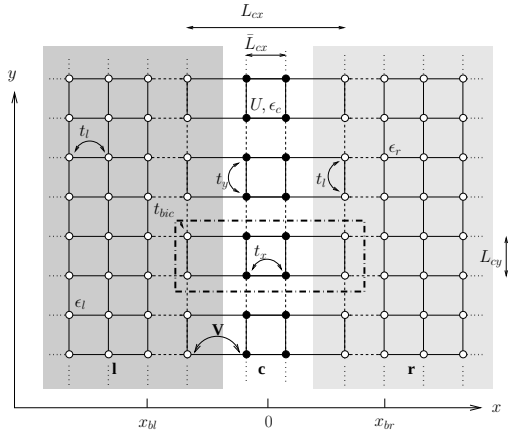

Figure 2.2.: Generic scheme of the model studied here: full (empty) circles indicate correlated (uncorrelated) lattice sites. Correlated sites define the correlated region (c), and are characterized by an on-site Hubbard interaction U, an on-site energy ϵ_c, and by hopping elements t_x and t_y in the x and y direction, respectively. The physical leads (l,r), indicated by the two shaded areas, consist of half-infinite planes described by uncorrelated tight-binding models with hopping t_L, on-site energies ϵ_l and ϵ_r, and chemical potentials μ_l and μ_r, respectively. The correlated region is connected to the leads via hoppings V. The width (number of sites in the x direction) of the correlated region is $\bar{L}_{cx}$. The height of the whole system in the y direction is infinite. Here, we study two cases, a strongly correlated chain ($\bar{L}_{cx} = 1$) and a strongly correlated two-leg ladder ($\bar{L}_{cx} = 2$), both perpendicular to the applied bias. In the variational cluster calculation the central region described by the unperturbed Hamiltonian h can differ from the physical one. The latter coincides with the correlated sites (white area in the figure). On the other hand, the former consists of disconnected clusters aligned along the y direction, one of them being represented by the dash-dotted rectangle in the figure. The corresponding equilibrium Green's function is determined by Lanczos exact diagonalization. The size of these clusters is $L_c = L_{cx} \times L_{cy}$ (4×2 in the example). The coordinates of the left and right boundary sites of the central region are indicated by x_{bl} and x_{br}, respectively. Accordingly, dashed lines represent hopping processes, which are omitted in the unperturbed (reference) Hamiltonian h and are re-included perturbatively within $\hat{T}$. Full lines indicate hopping terms present in h, which are thus treated exactly (see text).

smaller in size than the leads, so that the latter act as relaxation baths. At $\tau = \tau_0$, the single particle (i. e., hopping) Hamiltonian terms $\hat{V}_{lc}$ and $\hat{V}_{rc}$ are switched on. These connect the left and right reservoir, respectively, with the correlated region. The total time-dependent Hamiltonian is, thus, given by

$$H(\tau) = \bar{h} + \theta(\tau - \tau_0)\hat{\bar{T}} \,, \tag{2.92}$$

where $\bar{h} = \bar{h}_c + \bar{h}_l + \bar{h}_r$, and $\hat{\bar{T}} = \hat{V}_{lc} + \hat{V}_{rc}$. We consider here the fermionic case, although many concepts can be easily extended to bosons. After a time $\Delta\tau$ long enough for relaxation to take place, the system reaches a nonequilibrium steady-state, with a particle current flowing from left to right for $\mu_l > \mu_r$ and from right to left for $\mu_l < \mu_r$.

As discussed above, the total $\tau > \tau_0$ Hamiltonian $H \equiv H(\tau > \tau_0)$ is decomposed into an unperturbed part h and a perturbation $\hat{T}$:

$$H = h + \hat{T} \,. \tag{2.93}$$

In the simplest CPT approach for a "small" correlated region one can take $h = \bar{h}$, and $\hat{T} = \hat{\bar{T}}$. However, when the correlated region is extended, as in Fig. 2.2, it has to be further decomposed into smaller clusters that can be solved by exact diagonalization. Note, the uncorrelated leads can be solved exactly without being partitioned into clusters. In this case, the intercluster hopping is subtracted from h and must be included in $\hat{T}$. In addition, one can include part of the leads into the clusters (dashed lines in Fig. 2.2), so that $\hat{V}_{lc} + \hat{V}_{rc}$ are incorporated into h, while the leads intercluster hoppings (e.g. t_{bic} in the figure) are included in $\hat{T}$. Finally, in the spirit of VCA, arbitrary intracluster terms Δh can be added to the unperturbed Hamiltonian and subtracted perturbatively within $\hat{T}$. In other words, calling h_{cl} the Hamiltonian describing the physical cluster partition, and $\hat{T}_{cl}$ the one describing the intercluster hoppings (dashed lines in Fig. 2.2), we write $h = h_{cl} + \Delta h$, and $\hat{T} = \hat{T}_{cl} - \Delta h$ so that the total Hamiltonian remains unchanged, compare with Sec. 2.1.5:

$$H = h_{cl} + \hat{T}_{cl} = h + \hat{T} \,. \tag{2.94}$$

The arbitrariness in the choice of Δh can be exploited to optimize the unperturbed state. Here, we will adopt a different optimization criterion, see discussion below. Being a single-particle term, $\hat{T}$ is described by its hopping matrix T. This matrix has a block structure according to the three regions discussed above and shall be denoted by T_{lc}, T_{rc} and T_{cc}, respectively.

Nonequilibrium properties, in general, and nonlinear transport in particular can quite generally be determined in the frame of the Keldysh Green's function approach [121, 122, 123, 86, 87], see App. C.2. Here, we adopt the notation of Ref. [87], for which the 2×2 Keldysh Green's function matrix is expressed as

$$G(\mathbf{r}, \mathbf{r}'|\tau, \tau') = \begin{pmatrix} G^R & G^K \\ 0 & G^A \end{pmatrix} \,, \tag{2.95}$$

where the retarded (G^R), advanced (G^A), and Keldysh (G^K) Green's functions depend in general on two lattice sites $(\mathbf{r}, \mathbf{r}')$ and two times (τ, τ'). However, both for $\tau < \tau_0$

as well as in steady state, time translation invariance holds, so that Green's functions depend only on the time difference $\tau - \tau'$, and we can Fourier transform to frequency space ω.

We use uppercase letters G to denote Green's functions of the full Hamiltonian H, and lowercase g for the ones of the unperturbed Hamiltonian h. The advantage of using the Keldysh Green's function matrix representation is that one can express Dyson's equation in the same form as in equilibrium [86, 87]. In our case, we can express it in the form

$$G = g + g\ (T + \Delta\Sigma)\ G\ , \tag{2.96}$$

where $g = \mathrm{diag}\big(g_{ll},\, g_{cc},\, g_{rr}\big)$ is block diagonal, and the products have to be considered as matrix multiplications. In the time representation (2.95) they also include convolutions over internal times. However, since we are considering the steady state, Green's functions become diagonal in the frequency representation. In (2.96), $\Delta\Sigma = \Sigma - \Sigma_h$ is the difference between the (unknown) self-energy Σ of the total Hamiltonian H, including the coupling to the leads, and the self-energy Σ_h associated with the unperturbed Hamiltonian h.

The CPT approximation [64] precisely amounts to neglecting $\Delta\Sigma$. As pointed out in Ref. [114] this corresponds to neglecting irreducible diagrams containing interactions and one or more T terms. It should, however, be stressed that the self-energy of the isolated clusters is exactly included in g_{cc}, which is obtained by Lanczos exact diagonalization.

In this approximation, (2.96) can be used to obtain an equation for the Green's function G_{cc} projected onto the central region, which is still a matrix in the lattice sites of the central region and in Keldysh space[3] (this is a straightforward generalization of, e.g., the treatment in Ref. [86]):

$$G_{cc} = g_{cc} + g_{cc}\big(\ T_{cc}\ G_{cc} + \sum_{\alpha}^{\in\{l,r\}} T_{c\alpha}\ G_{\alpha c}\big) \tag{2.97}$$

and for the lead-central region Green's functions:

$$G_{\alpha c} = g_{\alpha\alpha}\ T_{\alpha c}\ G_{cc}\ , \qquad \text{with } \alpha \in \{l, r\}. \tag{2.98}$$

It is noteworthy that Eq. (2.98) is exact and not based on the CPT approximation, as the leads contain non-interacting particles. Insertion of (2.98) into (2.97) yields

$$G_{cc} = g_{cc} + g_{cc}\big(T_{cc} + \tilde{\Sigma}_{cc}\big)\ G_{cc} \tag{2.99}$$

with the lead-induced self-energy renormalization

$$\tilde{\Sigma}_{cc} = \sum_{\alpha}^{\in\{l,r\}} T_{c\alpha}\ g_{\alpha\alpha}\ T_{\alpha c}\ . \tag{2.100}$$

[3] Here, we use a notation to express projection of objects such as G, T, etc., which are matrices in lattice indices and in Keldysh space, onto one of the three regions c, l, or r. More specifically, let m be such a matrix, then m_{AB} refers to a sub-matrix of m in which the left (right) index is restricted to region A (B), with $A, B = c, l$, or r.

Here $g_{\alpha\alpha}$ stands for the Green's function of the isolated lead α. One finally obtains a Dyson form for the steady state Green's function of the coupled system at the central region

$$G_{cc}^{-1} = g_{cc}^{-1} - T_{cc} - \tilde{\Sigma}_{cc} \,. \tag{2.101}$$

Different from the usual Dyson equation, g_{cc} is the Green's function for the isolated clusters, which contains all many-body effects inside the cluster.

For the evaluation of the current from, say, the left lead to the central region one needs the G_{lc} Green's function, which is readily obtained by combining (2.98) with (2.101). This leads to the generalized Kadanoff-Baym equation (see e. g. Refs. [86, 88]), along with the fact that the central region is finite in x direction and the leads are infinite, one can rewrite the current into a Büttiker-Landauer type of formula

$$\begin{aligned} j = \int \frac{d\varepsilon}{2\pi} \big[f_F(\varepsilon - \mu_r) - f_F(\varepsilon - \mu_l) \big] \\ \times \mathrm{Tr} \left[\; \mathrm{G}_{cc}^{R} \, (\varepsilon) \Gamma_l(\varepsilon) \;\; \mathrm{G}_{cc}^{A} \, (\varepsilon) \Gamma_r(\varepsilon) \right] . \end{aligned} \tag{2.102}$$

where $G_{cc}^{R/A}$ is the retarded/advanced part of the Green's function G_{cc}, and the trace, as well as matrix products run over site indices in c, see App. C.3. Γ_α describes the inelastic broadening owing to the coupling to lead α, which in CPT is given by

$$\Gamma_\alpha = 2 \, \mathrm{Im} \left\{ T_{c\alpha} g_{\alpha\alpha}^{A} T_{\alpha c} \right\} ,$$

which represents the contribution of lead α to the imaginary part of $\tilde{\Sigma}_{cc}^{A}$. Interestingly, the expression for the current in CPT has the same structure as the Meir-Wingreen formula [88] for non-interacting particles, which is the basis for nonequilibrium ab-initio-calculations [117]. Here, however, the Green's function contains the many-body interactions of the correlated region. An advantage of this expression is that it yields an explicit connection to the Green function $G_{cc}^{R/A}$ of the scattering region and the influence of the itinerant electrons in the leads. A similar expression can be derived for the one-particle density matrix between two sites with the same y coordinate, which is required for the self-consistency condition discussed below.

As it is well known, all retarded and advanced Green's functions are evaluated without chemical potentials. The latter enter through the Keldysh Green's function or rather via the Fermi functions. While the chemical potential of the central region is wiped out in the steady state due to its small size in comparison to the size of the leads, the chemical potentials of the leads explicitly enter the expressions for the current and the density matrix, see Eq. (2.102). In the case investigated here, the central region is translation invariant in y direction and is split into identical clusters. In the end, as far as the main numerical task is concerned, one has to solve many-body problems for clusters of size $L = L_{cx} \times L_{cy}$, invert matrices of the same size, and sum over wave vectors q_y belonging to the Brillouin zone associated with the cluster supercell.

2.3.2. Self-consistency condition

Equation (2.101) is the expression for the Green's function of the central region within the CPT approximation. As discussed above, one would like to optimize the initial state in some appropriate way by suitably adjusting the parameters Δh of the unperturbed Hamiltonian h. The inclusion of additional terms Δh adds flexibility to the self-energy Σ_h which is included within this approximation. Obviously, it makes no difference in the case of non-interacting particles as the self-energy vanishes exactly, independently of Δh. This freedom can be exploited in order to improve the approximation systematically. A similar discussion on this issue has been given in Refs. [66, 57], and is at the basis of the VCA idea [49].

As discussed above, we need a variational condition associated with a "minimization" of the difference between unperturbed and perturbed state. In (cellular)-DMFT one requires the cluster projected Green's function to be equal to the unperturbed one

$$g_{cc} = \mathcal{P}(G_{cc}) \ , \tag{2.103}$$

where $\mathcal{P}$ projects the Green's function onto the cluster, i. e., it sets all its intercluster matrix elements to zero. Note that when the central region coincides with the cluster, $\mathcal{P}G_{cc} = G_{cc}$. In this case the solution of (2.104) is trivially obtained by taking the leads as auxiliary baths. Since here we have a finite number of variational parameters $\mathbf{p}$ that can be adjusted, we cannot satisfy (2.103). We, thus, propose a "weaker" condition, namely that the expectation values of operators coupled to the variational parameters contained in Δh (i. e., $d\Delta h/d\mathbf{p}$) be equal in the unperturbed and in the perturbed state. This condition corresponds to a generalized Hartree self-consistence. It physically amounts to require that certain "generalized densities" (more specifically some elements of the single-particle density matrix) coincide in the unperturbed and in the perturbed system, so that the effect of the perturbation is minimized. Which terms should coincide is determined by the choice of the variational parameters. Notice that by using the coupling to bath sites as variational parameters, one can also require dynamical contributions to the Green's function to coincide. More specifically, we impose the condition

$$\int \frac{d\omega}{2\pi} \operatorname{tr} \hat{\tau}_1 \frac{\partial \left(g_{0cc}\right)^{-1}}{\partial \mathbf{p}} \left(g_{cc} - G_{cc}\right) = 0 \ , \tag{2.104}$$

where $\hat{\tau}_1$ is the Pauli matrix in Keldysh space, and g_{0cc} is the Green's function associated with the noninteracting part of h.

It is interesting to note (see App. C.1) that by including into Δh a coupling to an infinite number of bath sites, the present method, with the self-consistence condition (2.104) whereby $\mathbf{p}$ are the bath parameters (hopping and on-site energies), becomes equivalent to nonequilibrium cluster DMFT. Generalization of the SFA condition to nonequilibrium should be, in principle, obtained by replacing g_{0cc} with Σ_h in (2.104).

A second systematic improvement of this nonequilibrium VCA approach consists in increasing the cluster size L_c. This can be done in two ways: (i) by extending the boundaries of the central region in y direction and thus treating more correlated sites

exactly and (ii) by extending the boundaries in x direction to include an increasing number of uncorrelated lattice sites, i. e., taking $L_{cx} > \bar{L}_{cx}$, *cf.* Fig. 2.2. This amounts to taking into account to some degree the V-induced renormalization of the self energy.

The $\hat{\tau}_1$ in (2.104) is due to our choice of convention (2.95) for the Keldysh matrix. If one uses the form containing the time- and anti-time-ordered Green's functions in the diagonal, and the greater and lesser in the off-diagonal elements, no $\hat{\tau}_1$ is present in the trace, see App. C.4.

2.3.3. Q-matrix formalism

Here we adopt the Q-matrix formalism to nonequilibrium VCA. We introduce the effective self energy

$$\Sigma^{\text{eff}} = T_{cc} + \tilde{\Sigma}_{cc} \; ,$$

where $\tilde{\Sigma}_{cc}$ is given by Eq. (2.100). It is convenient to group the central region to environment coupling and the cluster Green's functions as

$$T_{ec} \equiv \begin{pmatrix} T_{lc} \\ T_{rc} \end{pmatrix} \qquad g_{ee} \equiv \begin{pmatrix} g_{ll} & 0 \\ 0 & g_{rr} \end{pmatrix} .$$

Using the fact that $T_{c\alpha} = T^{\dagger}_{\alpha c}$, with $\alpha = \{l, r\}$, yields

$$\Sigma^{\text{eff}} = T_{cc} + T^{\dagger}_{ec} g_{ee} T_{ec} \; .$$

The central region Green's functions in Keldysh space [87] reads

$$g_{cc} = \begin{pmatrix} g^R & g^K \\ 0 & g^A \end{pmatrix} ,$$

where g^R (g^A) are the retarded (advanced) Green's functions and $g^K = G^< + G^> = \text{sign}(\omega - \mu)(g^R - g^A)$ is the Keldysh Green's function. The Q-matrix formalism allows to write the Lehmann representation of Green's functions in a compact form

$$\begin{aligned} g_R &= \tilde{Q}(\omega + i0^+ - \Lambda)^{-1} \tilde{S}\tilde{Q}^{\dagger} \equiv \tilde{Q} g^+ \tilde{S}\tilde{Q}^{\dagger} \\ g_A &= \tilde{Q}(\omega - i0^+ - \Lambda)^{-1} \tilde{S}Q^{\dagger} \equiv \tilde{Q} g^- \tilde{S}\tilde{Q}^{\dagger} \\ g_K &= \tilde{Q}\, \text{sign}(\omega - \mu)[g_+ - g_-]\tilde{S}\tilde{Q}^{\dagger} \equiv \tilde{Q} a \tilde{S}\tilde{Q}^{\dagger} \; . \end{aligned}$$

The matrix S takes into account the commutation relations of the particles and has the properties $S^2 = \mathbb{1}$ and $S^{-1} = S$, see Sec. 2.1. In Keldysh space

$$Q \equiv \begin{pmatrix} \tilde{Q} & 0 \\ 0 & \tilde{Q} \end{pmatrix} \qquad SQ^{\dagger} \equiv \begin{pmatrix} \tilde{S}\tilde{Q}^{\dagger} & 0 \\ 0 & \tilde{S}\tilde{Q}^{\dagger} \end{pmatrix}$$

We use these extended Q matrices to rewrite the decoupled central region Green's function

$$g_{cc} = \begin{pmatrix} \tilde{Q} & 0 \\ 0 & \tilde{Q} \end{pmatrix} \begin{pmatrix} g^+ & a \\ 0 & g^- \end{pmatrix} \begin{pmatrix} \tilde{S}\tilde{Q} & 0 \\ 0 & \tilde{S}\tilde{Q} \end{pmatrix} \equiv Q \bar{g}_{cc} S Q^{\dagger} \; .$$

Using $QSQ^\dagger = \mathbb{1}$ we find

$$\begin{aligned} G_{cc} &= g_{cc} + g_{cc}\Sigma^{\text{eff}}G_{cc} \\ &= g_{cc}(1 - \Sigma^{\text{eff}}g_{cc})^{-1} \\ &= Q\bar{g}_{cc}SQ^\dagger(1 + \Sigma^{\text{eff}}Q\bar{g}_{cc}SQ^\dagger + \Sigma^{\text{eff}}Q\bar{g}_{cc}SQ^\dagger\Sigma^{\text{eff}}Q\bar{g}_{cc}SQ^\dagger + \ldots) \\ &= Q\bar{g}_{cc}(1 + SQ^\dagger\Sigma^{\text{eff}}Q\bar{g}_{cc} + SQ^\dagger\Sigma^{\text{eff}}Q\bar{g}_{cc}SQ^\dagger\Sigma^{\text{eff}}Q\bar{g}_{cc} + \ldots)SQ^\dagger \\ &= Q\bar{g}_{cc}(1 - SQ^\dagger\Sigma^{\text{eff}}Q\bar{g}_{cc})^{-1}SQ^\dagger \end{aligned}$$

This formula is convenient for the numerical evaluation, since only matrices of the systems size have to be inverted. Finally, we have

$$G_{cc} = Q(\bar{g}_{cc}^{-1} - SQ^\dagger\Sigma^{\text{eff}}Q)^{-1}SQ^\dagger \ ,$$

with

$$g_{cc}^{-1} = \begin{pmatrix} (g^+)^{-1} & -(g^+)^{-1}a(g^-)^{-1} \\ 0 & (g^-)^{-1} \end{pmatrix} .$$

We recover the well-known equilibrium results when setting the central region to environment coupling to zero. In contrast to the equilibrium case, the above equation cannot be solved algebraically, by reducing it to a linear eigenvalue problem. Here, the equation is nonlinear, as Σ^{eff} is a function of the frequency. Nevertheless, the usage of the Q-matrices is advantageous, since for the reference system the poles Λ and their weights $SQ^\dagger Q$ are decoupled. This representation also demonstrates that the pseudoparticle approach is valid for nonequilibrium VCA.

Furthermore, generalizations for instance to mixtures of particle number sectors are straightforward. For mixtures the cluster Green's functions are simply superpositions of individual particle number sectors

$$g = \sum_m c_m g_m \ ,$$

where g_m is the Keldysh Green's function for a specific particle number sector m, compare also with Sec. 2.1.4.

3. Equilibrium properties of bosonic manybody systems

3.1. Bose-Hubbard model

Pioneering experiments on ultracold gases of atoms trapped in optical lattices allowed for a direct observation of quantum many-body phenomena, such as the quantum phase transition from Mott phase to superfluid phase [20, 21]. Optical lattices are realized by counterpropagating laser beams, which form a periodic potential [22]. The bosonic particles located on the optical lattice gain kinetic energy when tunneling through the potential wells of neighboring sites of the periodic potential and they exhibit a repulsive interaction when a lattice site is occupied by more than one atom. A condensate of ultracold atoms can be driven from superfluid phase to Mott phase by gradually increasing the intensity of the laser beams. The potential wells of the optical lattice are shallow for low laser-beam intensity. Thus the bosonic particles can overcome the barrier easily and are delocalized on the whole lattice. However, for large intensity of the laser beams the potential wells are deep and there is little probability for the atoms to tunnel from one lattice site to another. This physical behavior can be described by the Bose-Hubbard (BH) model [30] provided the gas of ultracold atoms is cooled such that only the lowest Bloch band of the periodic potential has to be taken into account [20]. The ground state of the BH model is superfluid when the local on-site repulsion between the atoms is small in comparison to the nearest-neighbor hopping strength whereas it is a Mott state for integer particle density and large on-site repulsion compared to the hopping strength. Due to these characteristics of the BH model the depth of the potential wells in optical lattices can be associated directly with the ratio of the on-site repulsion and the hopping strength. Ultracold atoms confined in optical lattices provide a very clean experimental realization of a strongly correlated many-body problem and the internal physical processes are well understood in comparison to conventional condensed-matter systems. There is large experimental control over the system parameters, such as the particle number, lattice size, and depth of the potential wells. Furthermore the sites of the optical lattice can be addressed individually due to the mesoscopic scale of the lattice [124, 36, 37].

The quantum phase transition from Mott phase to superfluid phase has been first observed experimentally for ultracold rubidium atoms trapped in a three-dimensional optical lattice [21] and subsequently as well in optical lattices of two dimensions [125, 126]. The corresponding theoretical model, the two-dimensional (2D) BH model, has already been investigated to some detail in literature. The phase diagram, which describes the quantum phase transition from Mott phase to superfluid phase, has been investigated

thoroughly at the mean-field level (possibly including Gaussian-fluctuation corrections) [30, 127, 128, 129, 130, 29, 131]. More accurate results for the phase diagram from quantum Monte Carlo [132] (QMC) simulations, variational approaches [133, 134], and strong-coupling perturbation theory [135, 136, 137, 138] are also available. The phase diagram for arbitrary integer fillings has been obtained recently using the so-called diagrammatic process chain approach [139, 140]. Spectral functions of the two-dimensional BH model have been evaluated within a strong-coupling approach [141, 137] and a variational mean field approach [142].

The (grand-canonical) Hamiltonian of the BH model [30] is given by

$$\hat{H} = -t \sum_{\langle i,\, j \rangle} \left(b_i^\dagger \, b_j + \text{H.c.} \right) + \frac{U}{2} \sum_i \hat{n}_i \left(\hat{n}_i - 1 \right) + \sum_i (\epsilon_i - \mu) \hat{n}_i \; , \tag{3.1}$$

where the operators $b_i^\dagger$ (b_i) create (annihilate) bosonic particles at lattice site i. The parameter t is the nearest-neighbor hopping strength, U is the local on-site repulsion, ϵ_i a site-dependent, local potential, and μ is the chemical potential, which controls the total particle number $\hat{N}_p = \sum_i \hat{n}_i = \sum_i b_i^\dagger \, b_i$. The angle brackets in the first part of the Hamiltonian specify to sum over pairs of nearest neighbors (each pair counted once). The total particle number $\langle \hat{N}_p \rangle$ is conserved, since $[\hat{H},\, \hat{N}_p] = 0$. The particles of the BH model obey the commutation relation $[b_i,\, b_j^\dagger] = \delta_{ij}$. The first term of the Hamiltonian models the hopping of a particle from lattice site j to lattice site i. The second part describes the local on-site repulsion, which remains zero when a lattice site is unoccupied or occupied by only one particle. However, it increases proportional to U for each additionally added particle. In the following calculations and discussions we use the local interaction U as unit of energy. The third part of the Hamiltonian models a local potential of strength $\epsilon_i - \mu$.

3.1.1. Normal Mott insulating phase

Here, we evaluate the border of the quantum phase transition from Mott phase to superfluid phase for the first two Mott lobes by means of the variational cluster approach (VCA) [28], and show that this method provides quite accurately the boundaries of the Mott phase, as compared with more demanding QMC simulations and perturbative expansions. In addition, we study in detail the spectral functions of the two-dimensional BH model in both the first and the second Mott lobe, which require computing the Green's function in real frequency domain. We also present the densities of states and momentum distributions corresponding to the spectral functions.

The BH model exhibits a quantum phase transition from a Mott to a superfluid phase when the ratio between the hopping strength and the on-site repulsion t/U is increased or when particles are added to or removed from the system. The Mott phase is characterized by an integer particle density, a gap in the spectral function and zero compressibility [30].

The first two Mott lobes of the 2D BH model obtained by means of VCA are shown in Fig. 3.1. We used the chemical potential $x = \{\mu\}$ as variational parameter, which ensures

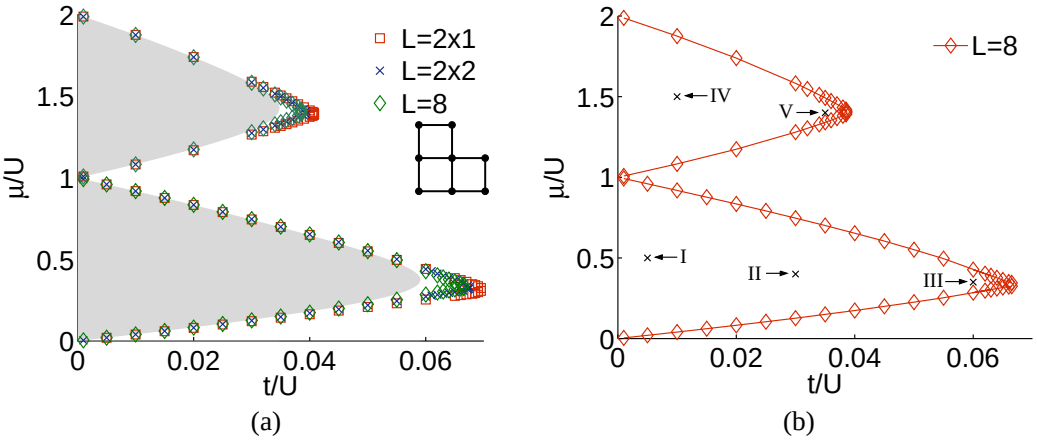

Figure 3.1.: (Color online) Phase boundaries of the Mott phase of the 2D BH model (Mott lobes). (a) Results of our VCA calculation with various cluster sizes for the reference system. The geometry of the 8-site cluster is visualized in the inset. The gray shaded area indicates the results of the process chain approach [139, 140]. (b) Phase boundaries obtained for the 8 site cluster. The marks refer to the parameters where we evaluated the spectral functions.

a correct particle density of the total system [51, 78]. In contrast to the one-dimensional results [51, 143] the Mott lobes of the 2D BH model are round shaped. The gray shaded area in Fig. 3.1 (a) presents the phase boundaries calculated within the process chain approach by N. Teichmann *et al.* in Refs. [139] and [140], which are basically identical to the QMC results by B. Capogrosso-Sansone *et al.*, see Ref. [132]. The agreement is quite good for small hopping. However, VCA seems to overestimate the critical value of the hopping $(t/U)_c$, which determines the tip of the Mott lobe. For the critical hopping of the first Mott lobe, we obtain approximately $(t/U)_c^1 = 0.067$ and for the second one $(t/U)_c^2 = 0.038$. Latest process chain approach [139, 140], QMC (Ref. [132]) and strong-coupling perturbation theory [137] results yield $(t/U)_c^1 = 0.059$ and $(t/U)_c^2 = 0.035$ for the critical parameter of the first and second Mott lobe, respectively.

The spectral functions $A(\mathbf{k}, \omega)$ and the densities of states $N(\omega)$ for parameters of the first Mott lobe are shown in Fig. 3.2. The spectral function is displayed on the conventional path around the Brillouin zone $\mathbf{k} = (0, 0)$ over (π, π) to $(\pi, 0)$ and back to $(0, 0)$, and we use an artificial imaginary-frequency broadening $\eta = 0.05$. A peculiarity of bosonic systems is that the hole band of the spectral function has negative spectral weight whereas the particle band has positive spectral weight. This follows from the definition of the bosonic Green's function which has a negative sign in front of the hole term, see Eq. (2.10). In the figures we always plot the absolute value of the spectral function. The local density of states is defined as a wave-vector summation of $A(\mathbf{k}, \omega)$. Therefore we observe a negative peak in the density of states, which corresponds to the hole band of the spectral function. For bosonic Green's functions the density of states is

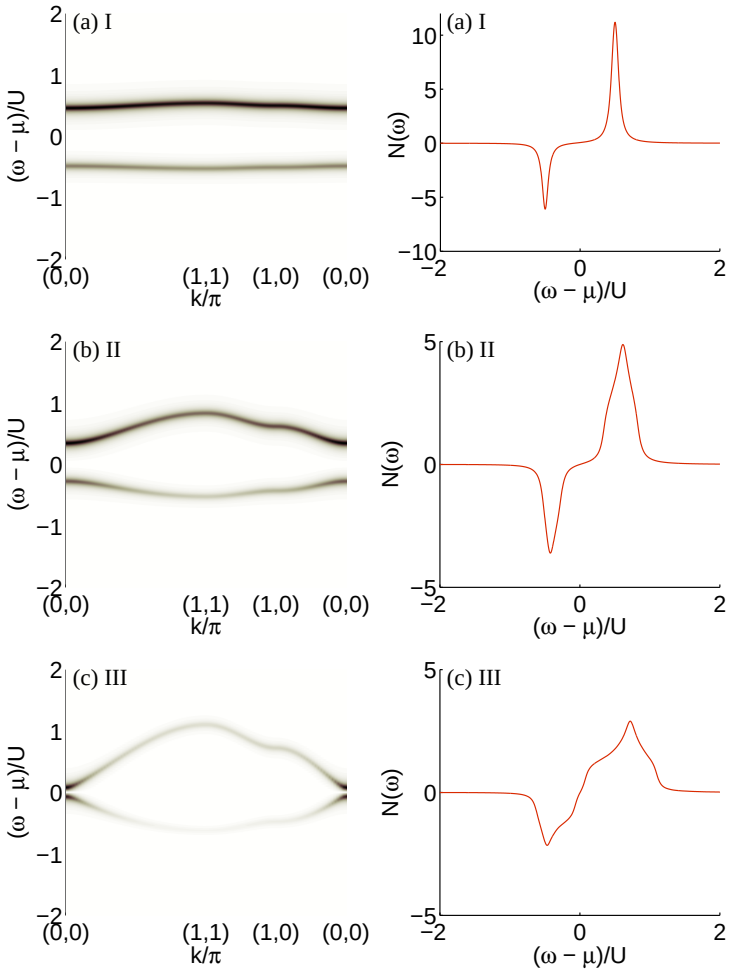

Figure 3.2.: Spectral function $A(\mathbf{k}, \omega)$, left column, and density of states $N(\omega)$, right column, in the first Mott lobe for the parameters (a) $t/U = 0.005$, $\mu/U = 0.5$, (b) $t/U = 0.03$, $\mu/U = 0.4$ and (c) $t/U = 0.06$, $\mu/U = 0.35$. The captions of the subfigures refer to the marks in Fig. 3.1 (b).

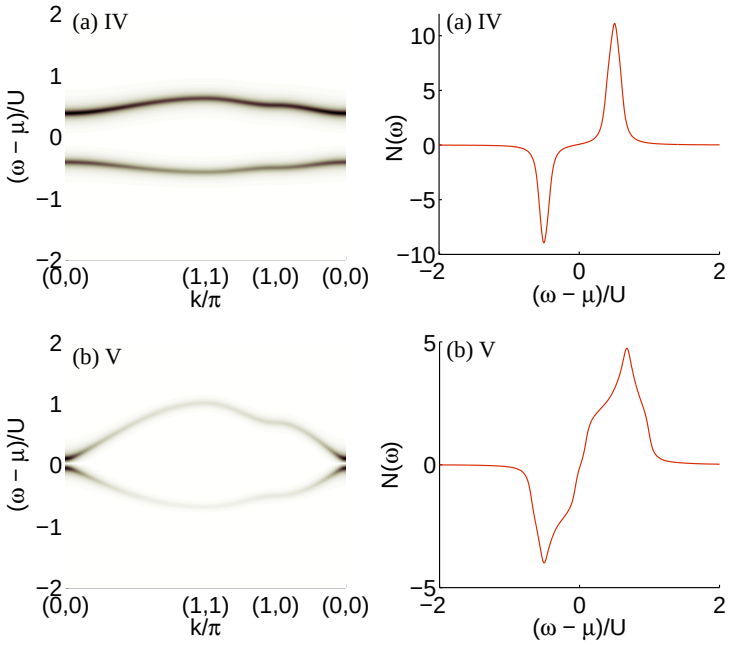

Figure 3.3.: Spectral function $A(\mathbf{k}, \omega)$, left column, and density of states $N(\omega)$, right column, in the second Mott lobe for the parameters (a) $t/U = 0.01$, $\mu/U = 1.5$ and (b) $t/U = 0.035$, $\mu/U = 1.4$. The captions of the subfigures refer to the marks in Fig. 3.1 (b).

not a probability distribution, as it contains negative values. Taking the absolute value would yield an all positive density of states, however, it would not be normed and is thus no probability distribution either. For small hopping, the gap in the spectral function is large and the bands are rather flat, i. e., the width of the bands is small, see Fig. 3.2. The corresponding density of states contains two well-separated peaks. For increasing hopping, the gap of the spectral function is decreasing and the width of the bands is increasing. Pursuant to the spectral function, the peaks in the density of states become broader for increasing hopping. The intensity of the two bands is almost constant for small hopping independent of the wave vector $\mathbf{k}$, whereas for large hopping a large intensity can be observed at $\mathbf{k} = \mathbf{0}$.

The boundaries of the Mott lobes correspond to the chemical potential of the state with one additional particle (hole), which is obtained directly from the single-particle (single-hole) minimum excitation energy. For this reason, we evaluate the phase diagram in Fig. 3.1 by taking the minimal gap of the spectral function for each t/U, which always occurs at $\mathbf{k} = \mathbf{0}$.

The spectral functions and densities of states in the second Mott lobe corresponding to the marks IV and V in Fig. 3.1 (b) are shown in Fig. 3.3. Qualitatively they are very similar to the spectral functions and densities of states in the first Mott lobe. Particularly, the intensity distribution of the bands seem to be strongly related. Yet the

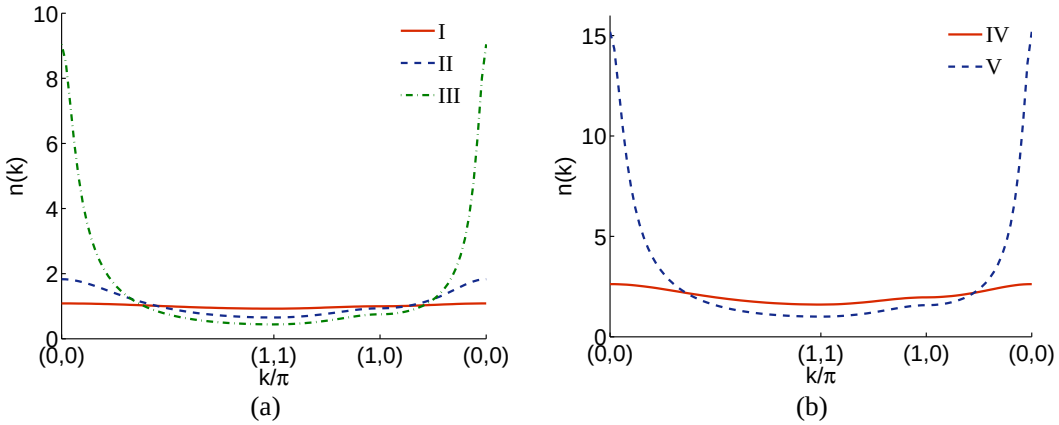

Figure 3.4.: Momentum distribution $n(\mathbf{k})$ in (a) the first Mott lobe and (b) the second Mott lobe. The Roman numerals in the legends refer to the parameters marked in Fig. 3.1 (b).

peaks of the density of states are larger due to the twice as large particle density within the second Mott lobe and thus the absolute value of the spectral weight in the second Mott lobe is larger than the one in the first Mott lobe.

The momentum distribution $n(\mathbf{k})$ corresponding to the spectral functions in the first and second Mott lobe are shown in Fig. 3.4. The particle density in the first Mott lobe is one and thus $n(\mathbf{k})$ is centered around one in Fig. 3.4 (a). For the second Mott lobe $n(\mathbf{k})$ is centered around two, see Fig. 3.4 (b). The particle density $n(\mathbf{k})$ is extremely flat for small hopping whereas it is peaked at $\mathbf{k} = \mathbf{0}$ for large hopping, which is already a precursor for the Bose-Einstein condensation where all macroscopic number of particles condense in the $\mathbf{k} = \mathbf{0}$ state. This behavior directly reflects the intensity distribution of the bands in the spectral function. There is excellent quantitative agreement between our VCA results for the momentum distribution and results obtained by means of QMC and a strong-coupling perturbation theory with scaling ansatz [144], see Fig. 3.5. We compare the momentum distributions for the parameters I ($t/U = 0.005$) and II ($t/U = 0.03$), and observe that the relative deviations between our VCA results and an approach obtained by combining strong-coupling perturbation theory with a scaling ansatz [144] are almost zero for small hopping $t/U = 0.005$ and less than one percent for medium hopping $t/U = 0.03$. This latter methods is certainly more accurate than VCA in the evaluation of the momentum distribution. However, it should be mentioned that the information about the critical point (critical exponents and critical hopping strength $(t/U)_c$) have to be inserted "by hand," in order to optimize the results. This information, in turn, must be extracted, e. g., from a QMC calculation. On the other hand, our VCA results are obtained directly without the need to introduce external parameters.

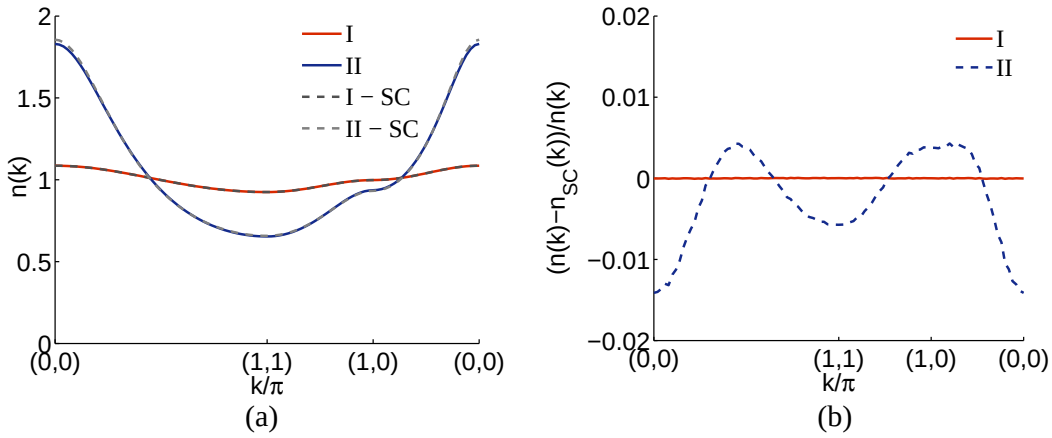

Figure 3.5.: Direct comparison (a) between the momentum distribution $n(\mathbf{k})$ obtained by means of VCA and a strong-coupling perturbation theory with scaling ansatz [144]. The data identified with the letters SC correspond to the strong-coupling results. The relative deviations between VCA results and strong-coupling results with scaling ansatz are shown in (b). The Roman numerals in the legends refer to the parameters marked in Fig. 3.1 (b).

Conclusions: In this section, we presented and discussed results obtained within the variational cluster approach for the spectral properties of the two-dimensional Bose-Hubbard Hamiltonian. This is a minimal model to describe bosonic ultracold atoms confined in optical lattices [20], and it undergoes a quantum phase transition from a Mott to a superfluid phase depending on the chemical potential μ, and the ratio between the hopping strength and the on-site repulsion t/U. In particular, we determined the first two Mott lobes of the phase diagram and found reasonable agreement with essentially exact results from QMC simulations and from the process chain approach. In particular, the variational cluster approach yields very good results for the phase boundaries apart from the region close to the lobe tip. Here, strong-coupling expansions and QMC calculations are, clearly, much more accurate. Yet it should be emphasized that the computational effort is considerably lower for VCA than for QMC. Furthermore, we evaluated spectral functions in the first and second Mott lobe. An important aspect of VCA is that the Green's function of the system is obtained directly in the real frequency domain, which allows for a direct calculation of the spectral function. On the other hand, QMC quite generally provides correlation functions in imaginary time. Imaginary-time correlation functions have to be analytically continued to real frequencies, which is a very ill-conditioned problem, as the data contain statistical errors. In QMC this analytical continuation is best carried out by means of the maximum entropy method. A very accurate dispersion (without spectral weight) has been also obtained by a strong-coupling expansion [137]. The intensity distribution of the spectral weight is similar for the spectral functions of both Mott lobes, leading to an evenly distributed spectral weight for

small hopping strengths and to a distribution sharply peaked at $\mathbf{k} = \mathbf{0}$ for large hopping strengths. The latter indicates a precursor to the Bose-Einstein condensation occurring above a certain critical hopping. We also evaluated the densities of states and momentum distributions corresponding to the calculated spectral functions. We compared our VCA results for the momentum distribution with strong-coupling perturbation-theory results, where a scaling ansatz has been used, and found excellent quantitative agreement.

3.1.2. Disordered lattice bosons

Interacting many-body systems with disorder are fascinating and challenging from both the experimental as well as the theoretical point of view. Understanding disordered bosonic systems has been of great interest ever since the pioneering works on the Bose-Hubbard (BH) model [30], which describes strongly interacting lattice bosons. Originally, the disordered BH model has been used to approximately describe various condensed matter systems, such as superfluid helium absorbed in porous media [145, 146], superfluid films on substrates [147], and Josephson junction arrays [148]. However, seminal experiments on ultracold gases of atoms trapped in optical lattices shed new light on interacting bosonic many-body systems, as these systems provide a *direct* experimental realization of the BH model [20, 22]. Intriguingly, these experiments allow to observe quantum many-body phenomena, such as the quantum phase transition from a superfluid to a Mott state [21]. The condensate of atoms can be driven across this phase transition by gradually increasing the laser beam intensity, which is directly related to the depth of the potential wells. There is a large experimental control over the system parameters such as the particle number or lattice depth, and in addition the parameters are tunable over a wide range. While optical lattices provide a very clean experimental realization of strongly correlated lattice bosons, they can be used to study disordered systems on a very high level of control as well. Disorder can be added to the regular optical lattice by several techniques, such as by superposing additional optical lattices with shifted wavelength and beam angles [149, 150, 151, 152, 153, 154], laser speckle fields [155, 156, 157, 158], or including atoms of a different species acting as impurities [159].

The disordered BH model has been widely investigated in the literature. Most of the work has been devoted to study the phase transitions occurring in the disordered BH model [160, 161, 162, 163, 164, 165, 166, 167, 168, 169, 170, 171, 172, 173, 174, 175]. At zero temperature the ground-state phase diagram depending on the chemical potential, the tunneling probability of the particles and the disorder strength, consists of three different phases: the Mott insulating, the superfluid, and the Bose glass phase. The first two phases are already present in the pure BH model, while the latter is a distinct feature of the disordered system. The Bose glass phase is characterized by being gapless and compressible, however, due to disorder the phase coherence does not extend over the entire system in contrast to the superfluid phase. While the phase diagram of the disordered BH model has been extensively studied, up to now spectral properties have not yet been investigated theoretically, even though they are experimentally accessible by Bragg spectroscopy, which allows to extract the wave vector dependent excitation

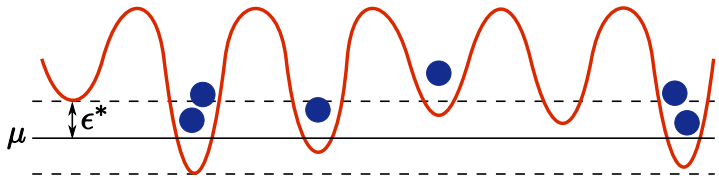

Figure 3.6.: (Color online) The periodic optical lattice potential is locally modified by disorder. In the illustration the disorder is bounded by ϵ^* corresponding to a situation obtained by the superposition of two incommensurate optical lattices.

energies of the system [42, 43, 44]. For low-energy excitations (typically $\omega/2\pi \lesssim 10$kHz) the response of the Bragg spectroscopy is ascribed to the structure factor, which corresponds to density fluctuations, whereas, for high excitation energies ($\omega/2\pi \gtrsim 30$kHz) the single-particle spectral function can be extracted [176, 177]. In this case, atoms excited into high-energy bands are not expected to interact with the lower bands. Therefore, the measured spectrum describes a convolution (without vertex corrections) of the density of states of the lower occupied with the upper unoccupied band. From this convolution the spectral function of the lower strong-correlated bands can be extracted [176].

In this section we study in detail the spectral properties of bosonic atoms in a disordered optical lattice, modeled by the one-dimensional BH model in which, for simplicity, the harmonic trap potential has been neglected. We focus on the strongly correlated regime and evaluate spectral properties for the hopping strength to the on-site interaction ratio of size $t/U = 0.05$. This ratio corresponds to an optical lattice depth of $11\,E_R$, where E_R is the recoil energy [178]. To evaluate this depth we considered laser beams with wave length $\lambda = 830\,nm$ and the scattering length of rubidium $a_s \approx 5\,nm$. In particular, we focus on the similarities and differences between the two common experimental methods used to induce disorder: (i) superposition of two laser fields with incommensurate wavevectors on the one hand, and (ii) the addition of a laser speckle field on the other hand.

One sample-configuration of disorder is denoted as $\eta = (\epsilon_1, \epsilon_2 \ldots \epsilon_N)$, where N is the number of lattice sites. The disorder modifies locally the depth of the optical lattice, see Fig. 3.6 for illustration. Random disorder is distributed according to a given probability distribution function (pdf) $p(\eta)$, which has to satisfy the normalization condition $\int p(\eta)\, d\eta = 1$. The average of a quantity X_η with respect to the pdf $p(\eta)$ is given by $X_p \equiv \langle X \rangle_p = \int p(\eta)\, X_\eta\, d\eta$. We consider ϵ_i as identically and independently distributed random variables leading to $p(\eta) = \prod_{i=1}^{N} q(\epsilon_i)$, where $q(\epsilon_i)$ is a pdf describing the disorder generated in the experiment. Experimentally, there are two main ways of introducing disorder, corresponding to two different pdf's. On the one hand, superposing two incommensurate optical lattices yields a shifted β distribution as demonstrated in the next subsection "Disorder distribution generated by incommensurate optical lattices." The distribution is bounded by a maximum disorder strength ϵ^*. This approach is used, for example, in the setup by Fallani *et al.* [150], where two laser beams with wave lengths

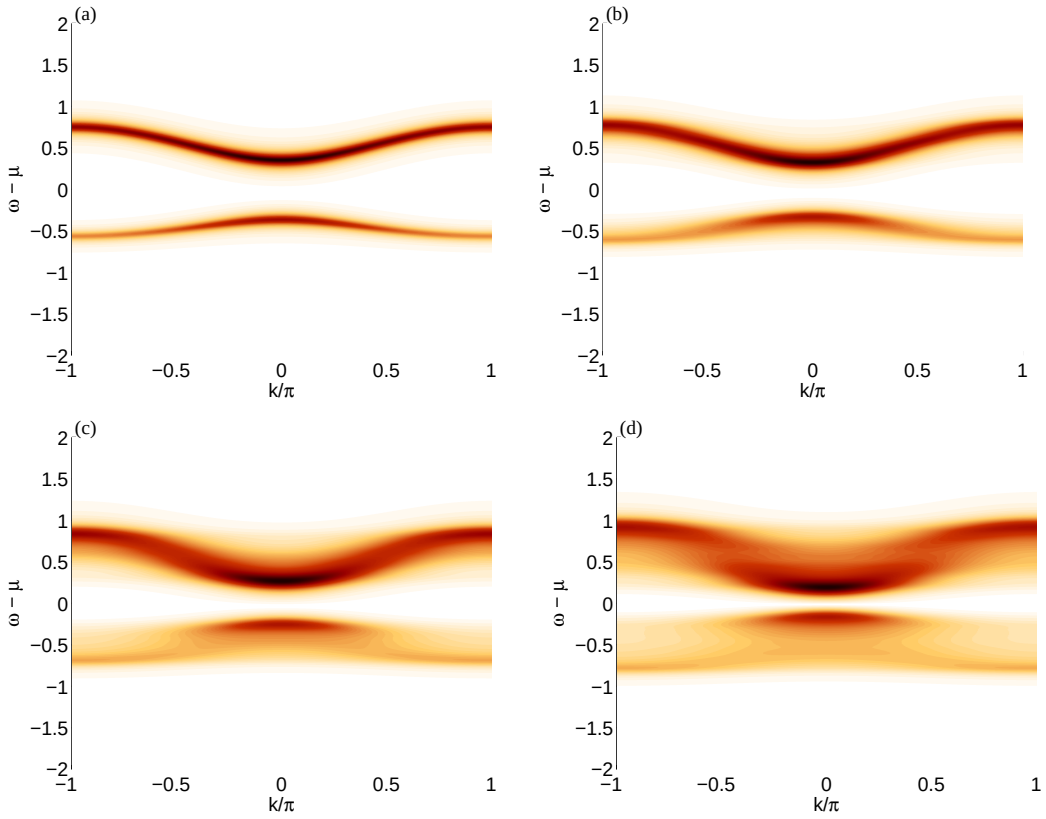

Figure 3.7.: Spectral function $A_p(\mathbf{k}, \omega)$ for disorder generated by superposition of incommensurate optical lattices. The parameters are $t = 0.05$, $\mu = 0.45$, and (a) $\epsilon^* = 0.0$, (b) $\epsilon^* = 0.1$, (c) $\epsilon^* = 0.2$, and (d) $\epsilon^* = 0.3$.

$\lambda_1 = 830$ nm and $\lambda_2 = 1\,076$ nm are superposed. Since these two wave lengths are highly incommensurable the disorder can be regarded as truly random, see Ref. [149]. Alternatively, disorder can be generated by superposing a laser speckle field [179, 180] to the regular optical lattice. In this case, one obtains an exponential distribution $q(\epsilon_i) = \theta(\epsilon_i) \exp(-\epsilon_i/\bar{\epsilon})/\bar{\epsilon}$ where $\bar{\epsilon}$ specifies the mean disorder strength [179, 180]. In our calculations the distribution is additionally shifted about its median $\bar{\epsilon} \ln 2$ to avoid modifications of the chemical potential due to disorder. The exponential distribution is asymmetric and unbounded and thus, strictly speaking, the Mott phase, which is controlled by the extrema of the distribution [163, 164, 171, 172] does not occur anymore. However, the goal of the present paper is to mimic the results of the experimental measurements, for which the effects of the tail of the distribution are too small to be observable. Therefore we introduce a cut off for the disorder distribution of $4\,\bar{\epsilon}\,\ln 2$. In other words, realizations far off the median are not considered.

We first investigate spectral properties for disorder realizations sampled from the shifted β distribution, which is realized experimentally by superposing two incommen-

surate optical lattices.

In particular, spectral functions $A_p(\mathbf{k}, \omega)$ are evaluated for hopping strength $t = 0.05$, chemical potential $\mu = 0.45$ and various strengths of disorder $\epsilon^* = \{0.0, 0.1, 0.2, 0.3\}$, see Fig. 3.7. The corresponding densities of states $N_p(\omega)$ are shown in Fig. 3.8.

For the numerical evaluation by means of VCA we use $M = 256$ disorder configurations, a reference system of size $L = 8$, and the VCA parameters $x = \{\mu, t, \delta\}$. The parameter δ is an additional on-site energy located at the boundaries of the cluster, whose introduction drastically improves the results, as shown in Ref. [181]. The artificial broadening parameter is chosen to be $0^+ = 0.05$ for spectral functions and $0^+ = 0.01$ for densities of states. As mentioned previously the occupied part of the single-particle spectral function is experimentally accessible by high-energy Bragg spectroscopy. For the pure system we obtain the well-known cosinelike shaped bands reminiscent of the dispersion of free particles on a lattice. For increasing disorder strength ϵ^* the minimal gap between the occupied and the unoccupied band shrinks. In addition, the bands become broader as the poles of the Green's function for a specific wave vector $\mathbf{k}$ are distributed over a large energy range. This behavior can also be seen in the density of states. Furthermore, for large disorder the bands seem to split in two sections separated by a pseudogap around $k = \pi$. This is a peculiarity of this disorder configuration which to some extend resembles a binary distribution. An ordered binary distribution would double the unit cell thus producing a true gap at $k = \pi$.

Experimentally the gap Δ present in Mott phase can be determined for instance by lattice modulation [38] or by Bragg spectroscopy [42]. In these experiments the amount of energy transferred to the system is related to the width of the central peak observed in time of flight images [38]. The width of the central peak is measured for various energies leading to the excitation spectrum. Indeed for increasing disorder strength ϵ^* a broadening of the excitation band has been observed [150] which is qualitatively in agreement with our results for the spectral function. In addition, it could be shown experimentally that the weight moves to lower excitation energies for increasing ϵ^* [150]. However, it is rather difficult to extract the precise value of the gap from the measured excitation spectra. Strictly speaking, the gap Δ is defined as the energy difference of the lowest lying poles in the occupied and unoccupied bands, respectively. Yet, our results show, that these poles quite generally carry only very little spectral weight. This means that it is virtually impossible to detect them in the experiment. For this reason, it might be useful to introduce the notion of a gap Δ^{mp}, that corresponds to the experimental situation and is determined by the distance between the maxima of the spectral weight observed in the center of the Brillouin zone. In Fig. 3.9 we compare Δ [Fig. 3.9 (a)] with Δ^{mp} [Fig. 3.9 (b)] which is obviously always larger than Δ. For increasing hopping strength t the gap Δ^{mp} decreases, however, it still remains finite (i. e., $\Delta^{mp} \approx 0.2$) at values of t for which the gap Δ determined from the smallest excitation energies is already almost zero. Therefore, a peak at finite energy will be observed in the experimental data, even when the system is already in the Bose-glass phase. Additionally, it is important to mention that the smallest excitation energy gap Δ can be predicted analytically for systems with infinitely many disorder realizations. In this case Δ is controlled by the

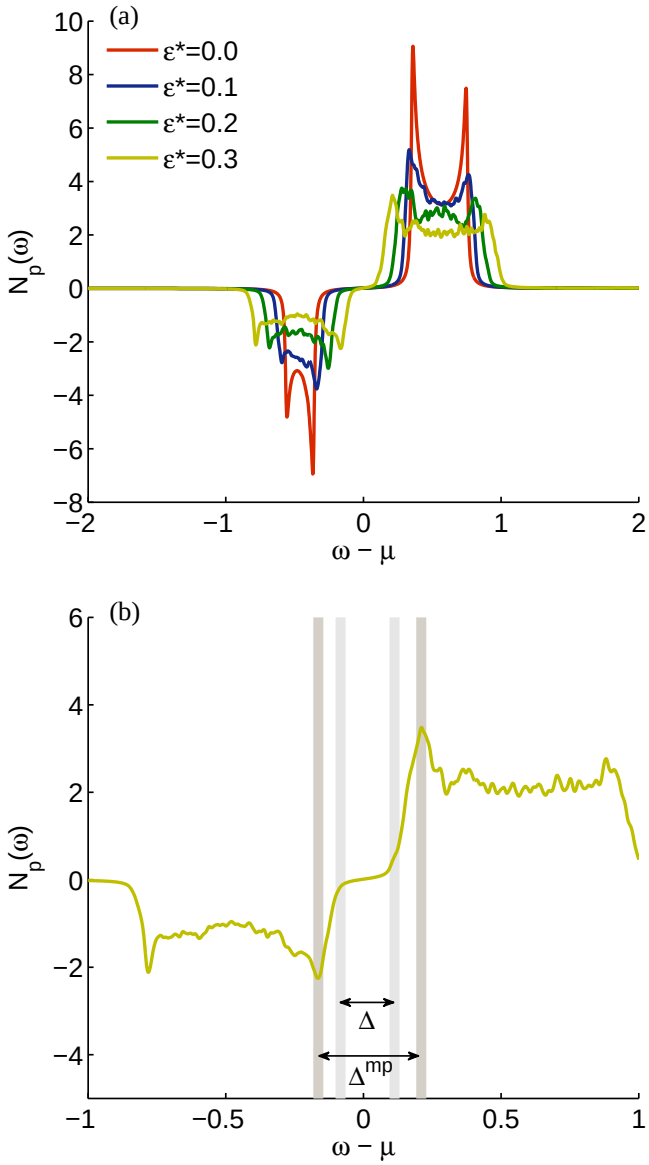

Figure 3.8.: (Color online) (a) Density of states $N_p(\omega)$ evaluated for the same parameters as in Fig. 3.7. (b) Illustration of the two "gaps" Δ and Δ^{mp} within a blowup of the the data for disorder strength $\epsilon^* = 0.3$. According to our definition (see text), Δ corresponds to the formal definition of the Mott gap based on minimal excitation energies, whereas Δ^{mp} corresponds to the minimum peak distance in the spectral weight, which is the quantity available from experiments.

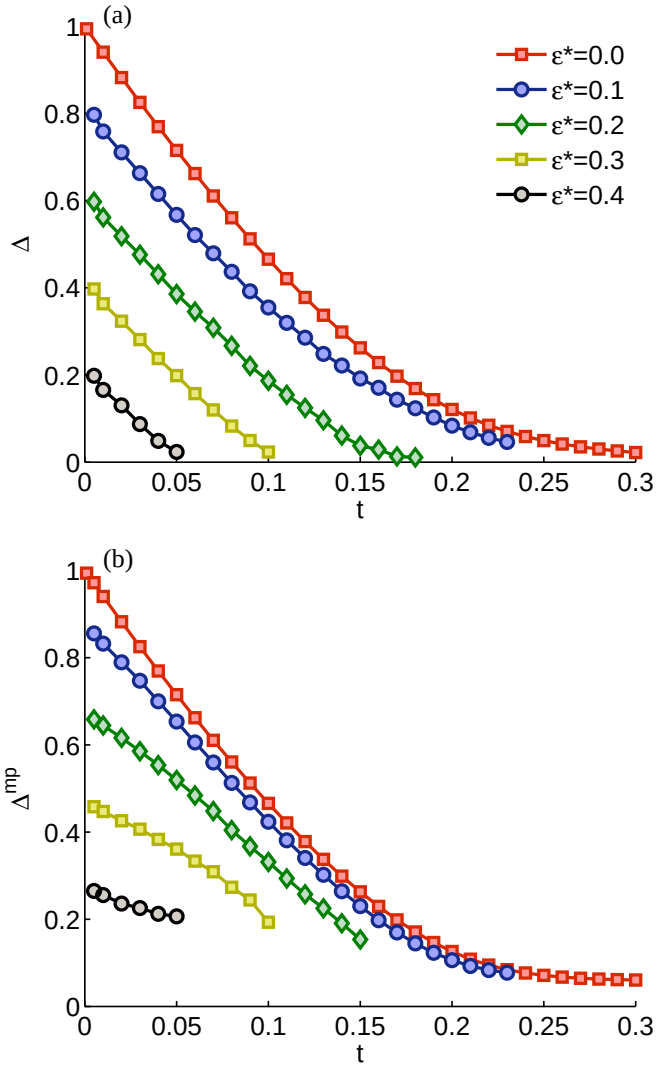

Figure 3.9.: Gap Δ obtained from (a) the smallest excitation energies and (b) Δ^{mp} obtained from the minimum peak energy difference of the occupied and unoccupied bands.

maximum disorder strength ϵ^* only. In particular, the phase boundary is shifted by $\pm\epsilon^*$ as there exist always rare regions where the chemical potential is either increased or decreased by ϵ^* [163, 164]. Here, however, we take into account a finite number of $L\,M = 2\,048$ random values for the on-site energies ϵ_i leading to larger gaps, since it is very unlikely that all values ϵ_i of one realization η are close to the extreme cases $\pm\epsilon^*$. This resembles more closely the experimental situation in which only a limited number of disorder realizations can be detected.

The second kind of disorder we are addressing in this paper follows the shifted exponential distribution, which is generated by superposing a laser speckle field. Spectral properties of the Bose-Hubbard model for this disorder distribution are shown in Fig. 3.10. In contrast to the disorder realized by the superposition of two incommensurate optical lattices, the spectral signatures evaluated for the exponential distribution clearly exhibits an asymmetric shape. This becomes particular visible when comparing the densities of states for various disorder strengths, see Fig. 3.10 (b). In particular, the poles are smeared out toward higher excitation energies and thus reflect the tail of the exponential distribution. No pseudogap behavior around $k = \pi$ is observed here, due to the shape of the exponential distribution which is in contrast to the β distribution not peaked at the edges.

Conclusions: In the present work we investigated for the first time spectral properties of the disordered Bose-Hubbard model. In view of a realistic description of the experimental results, we focused on disorder distributions which are relevant for ultracold gases of atoms in optical lattices. In particular, we studied the differences between disorder realized by the superposition of incommensurate laser fields with the one obtained by laser speckle fields. In both cases we evaluated spectral functions and densities of states and showed that the resulting spectral weight strongly depends on the underlying shape of the disorder distribution. Furthermore, we determined the gap present in the Mott phase for disorder generated by incommensurate optical lattices. On the one hand, we evaluated the gap Δ from the minimal excitation energies of the system and on the other hand we determined the gap Δ^{mp} from the minimum peak distance in the spectral weight located at the center of the Brillouin zone. Whereas Δ cannot be observed directly in the experiment since the low-energy excitations carry very little spectral weight, Δ^{mp} is directly measurable. Furthermore, Δ^{mp} is always larger than Δ and thus Δ^{mp} remains finite even at the Mott to Bose-glass transition. In our calculations, we neglected the harmonic trap potential present in the experiments with ultracold gases of atoms. In principle, this effect can be included in our formalism, however, with a significantly major effort which goes beyond the goal of the present work. There are two cases in which neglecting the trap potential is justified. As in the ordered case, one can expect for sufficiently small disorder strength the trap potential to lead to multiple ringlike regions which are alternately Mott gapped and gapless. Quite generally, one should be able to choose the parameters so that the volume of the gapless regions is much smaller than the one of the $\hat{N}_p = N$ Mott region in which we are interested. In this case, the spectrum will display a nonvanishing weight within the gap originating from the gapless regions.

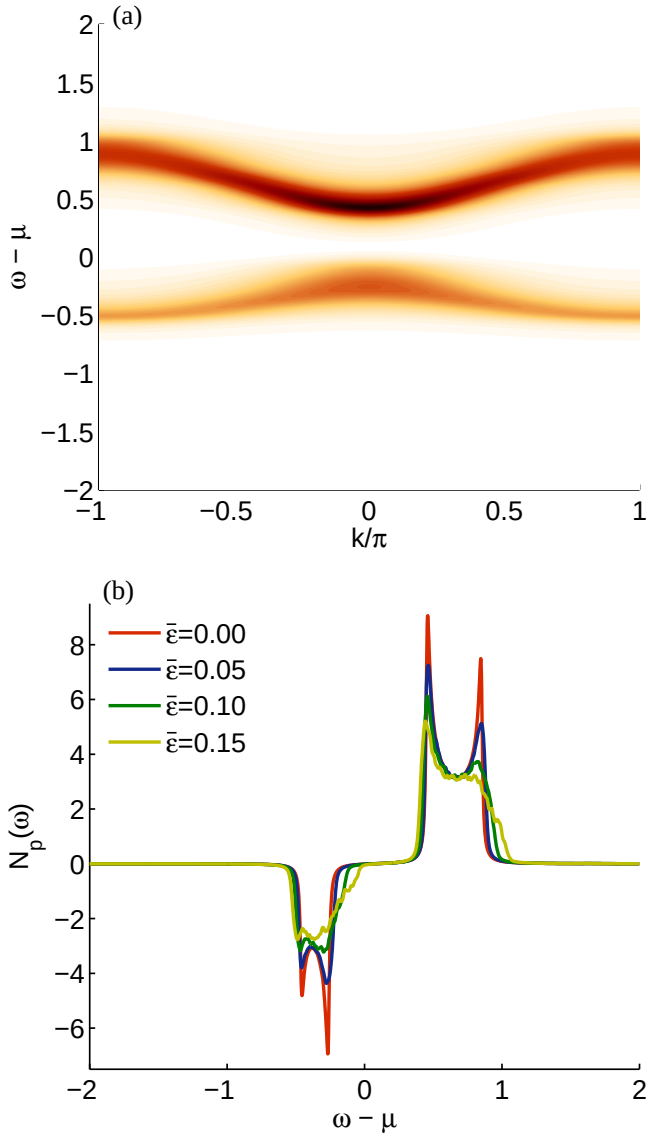

Figure 3.10.: Spectral properties for a disorder distribution generated by laser speckle fields. The parameters are $t = 0.05$, and $\mu = 0.35$. Panel (a) shows the spectral function $A_p(\mathbf{k}, \omega)$ evaluated for $\bar{\epsilon} = 0.15$ and panel (b) shows the densities of states for various disorder strengths $\bar{\epsilon} = \{0.0, 0.05, 0.1, 0.15\}$.

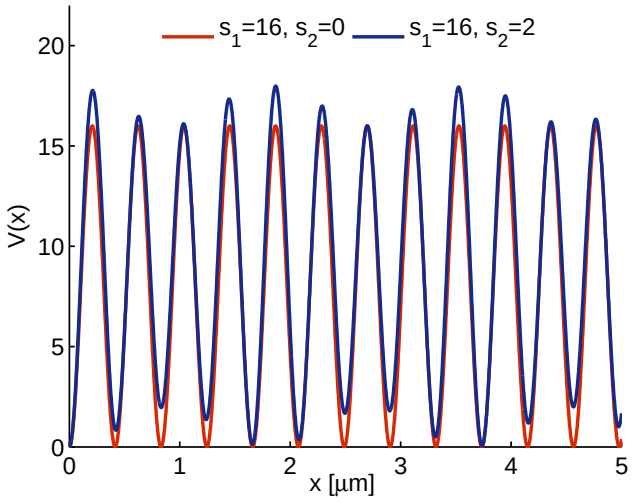

Figure 3.11.: Total lattice potential created by the superposition of the main optical lattice with depth s_1 and the disorder lattice with depth s_2.

However, we expect this to be small enough, at least for $\omega \neq 0$, so that the peaks defining the experimental gap Δ^{mp} remain discernible. Alternatively, spectroscopy experiments probing the system locally should be able to probe directly the Mott insulating region with no contributions from the gapless areas.

Disorder distribution generated by incommensurate optical lattices

Here, we show that the potential distribution, which results from the superposition of two optical lattices, follows a shifted β distribution. In particular, we focus on the experimental setup of Fallani *et al.* [150], who used for the main optical lattice a laser at wavelength $\lambda_1 = 830$ nm. Disorder is generated by superposing an additional lattice created from a weak laser beam at $\lambda_2 = 1\,076$ nm. The resulting potential is given by

$$V(x) = s_1 E_{R1} \sin^2 2\pi x/\lambda_1 + s_2 E_{R2} \sin^2 2\pi x/\lambda_2 \ ,$$

where x is the spatial position, s_1 and s_2 are related to the depth of the potential generated from the laser beams at λ_1 and λ_2, respectively. The constants E_{R1} and E_{R2} are the corresponding recoil energies. In this Appendix, the lattice depths s_1 and s_2 will always be stated in units of their recoil energies. The depth s_2 of the disorder-inducing wave is related to the maximal disorder strength ϵ^* by $\epsilon^* = s_2/2$. Since the wave lengths λ_1 and λ_2 are incommensurable the disorder imitates a true random behavior [149]. Here we reconstruct the histogram of the disorder distribution and find a mathematical expression, which reproduces the behavior of these physical systems.

In the experiments typical values for the lattice depths are $s_1 = 16$ and $s_2 = 2$, see Ref. [150]. Figure 3.11 compares the potential $V(x)$ for the previously mentioned values

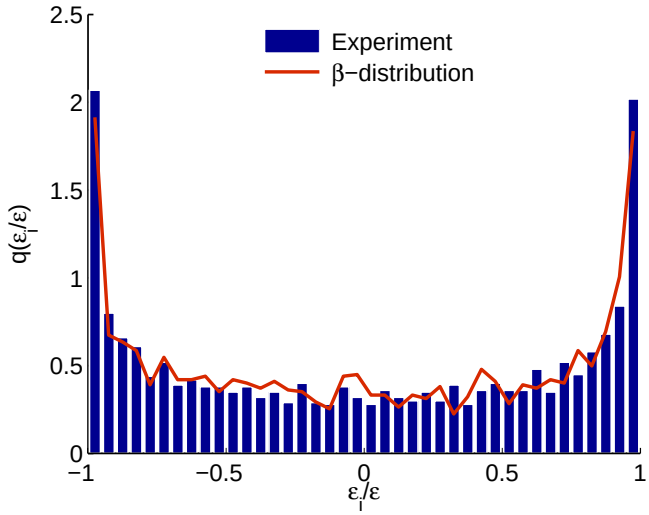

Figure 3.12.: Distribution of the on-site energy ϵ_i observed in the experiment (histogram) compared with random samples drawn from the shifted β distribution (solid line).

of $s_1 = 16$ and $s_2 = 2$ with the pure case, where the second laser beam at λ_2 is switched off, i. e., $s_1 = 16$ and $s_2 = 0$. It can be seen that the on-site energy varies for distinct lattice sites mimicking a random potential. Actually, the parameter s_2 just scales the disorder and thus our considerations are valid for arbitrary disorder strength ϵ^*. To evaluate a histogram of the energy distribution we subtract the disordered potential at the lattice sites from the pure potential and shift the difference by its mean ϵ^*. This yields a distribution which is centered around zero. The shift could have been absorbed as well in the definition of the chemical potential μ. The histogram for 2 048 lattice sites is shown in Fig. 3.12. In the center the distribution is rather flat, yet, there are important features at the boundary. Such a distribution can be well described by a shifted β distribution.

The β distribution $q_\beta(u|a,\, b)$, which is defined on the interval $u \in [0,\, 1]$, is given by

$$q_\beta(u|a,\, b) \equiv \frac{1}{B(a,\, b)}\, u^{a-1}\,(1-u)^{b-1}\,,$$

where

$$B(a,\, b) = \int_0^1 dp\, p^{a-1}(1-p)^{b-1} = \frac{\Gamma(a)\Gamma(b)}{\Gamma(a+b)}\,.$$

The expectation value of $q_\beta(u|a,\, b)$ is

$$\langle u\rangle = \frac{a}{a+b} \tag{3.2}$$

and its variance is

$$\mathrm{var}(u) = \frac{\langle u\rangle(1-\langle u\rangle)}{a+b+1}\,. \tag{3.3}$$

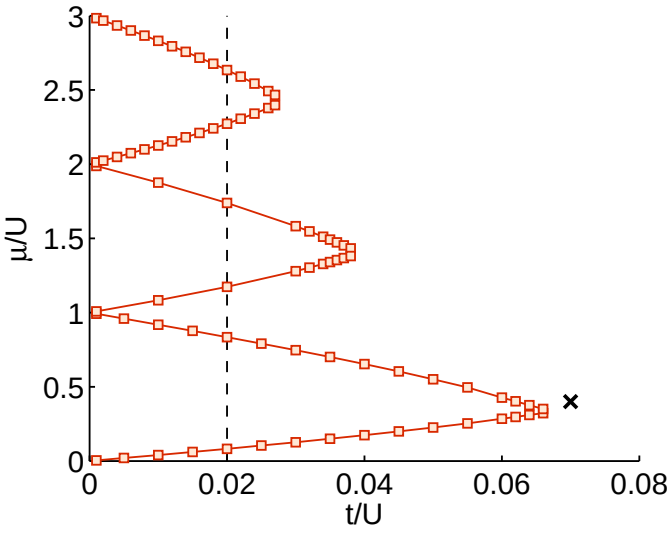

Figure 3.13.: Phase boundary for the first three Mott lobes corresponding to filling $n = 1$, 2 and 3. The data for the first two Mott lobes have been published in Ref. [54]. Static quantities are evaluated along the dashed line, i. e., for $t/U = 0.02$ and μ/U ranging from 0 to 3, whereas, the dynamic single-particle spectral function is evaluated at $t = 0.07$ and $\mu = 0.4$, see mark x.

To obtain a distribution which is symmetric around zero and bounded by $[-1, 1]$ we set $\langle u \rangle = 0.5$, shift the whole β distribution by this value and scale it by a factor of 2. Resolving Eqs. (3.2) and (3.3) under the condition that $\langle u \rangle = 0.5$ leads to $a = b = [\mathrm{var}(u)/4 - 1]/2$. For $\mathrm{var}(u) > 1/12$ (where $1/12$ is the variance of the uniform distribution), the probability density is shifted toward the boundaries of the distribution. In particular we set $\mathrm{var}(u) = 0.12$. Finally, we draw 2 048 samples from this specific shifted β distribution, which we denote as $q(\epsilon_i/\epsilon^*)$. The resulting distribution of the 2 048 samples is indicated by the solid line in Fig. 3.12, which reproduces well the distribution obtained from the experiment with two incommensurate optical lattices.

3.1.3. Superfluid phase

In this section, we present the first nontrivial application of the VCA theory, extended to the superfluid phase, to the two-dimensional BH (BH) model and compare the results with unbiased quantum Monte Carlo (QMC) calculations. We evaluate static quantities, such as the particle density n and the condensate density n_c as well as the dynamic single-particle spectral function $A(\mathbf{k}, \omega)$. The phase boundary of the first three Mott lobes as obtained in VCA is shown in Fig. 3.13. The data for the first two lobes have been published in Ref. [54]. Static quantities are evaluated for constant hopping strength $t/U = 0.02$ and distinct values of the chemical potential μ/U ranging from 0 to 3,

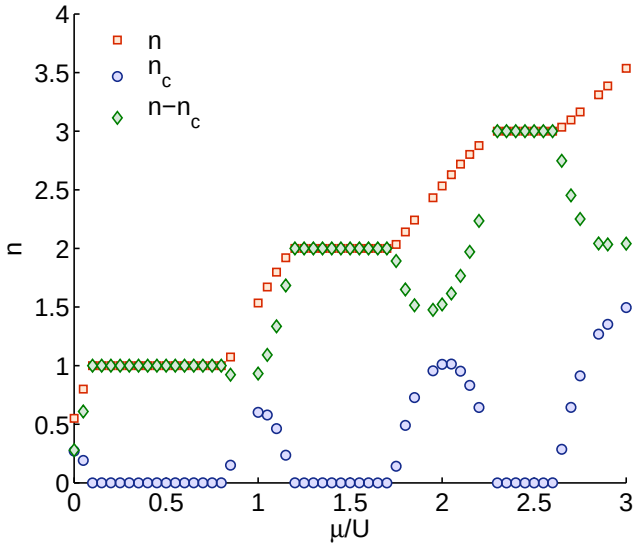

Figure 3.14.: Total particle density n, condensate density n_c, and density of the particles which are not condensed $n - n_c$ evaluated along the dashed line shown in Fig. 3.13.

scanning through various Mott lobes separated by the superfluid phase; see the dashed line in Fig. 3.13. The single-particle spectral function is evaluated for the parameter set marked by x in Fig. 3.13, which is located in the superfluid phase close to the tip of the first Mott lobe. For the numerical evaluation we used the chemical potential μ' and the strength of the source-and-drain coupling term F of the reference system as variational parameters. If not stated differently, the reference system consists of a cluster of size $L = 2 \times 2$.

The total particle density n evaluated using Eq. (2.62) is shown in Fig. 3.14 along with the condensate density $n_c = \langle A^\dagger \rangle \langle A \rangle / 2L$, and the density of the particles which are not condensed $n - n_c$. From Fig. 3.15 it can be observed that the particle density n evaluated for reference systems of size $L = 1 \times 1$ and of size $L = 2 \times 2$ are almost identical. The same holds for the condensate fraction n_c/n, which is shown in the inset of Fig. 3.15. In the same figure, we also compare our results with QMC calculations. The densities obtained from the two methods show an excellent agreement. The QMC data have been obtained for a system of size 32×32 and temperature $U/T = 128$ using the ALPS library [182] and the ALPS applications [183].

The single-particle spectral function $A(\mathbf{k}, \omega)$ evaluated for the parameter set, marked by x in Fig. 3.13, i. e., in the superfluid phase close to the tip of the first Mott lobe, is depicted in Fig. 3.16. The colored density plot corresponds to VCA results and the dots with errorbars to latest QMC results of Ref. [184]. The VCA spectral function $A(\mathbf{k}, \omega)$ consists of four bands, which is in agreement with results obtained by means of a variational mean field calculation [142], a strong coupling approach [141], and random phase

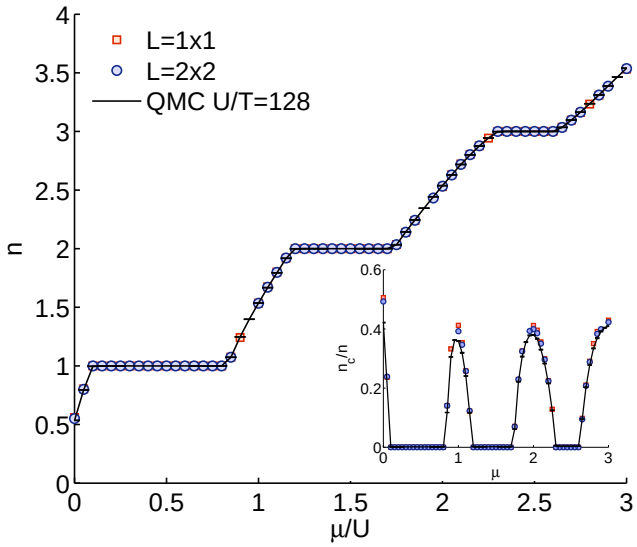

Figure 3.15.: Comparison of the total particle density n evaluated by means of VCA and QMC for parameters along the dashed line in Fig. 3.13 ($t/U = 0.02$). The inset compares VCA and QMC results for the condensate fraction n_c/n. VCA results are obtained for reference systems of size $L = 1 \times 1$ and $L = 2 \times 2$ and essentially infinitely large physical systems. QMC results are obtained for physical systems of size 32×32 inverse temperature $U/T = 128$.

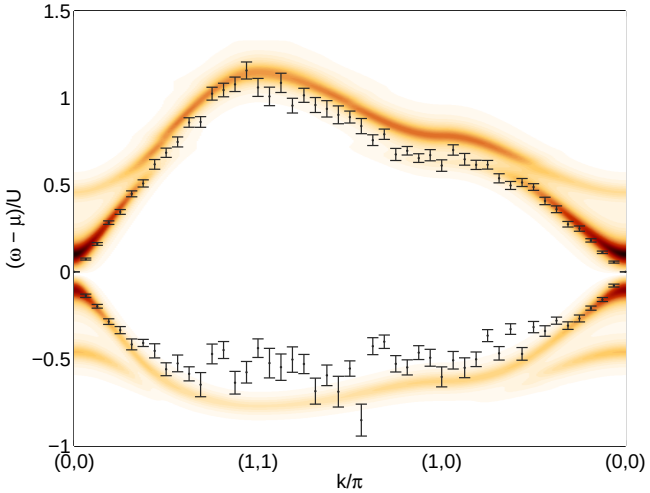

Figure 3.16.: Single-particle spectral function $A(\mathbf{k}, \omega)$ evaluated at $t/U = 0.07$ and $\mu/U = 0.4$. The colored density plot corresponds to VCA results and the dots with errorbars to latest QMC results of Ref. [184].

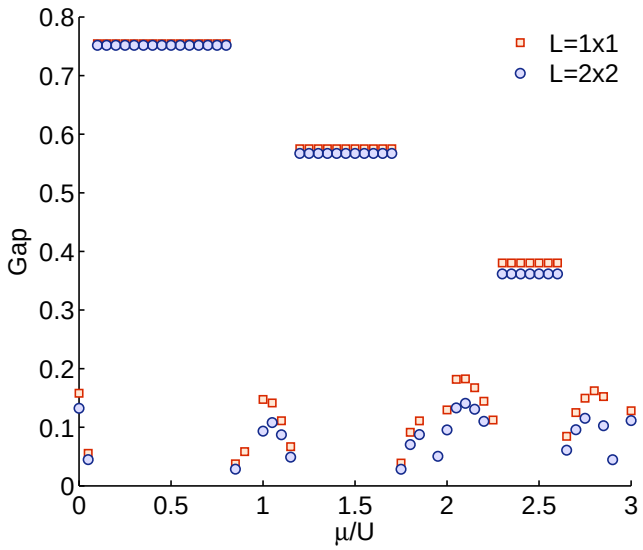

Figure 3.17.: Gap of the inner modes present in the single-particle spectral function measured at $\mathbf{k} = \mathbf{0}$ and evaluated along the dashed line shown in Fig. 3.13 for reference systems of size $L = 1 \times 1$ and $L = 2 \times 2$, respectively.

approximation (RPA) calculations [185, 131]. The advantage of VCA in comparison to the above mentioned approaches is that the results can be systematically improved by increasing the cluster size of the reference system. For each wave vector $\mathbf{k}$ the weight is concentrated in one of the two bands present at positive and negative energy, respectively. We observe that the outer two modes exhibit a wide gap at $\mathbf{k} = \mathbf{0}$, which is approximately of size U. The inner two, low-energy modes are also gapped at $\mathbf{k} = \mathbf{0}$. However, the gap is tiny, and away from $\mathbf{k} = \mathbf{0}$ the spectrum quickly develops a linear behavior, which is in agreement with the expected dispersion of Goldstone modes. The failure in obtaining a gapless long-wavelength excitation is a common problem of conserving approximations, i. e., of approximations for which macroscopic conservation laws are fulfilled. Similar aspects occur in dynamical mean-field theory calculations of two-component ultracold atoms as well [186]. In VCA there exists the additional possibility to systematically improve the obtained results by increasing the cluster size L of the reference system. Figure 3.17 compares the $\mathbf{k} = \mathbf{0}$ gap of the inner modes for reference systems of size $L = 1 \times 1$ and $L = 2 \times 2$. The gap is evaluated along the dashed line shown in Fig. 3.13. The first observation is that the gap present in the condensed phase is almost an order of magnitude smaller than the gap in the Mott phase. It vanishes at the Mott-to-superfluid transition and, most importantly, shrinks with increasing cluster size L. This behavior signals convergence toward the correct result.

In Fig. 3.16 we also compare our VCA results for the single-particle spectral function to latest QMC results obtained in Ref. [184]. In this figure QMC results are indicated by dots with errorbars, which quantify the peak position of the spectral weight. Overall,

we find good agreement in the low-energy spectrum. Only very close to $\mathbf{k} = \mathbf{0}$ the two results differ slightly and the QMC dispersion possesses the correct gapless behavior. The QMC spectral function, exhibits only two instead of four bands. This is, however, not surprising since for the considered parameter set and at a specific wave vector $\mathbf{k}$ the weight of one positive (negative) energy band dominates drastically over the other one located at positive (negative) energy. Thus the four bands are extremely difficult to resolve by means of the maximum entropy method, which has been used to infer the spectra from QMC data; see Ref. [184] for details concerning the QMC results. This reference also contains a comparison between VCA data and QMC data for the spectral function evaluated in the Mott phase, where the results obtained from the two approaches coincide very well for all $\mathbf{k}$ values.

We also evaluated the particle density n for the parameter set in the superfluid phase used in Fig. 3.16 and compared it to the QMC results. VCA yields $n = 1.0321$ in excellent agreement with the QMC result $n^{\mathrm{QMC}} = 1.03068(2)$ obtained at $U/T = 128$ for a system of size 32×32.

In the following we provide some additional remarks on the fact that the single-particle spectral function, obtained within our approach, is gapped in the long wavelength limit, i. e., close to $\mathbf{k} = \mathbf{0}$, for modes which ought to be identified with the Goldstone modes. This issue is a commonly known problem of conserving approximations [187]. One condition for an approximation to be conserving is, for example, to be Φ-derivable and self-consistent (see Ref. [188, 189, 71, 190, 191] for details). VCA is Φ-derivable but not self-consistent: The self-energy is the derivative of a functional of the Green's function, but the latter is not the Green's function obtained from Dyson's equation. Thus VCA is not completely conserving. However, many conservation laws are fulfilled at the stationary point of the self-energy functional, depending on which variational parameters are taken into account (see Ref. [192] for a more detailed discussion).

To obtain a gapless spectrum, a system of condensed bosons has to fulfill an *independent* condition, which is the Hugenholtz-Pines theorem [193, 190, 194]. There are only very few systematic approximation schemes which satisfy both conditions simultaneously. One notable exception occurs for interacting bosons composed of paired fermions. In this case, a consistent and gapless approximation can be developed provided the theory is expressed in terms of the constituent fermions [195]. In a different work [196] it was suggested to include an additional Lagrange multiplier in the form of a chemical potential, in order to explicitly enforce the Hugenholtz-Pines condition. Unfortunately, the Hugenholtz-Pines theorem is not fulfilled in VCA, and thus the low-energy modes of the single-particle spectral function are gapped in the long wavelength limit. Yet, the gap present in the VCA single-particle spectral function is small, and the spectrum quickly develops a linear behavior reminiscent of the gapless and linear Goldstone modes. Furthermore, in VCA there exists the possibility to systematically improve the results by increasing the cluster size of the reference system.

It is also interesting to mention that the related strong coupling approximation RPA, which yields a gapless spectrum, yet is not conserving [185, 131] can be obtained within certain limits of the extended VCA formalism. Specifically, the limits to consider are (i)

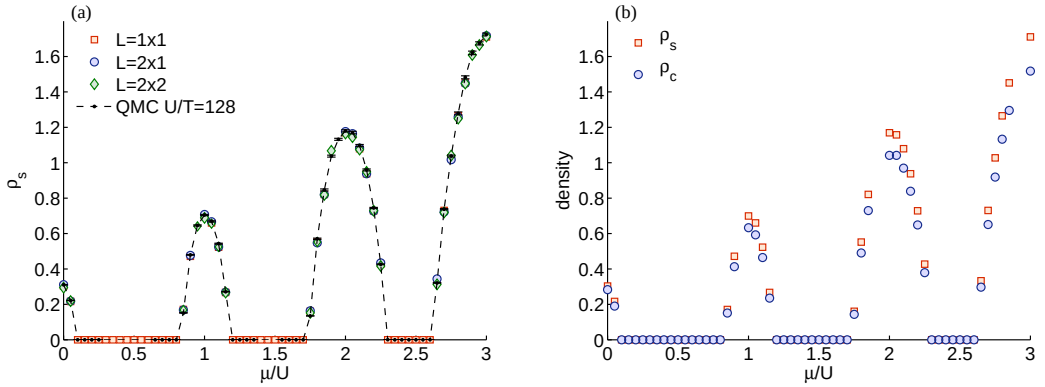

Figure 3.18.: Superfluid density ρ_s (a) evaluated for constant hopping strength $t/U = 0.02$ as a function of the chemical potential μ/U. VCA results for reference systems of size $L = 1 \times 1$, $L = 2 \times 1$, and $L = 2 \times 2$ and for essentially infinitely large physical systems are compared to QMC results for physical systems of size 32×32 and inverse temperature $U/T = 128$. Comparison of the superfluid density ρ_s and condensed density ρ_c (b) for reference systems of size $L = 1 \times 1$ and essentially infinitely large physical systems, *cf.* Ref. [57].

to use clusters of size $L = 1 \times 1$, (ii) not to use the chemical potential μ as variational parameter and (iii) to determine the source-and-drain coupling strength F self-consistently within a mean-field approach, whereby intercluster hopping terms $a_i^\dagger\, a_j$ are replaced with their mean-field value $\langle a_i^\dagger \rangle\, a_j + a_i^\dagger\, \langle a_j \rangle$ in the reference Hamiltonian. This leads to the selfconsistency condition $F = z\, t\, \langle A \rangle$, where $\langle A \rangle$ is given by Eq. (2.57) and z is the coordination number of the lattice. Our formalism provides a natural way to improve on RPA in a gapless, yet nonconserving, way by simply increasing the cluster size L and fixing F using the mean-field condition discussed above. However, it has to be emphasized that VCA yields much better results than RPA, even if RPA is extended to clusters of size L. Specifically, the particle density, the condensate density and the location of the phase boundary [54, 181] can be determined much more accurately by means of VCA only because we allowed for a variation in the chemical potential μ', i. e., allowed for macroscopic conservation laws to be fulfilled.

In the following, we discuss the evaluation of the superfluid density ρ_s within our extended SFA/VCA theory and present results for the two-dimensional BH model.

The superfluid density is related to the response of the system to a phase-twisting field [197, 198], leading to twisted boundary conditions (BC) in one spatial direction, which we choose to be the $\mathbf{e}_x$-direction, and periodic BC in the others. The many-body wave function $|\Psi\rangle$ has to obey these BC and thus

$$\hat{T}(N_x\, \mathbf{e}_x)\, |\Psi\rangle = e^{i\Theta}\, |\Psi\rangle \ ,$$

where the operator $\hat{T}(\mathbf{r})$ translates the particles by the vector $\mathbf{r}$, N_x is the lattice ex-

tension in $\mathbf{e}_x$-direction, and Θ is the phase twist applied to to the system. The twisted BC can be mapped by a unitary transformation onto the lattice Hamiltonian, leading to complex-valued hopping integrals [199, 200, 201]. The resulting Hamiltonian can be interpreted as a cylinder rolled up along the x-direction, which is threaded by an effective magnetic field with total flux Θ. When a particle is translated by N_x in the $\mathbf{e}_x$-direction a phase $\exp[-i\Theta]$ is picked up [202]. Due to gauge invariance, one is free to choose where the phase is collected when the particle propagates across the lattice. The usual choice is that each hopping process in the $\mathbf{e}_x$ direction, i. e., from site $\mathbf{r}' = (r_x - 1,\, r_y)$ to $\mathbf{r} = (r_x,\, r_y)$, is multiplied by a phase factor $\exp[-iA]$, where the associated vector potential is

$$A = \Theta / N_x \; . \tag{3.4}$$

When choosing the phase in that way, the reference system $\hat{H}'$ also depends on the vector potential A and the intra-cluster hopping terms become complex-valued along the $\mathbf{e}_x$-direction. For a Hamiltonian with nearest-neighbor hopping t, the superfluid density is determined from [202]

$$\rho_s = \frac{1}{t} \frac{1}{N_x\, N_y} \frac{\partial^2 \Omega_\Theta}{\partial\, A^2} \; , \tag{3.5}$$

where $N_x\, N_y$ is the total number of lattice sites of the physical system, and Ω_Θ is the grand potential of the physical system, subject to a phase twist Θ, as discussed above. Plugging in the vector potential of Eq. (3.4) yields

$$\rho_s = \frac{1}{t} \frac{N_x}{N_y} \frac{\partial^2 \Omega_\Theta}{\partial\, \Theta^2} \; . \tag{3.6}$$

In practice, the grand potential Ω_Θ is evaluated at the stationary point of Eq. (2.91), and is determined self-consistently for several values of Θ. From this data the curvature of Ω_Θ with respect to Θ is extracted from a fit. Using the curvature, the superfluid density is evaluated according to Eq. (3.6). Note that a finite cluster is embedded in an essentially infinitely large system and thus the limits are taken in the correct order to obtain the superfluid density [202].

In the following, we apply this procedure to the two-dimensional BH model [30]

$$\hat{H} = \sum_{\langle i,\, j \rangle} t_{ij}\, a_i^\dagger\, a_j + \frac{U}{2} \sum_i \hat{n}_i \, (\hat{n}_i - 1) - \mu \sum_i \hat{n}_i \; ,$$

where we extended the hopping integrals t_{ij} such that $t_{ij} = -t$ for hopping processes along the $\mathbf{e}_y$-direction and $t_{ij} = -t \exp[i\, A\, (\mathbf{r}_i - \mathbf{r}_j) \mathbf{e}_x]$ for hopping processes along the $\mathbf{e}_x$-direction. The reference system $\hat{H}'$ consists of a cluster decomposition of the physical system $\hat{H}$ plus a $U(1)$ symmetry breaking source term

$$\begin{aligned} \hat{H}' = \sum_{\mathbf{R}} \Big[\sum_{\langle \alpha,\, \beta \rangle} t'_{\alpha\beta} a^\dagger_{\alpha,\mathbf{R}}\, a_{\beta,\mathbf{R}} + \frac{U}{2} \sum_\alpha \hat{n}_{\alpha,\mathbf{R}} \, (\hat{n}_{\alpha,\mathbf{R}} - 1) \\ - \mu' \sum_\alpha \hat{n}_{\alpha,\mathbf{R}} - \sum_\alpha (a^\dagger_{\alpha,\mathbf{R}}\, f_\alpha + f^*_\alpha\, a_{\alpha,\mathbf{R}}) \Big] \; , \end{aligned}$$

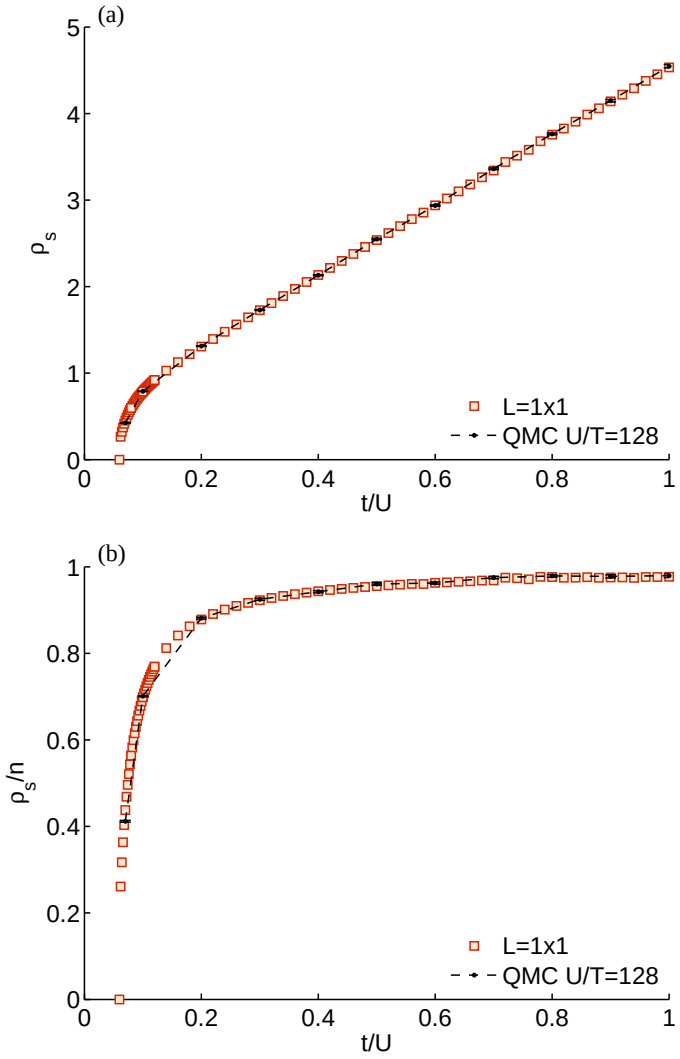

Figure 3.19.: Superfluid density ρ_s (a) and superfluid fraction ρ_s/n (b) ranging deep in the superfluid phase evaluated for constant chemical potential $\mu/U = 0.4$ as a function of the hopping strength t/U. Results obtained by means of VCA for reference systems of size $L = 1 \times 1$ and essentially infinitely large physical systems are compared to QMC results for physical systems of size 32×32 and inverse temperature $U/T = 128$.

where the lattice site indices i have been decomposed into an index $\mathbf{R}$, that specifies the cluster and into an index α, that specifies the lattice sites within a cluster [57, 54]. Analogously to the physical system, the hoping integrals are $t'_{\alpha\beta} = -t'$ and $t'_{\alpha\beta} = -t' \exp[i\, A\, (\mathbf{r}_{\mathbf{R}\alpha} - \mathbf{r}_{\mathbf{R}\beta})\mathbf{e}_x]$ for nearest-neighbor hopping processes along the $\mathbf{e}_y$- and the $\mathbf{e}_x$-direction, respectively, and zero otherwise. In our calculation, we use the chemical potential μ' and the source coupling strength f_α of the reference system as variational parameters in the optimization prescription. Since the reference system is complex valued, the source coupling strength f_α is complex valued too, i. e., $f_\alpha = |f_\alpha| \exp[\phi_\alpha]$. Thus, in general, $2L$ variational parameters have to be considered, where L is the number of cluster sites. However, for different cluster sites α the source coupling strengths f_α are interrelated, as can be seen from mean field arguments, leading effectively to two variational parameters $|f|$ and ϕ, which we use—in addition to the chemical potential μ'—to treat complex valued reference systems.

In Fig. 3.18 we present the superfluid density ρ_s for different sizes of the reference system ranging from $L = 1 \times 1$, over $L = 2 \times 1$, to $L = 2 \times 2$ and essentially infinitely large physical systems. For the largest cluster we restrict the variational search space to real valued order parameters, i. e., we set $\phi_\alpha = 0$. Figure 3.18 (a) demonstrates that this choice leads to comparable results as obtained with the full variational space. Yet, for the restricted variational space the computational effort as well as the numerical complexity is reduced, since the reference system remains real valued. Figure 3.18 (a) shows the superfluid density ρ_s, as a function of the chemical potential μ/U evaluated for fixed hopping strength $t/U = 0.02$. The chemical potential ranges from $\mu/U = 0$ to $\mu/U = 3$. As the hopping strength is small, three regions with $\rho_s = 0$ are present, corresponding to the Mott insulating phase. In between these regions, we observe a finite superfluid density ρ_s indicating the occurrence of the superfluid phase. In addition to the VCA results, we show QMC results with errorbars (barely visible) for physical systems of size 32×32 and inverse temperature $U/T = 128$. The QMC calculations were performed with the ALPS library [182] and the ALPS applications [183]. Particularly, we use the stochastic series expansion representation of the partition function with directed loop updates [203, 204, 205], where the superfluid density is evaluated via the winding number [206, 207]. The superfluid density ρ_s obtained from VCA agrees remarkable well with the QMC results. Furthermore, VCA results are almost independent of the size L of the reference system, signaling convergence to the correct results even for $L = 1 \times 1$ site clusters. The superfluid density ρ_s is compared to the condensate density $\rho_c = \langle a_i \rangle$ in Fig. 3.18 (b), *cf.* Ref. [57]. It can be observed that the superfluid density is always larger than the density of the Bose-Einstein condensate. However, the difference between the two densities is rather small, since a very dilute Bose gas is investigated.

In Fig. 3.19 we evaluate (a) the superfluid density ρ_s and (b) the superfluid fraction ρ_s/n (n is the particle density) for fixed chemical potential $\mu/U = 0.4$ as a function of the hopping strength t/U. The hopping strength ranges from $t/U = 0$ to $t/U = 1$, which is already very deep in the superfluid phase. For $\mu/U = 0.4$ the phase boundary between the Mott and the superfluid phase is located at $t/U \approx 0.06$. In the superfluid phase close to the phase boundary the superfluid density rises quickly from zero developing

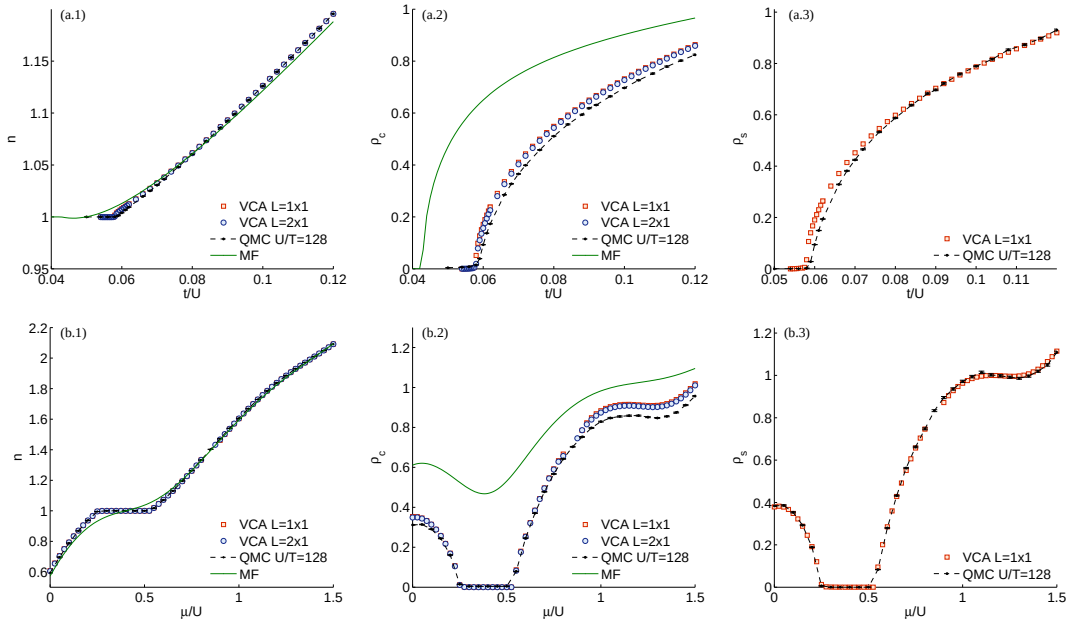

Figure 3.20.: Particle density n (left), condensate density ρ_c (middle), and superfluid density ρ_s (right) evaluated around the quantum critical region close to the tip of the first Mott lobe. Comparison of the data obtained by means of VCA (for essentially infinitely large physical systems and reference systems as stated in the legends), QMC (for physical systems of size 32×32 and inverse temperatures $U/T = 128$), and mean-field. The first row (a.$*$) shows results for fixed chemical potential $\mu/U = 0.4$ as a function of the hopping strength t/U, whereas the second row (b.$*$) shows results for fixed hopping strength $t/U = 0.05$ as a function of the chemical potential μ/U.

an almost linear behavior for $t/U \gtrsim 0.2$. In the latter parameter regime the superfluid fraction is larger than 90% signaling that already a very large amount of the lattice bosons is superfluid. As emphasized in Ref. [208], a relatively sharp crossover from a strongly-correlated superfluid, characterized by a superfluid fraction which is well below 1, to a weakly-correlated superfluid, where the superfluid fraction is almost 1, can be observed, see Fig. 3.19 (b). In addition to the VCA results evaluated for reference systems of size $L = 1 \times 1$ and essentially infinitely large physical systems, we show QMC results for physical systems of size 32×32 and inverse temperature $U/T = 128$, which again exhibit perfect agreement.

In Fig. 3.20 we focus on the quantum critical region close to the tip of the first Mott lobe, which is the most challenging one. In particular, we evaluate the particle density n, the condensate density ρ_c, and superfluid density ρ_s. In the first row we show results for fixed chemical potential $\mu/U = 0.4$ as a function of the hopping strength t/U, whereas in the second row we keep hopping strength fixed at $t/U = 0.05$ and vary the chemical

potential μ/U. We compare VCA results with QMC and mean-field (MF). The most important observation is that MF is far off QMC and VCA. For $\mu/U = 0.4$ MF predicts the phase transition to be at a much smaller value of t/U than QMC and VCA. This leads to significant deviations in both the density and condensate density as compared to QMC and VCA. For fixed $t/U = 0.05$ MF does not enter the Mott region and thus does not predict a plateau in the density. For both investigated situations (fixed μ/U and fixed t/U) the results obtained by means of VCA and QMC agree quite well. For the QMC simulations we used lattices of size 32×32 and inverse temperatures of $U/T = 128$. The VCA results are obtained at zero temperature for clusters of size 1×1 and 2×1, respectively, and essentially infinitely large physical systems. In this challenging regime small differences between VCA and QMC are observable for the condensate density. For the reference system sizes considered here, results are almost identical. Larger reference systems might still reduce the difference between VCA and QMC. However, close to the phase transition finite size and finite temperature effects might still be important for the QMC results, and thus a proper finite size scaling of these data might also reduce the discrepancy between the two approaches. Note that for fixed hopping $t/U = 0.05$ there is a very small region at $\mu/U \approx 0.85$, where it is difficult to numerically determine the stationary point of the grand potential. Such a region is also present between the first and the second and between the second and the third Mott lobe in Fig. 3.18. However, there it is barely visible since the spacing between two consecutive μ datapoints is larger than this gap. This failure appears to be related to the fact that two solutions adiabatically connected to two sectors with different particle numbers, i. e. the two neighboring Mott regions, meet and try to avoid each other. However, we want to emphasize that this problem affects only a tiny region of the phase diagram. When keeping the chemical potential fixed at $\mu/U = 0.4$ solutions can be easily found for all values of the hopping strength.

Finally, we want to emphasize that the VCA results are obtained with very modest computational effort and that excellent agreement with QMC can be observed, even for very small reference systems.

Conclusions: As a first nontrivial application of the extended version of the variational cluster approach we chose the two-dimensional Bose-Hubbard model and evaluated static quantities such as the total particle density and the condensate density, as well as the dynamic single-particle spectral function. We compared the single-particle spectral function with recent Quantum Monte-Carlo results [184] and found good agreement between the two approaches. It has to be pointed out that our extended variational cluster approach, while fulfilling many conservation laws, does not fulfill the Hugenholtz-Pines theorem. From this fact follows that the low-energy excitations of the spectrum have a small but nonzero gap in the long wavelength limit. This is a common aspect, which is already present in theories of the dilute Bose gas [187, 209, 210]. However, for wavevectors away from $\mathbf{k} = \mathbf{0}$ the spectra obtained within this approach quite soon exhibit a correct linear behavior and agree very well with the Quantum Monte-Carlo results. Moreover, the gap shrinks with increasing cluster size, corroborating that the variational cluster

approach becomes exact in the infinite cluster limit. Due to the fact this approach fulfills several conservation laws, the particle density, the condensate density as well as the phase boundary [54, 181] delimiting the Mott from the superfluid phase can be evaluated very accurately. We demonstrated, that our variational cluster approach results for the densities evaluated in both, the Mott and the superfluid phase, match perfectly with Quantum Monte-Carlo results.

We also presented how the superfluid density can be evaluated by means of this extended variational cluster approach. To this end we applied a phase twisting field to the system. We evaluated the superfluid density for the two-dimensional Bose-Hubbard model and compared the extended variational cluster approach results with unbiased quantum Monte Carlo results, yielding remarkable agreement. We want to emphasize that the extended self-energy functional approach is not only applicable to the Bose-Hubbard model but to a large class of lattice models, which exhibit a condensed phase. This includes experimentally interesting systems such as disordered bosons, multicomponent systems (Bose-Bose mixtures or Bose-Fermi mixtures) and light matter systems [23, 24]. Strictly speaking, the method cannot treat long-range interactions, such as dipolar ones, exactly [211, 212]. However, the long-range part can be incorporated on a mean-field level [213]. In principle, the present approach can be applied to systems with broken translational invariance as well, and, for example, can consider the effect of a confining magnetic trap. However, in this case one has to abandon the Fourier transform in the cluster vectors and work in real space and, thus, deal with larger matrices and a larger number of variational parameters. A convenient, numerically less expensive alternative, is to adopt the so-called local density approximation [214].

3.2. Jaynes-Cummings lattice model

The experimental progress in controlling quantum optical and atomic systems, which has been achieved over the last few years, prompted ideas for new realizations of strongly correlated many body systems, such as ultracold gases of atoms trapped in optical lattices [20, 21, 22] or light-matter systems [215, 216, 23]. The latter consist of photons, which interact with atoms or atomiclike structures. Normally, the interaction between photons and atoms is very weak, since the interaction time is small. However, a strong interaction can be achieved when photons are confined within optical cavities. In this case, the coupling between photons and atoms leads to an effective repulsion between photons, which means that it costs energy to add additional photons to the cavity. The arrangement of such cavities on a lattice, see Fig. 3.21, allows the photons to "hop" between neighboring sites, provided the cavities are coupled. Quantum mechanically the coupling of adjacent cavities means that their photonic wave functions overlap. Due to the strong interaction between photons and atoms, and the introduction of a lattice of coupled cavities, a strongly correlated phase emerges where photons are present. The light-matter models share some basic properties with the Bose-Hubbard (BH) model [30], such as the quantum phase transition from a Mott phase, where particles are localized on the lattice sites, to a superfluid phase, where particles are delocalized on the

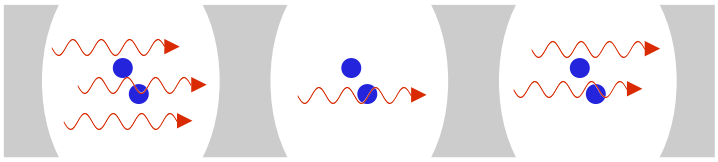

Figure 3.21.: Cavities forming a one-dimensional chain lattice. The blue dots represent atomic systems, whereas the red wavy arrows indicate photons.

whole lattice [215]. Yet the physics of the light-matter models is far richer because two distinct particles, namely, photons and atomiclike excitations, are present.

A major advantage of these man-made realizations of strongly correlated many-body systems is that they can be tailored to correspond to a many-body model, whose parameters can be directly controlled in the experiment. Furthermore local quantities, such as the particle density at a specific lattice site, can be addressed individually due to the mesoscopic scale of the cavities and both lattice size and geometry can be controlled in the fabrication process. An experimental realization of these light-matter systems is still missing but there are several promising approaches, such as photonic crystal cavities or toroidal and disk-shaped cavities [23]. If light-matter systems can be realized, they will undoubtedly provide fascinating insight in the physics of strongly correlated many-body systems. The realizations might be used as quantum simulators for other quantum mechanical problems or even more intriguing for quantum information processing applications [217].

Recently, there has been a lot of research activity in the field of light-matter systems. Most of the work has been devoted to investigate the quantum phase transition from the Mott to the superfluid phase. Some basic characteristics of the quantum phase transition have been evaluated from small systems of a few cavities by means of exact diagonalization [216, 218, 219, 220, 221]. Results are available at mean-field level [215, 222, 223, 224] as well or more accurately from analytical strong coupling perturbation theory calculations [225], and from simulations based on the density matrix renormalization group (DMRG) [226, 227], the variational cluster approach [69] and Quantum Monte Carlo [228]. Spectral properties of light-matter systems have been investigated in Refs. [225], [69], and [229].

Here, we study in detail the spectral properties of a one-dimensional light-matter system. In particular, we evaluate both photonic as well as atomic-excitation spectral functions. The investigation of both spectral functions allows us to characterize the polariton excitations in light-matter models. In addition to the spectral functions, we present densities of states, momentum distributions and spatial correlation functions. For completeness we also show the first two lobes delimiting the Mott transition.

3.2.1. Model

From the great variety of possible theoretical descriptions of light-matter systems [215, 216, 23, 226, 230, 231] we concentrate on the simplest one, which consists of an array of

cavities each of which contains a two-level system [215]. The physics of the i-th cavity can be described by the Jaynes-Cummings (JC) Hamiltonian [232], which for $\hbar = 1$ is given by

$$\hat{H}_i^{JC} = \omega_c \, a_i^\dagger \, a_i + \epsilon \, \sigma_i^+ \, \sigma_i^- + g \left(a_i \, \sigma_i^+ + a_i^\dagger \, \sigma_i^- \right) \, , \tag{3.7}$$

where ω_c is the resonance frequency of the cavity, i. e., the frequency of the confined photons, ϵ is the energy spacing of the two-level system, and g is the atom-field coupling constant. The operator $a_i^\dagger$ creates a photon with frequency ω_c, whereas a_i annihilates one. The two-level system can be mathematically described by Pauli spin algebra. Thus, we identify the ground state of the two-level system with $|{\downarrow_i}\rangle$ and the excited state with $|{\uparrow_i}\rangle$. With that the atomic raising operator is defined as $\sigma_i^+ \equiv |{\uparrow_i}\rangle \langle{\downarrow_i}|$ and the atomic lowering operator as $\sigma_i^- \equiv |{\downarrow_i}\rangle \langle{\uparrow_i}|$, respectively. In order to obtain the JC Hamiltonian the rotating wave approximation, which is justified for $|\omega_c - \epsilon| \ll \omega_c, \, \epsilon$ [233], has been assumed. The deviation between the resonance frequency and the energy spacing of the two-level system, $\Delta \equiv \omega_c - \epsilon$, is termed detuning. For the JC Hamiltonian the particle number $\hat{n}_i = a_i^\dagger \, a_i + \sigma_i^+ \, \sigma_i^-$ is a conserved quantity, as $[\hat{H}_i^{JC}, \, \hat{n}_i] = 0$. This is a consequence of the rotating wave approximation [233].

The full model consists of an array of N cavities, which form a lattice and hence we refer to this model as the Jaynes-Cummings lattice (JCL) model. Due to the coupling of the cavities, photons are allowed to hop between neighboring lattice sites. This leads to the JCL Hamiltonian

$$\hat{H}^{JCL} = -t \sum_{\langle i, \, j \rangle} a_i^\dagger \, a_j + \sum_i \hat{H}_i^{JC} - \mu \, \hat{N}_p \, , \tag{3.8}$$

where t is the hopping strength and μ the chemical potential, which controls the total particle number $\hat{N}_p$ of the system. The first sum with the angle brackets around the summation indices is restricted to nearest-neighbor sites. In the case of the JCL model, the particle number of a specific cavity $\hat{n}_i$ is not conserved anymore. However, the total particle number $\hat{N}_p = \sum_i \hat{n}_i$ is a conserved quantity. In summary, the JCL Hamiltonian can be rewritten as

$$\begin{aligned} \hat{H}^{JCL} = & - t \sum_{\langle i, \, j \rangle} a_i^\dagger \, a_j - \Delta \sum_i \sigma_i^+ \, \sigma_i^- \\ & + g \sum_i (a_i \, \sigma_i^+ + a_i^\dagger \, \sigma_i^-) - (\mu - \omega_c) \, \hat{N}_p \, . \end{aligned} \tag{3.9}$$

From Eq. (3.9) and from the fact that we consider the coupling strength g as unit of energy, it follows that the physics only depends on three independent parameters, namely the hopping strength t, the detuning Δ and the modified chemical potential $\mu - \omega_c$. In order to fulfill the condition for the rotating wave approximation the resonance frequency ω_c has to be large in comparison with the detuning Δ, which can be always satisfied theoretically as solely the difference between the chemical potential and the resonance frequency appears in the grand-canonical Hamiltonian $\hat{H}^{JCL}$.

3.2.2. Peculiarities of the variational cluster approach

The basic concept of VCA for bosonic particles is explained in Sec. 2.1. Here, we report on the peculiarities in VCA appearing due to the atomic excitations, which are modeled as two-level systems.

In order to guarantee that a given physical quantity (such as the number of particles) is thermodynamically consistent, it is necessary that the grand potential Ω is stationary with respect to the associated coupling constant (here the chemical potential) [78]. Therefore, varying ω_c ensures that the total number of photons is thermodynamically consistent. On the other hand, it would be advisable for a conserved quantity, i. e., $\hat{N}_p$ to be consistent as well. Otherwise uncommon situations could occur. For example, as we show below, the total particle density $\hat{N}_p/N$, evaluated as a trace of the Green's functions is not integer in the Mott phase. This effect becomes stronger close to the tip of the Mott lobe, see Fig. 3.23 (b). The noninteger particle density, occurring when μ is not taken as a variational parameter, clearly introduces an uncertainty in the determination of the phase boundary.

In principle, however, there is a formal difficulty in taking μ as a variational parameter. The problem is related to the coupling of μ with atomic excitations, which, in contrast to photons, cannot be seen as noninteracting particles. This is, in general, not allowed within VCA, whereby the reference system can differ from the physical one by a single-particle Hamiltonian only. The solution is readily overcome by observing that the two-level atomic system can be mapped onto a hard-core boson model. In this way, μ couples to the total number of "atomic" bosons plus photons, i. e., a noninteracting Hamiltonian. The hard-core constraint simply becomes a local (in principle infinite) interaction, which is common to the reference and to the physical system.

The mapping of the two-level excitations onto hard-core bosons is mathematically achieved by the following replacements

$$\begin{aligned} \sigma_i^+ \to b_i^\dagger \,, \qquad \sigma_i^- \to b_i \,, \\ |{\downarrow_i}\rangle \to |0_i\rangle \text{ and } \ |{\uparrow_i}\rangle \to |1_i\rangle \ . \end{aligned}$$

This is valid provided one excludes states with double occupation of b particles *even as intermediate states*. This implies, for example, that for some operator products, such as $b_i b_i^\dagger \neq \sigma_i^- \sigma_i^+$, the mapping is not correct. With this mapping the JCL Hamiltonian reads

$$\begin{aligned} \hat{H}^{JCL} = &- t \sum_{\langle i,\, j\rangle} a_i^\dagger \, a_j - \Delta \sum_i b_i^\dagger \, b_i + g \sum_i (a_i \, b_i^\dagger + a_i^\dagger \, b_i) \\ &- (\mu - \omega_c) \, \hat{N}_p + \lim_{U\to\infty} \frac{U}{2} \sum_i b_i^\dagger \, b_i (b_i^\dagger \, b_i - 1) \,, \end{aligned} \tag{3.10}$$

where we have formally implemented the hard-core constraint by introducing an infinite interaction for b particles. In the restricted Hilbert space of zero or one hard-core boson per lattice site, the matrix elements of the two representations are identical. In principle,

states with higher occupation number $b_i^\dagger b_i > 1$ have to be considered in the bosonic version as well. However, the occupation of such states would cost infinite energy and, therefore, they do not influence the energies obtained from the Hilbert space sector with occupation numbers $b_i^\dagger b_i \leq 1$. We have checked this aspect numerically for very large U. It can also be verified easily when the sector of the Hilbert space with $b_i^\dagger b_i > 1$ is included perturbatively. These considerations can be straightforwardly extended to light-matter models with more than one atom or atomiclike structure (with two relevant levels) per cavity. In this case, one introduces a boson species for each atom and the hard-core constraint is enforced for each boson species.

In our calculation we take both parameters ω_c and ϵ of the reference system as variational parameters (μ is just a linear combination), which ensures thermodynamic consistency for the particle number of both species, and, consequently, of the total particle number. We show below, that varying both parameters instead of just ω_c provides an improvement in the accuracy of the phase boundaries for a given cluster size, see Tab. 3.1.

In VCA, the reference system is chosen to be a decomposition of the total system into identical clusters, which means that the total lattice of N sites is divided into clusters of size L. Mathematically this can be described by introducing a superlattice, such that the original lattice is recovered when a cluster is attached to each lattice site of the superlattice. The reference system defined on a cluster is solved by means of the band Lanczos method [53, 72]. The initial vector of the iterative band Lanczos method for the single-particle excitation term of the cluster Green's function contains $2L$ elements and is given by

$$\{a_1^\dagger |\psi_0\rangle\,,\, a_2^\dagger |\psi_0\rangle \,\ldots\, a_L^\dagger |\psi_0\rangle\,,\, \sigma_1^+ |\psi_0\rangle \,\ldots\, \sigma_L^+ |\psi_0\rangle\}\,, \tag{3.11}$$

where $|\psi_0\rangle$ is the N_p particle ground state. For the single-hole excitation term the initial vector of the band Lanczos method is obtained by replacing the creation operators in Eq. (3.11) by annihilation operators.

To evaluate the grand potential and the single-particle Green's function of the original system we use the bosonic Q-matrix formalism [54]. This formalism yields the Green's function $G(\tilde{\mathbf{k}}, \omega)$ in a mixed representation, partly in real space and partly in reciprocal space, see App. D.1. The matrix $G(\tilde{\mathbf{k}}, \omega)$ is of size $2L \times 2L$ and $\tilde{\mathbf{k}}$ belongs to the first Brillouin zone of the superlattice. Due to the specific order of the creation operators in the initial vector of the band Lanczos method we are able to extract the Green's function for photons $G^{ph}(\tilde{\mathbf{k}}, \omega)$ and the Green's function for two-level excitations $G^{ex}(\tilde{\mathbf{k}}, \omega)$ from $G(\tilde{\mathbf{k}}, \omega)$ in the following way

$$\begin{aligned} G^{ph}_{r,s}(\tilde{\mathbf{k}}, \omega) =& G_{r,s}(\tilde{\mathbf{k}}, \omega) \qquad \text{and} \\ G^{ex}_{r,s}(\tilde{\mathbf{k}}, \omega) =& G_{r+L,s+L}(\tilde{\mathbf{k}}, \omega)\,, \end{aligned}$$

where $r, s \in [1 \,\ldots\, L]$. The application of the periodization prescription proposed in Ref. [64] (Green's function periodization) yields the fully $\mathbf{k}$ dependent Green's functions $G^{ph}(\mathbf{k}, \omega)$ and $G^{ex}(\mathbf{k}, \omega)$. From that we are able to evaluate the single-particle spectral function

$$A^x(\mathbf{k}, \omega) \equiv -\frac{1}{\pi} \mathrm{Im}\, G^x(\mathbf{k}, \omega)\,, \tag{3.12}$$

the density of states

$$N^x(\omega) \equiv \int A^x(\mathbf{k},\,\omega)\,d\mathbf{k} = \frac{1}{N}\sum_{\mathbf{k}} A^x(\mathbf{k},\,\omega) \tag{3.13}$$

and the momentum distribution

$$n^x(\mathbf{k}) \equiv -\int_{-\infty}^{0} A^x(\mathbf{k},\,\omega)\,d\omega\ , \tag{3.14}$$

where x can be either ph for photons or ex for two-level excitations. We use the Q-matrix formalism to evaluate the momentum distribution, since this approach yields particularly accurate results [54]. Furthermore we calculate the spatial correlation functions

$$C_{ij}^{ph} \equiv \langle a_i^\dagger\, a_j\rangle \quad \text{and} \quad C_{ij}^{ex} \equiv \langle \sigma_i^+\,\sigma_j^-\rangle\ , \tag{3.15}$$

which just depend on the distance between two cavities i and j, i. e., $C_{ij}^x = C^x(|\mathbf{r}_i - \mathbf{r}_j|)$. Notice that the poles of the hard-core boson Green's function coincide with the poles of the two-level excitation Green's function as the energies of both representations are identical. However, the hard-core boson Green's function exhibits additional poles located at energies of the order $U \to \infty$. The additional poles which have finite weight result from the fact that excitations such as $b_i^\dagger\ |1_i\rangle$ are in principal allowed but cost infinite energy, whereas the corresponding excitation $\sigma_i^+\ |{\uparrow_i}\rangle$ is strictly forbidden. Therefore, the single-particle correlation functions $\langle b_{\mathbf{k}}(t)\, b_{\mathbf{k}}^\dagger\rangle$ and $\langle \sigma_{\mathbf{k}}^-(t)\,\sigma_{\mathbf{k}}^+\rangle$ differ only by contributions from frequencies of the order $U \to \infty$. Yet it should be mentioned that the single-hole correlations function of hard-core bosons is not affected by these considerations as $\langle b_{\mathbf{k}}^\dagger(t)\, b_{\mathbf{k}}\rangle$ is always equivalent to $\langle \sigma_{\mathbf{k}}^+(t)\,\sigma_{\mathbf{k}}^-\rangle$. This also implies that the spectral weight of the poles with negative energy are identical for both representations and that the particle density of the two-level system is equal to the particle density of the hard-core bosons. In the following, we will always speak loosely about two-level excitation Green's functions but we have to keep in mind that there are differences in the single-particle spectral weight of the hard-core boson and two-level excitation Green's functions at infinite energies.

3.2.3. Polariton properties of the quasiparticles

In the next step, we want to investigate the polaritonic properties of the JCL model, which arise due to the coupling between the photons and the two-level excitations.

Adding a particle or hole to the many-body ground state may result in quasiparticle or collective excitations which are built up by the $(N_p \pm 1)$-particle eigenstates of the many-body system entering the Green's function. These many-body eigenstates for the infinite system can be extracted within the VCA framework from the VCA Green's function. As shown in App. D.1, they are linear combinations of the particle and hole excitations of the cluster Green's function weighted by the eigenvector matrix X, defined in App. D.1.

Our goal is to describe the eigenvectors of the $(N_p \pm 1)$-particle Hilbert space, which form the quasiparticle excitations of the Green's function by polaritonic quasiparticles

added to the exact N_p particle groundstate $|\psi_0\rangle$. To this end, we introduce the polariton creation operators $p^\dagger_{\alpha,\mathbf{k}}$ for particle excitations and $h^\dagger_{\alpha,\mathbf{k}}$ for hole excitations as appropriate linear combinations of photons and two-level excitations

$$p^\dagger_{\alpha,\mathbf{k}} = \beta^\alpha_p(\mathbf{k})\, a^\dagger_{\mathbf{k}} + \gamma^\alpha_p(\mathbf{k})\, \sigma^+_{\mathbf{k}} \;, \tag{3.16a}$$

$$h^\dagger_{\alpha,\mathbf{k}} = \beta^\alpha_h(\mathbf{k})\, a_{\mathbf{k}} + \gamma^\alpha_h(\mathbf{k})\, \sigma^-_{\mathbf{k}} \;. \tag{3.16b}$$

It should be stressed that the hole creation operator is not the adjoint of the particle creation operator or its annihilation counterpart, which it would be in the case of noninteracting particles. As we will see, the coefficients or weights of the linear combinations $\beta^\alpha_{p/h}(\mathbf{k})$ and $\gamma^\alpha_{p/h}(\mathbf{k})$ depend on the wave vector $\mathbf{k}$, the quasiparticle band α, and additionally on the filling n, which is not explicitly written in Eq. (3.16), since the filling dependence is not important for the present discussions. The normalized polariton quasiparticle states are defined by applying the polaritonic operators on the exact N_p particle ground state $|\psi_0\rangle$ yielding

$$|\tilde{\psi}^\alpha_{p,\mathbf{k}}\rangle = \frac{p^\dagger_{\alpha,\mathbf{k}}\,|\psi_0\rangle}{\sqrt{\langle\psi_0|\, p_{\alpha,\mathbf{k}}\, p^\dagger_{\alpha,\mathbf{k}}\,|\psi_0\rangle}} \text{ and} \tag{3.17a}$$

$$|\tilde{\psi}^\alpha_{h,\mathbf{k}}\rangle = \frac{h^\dagger_{\alpha,\mathbf{k}}\,|\psi_0\rangle}{\sqrt{\langle\psi_0|\, h_{\alpha,\mathbf{k}}\, h^\dagger_{\alpha,\mathbf{k}}\,|\psi_0\rangle}} \;, \tag{3.17b}$$

respectively. The normalization terms can be rewritten as

$$\langle\psi_0|\, p_{\alpha,\mathbf{k}}\, p^\dagger_{\alpha,\mathbf{k}}\,|\psi_0\rangle = \mathbf{z}^{\alpha\dagger}_p(\mathbf{k})\, S_p(\mathbf{k})\, \mathbf{z}^\alpha_p(\mathbf{k}) \text{ and} \tag{3.18a}$$

$$\langle\psi_0|\, h_{\alpha,\mathbf{k}}\, h^\dagger_{\alpha,\mathbf{k}}\,|\psi_0\rangle = \mathbf{z}^{\alpha\dagger}_h(\mathbf{k})\, S_h(\mathbf{k})\, \mathbf{z}^\alpha_h(\mathbf{k}) \;. \tag{3.18b}$$

In Eq. (3.18) the vectors $\mathbf{z}^\alpha_{p/h}(\mathbf{k})$ are defined as $\mathbf{z}^\alpha_{p/h}(\mathbf{k}) \equiv (\beta^\alpha_{p/h}(\mathbf{k}),\, \gamma^\alpha_{p/h}(\mathbf{k}))^T$ and $S_{p/h}(\mathbf{k})$ are the overlap matrices of single-particle excitations and single-hole excitations, respectively. The overlap matrix for the hole excitations is given by

$$S_h(\mathbf{k}) = \begin{pmatrix} \langle a^\dagger_{\mathbf{k}}\, a_{\mathbf{k}}\rangle & \langle a^\dagger_{\mathbf{k}}\, \sigma^-_{\mathbf{k}}\rangle \\ \langle a^\dagger_{\mathbf{k}}\, \sigma^-_{\mathbf{k}}\rangle^* & \langle \sigma^+_{\mathbf{k}}\, \sigma^-_{\mathbf{k}}\rangle \end{pmatrix}$$

where the static correlation functions are evaluated in the N_p particle ground state $|\psi_0\rangle$. All quantities entering S_h are correctly evaluated in the hard-core boson model as no excitations of the "two-level bosons" into the $n > 1$ sector occur. For the particle case the situation is different, as we need to evaluate

$$S_p(\mathbf{k}) = \begin{pmatrix} \langle a_{\mathbf{k}}\, a^\dagger_{\mathbf{k}}\rangle & \langle \sigma^-_{\mathbf{k}}\, a^\dagger_{\mathbf{k}}\rangle^* \\ \langle \sigma^-_{\mathbf{k}}\, a^\dagger_{\mathbf{k}}\rangle & \langle \sigma^-_{\mathbf{k}}\, \sigma^+_{\mathbf{k}}\rangle \end{pmatrix} \;.$$

The term $\langle \sigma^-_{\mathbf{k}}\, \sigma^+_{\mathbf{k}}\rangle$ of the two-level system cannot be directly evaluated in the hard-core boson model. Using the commutator property $[\sigma^-_i, \sigma^+_j] = 0$ for $i \neq j$ and the local

anticommutation relation $\{\sigma_i^-, \sigma_i^+\} = 1$, we end up with an expression that only contains static correlation functions which can be computed correctly within the hard-core boson model

$$S_p(\mathbf{k}) = \begin{pmatrix} \langle a_\mathbf{k} a_\mathbf{k}^\dagger \rangle & \langle \sigma_\mathbf{k}^- \, a_\mathbf{k}^\dagger \rangle^* \\ \langle \sigma_\mathbf{k}^- \, a_\mathbf{k}^\dagger \rangle & 1 + \langle \sigma_\mathbf{k}^+ \, \sigma_\mathbf{k}^- \rangle - \frac{2}{N} \sum_\mathbf{k} \langle \sigma_\mathbf{k}^+ \, \sigma_\mathbf{k}^- \rangle \end{pmatrix} .$$

In order to derive a formalism to construct the optimal polariton weights, we start out with the analysis of an exact eigenvector $|\psi_{\nu,\mathbf{k}}^{N_p+1}\rangle$ of the Hamiltonian in the (N_p+1)-particle sector. For the sake of clarity we will suppress in the following considerations the index $\mathbf{k}$ for all quantities, and the indices α and p for quasiparticle weights and wave functions. The optimality criterion in this case is clearly the overlap of the exact eigenvector with the approximate (normalized) vector given in Eqs. (3.17) and (3.18)

$$|\tilde{\psi}_\nu\rangle = \frac{1}{\sqrt{\mathbf{z}^{\nu\dagger} \, S_p \, \mathbf{z}^\nu}} \sum_I z_I^\nu \, d_I^\dagger \, |\psi_0\rangle \ ,$$

where I denote the components of the two-dimensional vectors, and $d_{1,\mathbf{k}} \equiv a_\mathbf{k}$ and $d_{2,\mathbf{k}} \equiv \sigma_\mathbf{k}^-$, see App. D.1. The maximization of $|\langle \psi_\nu^{N+1} | \tilde{\psi}_\nu \rangle|^2$ leads to the generalized eigenvalue problem

$$A^\nu \, \tilde{\mathbf{z}}^\nu = \lambda \, S_p \, \tilde{\mathbf{z}}^\nu \ , \tag{3.19}$$

where the elements of the 2×2 matrix A^ν are

$$A_{IJ}^\nu = \langle \psi_0 | \, d_I \, |\psi_\nu^{N_p+1}\rangle \, \langle \psi_\nu^{N_p+1}| \, d_J^\dagger \, |\psi_0\rangle \ .$$

In Eq. (3.19) we replaced $\mathbf{z}^\nu$ by $\tilde{\mathbf{z}}^\nu$ as the eigenvalues are just determined except for a constant Z, which will be specified later. As the eigenvalue corresponds to the value of the overlap squared $\lambda = |\langle \psi_\nu^{N+1} | \tilde{\psi}_\nu \rangle|^2$, the deviation of the eigenvalue from one is a measure of the quality of the polariton approximation. It also points out that the eigenvector corresponding to the largest eigenvalue determines the optimal polariton coefficients. Interestingly, A_{IJ}^ν is the contribution of the excitation ν to the corresponding spectral function, i. e., its *quasiparticle weight*. In general, the quasiparticle peak is a superposition of several exact many-body eigenstates. Hence, the obvious generalization of the optimality criterion is to sum over all eigenstates ν, which contribute to the quasiparticle excitation α. To this end we define an energy window Ω_α in which the quasiparticle peak α is located and we integrate the spectral density in this energy window resulting in

$$\tilde{A}_{IJ}(\mathbf{k}, \, \Omega_\alpha) \equiv \sum_{\nu, \, \omega_\nu(\mathbf{k}) \in \Omega_\alpha} A_{IJ}^\nu \ .$$

The polariton coefficients are again obtained by the generalized eigenvalue problem

$$\tilde{A}(\mathbf{k}, \, \Omega_\alpha) \, \tilde{\mathbf{z}} = \lambda \, S_p \, \tilde{\mathbf{z}} \ .$$

and the eigenvalue is given by

$$\lambda = \frac{\tilde{\mathbf{z}}^\dagger \, \tilde{A}(\mathbf{k},\, \Omega_\alpha) \, \tilde{\mathbf{z}}}{\tilde{\mathbf{z}}^\dagger \, S_p \, \tilde{\mathbf{z}}} \, . \tag{3.20}$$

The eigenvalues are still restricted to the unit interval $[0, 1]$. The lower limit is due to the positivity of $\tilde{A}$ and S_p. The upper limit follows from the property that a summation of the integrated spectral density over all nonoverlapping energy intervals Ω_α is given by

$$\sum_{\alpha}^{\text{particles}} \tilde{A}_{IJ}(\mathbf{k}, \Omega_\alpha) = \langle d_{I,\mathbf{k}} d^\dagger_{J,\mathbf{k}} \rangle = (S_p)_{IJ} \, .$$

Of course, $\tilde{\mathbf{z}}$ and, hence, the polariton operators will depend on the wave vector $\mathbf{k}$, the quasiparticle band index α and the filling n, i. e., the Mott lobe. The discussion so far was for the particle case only, however, it is straightforward to iterate the procedure for the hole case.

Eventually, we merely need the integrated spectral density $A(\mathbf{k},\, \Omega_\alpha)$ determined within the VCA framework, which is given by

$$\tilde{A}_{IJ}(\mathbf{k}, \Omega_\alpha) \equiv - \sum_{\nu,\, \omega_\nu(\mathbf{k}) \in \Omega_\alpha} (\tilde{Q} X)_{I,\nu} (X^{-1} S \tilde{Q}^\dagger)_{\nu,J} \, .$$

Details are presented in App. D.1 as well as the proof that all contributions of the sum have the same sign, which is necessary for the optimality criterion to make sense at all. The optimality criterion as well as the eigenvalue problem only fix the coefficient vector $\mathbf{z}$ up to a normalization factor Z, i. e., $\mathbf{z} = Z \, \tilde{\mathbf{z}}$. The latter is determined by the condition that the total spectral weight should be conserved

$$Z^2 \, \tilde{\mathbf{z}}^\dagger \, \tilde{A} \, \tilde{\mathbf{z}} \stackrel{!}{=} \operatorname{tr} \, \tilde{A} \, . \tag{3.21}$$

As the excitations can now be described by wave vector, band and filling dependent polaritonic quasiparticles, it remains to evaluate the polariton spectral function $A^p(\mathbf{k},\, \omega)$, which is due to the invariance of the trace in Eq. (3.21) equal to the sum of the photon spectral function $A^{ph}(\mathbf{k},\, \omega)$ and the two-level excitation spectral function $A^{ex}(\mathbf{k},\, \omega)$.

3.2.4. Results

In this section, we present the results of our calculations. Specifically, we discuss the quantum phase transition from Mott phase to superfluid phase occurring in the JCL model and investigate the impact of the variational parameter space on the accuracy of the results. Subsequently, we study the spectral properties of both photons as well as two-level excitations. The first two subsections refer to results obtained for zero detuning $\Delta = 0$, whereas nonzero detuning is considered in the third subsection. Finally, we study the polaritonic properties of the JCL model. In particular, we introduce polariton quasiparticles as wave vector and filling dependent linear combinations of photons and two-level excitations and analyze the weights of their constituents.

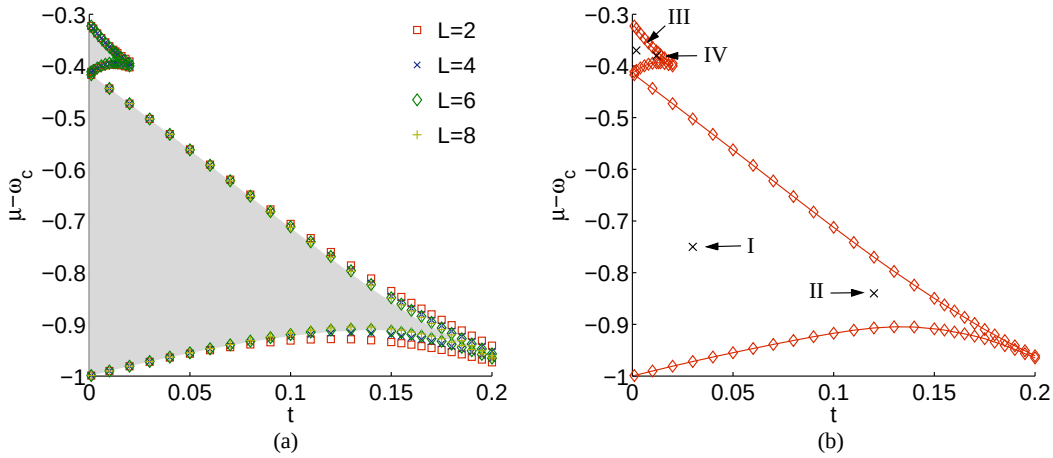

Figure 3.22.: Phase boundaries of the JCL model in one dimension for zero detuning $\Delta = 0$. (a) VCA results for the variational parameters $x = \{\omega_c, \epsilon\}$ and various cluster sizes of the reference system. The gray shaded area indicates DMRG data [226]. (b) Phase boundaries obtained for the largest cluster ($L = 8$ for the first Mott lobe and $L = 6$ for the second Mott lobe). The marks refer to parameters where spectral functions are evaluated.

Quantum phase transition

The JCL model exhibits, comparable to the BH model [30], a quantum phase transition from a localized Mott phase to a delocalized superfluid phase. For integer particle density and small hopping strength t, the ground state of the system is a Mott state. The first two Mott lobes of the one-dimensional (1D) JCL model for zero detuning $\Delta = 0$ obtained by means of VCA with the variational parameters $x = \{\omega_c, \epsilon\}$ are shown in Fig. 3.22. As discussed in the previous section, including ϵ in the set of variational parameters is nontrivial and is solely possible since the two-level excitations can be mapped onto hard-core bosons. The gray shaded area in Fig. 3.22 (a) indicates DMRG results for the phase boundary obtained by D. Rossini *et al.* in Ref. [226]. We find excellent agreement between the phase boundary evaluated by means of VCA with the variational parameter set $x = \{\omega_c, \epsilon\}$ and the DMRG results, even at the lobe tip, where quantum fluctuation effects are most important, and even for moderate cluster sizes $L \gtrsim 4$. Figure 3.23 (a) compares the phase boundaries at the tip of the first Mott lobe for different variational parameters. The results obtained with $x = \{\omega_c, \epsilon\}$ are connected by lines, whereas the open symbols correspond to $x = \{\omega_c\}$. We observe that using both on-site energies as variational parameters improves the results for the phase boundary and also yields a better approximation for the slope of the lobe tip. A quantitative measure for the quality χ of the calculated phase boundary is given by the absolute deviation from the

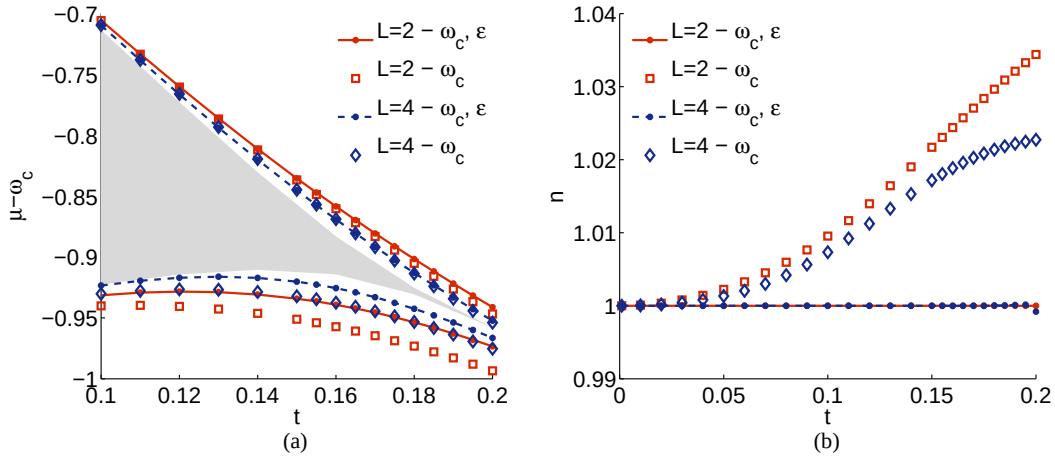

Figure 3.23.: Comparison between the results obtained with the variational parameters $x = \{\omega_c, \epsilon\}$ and $x = \{\omega_c\}$, respectively, for small clusters of size $L = 2$ and $L = 4$. (a) Phase boundaries at the tip of the first Mott lobe. The gray shaded area indicates DMRG results [226]. (b) Total particle density n, which is the sum of the photon density and the two-level excitation density, across the first Mott lobe.

DMRG data per phase boundary point

$$\chi = \frac{1}{M_p} \sum_i \left| p_i^V - p_i^D \right| , \tag{3.22}$$

where p_i^V and p_i^D are corresponding phase boundary points calculated by means of VCA and DMRG, respectively, and M_p is the number of phase boundary points, which contribute to the sum. In Tab. 3.1 we compare the quality $\chi/10^{-3}$ of the phase boundary between the two sets of variational parameters for various cluster sizes. When using the augmented set of variational parameters $x = \{\omega_c, \epsilon\}$ in contrast to $x = \{\omega_c\}$ we observe an improvement in the quality of the phase boundary which ranges from 1.3 to 1.7 depending on the cluster size of the reference system. Using both the resonance frequency ω_c of the cavities and the energy spacing ϵ of the two-level system as variational parameters thus provides a significant improvement with respect to the case of a single variational parameter [69]. As discussed in Refs. [51] and [78], a correct particle density in the original system can only be obtained when the corresponding on-site energies are included in the set of variational parameters, i. e., in the case of the JCL model $x = \{\omega_c, \epsilon\}$. This is demonstrated in Fig. 3.23 (b), where the total particle density n, which consists of a photon and a two-level excitation contribution, is evaluated along the first Mott lobe. For $x = \{\omega_c\}$ the deviation of the particle density from one is growing with increasing hopping strength t but shrinking with increasing cluster size L. However, when ϵ is included as variational parameter the total particle density n is as

Table 3.1.: Quality $\chi/10^{-3}$ of the phase boundary for $x = \{\omega_c\}$ and $x = \{\omega_c, \epsilon\}$, respectively. The quality χ is evaluated using Eq. (3.22).
L ... number of cluster sites
ϵ, ω_c ... variational parameters
IMP ... improvement in quality when using the variational parameters $x = \{\omega_c, \epsilon\}$ instead of $x = \{\omega_c\}$

L	$\{\omega_c\}$	$\{\omega_c, \epsilon\}$	*IMP*
2	15.95	11.34	1.41
4	8.20	4.92	1.67
6	5.34	3.16	1.69
8	3.95	3.07	1.29

desired equal to one across the whole first Mott lobe. A deviation of about 0.001 can be observed for $t = 0.2$. Yet, the hopping strength $t = 0.2$ is probably even slightly above the critical hopping strength t^*, which indicates the tip of the Mott lobe [226].

The phase diagram of the 1D JCL model is in many aspects similar to the phase diagram of the 1D BH model [51, 143]. Particularly, the Mott lobes are point shaped and a reentrance behavior can be observed, which means that for certain values of μ upon increasing t the system leaves the Mott phase and later on enters it again. Yet a very important difference is that the width of the lobes of the JCL model at zero hopping is shrinking with increasing particle density. This comes from the fact that the effective on-site repulsion of the JCL lattice model, which is hidden in the interaction between photons and two-level excitations, is not constant, as in the Bose-Hubbard model. The exact location of the phase boundaries at zero hopping is derived as a by-product in App. D.2, whose major intention is, however, to introduce the notation used for the dressed states $|n, \alpha\rangle$ and for the corresponding energies $E_{|n,\alpha\rangle}$, where $\alpha \in \{-, +\}$ describing the ground state and the excited state in the corresponding constant particle number sector of the single-cavity Hilbert space.

Spectral properties of photons and two-level excitations

The spectral function for photons $A^{ph}(\mathbf{k}, \omega)$, the spectral function for two-level excitations $A^{ex}(\mathbf{k}, \omega)$ and the corresponding densities of states $N^{ph}(\omega)$ and $N^{ex}(\omega)$ evaluated by means of VCA for parameters belonging to the first Mott lobe are shown in Fig. 3.24. We use an artificial broadening $\eta = 0.03$ and the variational parameter set $x = \{\omega_c, \epsilon\}$ for the numerical evaluation of the spectral functions. Both spectral functions $A^{ph}(\mathbf{k}, \omega)$ and $A^{ex}(\mathbf{k}, \omega)$ have the same gap as the photons and the two-level excitations are coupled. The spectral functions of the JCL model generally consist of four bands. This can best be understood in terms of the analytic solution of the JCL model for zero hopping strength $t = 0$. The ground state $|\psi_0\rangle$ of the JCL model in the Mott phase with particle

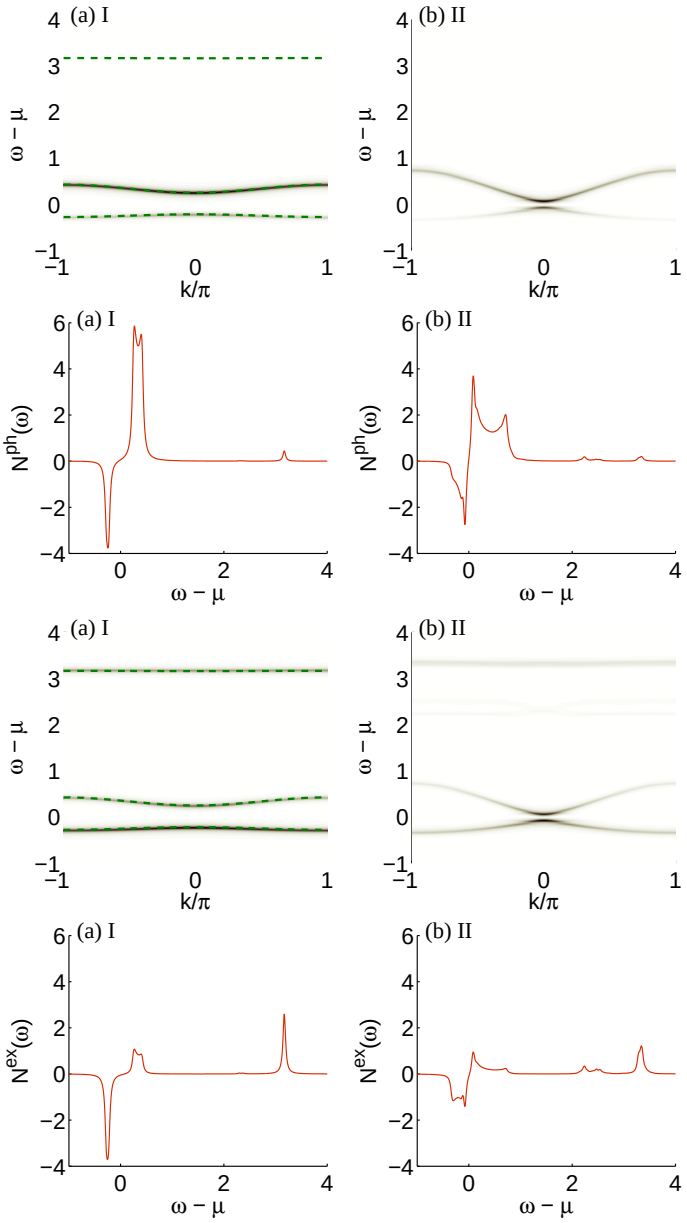

Figure 3.24.: Photon spectral function $A^{ph}(\mathbf{k}, \omega)$, first row, and density of states $N^{ph}(\omega)$, second row. Two-level excitation spectral function $A^{ex}(\mathbf{k}, \omega)$, third row, and density of states $N^{ex}(\omega)$, fourth row. The spectral functions are evaluated for the parameters (a) $t = 0.03$, $\mu - \omega_c = -0.75$, $\Delta = 0$ and (b) $t = 0.12$, $\mu - \omega_c = -0.84$, $\Delta = 0$, which belong to the first Mott lobe. The dashed lines in the spectral functions in (a) correspond to first-order degenerate perturbation theory results, see App. D.3. The Roman numerals in the captions of the subfigures refer to the marks in Fig. 3.22 (b).

density n for zero hopping is given by the tensor product state

$$|\Psi_0\rangle = \bigotimes_{\nu=1}^{N} |n,\,-\rangle_\nu \ , \tag{3.23}$$

where $|n,\,-\rangle_\nu$ is the dressed n particle ground state of lattice site ν. The states with a single-particle excitation are those, where $N-1$ sites remain in the dressed state $|n,\,-\rangle$ and one site is excited to the state $|n+1,\,\alpha\rangle$. Similarly, for the single-hole excitation $N-1$ sites remain in the state $|n,\,-\rangle$ and one site is excited to the state $|n-1,\,\alpha\rangle$. In both cases, the excited states are N fold degenerate as the particle/hole excitation can be located on any of the N lattice sites. The degenerate states have thus the structure

$$|\Psi_p^{\alpha,\,l}\rangle \equiv |n+1,\,\alpha\rangle_l \bigotimes_{\substack{\nu=1\\ \nu\neq l}}^{N} |n,\,-\rangle_\nu \text{ and} \tag{3.24a}$$

$$|\Psi_h^{\alpha,\,l}\rangle \equiv |n-1,\,\alpha\rangle_l \bigotimes_{\substack{\nu=1\\ \nu\neq l}}^{N} |n,\,-\rangle_\nu \ , \tag{3.24b}$$

respectively. Two of the four bands, we refer to them as lower modes $\omega_{p/h}^-$, emerge from the excitation of site i from the dressed state $|n,\,-\rangle_i$ to the states $|n\pm1,\,-\rangle_i$, which are ground states of the corresponding Hilbert-space sector with constant particle number. Analogously, we refer to the bands which emerge from the excitation of site i from $|n,\,-\rangle_i$ to the excited states in the corresponding particle sector $|n\pm1,\,+\rangle_i$ as upper modes $\omega_{p/h}^+$. The presence of the upper modes has been first noted by S. Schmidt *et al.* in Ref. [225] and has been numerically observed in latest QMC calculations [229] as well. The two upper modes $\omega_{p/h}^+$ indicate a clear deviation from the BH physics, which emerges due to the composition of two distinct particles. As discussed in the previous section, the two particle bands ω_p^α, $\alpha\in\{-,\,+\}$, determine the polariton particle creation operators $p_{\alpha,\mathbf{k}}^\dagger$ whereas the two hole bands ω_h^α specify the hole creation operators $h_{\alpha,\mathbf{k}}^\dagger$.

In the spectral functions of Fig. 3.24, the lower modes $\omega_{p/h}^-$ correspond to the cosinelike shaped bands centered around $\omega-\mu=0$. The intensities of the lower modes $\omega_{p/h}^-$ are contrary for the photon spectral function $A^{ph}(\mathbf{k},\,\omega)$ and the two-level excitation spectral function $A^{ex}(\mathbf{k},\omega)$. For $A^{ph}(\mathbf{k},\,\omega)$ the particle band ω_p^- is more intense than the hole band ω_h^- whereas the hole band is more intense than the particle band for $A^{ex}(\mathbf{k},\omega)$. For the first Mott lobe the upper hole mode ω_h^+ does not exist as this would require to excite a single-site i from the dressed state $|1,\,-\rangle_i$ to the non-existing state $|0,\,+\rangle_i$. Thus, only the upper particle mode ω_p^+ can be observed in the spectral functions shown in Fig. 3.24, which corresponds to the essentially flat band located at $\omega-\mu\approx 3$. In App. D.3, we evaluate the single-particle and single-hole excitation bands by means of first-order degenerate perturbation theory, which yields

$$\omega_{p,1}^\alpha = (\omega_c-\mu) + \alpha\, q(n+1) + q(n) - 2\,\tilde{t}_p^\alpha \cos k \text{ and} \tag{3.25a}$$

$$\omega_{h,1}^\alpha = (\omega_c-\mu) - \alpha\, q(n-1) - q(n) + 2\,\tilde{t}_h^\alpha \cos k \ , \tag{3.25b}$$

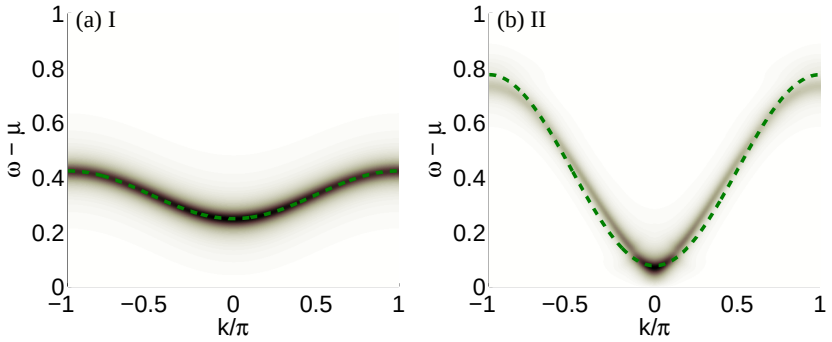

Figure 3.25.: Extract of the lower particle band ω_p^- of the photon spectral functions $A^{ph}(\mathbf{k}, \omega)$ shown in Fig. 3.24, where the parameters (a) $t = 0.03$, $\mu - \omega_c = -0.75$, $\Delta = 0$ and (b) $t = 0.12$, $\mu - \omega_c = -0.84$, and $\Delta = 0$ have been used. VCA results (density plot) are compared with bands evaluated by means of first-order degenerate perturbation theory (dashed lines).

respectively, where $\tilde{t}^{\alpha}_{p/h}$ is the renormalized hopping strength. Figure 3.24 (a) shows, additionally to the spectral functions obtained by means of VCA, the perturbation results for the bands. For small hopping strength we observe, as expected, good agreement between the two approaches. From the analytic solution of the bands we are able to extract their width, which is given by $2\,\tilde{t}^{\alpha}_{p/h}$. The renormalization factor in $\tilde{t}^{\alpha}_{p/h}$ essentially consists of a square of the form $(a + b)^2$, see Eqs. (D.13) and (D.15). Evaluating these expressions shows that a, $b > 0$ for the lower modes $\omega^-_{p/h}$ but $a > 0$ and $b < 0$ for the upper modes $\omega^+_{p/h}$. Therefore, a and b almost cancel each other in the latter case, which yields a small renormalized hopping strength of the upper modes $\tilde{t}^+_{p/h}$ in comparison to the one of the lower modes $\tilde{t}^-_{p/h}$ and thus, essentially flat upper particle/hole bands $\omega^+_{p/h}$ [225]. Plugging in the value of the modified chemical potential $\mu - \omega_c = -0.75$, which has been used to evaluate the spectral function shown in Fig. 3.24 (a), into Eq. (3.25a) yields $\omega^+_{p,1} \approx 3.16$, where we neglected the dependence on the wave vector. This matches perfectly with the VCA results. In addition to previous work [225, 229] we evaluate the upper modes not only for photons but also for two level-excitations. Interestingly, the spectral weight differs significantly for the two types of particles. In particular, the upper particle mode ω^+_p has a very large intensity in the two-level excitation spectral function $A^{ex}(\mathbf{k}, \omega)$, but is almost not visible in the photon spectral function $A^{ph}(\mathbf{k}, \omega)$. For the spectral function shown in Fig. 3.24 (b) a different chemical potential $\mu - \omega_c = -0.84$ has been used. Thus, the upper particle mode is shifted slightly upwards in comparison to Fig. 3.24 (a) and is located at $\omega^+_{p,1} \approx 3.25$. Figure 3.25 shows the lower particle band ω^-_p of the photon spectral function $A^{ph}(\mathbf{k}, \omega)$ for the same parameters as in Fig. 3.24. In this figure we compare the VCA results for different hopping strengths with the results obtained by means of first-order degenerate perturbation theory. For small hopping strength, $t = 0.03$, see Fig. 3.25 (a), the perturbative results agree very well with the

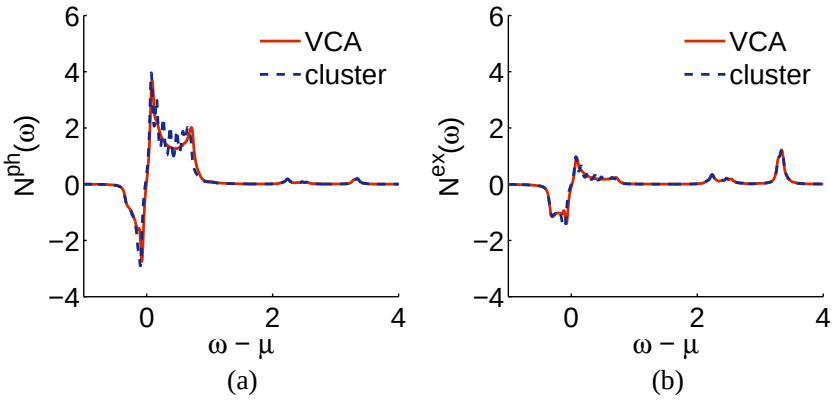

Figure 3.26.: Comparison between the density of states obtained from the VCA Green's function, solid lines, and the density of states obtained from the cluster Green's function, dashed lines. (a) density of states of photons $N^{ph}(\omega)$ and (b) density of states of two-level excitations $N^{ex}(\omega)$. The parameters used for these plots are the same as in Fig. 3.24 (b).

VCA results in both the width as well as the shape of the band. However, for large hopping strength $t = 0.12$, which is already close to the tip of the Mott lobe, the lower particle band does not exhibit a simple cosine shape anymore, see Fig. 3.25 (b). In addition the width of the band is slightly overestimated by first-order degenerate perturbation theory.

In the spectral functions shown in Fig. 3.24 (b) there is additional spectral weight located at $\omega - \mu \approx 2$. We can exclude that this additional weight stems from the periodization prescription used in VCA or from any other VCA internal processes as it also appears in the cluster Green's function, which is solved by exact diagonalization. This can be verified best by comparing the density of states obtained from the VCA Green's function with the density of states obtained from the cluster Green's function, see Fig. 3.26. Both densities of states, the one obtained from the cluster Green's function and the one obtained from the VCA Green's function, exhibit a peak located at $\omega - \mu \approx 2$. The additional peak can be revealed in the framework of perturbation theory. First-order local particle fluctuations in the ground state will have contributions of the form

$$|\Delta\psi^{(1)}\rangle = \frac{t}{\Delta E}\,|n+1,\,\alpha\rangle_l \otimes |n-1,\,\beta\rangle_{l'} \bigotimes_{\substack{\nu=1\\ \nu\neq l,l'}}^{N} |n,\,-\rangle_\nu \ ,$$

where l, l' correspond to nearest-neighbor sites. Due to the energy denominator ΔE the predominant terms are those with $\alpha = \beta = -$. The correction term $|\Delta\psi^{(1)}\rangle$ is proportional to the hopping strength t, which explains, why the additional peak is not present in Fig. 3.24 (a). The particle excitation couples to final states with an additional

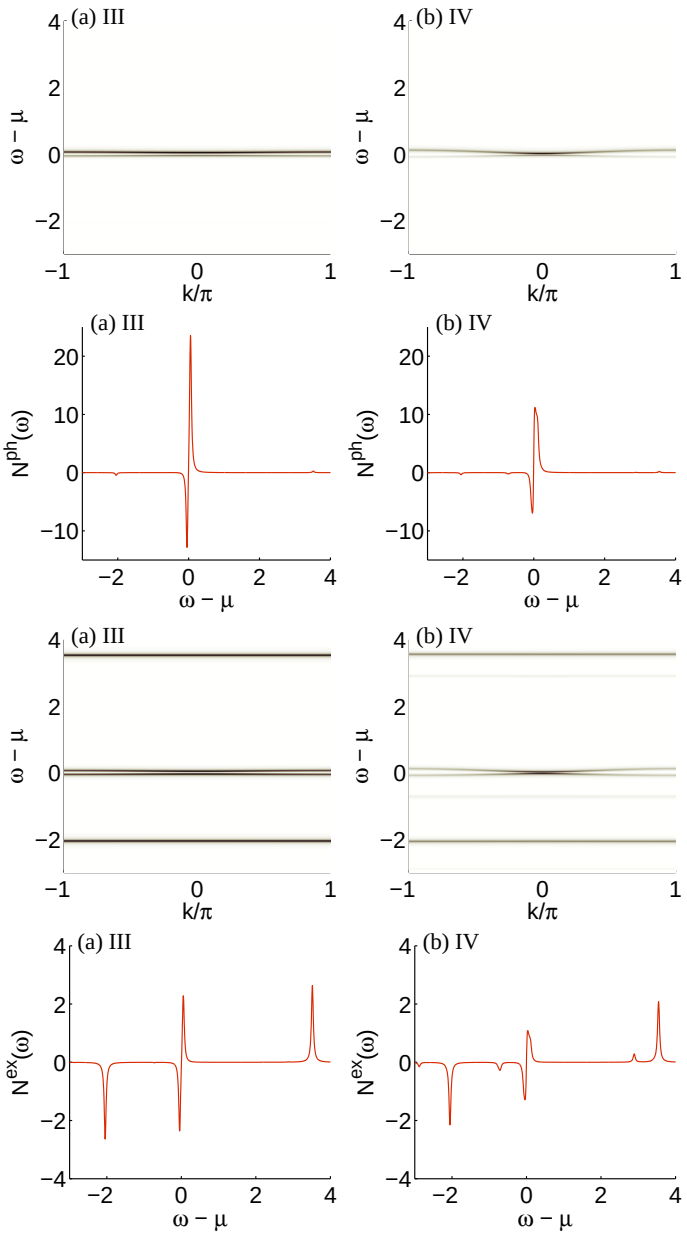

Figure 3.27.: Photon spectral function $A^{ph}(\mathbf{k}, \omega)$, first row, and density of states $N^{ph}(\omega)$, second row. Two-level excitation spectral function $A^{ex}(\mathbf{k}, \omega)$, third row, and density of states $N^{ex}(\omega)$, fourth row. The spectral functions are evaluated for the parameters (a) $t = 0.002$, $\mu - \omega_c = -0.37$, $\Delta = 0$ and (b) $t = 0.012$, $\mu - \omega_c = -0.38$, and $\Delta = 0$, which belong to the second Mott lobe. The Roman numerals in the captions of the subfigures refer to the marks in Fig. 3.22 (b).

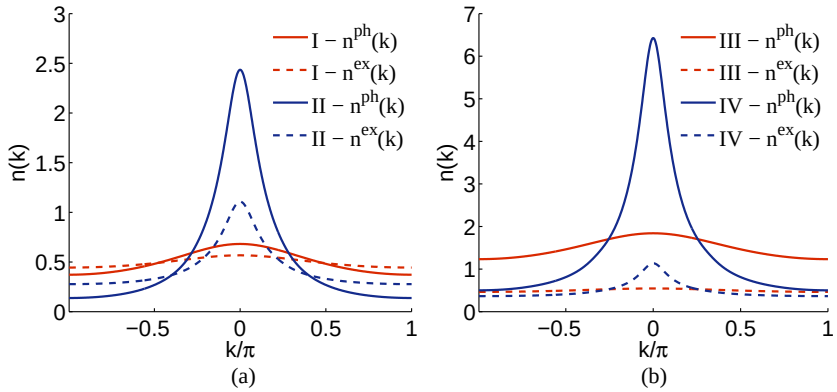

Figure 3.28.: Momentum distribution (a) in the first Mott lobe and (b) in the second Mott lobe for the parameters marked with Roman numerals in Fig. 3.22 (b). Solid lines correspond to the momentum distributions of photons $n^{ph}(\mathbf{k})$ and dashed lines to the momentum distributions of two-level excitations $n^{ex}(\mathbf{k})$.

particle either on site l, l' or on one of the remaining sites. A detailed analysis shows that the excitation, responsible for the additional peak at about $\omega - \mu \approx 2$, is

$$|\psi^{N_p+1}\rangle = |n+1,-\rangle_l \otimes |n,+\rangle_{l'} \bigotimes_{\substack{\nu=1 \\ \nu\neq l,l'}}^{N} |n,-\rangle_\nu \ .$$

The corresponding excitation energy is given by

$$\begin{aligned}\tilde{\omega}_p &= E_{|n+1,-\rangle} + E_{|n,+\rangle} + (N-2)E_{|n,-\rangle} - E_0^N \\ &= E_{|n+1,-\rangle} + E_{|n,+\rangle} - 2E_{|n,-\rangle} \\ &= \omega_c - \mu - q(n+1) + 3q(n) \ .\end{aligned}$$

For zero detuning and $\mu - \omega_c = -0.84$ the energy is $\tilde{\omega}_p = \omega - \mu = 2.4$.

As discussed before the upper hole mode ω_h^+ does not exist in the first Mott lobe. Yet, the mode ω_h^+ is present in spectral functions of the second Mott lobe, see Fig. 3.27. According to Eq. (3.25) the upper modes are located at $\omega_{p,1}^+ \approx 3.52$ and $\omega_{h,1}^+ \approx -2.04$ for the parameters used in Fig. 3.27 (a). This matches very well the results obtained by means of VCA. The chemical potential of the spectral function shown in Fig. 3.27 (b) differs from the one of (a) merely about 0.01. Thus, the bands $\omega_{p/h}^+$ are located at rather the same position in both spectral functions.

The momentum distribution for photons $n^{ph}(\mathbf{k})$ and two-level excitations $n^{ex}(\mathbf{k})$ in the first and second Mott lobe are shown in Fig. 3.28. For increasing hopping strength t the momentum distribution becomes more peaked for both the photons and the two-level excitations. In the first Mott lobe the momentum distributions $n^{ph}(\mathbf{k})$ and $n^{ex}(\mathbf{k})$ are

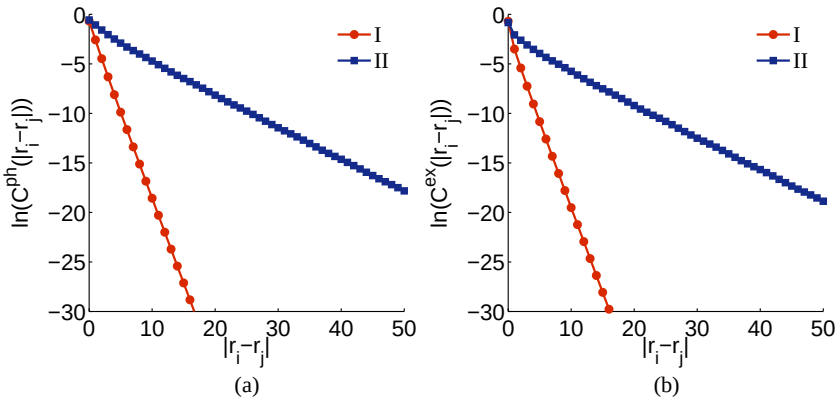

Figure 3.29.: Correlation function (a) for photons and (b) for two-level excitations in the first Mott lobe. The Roman numerals in the legend refer to the parameters marked in Fig. 3.22 (b).

centered around 0.5, which means that the cavities are on average equally occupied by photons and two-level excitations. In the second Mott lobe $n^{ph}(\mathbf{k})$ is centered around 1.5. However, $n^{ex}(\mathbf{k})$ is still centered around 0.5, as the maximum local occupation number of the two-level systems is restricted to one.

In order to display the slowing down of correlations upon approaching the boundary of the Mott phase, we evaluate the spatial correlation function $C^x(|\mathbf{r}_i - \mathbf{r}_j|)$ in the first Mott lobe (Fig. 3.29). The spatial correlation function can be obtained from the Fourier transform of the momentum distribution. For small distances $|\mathbf{r}_i - \mathbf{r}_j|$ between sites i and j the correlation function is a superposition of multiple exponential functions with distinct strengths of decay. For large distances, however, the exponential function with the smallest decay dominates and thus the correlation function is of the form

$$C^x(|\mathbf{r}_i - \mathbf{r}_j|) \propto e^{-\alpha^x |\mathbf{r}_i - \mathbf{r}_j|} , \tag{3.26}$$

as expected in the insulating phase. Using VCA we are able to extract the correlation length $\xi^x = 1/\alpha^x$, as data are available for large distances between two sites i and j. From a linear fit for sufficiently large distances we obtain $\alpha^{ph}_{\mathrm{I}} = \alpha^{ex}_{\mathrm{I}} = 1.711 \pm 0.001$ for the parameters I, see marks in Fig. 3.22 (b), and $\alpha^{ph}_{\mathrm{II}} = \alpha^{ex}_{\mathrm{II}} = 0.317 \pm 0.001$ for the parameters II. Therefore, the slope of the correlation function is the same for the two particle species, which is due to the coupling between the photons and the two-level excitations. As in the BH model [140] the absolute slope α^x of the correlation function shrinks with increasing hopping strength, which is a precursor of the superfluid phase, where the correlation between sites persists up to long distances.

Nonzero detuning

The detuning Δ, which is the difference between the resonance frequency ω_c of the cavities and the energy spacing ϵ of the two-level systems, is a very important parameter

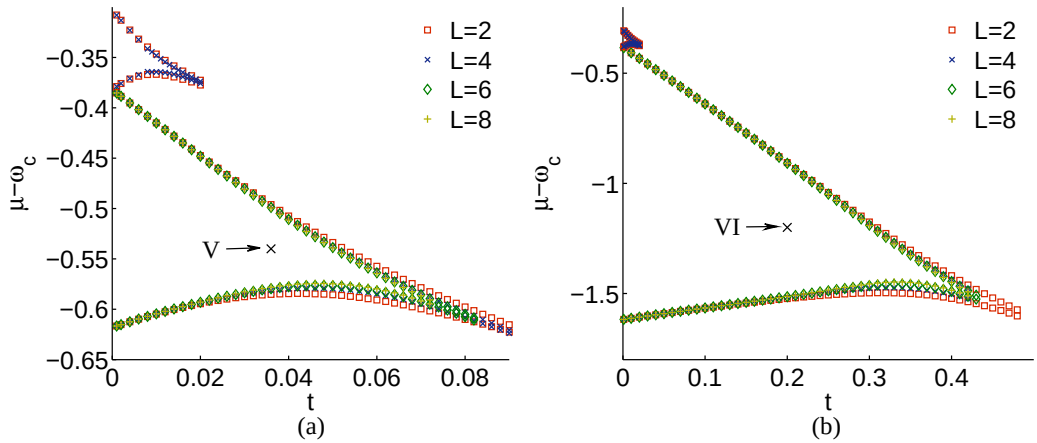

Figure 3.30.: Phase boundaries of the 1D JCL model for the detuning (a) $\Delta = -1$ and (b) $\Delta = 1$. The marks refer to the parameters where spectral functions are evaluated.

of the JCL model. By varying the detuning it is possible to change the width of the Mott lobes. Phase boundaries obtained by means of VCA with the set of variational parameters $x = \{\omega_c, \epsilon\}$ for $\Delta = -1$ and $\Delta = 1$ are shown in Fig. 3.30. For the parameters marked with x we evaluate the spectral function of photons $A^{ph}(\mathbf{k}, \omega)$ and two-level excitations $A^{ex}(\mathbf{k}, \omega)$, see Fig. 3.31. An interesting effect can be observed in the spectral functions $A^{ex}(\mathbf{k}, \omega)$. Namely, the intensity of the upper band ω_p^+ depends significantly on the detuning Δ. For negative detuning $\Delta = -1$, the upper mode in $A^{ex}(\mathbf{k}, \omega)$ is very intense, see Fig. 3.31 (a), whereas it is almost not visible for positive detuning $\Delta = 1$. This behavior remains valid when the spectral functions for positive and negative detuning are evaluated for identical hopping strength. The zero-hopping result for the energy of the upper mode is $\omega_{p,1}^+ \approx 3.15$ for the spectral function shown in Fig. 3.31 (a) and $\omega_{p,1}^+ \approx 3.82$ for the spectral function shown in Fig. 3.31 (b). The momentum distributions of photons $n^{ph}(\mathbf{k})$ and two-level excitations $n^{ex}(\mathbf{k})$ for the parameters marked in Fig. 3.30 are shown in Fig. 3.32. For negative detuning it is energetically more expensive to excite the two-level system than to add a photon to the cavity. Thus, the momentum distribution of photons $n^{ph}(\mathbf{k})$ dominates over the momentum distribution of two-level excitations $n^{ex}(\mathbf{k})$. For positive detuning the situation is reversed and $n^{ex}(\mathbf{k})$ is larger than $n^{ph}(\mathbf{k})$ for all values of the momentum.

Polariton quasiparticles

Up to now we investigated the photon properties and the two-level excitation properties of the JCL model separately, by extracting the Green's function of photons $G^{ph}(\mathbf{k}, \omega) = G_{a_\mathbf{k} a_\mathbf{k}^\dagger}(\omega)$ and the Green's function of two-level excitations $G^{ex}(\mathbf{k}, \omega) = G_{\sigma_\mathbf{k}^- \sigma_\mathbf{k}^+}(\omega)$ from

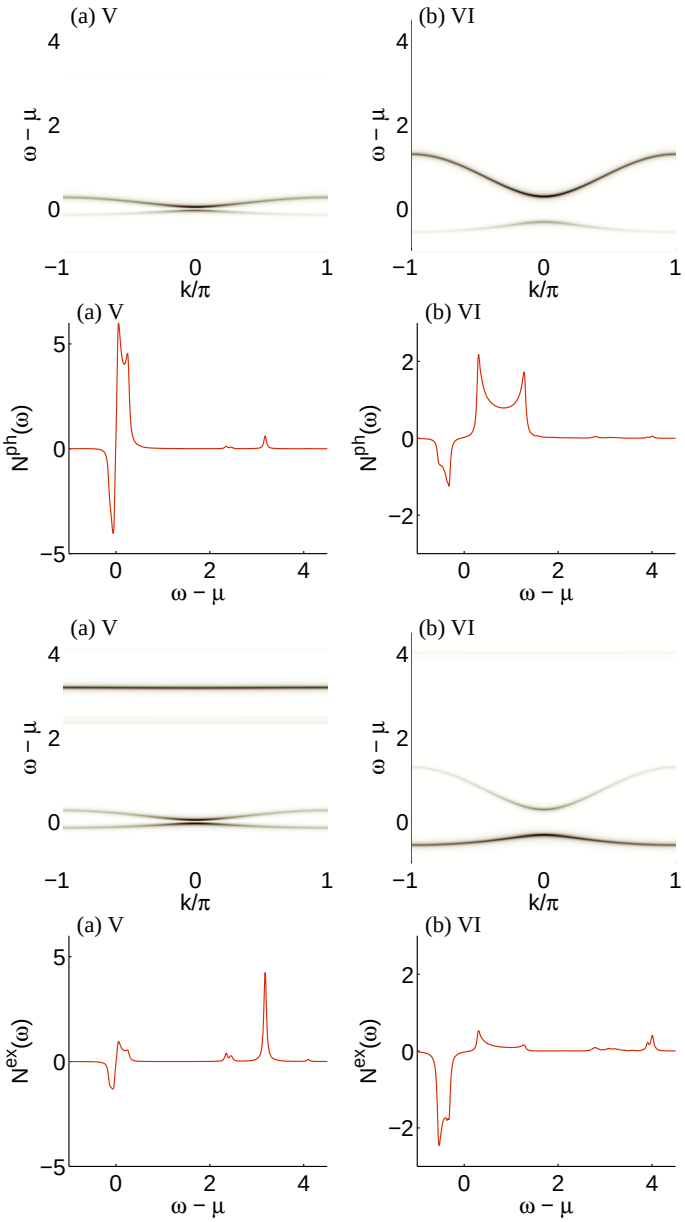

Figure 3.31.: Photon spectral function $A^{ph}(\mathbf{k}, \omega)$, first row, and density of states $N^{ph}(\omega)$, second row. Two-level excitation spectral function $A^{ex}(\mathbf{k}, \omega)$, third row, and density of states $N^{ex}(\omega)$, fourth row. The spectral functions are evaluated for the parameters (a) $t = 0.036$, $\mu - \omega_c = -0.54$, $\Delta = -1$ and (b) $t = 0.2$, $\mu - \omega_c = -1.2$, $\Delta = 1$. The Roman numerals in the captions of the subfigures refer to the marks in Fig. 3.30.

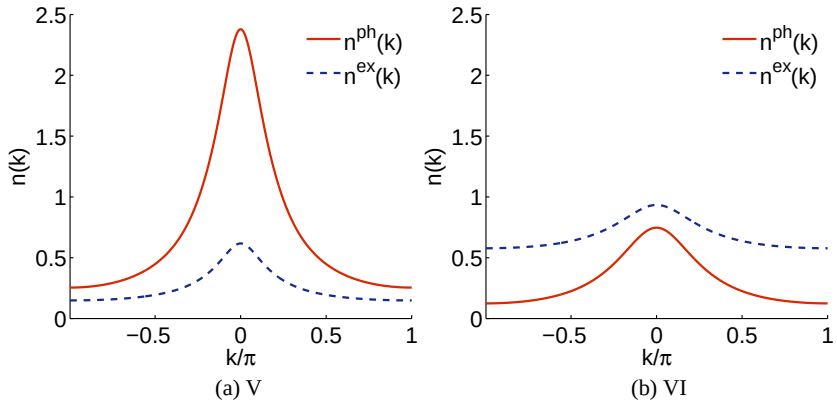

Figure 3.32.: Momentum distribution evaluated for the parameters marked in Fig. 3.30, where (a) corresponds to the parameters V, i. e., negative detuning $\Delta = -1$ and (b) to the parameters VI, i. e., positive detuning $\Delta = 1$.

the compound Green's function $G(\mathbf{k}, \omega)$, which is a 2×2 matrix of the form

$$G(\mathbf{k}, \omega) = \begin{pmatrix} G_{a_\mathbf{k} a_\mathbf{k}^\dagger}(\omega) & G_{a_\mathbf{k} \sigma_\mathbf{k}^+}(\omega) \\ G_{\sigma_\mathbf{k}^- a_\mathbf{k}^\dagger}(\omega) & G_{\sigma_\mathbf{k}^- \sigma_\mathbf{k}^+}(\omega) \end{pmatrix} . \tag{3.27}$$

Next we will discuss the polaritonic properties of the JCL model. We start out with the first Mott lobe for zero detuning and focus again on the parameter set marked as II in Fig. 3.22, i. e., $t = 0.12$, $\mu - \omega_c = -0.84$ and $\Delta = 0$. The polaritonic spectral function $A^p(\mathbf{k}, \omega)$ and the corresponding density of states $N^p(\omega)$, which is by construction identical to the total density of states of photons plus two-level excitations, is shown in Fig. 3.33. For the first Mott lobe the hole case is special since both, $\sigma^- |n, -\rangle \propto |0, -\rangle$ and $a |n, -\rangle \propto |0, -\rangle$ yield the exact zero-particle state. Consequently, the polariton can be chosen ad libitum, it will always be exact. Therefore in Fig. 3.34 only the particle part of the polaritonic weights is depicted. The right panel represents the result for the lower particle excitation. The polariton has very pronounced photonic character and the weights of photons and two-level system have opposite sign. Interestingly, the lower particle excitation can very well be mimicked by a single polariton on top of the N_p-particle ground state, as can be inferred from the fact that $\lambda \approx 1$. Moreover, a slight $\mathbf{k}$-dependence of the weights is observed. Contrarily in the upper particle band, the polariton has pronounced two-level-system character, the weights have the same sign, there is almost no $\mathbf{k}$-dependence, and the polariton description is poor ($\lambda \approx 0.2$).

Now we turn to the second Mott lobe, which allows us to study the hole polariton as well. The polariton spectral function and the corresponding density of states evaluated for the parameters IV, i. e., $t = 0.012$, $\mu - \omega_c = -0.38$, and $\Delta = 0$, are shown in Fig. 3.35. The weights are shown along with the overlap λ in Fig. 3.36. The lower bands $\omega_{p/h}^-$ are well described by the quasiparticles as the overlap λ is almost one for both bands. The upper bands $\omega_{p/h}^+$, however, are not described that well. In particular $\lambda \approx 0.2$ for

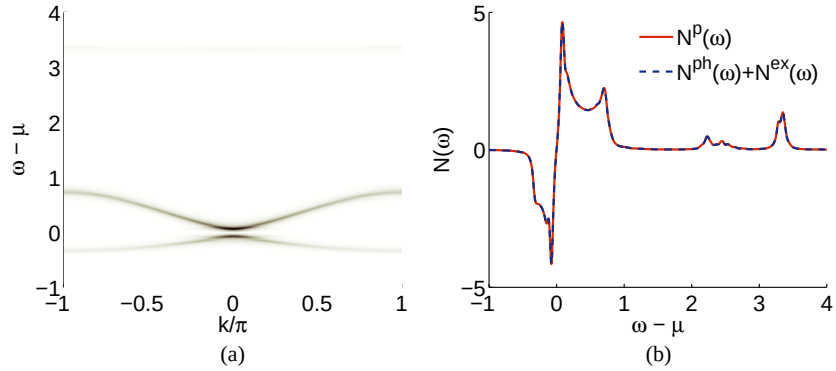

Figure 3.33.: Polariton spectral function (a) and density of states (b) evaluated for the parameters II corresponding to the first Mott lobe, i. e., $t = 0.12$, $\mu - \omega_c = -0.84$, and $\Delta = 0$. In (b) the polariton density of states $N^p(\omega)$ is compared with the sum of the photon density of states $N^{ph}(\mathbf{k}, \omega)$ and the two-level excitation density of states $N^{ex}(\mathbf{k}, \omega)$, which coincide by definition.

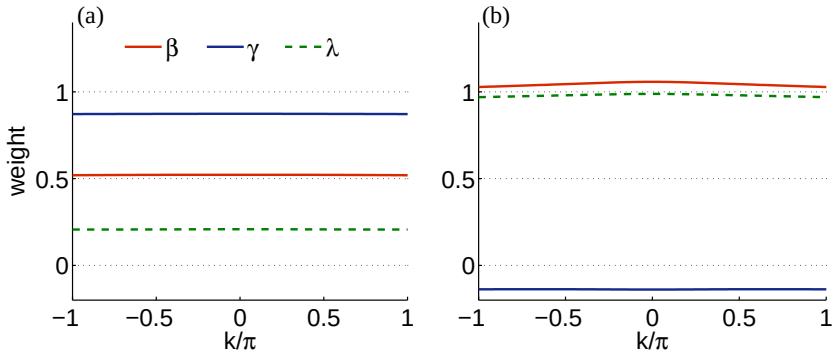

Figure 3.34.: Photon contribution β and two-level excitation contribution γ to the polariton quasiparticles. (a) shows the results for $p^\dagger_{+,\mathbf{k}}$ corresponding to the upper particle band ω_p^+ and (b) for $p^\dagger_{-,\mathbf{k}}$ corresponding the lower particle band ω_p^-. Additionally to the weights β and γ the overlap λ is shown.

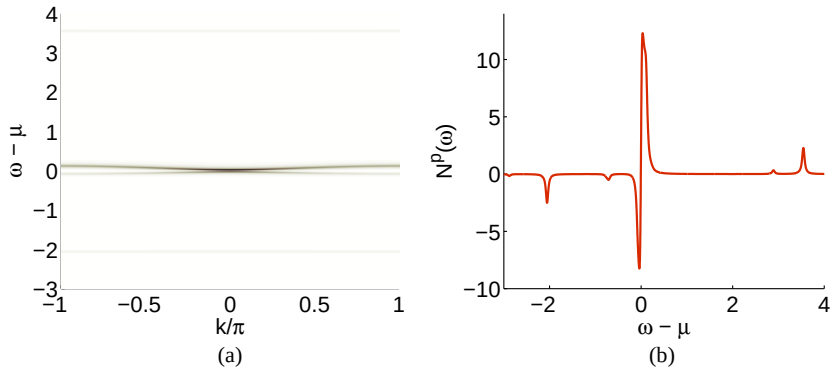

Figure 3.35.: Polariton spectral function (a) and density of states (b) evaluated for the parameters IV corresponding to the second Mott lobe, i. e., $t = 0.012$, $\mu - \omega_c = -0.38$, and $\Delta = 0$.

the upper particle band and $\lambda \approx 0.85$ for the upper hole band. The weights β and γ are significantly more wave vector dependent, especially for the upper bands $\omega^+_{p/h}$, i. e., $\alpha = +$. Apart from the more pronounced $\mathbf{k}$-dependence, the weights for the particle case are rather similar to those of the first Mott lobe. However, there are striking differences in the weights for the particle and hole part within the second Mott lobe. First, the $\mathbf{k}$ dependence is more pronounced. Second, the sign of the relative weights is positive for both bands $\alpha = \pm$, and finally, the composition of the polariton in the two bands is reverse. The lower band has predominantly photonic character, while opposite holds for the upper band.

Eventually, we want to compare the VCA results with those of the single-site problem, which are derived in App. D.4. In the single-site problem the sign of the relative polaritonic weights is the same as that observed in the lattice. In the first Mott lobe the relative weights for the particle case are for the upper band $q_+ \equiv \gamma^+_{p,n=1}/\beta^+_{p,n=1} = \sqrt{2}+1$ and for the lower band the reciprocal relation holds $q_- \equiv \beta^-_{p,n=1}/\gamma^-_{p,n=1} = -q_+$. There is agreement in the relative signs and the composition of the polariton between the single-site limit and the lattice system, but the reciprocal property is strongly violated in the lattice case. This might be understood as follows. The itinerant particles are the photons. In order to gain kinetic energy it is convenient for the system to increase the photonic character in the dispersive lower band, depicted in Fig. 3.35 (a). The upper band, on the other hand, has little dispersion and behaves more like the single-site limit.

In the second Mott lobe, the relative weights obtained in the single-site limit for particle excitations are $q_+ = \sqrt{3}+\sqrt{2}$ and $q_- = -q_+$. Like in the lattice case, the weights of the particle part are comparable in the first and second Mott lobe. Quantitatively, the relative weight $|q_\pm|$ is roughly 30% larger in the second Mott lobe, which is also the case in the lattice system. As far as the hole part is concerned, the single-site limit nicely corroborates all observations of the lattice model.

In the single-site problem, the exact many-body eigenstates $|n \pm 1, \alpha\rangle$ can be generated

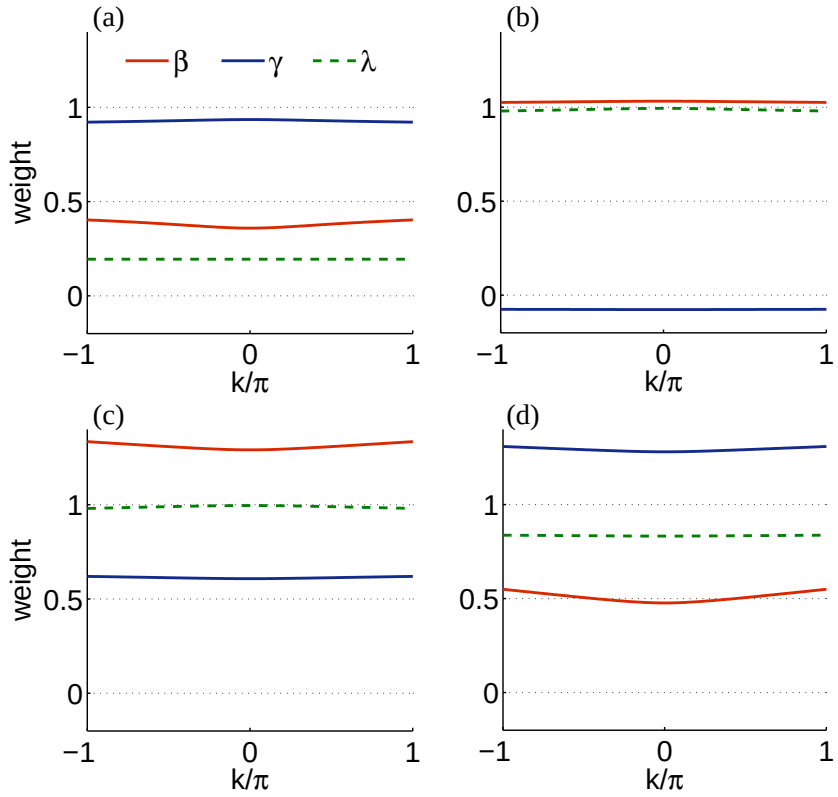

Figure 3.36.: Photon contribution β and two-level excitation contribution γ to the polariton quasiparticles. (a) shows the results for $p^{\dagger}_{+,\mathbf{k}}$ corresponding to the upper particle band ω_p^+, (b) for $p^{\dagger}_{-,\mathbf{k}}$ corresponding the lower particle band ω_p^-, (c) for $h^{\dagger}_{-,\mathbf{k}}$ corresponding to the lower hole band ω_h^- and (d) for $h^{\dagger}_{+,\mathbf{k}}$ corresponding to the upper hole band ω_h^+. Additionally to the weights β and γ the overlap λ is shown.

exactly by suitable polariton operators acting on the state $|n,-\rangle$. This is no longer the case in the lattice due to local particle number fluctuations induced by particle motion. Already in the single-site limit, the polariton operators are, however, not universal, they depend on the filling n and in the lattice case even on the wave vector $\mathbf{k}$. On top of that, the polariton operator for holes is not the adjoint of the corresponding polariton creation operator of the particle type, or in other word its annihilation operator.

Conclusions: In this section we presented and discussed the spectral properties of the Jaynes-Cummings lattice model in one dimension obtained within the variational cluster approach. Using the resonance frequency ω_c of the cavities and the energy spacing ϵ of the two-level systems as variational parameters in the variational cluster approach procedure provides a significant improvement with respect to the case of a single variational parameter. On the one hand, varying both ω_c as well as ϵ (or, at least μ) is necessary to achieve a correct particle density in the original system and on the other hand improved results for the phase boundaries, and thus, for the spectral functions as well, are obtained due to the augmented set of variational parameters. In order to apply the variational cluster approach and include ϵ as variational parameter the two-level systems have been mapped onto hard-core bosons, which yields correct poles of the Green's function in the relevant energy range. We evaluated and discussed spectral functions for photons and two-level excitations. The spectral functions generally consist of four bands, cosinelike shaped lower particle/hole bands, which are centered around zero energy, and essentially flat upper particle/hole bands. An exception are the spectral functions in the first Mott lobe, which contain the two lower bands but from the upper bands only the particle part. Using first-order degenerate perturbation theory, we evaluated analytical expressions for the bands, which allowed us to explain why the upper modes are essentially flat whereas the lower modes exhibit a pronounced cosinelike shape. Additionally, we compared the analytical solution for the bands with the variational cluster approach results. For small hopping strength t we observe, as expected, good agreement between the two approaches. However for parameters located close to the tip of the Mott lobe, first-order degenerate perturbation theory yields results that differ from the exact ones in both, shape and width of the bands. Furthermore, we evaluated densities of states, momentum distributions and spatial correlation functions for photons and two-level excitations. We also investigated detuning effects on the spectral properties and found indications that the intensity of the upper particle band of the two-level excitation spectral function depends strongly on the detuning. Based on the information obtained from the photons and two-level excitations we investigated the polaritonic properties of the Jaynes-Cummings lattice model. Therefore we introduced wave vector and filling dependent polariton particle creation and hole creation operators, which are linear combinations of photon and two-level excitation creation operators. We evaluated spectral functions and densities of states based on the polariton quasiparticles and analyzed the weights of their constituents. We have seen that the polariton operators are nontrivial combinations of photon and two-level system operators, which depend on the wave vector, the quasiparticle band, and the filling, or rather the Mott

lobe. On top of that, the polariton operators of particle and hole type are not adjoint operators. It is therefore not possible to describe the JCL model by a simple single-band polariton model.

3.3. Tavis-Cummings lattice model

The push towards the experimental realization of quantum computers lead to incredible advances in the fields of quantum optics and atomic physics. Unprecedented experimental control in these fields allowed to envision new realizations of strongly correlated many-body systems, which operate with light [216, 215, 219, 23]. Confined light modes in coupled cavity arrays are able to tunnel between adjacent sites and thus propagate on a lattice of cavities. Strong correlations in turn can be observed when a repulsive interaction between photons is present.[1] This repulsion, which is termed optical nonlinearity, can be achieved by coupling the light modes to matter in the form of atoms or atomiclike structures present within each cavity. The interaction between the light modes and atomic like structures is achieved by means of dipole coupling. In theory there exist two major schemes to obtain this interaction. The first is to model the atomiclike structures by two-level systems, leading to an interaction of the Jaynes-Cummings type [232, 215], whereas the second approach is based on electromagnetically induced transparency [235] and uses four-level systems [216]. In both cases optical nonlinearities between photons arise as the energy for adding two photons to the cavity is larger than twice the energy needed to add one photon. This behavior leads to intriguing experiments such as the photon blockade effect [236], where only one elementary excitation is present in the cavity at the same time. The elementary excitations in light matter systems are termed polaritons. Polaritons are superpositions of both particle species, namely photons as well as excitations of the atomiclike structures. Following these considerations and arranging multiple cavities on a lattice leads to a strongly correlated phase in which photons are involved. As a result, light-matter systems exhibit a quantum phase transition from Mott phase where polaritons are localized in the cavities to superfluid phase where polaritons are delocalized on the whole lattice [216, 215, 219].

Up to now an experimental realization of light-matter systems is still missing, however, there are several promising approaches such as quantum dots grown in photonic crystal cavities, transmission line cavities and toroidal or disk shaped cavities [23]. The advantage of light-matter systems is that they are of mesoscopic size and thus allow for a direct addressability of each lattice site and good experimental control on the system parameters. Exhibiting these valuable properties light-matter systems might be used as quantum simulators for other strongly correlated many-body systems such as the Bose-Hubbard model [30], or find their applications in quantum information processing.

Experimentally it might be more feasible to place multiple atomiclike structures within one cavity. Therefore it is important to study light-matter systems which contain more than one two-level system per cavity. The theoretical model describing a single cavity

[1] Alternatively, it has been shown in Ref. [234] that two-particle losses can lead to strongly correlated phases as well.

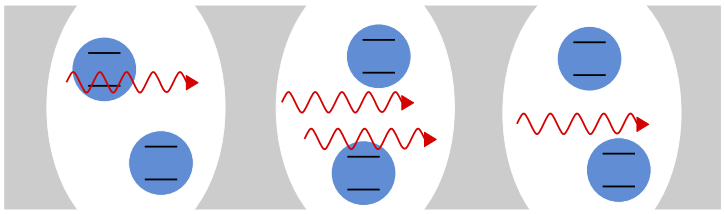

Figure 3.37.: Illustration of the TCL model. Blue bubbles represent two-level systems and red wavy arrows photons. Photons and two-level system interact via dipole coupling.

with N two-level systems is termed Tavis-Cummings model [237, 238]. In the case of $N = 1$ it reduces to the Jaynes-Cummings model [232]. Light-matter systems with coupled Jaynes-Cummings cavities have already been investigated to some detail in Refs. [215, 226, 227, 69, 220, 221, 222, 225, 229, 60] and will thus not be addressed here anymore. However, systems of coupled-cavity arrays with more than one two-level system per cavity have been rarely studied in literature. In particular, the quantum phase transition has been investigated on mean field level by N. Na *et al.* in Ref. [224], and in one-dimension with density matrix renormalization group (DMRG) by D. Rossini *et al.* in Ref. [226]. In the present paper, we investigate the quantum phase transition and the elementary excitations—the polaritons—of coupled Tavis-Cummings cavities arranged on a two-dimensional lattice. In particular, we evaluate the phase boundary delimiting Mott phase from superfluid phase for different number of two-level systems per cavity. Furthermore, we study spectral properties of both photons as well as atomic excitations which in turn allows us to characterize the polaritonic properties of the system. In order to evaluate the quantum phase transition and the spectral excitations we employ the variational cluster approach [28].

A single cavity at lattice site i containing N two-level systems is modeled by the Tavis-Cummings (TC) Hamiltonian [237, 238],

$$\hat{H}_i^{TC} = \omega_c \, a_i^\dagger \, a_i + \epsilon \, (S_i^z + \frac{N}{2}) + g \, (a_i \, S_i^+ + a_i^\dagger \, S_i^-) \, , \tag{3.28}$$

where ω_c is the resonance frequency of the cavity, ϵ is the energy spacing of the two-level systems, and g is the atom-field coupling constant (see a single cavity in Fig. 3.37 for illustration). The operators $a_i^\dagger$ and a_i, respectively, create and annihilate photons in the cavity i. The ensemble of two level systems is described by collective spin operators $S_j^\alpha = \sum_{\nu=1}^N \sigma_{\nu,j}^\alpha$, where $\alpha \in \{z, +, -\}$, and $\sigma_{\nu,j}^\pm = \sigma_{\nu,j}^x \pm i\sigma_{\nu,j}^y$ are the spin raising and lowering operators. When starting from the dipole interaction between photons and two-level systems two additional terms arise in the Hamiltonian, which are proportional to $a_i^\dagger \, S_i^+$ and $a_i \, S_i^-$. However, for the condition $|\omega_c - \epsilon| \ll \omega_c, \epsilon$ these terms are fast oscillating in comparison to $a_i \, S_i^+$ and $a_i^\dagger \, S_i^-$ and can thus be neglected, which is known as rotating wave approximation [233]. The difference between the resonance frequency

of the cavity ω_c and the energy spacing of the two-level system ϵ is termed detuning $\Delta = \omega_c - \epsilon$. As a consequence of the rotating wave approximation the total number of excitations $\hat{n}_i = a_i^\dagger a_i + S_i^z + N/2$ is conserved. Additionally, the total spin S^2 is a conserved quantity as well. The ground state of the TC model is always in the sector of maximum spin $S = N/2$ [226], which will thus be considered in further calculations.

The full model consists of M coupled cavities, which are arranged on a lattice. Therefore we refer to this model as Tavis-Cummings lattice (TCL) model. The TCL Hamiltonian is given by

$$\hat{H}^{TCL} = -t \sum_{\langle i,j \rangle} a_i^\dagger a_j + \sum_i \hat{H}_i^{TC} - \mu \hat{N}_p \,, \tag{3.29}$$

where the first term allows photons to tunnel between cavities i and j. The tunneling strength t is given by the overlap integral of the photonic wave functions, which is considered to be nonzero only for nearest-neighbor sites i and j. The restriction to nearest neighbors is denoted by the angle brackets $\langle \cdots \rangle$ around the summation indices. The second term of Eq. (3.29) describes the physics of the individual cavities and the last term controls the average particle number of the system, where μ is the chemical potential and $\hat{N}_p = \sum_i \hat{n}_i$ is the total particle number. Figure 3.37 illustrates the TCL model. For the TCL model the total particle number $\hat{N}_p$ is conserved as well as the total spin S^2 of each cavity. As in the case of the Jaynes-Cummings lattice model [232] the TCL model can be rewritten as

$$\begin{aligned} \hat{H}^{TCL} = &- t \sum_{\langle i,j \rangle} a_i^\dagger a_j - \Delta \sum_i (S_i^z + \frac{N}{2}) \\ &+ g \sum_i (a_i \, S_i^+ + a_i^\dagger \, S_i^-) - (\mu - \omega_c) \, \hat{N}_p \,. \end{aligned} \tag{3.30}$$

In the forthcoming discussions and calculations we use the dipole coupling g as unit of energy. Therefore the physics of the TCL model depends only on three independent parameters, namely, the hopping strength t, the detuning Δ, and the modified chemical potential $\mu - \omega_c$.

3.3.1. Quantum phase transition

The nonlinearities which arise due to the coupling of the photons to the ensemble of two-level systems lead to a quantum phase transition from Mott phase to superfluid phase. The elementary excitations in light-matter systems—the polaritons—are linear combinations of photons and atomic excitations. The Mott phase is characterized by integer polariton density, zero compressibility, and a gap in the spectral function. Intriguingly, polaritons in Mott phase are localized in cavities, which in turn means that the photons are not able to tunnel to adjacent cavities, since too much energy would be needed for this process. Hence, the Mott phase can be considered as a stable state of frozen light. In superfluid phase, however, the polaritons are delocalized on the whole lattice and Bose condense in the state of zero momentum.

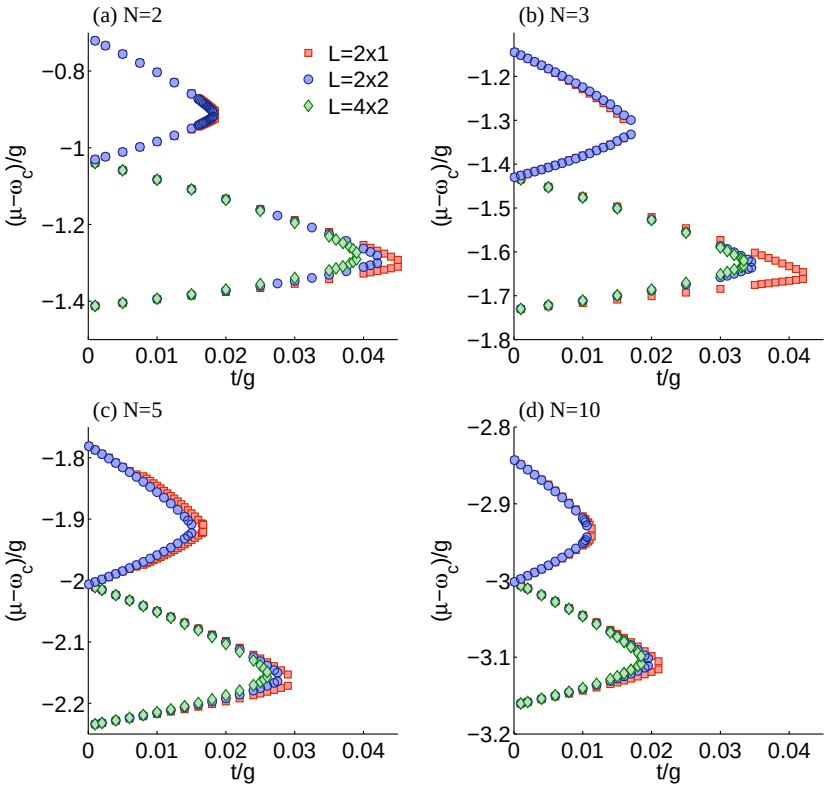

Figure 3.38.: Phase boundary of the two-dimensional TCL model evaluated for zero detuning $\Delta = 0$, reference systems of size L, and N two-level systems per cavity, where in (a) $N = 2$, (b) $N = 3$, (c) $N = 5$, and (d) $N = 10$.

We determine the phase boundary of the two-dimensional TCL model for zero detuning $\Delta = 0$. The first two Mott lobes with polariton density $n_p = 1$ and $n_p = 2$, respectively, are shown in Fig. 3.38 for distinct values of the two-level system number $N = \{2, 3, 5, 10\}$. The boundary of the quantum phase transition is given by the minimal amount of energy necessary to add (remove) a particle to (from) the system and can therefore be evaluated directly from the minimal gap of the single-particle spectral function obtained by means of VCA. The size of the gap does not depend on the particle species the spectral function is evaluate for, since photons and atomic excitations are coupled by g. As already mentioned before, we use the variational parameters $x = \{\omega_c, \epsilon, t\}$, which allow for thermodynamic consistency in the total polariton number. In contrast to the results in one dimension [226] the lobes are round shaped and no reentrance behavior can be observed for increasing hopping strength t. For increasing number of two-level systems N the width of the Mott lobes with different polariton density n_p becomes more similar, see Tab. 3.2. The critical hopping strength t^*, which determines the tip of the Mott lobes, depends on both the filling n_p and the number of two-level systems per cavity N. In particular, $t^*(N)$ is shrinking for increasing N for a

Table 3.2.: Ratio w_1/w_i of the width of Mott lobe 1 with polariton density $n_p = 1$ and Mott lobe i with polariton density $n_p = i$ for N two-level systems per cavity.

N	w_1/w_2	w_1/w_3	w_1/w_4
2	1.18	2.84	4.83
3	1.05	1.38	2.26
5	1.02	1.09	1.25
10	1.00	1.02	1.04

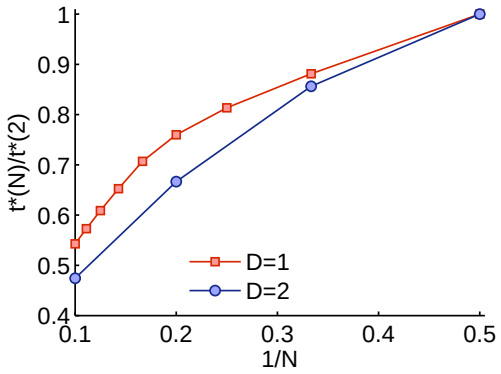

Figure 3.39.: Critical hopping strength ratio $t^*(N)/t^*(2)$ for the first Mott lobe in dependence on the dimension D. Results for one dimension are obtained from Ref. [226].

fixed polariton density n_p. In Fig. 3.39 we investigate for the first Mott lobe, i. e., for $n_p = 1$, the dimensionality dependence of the ratio $t^*(N)/t^*(2)$, which specifies how fast the lobes are shrinking with increasing N. To this end, we compare our VCA results for two dimensions with DMRG results for one dimension obtained by D. Rossini *et al.* in Ref. [226]. It can be observed that with increasing N the lobes are shrinking faster in two dimensions than in one dimension.

The phase boundary at zero hopping can be determined analytically, as the model decouples into M single-cavity problems, i. e., into M TC systems shifted by the chemical potential $-\mu\hat{n}_p$. The TC model has been solved exactly for zero detuning [237, 238] and for nonzero detuning [238, 239]. Since the full analytic solution is involved we concentrate here in determining the zero hopping phase boundary of the first Mott lobe for zero detuning, which is relevant for our data. To this end, we diagonalize the TC model for $n_p = 0$, 1, and 2 polaritons which yields

$$E_0 = 0 \tag{3.31a}$$

$$E_1 = \{(\omega_c - \mu) \pm \sqrt{N}\} \tag{3.31b}$$

$$E_2 = \{2(\omega_c - \mu) \pm \sqrt{2(2N-1)},\ 2(\omega_c - \mu)\}\ . \tag{3.31c}$$

The number of eigenstates for the sector of n_p polaritons is n_p+1 if $n_p < N$ and $N+1$ if $n_p \geq N$ [224, 240]. The phase boundary is evaluated by comparing the ground-state energies of adjacent sectors, which yields $\mu - \omega_c = -\sqrt{N}$ for the boundary between $n_p = 0$ and $n_p = 1$ and $\mu - \omega_c = \sqrt{N} - \sqrt{2(2N-1)}$ for the boundary between $n_p = 1$ and $n_p = 2$. This is of course in full agreement with our numerical results. In light-matter systems the optical nonlinearities arise as the energy which is needed to add the first excitation to the system is smaller than the one to add the second excitation. This results in a repulsive interaction of size $2\sqrt{N} - \sqrt{2(2N-1)}$, which is approximately $1/2\sqrt{N}$ for large N.

3.3.2. Excitations

In this section we investigate the excitations of the TCL model. In particular, we evaluate single-particle spectral functions and densities of states of photons and atomic excitations. Furthermore we present the momentum distribution for both particle species. Based on the spectral information we characterize polaritons, which are the elementary excitations in light-matter systems.

Spectral properties of photons and atomic excitations

Photon spectral functions $A^{ph}(\mathbf{k}, \omega)$ evaluated by means of VCA for fixed hopping strength $t = 0.015$ and zero detuning $\Delta = 0$ are shown in Fig. 3.40 for $N = \{2, 3, 5, 10\}$ two-level systems located in each cavity. For increasing number of two-level systems N the Mott lobes shrink and thus the gap in the spectral function is decreasing. The modified chemical potential $\mu - \omega_c$ is chosen such that the spectral function is evaluated approximately in the middle of the Mott lobe. We used the variational parameters $x = \{\omega_c, \epsilon, t\}$, reference systems of size $L = 4 \times 2$, and an artificial broadening $0^+ = 0.01$ for the numerical evaluation.

The number of particle and hole bands, present in the single-particle spectral function and their approximate energies can be already determined from the single-cavity solution. For large enough filling ($n_p > N$) there are $N+1$ eigenstates in the sectors of $n_p \pm 1$ particles which leads to $N+1$ particle and hole bands, respectively. However, we investigate spectral properties in the first Mott lobe ($n_p = 1$) and thus we have to examine the zero- and two-particle sectors. The zero-particle sector ($n_p = 0$) consists of only one state leading to one hole band ω_h and the two-particle sector ($n_p = 2$) consists for all $N \geq 2$ of three states, which leads to three particle bands ω_p^i, where $i \in \{1, 2, 3\}$. We choose the order of the bands such that the excitation energy increases with increasing index i. For clarity Fig. 3.40 shows only the hole band ω_h and the lowest-lying particle band ω_p^1. The approximate location of the particle bands is obtained from the energy difference of the eigenenergies of the two particle sector and the ground-state energy of the one-particle sector, see Eq. (3.31), leading to

$$\omega_p^1 \approx (\omega_c - \mu) - \sqrt{2(2N-1)} + \sqrt{N}$$
$$\omega_p^2 \approx (\omega_c - \mu) + \sqrt{N}$$

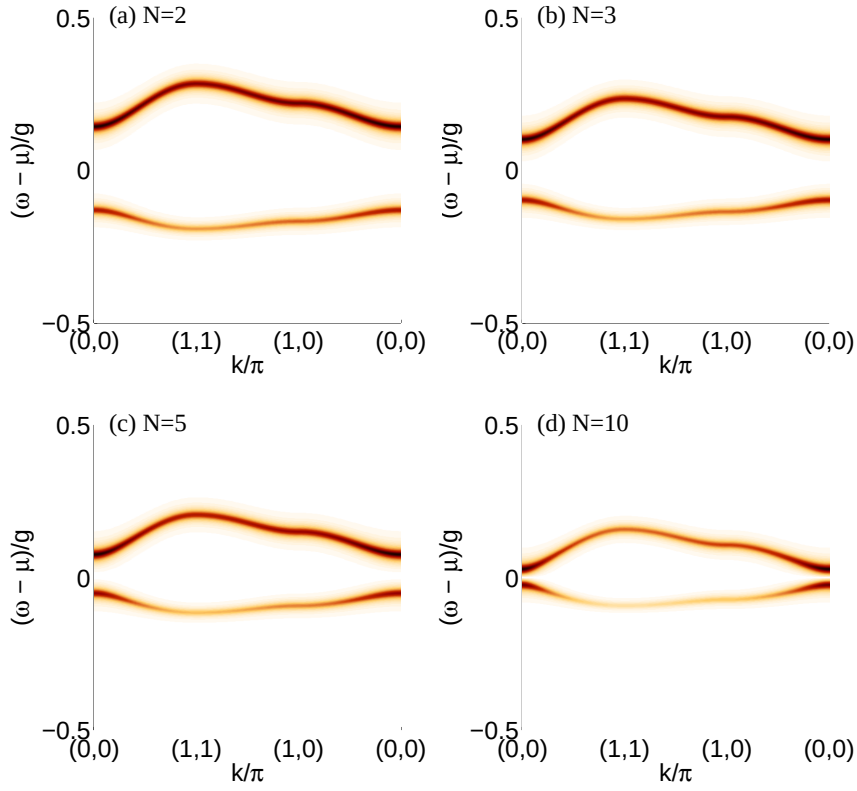

Figure 3.40.: Hole band ω_h and the lowest-lying particle band ω_p^1 of the photon single-particle spectral function $A^{ph}(\mathbf{k}, \omega)$ for fixed hopping strength $t = 0.015$ and zero detuning $\Delta = 0$. The modified chemical potential and the number of two-level systems is (a) $\mu - \omega_c = -1.25$, $N = 2$, (b) $\mu - \omega_c = -1.6$, $N = 3$, (c) $\mu - \omega_c = -2.15$, $N = 5$, and (d) $\mu - \omega_c = -3.1$, $N = 10$.

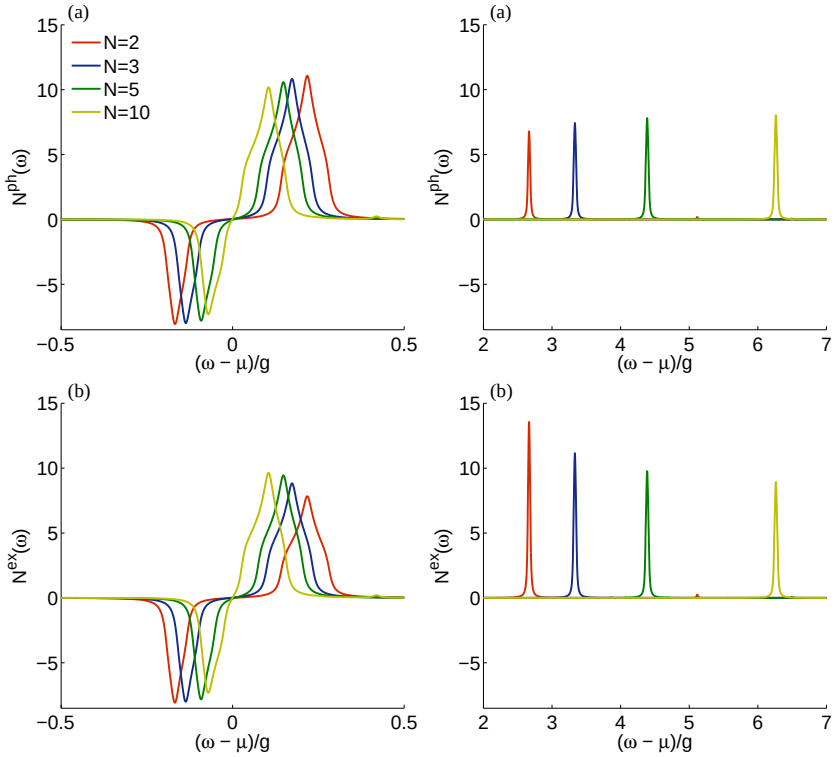

Figure 3.41.: Density of states of (a) photons $N^{ph}(\omega)$ and (b) atomic excitations $N^{ex}(\omega)$ for parameters as in Fig. 3.40. The left column shows contributions from the bands ω_h and ω_p^1 and the right column from the bands with higher energy ω_p^2 and some of the ω_p^3.

$$\omega_p^3 \approx (\omega_c - \mu) + \sqrt{2(2N-1)} + \sqrt{N} \; .$$

Analogously, one obtains for the hole band

$$\omega_h \approx (\omega_c - \mu) - \sqrt{N} \; .$$

The densities of states of both photons $N^{ph}(\omega)$ as well as atomic excitations $N^{ex}(\omega)$ are shown in the first and second row, respectively, of Fig. 3.41 for identical parameters as in the case of the single-particle spectral function. The left column contains the density of states of a small energy window centered around zero, showing the low-lying excitation bands ω_h and ω_p^1. The right column contains data for higher excitation energies. The bands ω_p^2 carry significant spectral weight whereas the bands ω_p^3 are barely visible for $N = 2$ ($\omega_p^3 \approx 5.1$) and $N = 3$ ($\omega_p^3 \approx 6.5$). For more than three two-level systems per cavity the excitation energy is already larger than the maximum energy considered in the plot. The position of the bands matches well with the approximate results obtained from the single-cavity limit. In the photon density of states $N^{ph}(\omega)$, first row, the spectral weight of the low-lying particle band ω_p^1 decreases with increasing two-level

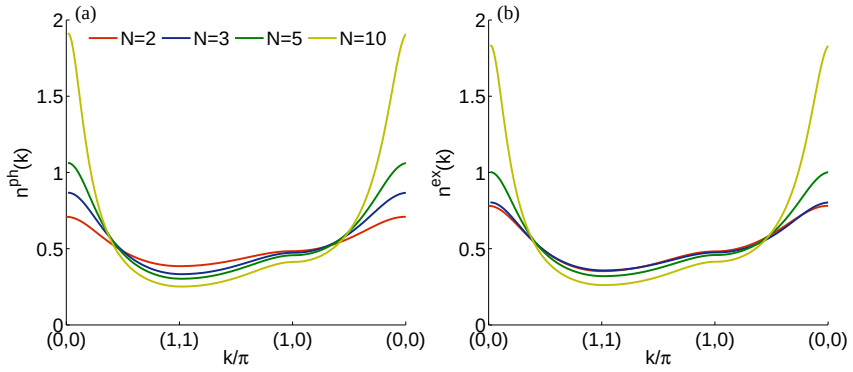

Figure 3.42.: Momentum distribution of (a) photons $n^{ph}(\mathbf{k})$ and (b) atomic excitations $n^{ex}(\mathbf{k})$ for parameter as in Fig. 3.40.

system number N, whereas the spectral weight of ω_p^2 increases. The opposite is true for the atomic excitation density of states $N^{ex}(\omega)$, second row. Interestingly, due to this behavior photon and atomic excitation densities of states become more similar for increasing two-level system number N, which is due to the fact that the ensemble of two-level systems behaves more like free bosons for large N [224, 240].

The momentum distribution of both particle species, which can be evaluated with high accuracy by means of the Q-matrix formalism [54], is shown in Fig. 3.42. The momentum distribution of photons (left panel) and the atomic excitations (right panel) do not exhibit major differences. For increasing number of two-level systems N and fixed hopping strength t, the tip of the Mott lobe is approached, see Fig. 3.38. From this in turn it follows that the density in the center of the Brillouin zone is increasing for increasing N, which is in accordance with our results.

Polaritons

Here, we investigate properties of polaritons, the elementary excitations of the TCL model, which are linear combinations of photons and atomic excitations. Our goal is to describe these excitations by polaritonic quasiparticles added to the N_p-particle ground state $|\psi_0\rangle$. Hence, we introduce the polariton creation operators $p^\dagger_{\alpha,\mathbf{k}}$ for particle excitations and $h^\dagger_{\alpha,\mathbf{k}}$ for hole excitations as suitable linear combinations of photons and hard-core bosons,

$$p^\dagger_{\alpha,\mathbf{k}} = \beta_p^\alpha(\mathbf{k})\, a^\dagger_{\mathbf{k}} + \gamma_p^\alpha(\mathbf{k})\, b^\dagger_{\mathbf{k}} \,, \tag{3.32a}$$

$$h^\dagger_{\alpha,\mathbf{k}} = \beta_h^\alpha(\mathbf{k})\, a_{\mathbf{k}} + \gamma_h^\alpha(\mathbf{k})\, b_{\mathbf{k}} \,. \tag{3.32b}$$

The weights $\beta_p^\alpha(\mathbf{k})$ and $\gamma_p^\alpha(\mathbf{k})$ of the polariton creation operators depend on the wave vector $\mathbf{k}$, the quasiparticle band index α, and the filling n_p. The dependence on the latter is not explicitly included in the notation as we solely focus on the first Mott lobe with particle density $n_p = 1$. It is important to notice that the hole creation operator

is neither the adjoint of the particle creation operator nor its annihilation counterpart. The normalized polariton quasiparticle states are generated by applying the polariton particle and hole creation operators on the N_p-particle ground state,

$$|\tilde{\psi}^{\alpha}_{p,\mathbf{k}}\rangle = \frac{p^{\dagger}_{\alpha,\mathbf{k}}\,|\psi_0\rangle}{\sqrt{\langle\psi_0|\,p_{\alpha,\mathbf{k}}\,p^{\dagger}_{\alpha,\mathbf{k}}\,|\psi_0\rangle}}\,, \tag{3.33a}$$

$$|\tilde{\psi}^{\alpha}_{h,\mathbf{k}}\rangle = \frac{h^{\dagger}_{\alpha,\mathbf{k}}\,|\psi_0\rangle}{\sqrt{\langle\psi_0|\,h_{\alpha,\mathbf{k}}\,h^{\dagger}_{\alpha,\mathbf{k}}\,|\psi_0\rangle}}\,. \tag{3.33b}$$

The weights β and γ of the linear combination are determined by maximizing the overlap between the exact eigenvectors $|\psi^{N_p\pm1}_{\alpha,\mathbf{k}}\rangle$ of the TCL model in the $(N_p\pm1)$-particle sector. This yields a generalized eigenvalue problem which is used to determine the weights β and γ, see Ref. [60] for a detailed derivation and discussion. The eigenvalue λ of the generalized eigenvalue problem specifies the quality of the quasiparticle description. More specifically, λ is bound by the interval [0, 1], where $\lambda = 1$ corresponds to a perfect description by polariton quasiparticles, i. e., to maximal overlap between the true $(N_p \pm 1)$-particle states and the polariton states $|\tilde{\psi}^{\alpha}_{p/h,\mathbf{k}}\rangle$, whereas small values of λ indicate a modest quasiparticle description. The generalized eigenvalue problem fixes the weights β and γ only upon a constant, which is determined by the condition that the total spectral weight consisting of the spectral weight of photons and atomic excitations is conserved.

For the hole band ω_h the weights β and γ can be chosen freely, as both $a_{\mathbf{k}}$ and $b_{\mathbf{k}}$ applied on the ground state with particle density $n_p = 1$ are proportional to the same state. Thus we investigate only the weights β and γ for the particle bands ω^1_p, ω^2_p, and ω^3_p, which are shown in Fig. 3.43 from top to bottom for $N = \{2, 3, 5, 10\}$ two-level systems per cavity. The photon weight β corresponds to the solid line and the atomic-excitation weight to the dashed line. For the band with lowest excitation energy ω^1_p the weights β and γ are of opposite sign, whereas the sign is equal for the bands ω^2_p and ω^3_p. The bands ω^1_p and ω^2_p are very well described by the polariton picture as $\lambda \approx 1$. Yet, the band with highest energy ω^3_p is very poorly represented by the polariton creation operators as $\lambda \approx 0.01$. For increasing number of two-level systems N per cavity the weights of the two constituents become similar. This might indicate, as in the case of the spectral weight, that the atomic excitations behave for large N like bosonic particles. In the case of a single two-level system per cavity $N = 1$, i. e., the Jaynes-Cummings lattice model, the asymmetry in the coefficients is much more pronounced than it is here [54].

Conclusions: We presented and discussed the quantum phase transition and the excitations of the Tavis-Cummings lattice model in two dimensions obtained within the variational cluster approach. The Tavis-Cummings lattice model describes light-matter systems which contain multiple two-level structures in each cavity. Due to this fact the Tavis-Cummings lattice model might be easier to realize in the experiment than its counterpart, the Jaynes-Cummings lattice model, which contains exactly one two-level systems per cavity. As a goal for future research, a detailed study of cavities with

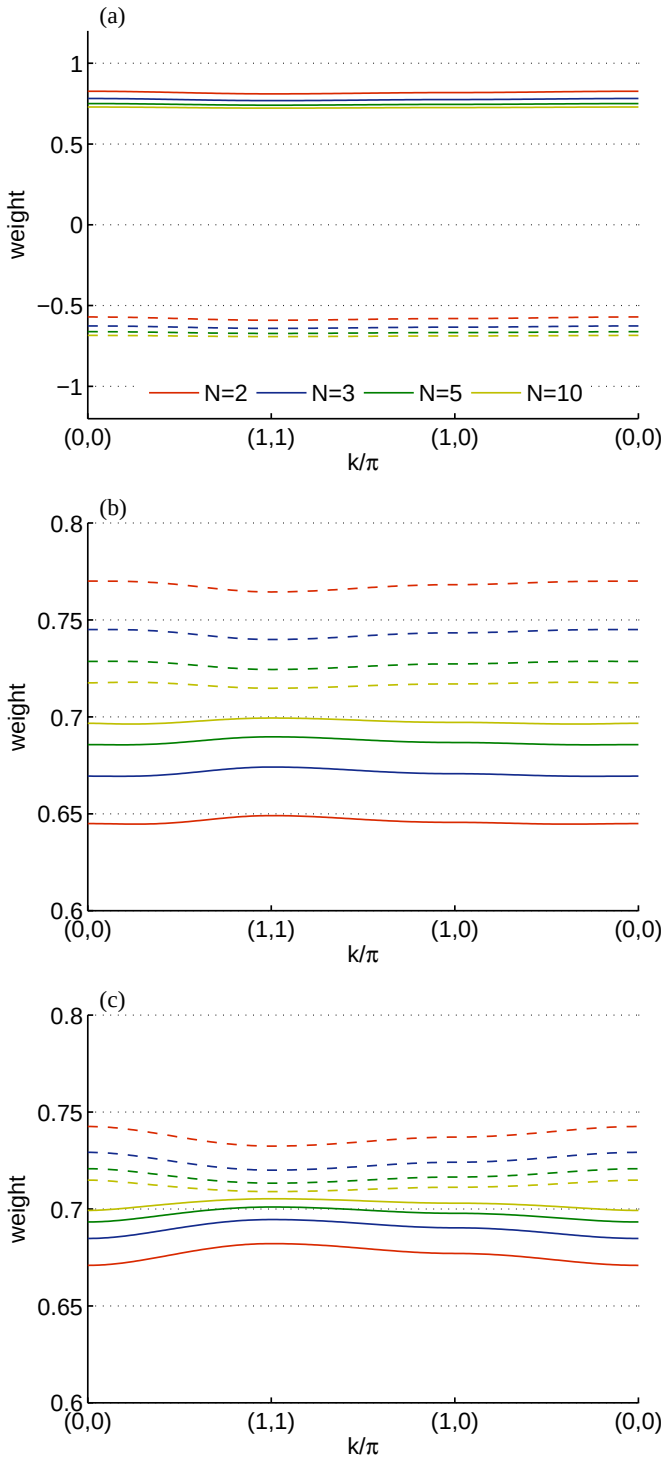

Figure 3.43.: Photon weights β (solid lines) and atomic excitation weights γ (dashed lines) of the polaritonic quasiparticle creation operators $p^{\dagger}_{\alpha,\mathbf{k}}$ for the bands (a) ω_p^1, (b) ω_p^2, (c) ω_p^3, and $N = \{2, 3, 5, 10\}$ two-level systems per cavity.

a random number of two-level systems might provide further interesting insight into light-matter systems.

In this paper, we determined the quantum phase transition delimiting Mott phase, in which polaritons are localized in each cavity, from superfluid phase, in which polaritons are delocalized on the whole lattice. We studied the dependence of this phase boundary for various two-level system numbers per cavity. For increasing number of two-level systems the Mott lobes become narrower, however, the width of the Mott lobes for distinct filling becomes more equal. We also compared the dependence of the critical hopping strength, which determines the tip of the Mott lobe, on the dimension of the coupled cavity system. Additionally to the phase boundary, we investigated spectral functions and corresponding densities of states. The variational cluster approach allows us to extract spectral properties for both photons as well as atomic excitations, provided the latter are mapped onto hard-core bosons. By investigating the zero-hopping limit, which corresponds to investigating a single cavity, we determine the number of bands in the spectral function and their approximate location. For the first Mott lobe there exist three particle bands and one hole band. The particle band and the hole band with smallest energy are reminiscent of the excitations in the Bose-Hubbard model. Particularly, they are also cosine shaped and the density distribution of the weight is similar [137, 141, 142, 54, 184]. The additional two particle bands lie at considerably higher energies. The band with second highest excitation energy carries significant spectral weight whereas the one with highest energy is barely visible in the spectra. Interestingly, for increasing two-level system number the weight of the photon spectra becomes more and more similar to the weight of the atomic excitation spectra. We investigated the momentum distribution as well, which is rather similar for photons and atomic excitations. Yet, for increasing two-level system number and constant hopping strength, a larger density can be observed in the center of the Brillouin zone, which arises due to the fact that the Mott lobe is shrinking with increasing number of two-level systems. Therefore, for identical hopping strength the boundary to superfluid phase is approaching, which is responsible for the increasing density in the center of the Brillouin zone. Finally, we studied the properties of polaritons, the elementary excitations in light-matter systems. Since we evaluated spectral properties of both particle species, we were able to introduce polariton quasiparticle and quasihole creation operators as linear combinations of photons and atomic excitations. The polariton creation operators depend on the wave vector, band index and filling. We investigated the photon and atomic excitation weights of the linear combination and analyzed their dependence on the number of two-level systems located in each cavity.

4. Nonequilibrium steady state

4.1. Model

In this section, we present an application of the nonequilibrium VCA method described in Sec. 2.3. Specifically, we study nonlinear transport properties across an extended correlated region (denoted as c in Fig. 2.2), which we take to be a Hubbard chain ($\bar{L}_{cx} = 1$) or a Hubbard ladder ($\bar{L}_{cx} = 2$) with nearest-neighbor hoppings t_x and t_y, on-site interaction U, on-site energy ϵ_c, and chemical potential μ_c

$$\bar{h}_c = \sum_{\langle i,j\rangle,\,\sigma} t_{ij} c^\dagger_{i\sigma} c_{j\sigma} + U \sum_i \hat{n}_{i\uparrow}\hat{n}_{i\downarrow} + (\epsilon_c - \mu_c) \sum_{i,\sigma} \hat{n}_{i\sigma} \ ,$$

in usual notation, and where $t_{ij} = t_x$ ($t_{ij} = t_y$) for i and j being nearest neighbors in x direction (y direction). The leads (shaded regions in Fig. 2.2) are described by two-dimensional semi-infinite tight-binding models with nearest-neighbor hopping t_L, on-site energies ϵ_l and ϵ_r, and chemical potentials μ_l and μ_r for the left and right lead, respectively. We apply a bias voltage V_b to the leads by setting $\mu_r = \epsilon_r = V_b/2$ and restrict to the particle-hole symmetric case where $\epsilon_c = -U/2$, $\mu_c = 0$, $\epsilon_r = -\epsilon_l$, and $\mu_l = -\mu_r$. For simplicity, we neglect the long-range part of the Coulomb interaction. Under some conditions, this can be absorbed within the single-particle parameters of the Hamiltonian, in a mean-field sense [86].

As discussed above, the unperturbed Hamiltonian h does not necessarily coincide with the physical partition into leads and correlated region. h is obtained by tiling the total system into small clusters as illustrated in Fig. 2.2, as well as by adding an intracluster variational term Δh.

In the present work Δh describes a correction Δt_x to the intra-ladder hopping. Further options could include, for instance, a site-dependent change in the on-site energy $\Delta\epsilon_c(x)$. Particle-hole symmetry can be preserved by constraining this change to be antisymmetric: $\Delta\epsilon_c(x) = -\Delta\epsilon_c(-x)$. In this paper, whose goal is to carry out a first test of the method, we restrict, for simplicity, to a single variational parameter. The choice of Δt_x as a variational parameter is motivated by the fact that this term is important for the current flowing in x direction. According to the prescription discussed above, we require the expectation value of the one-particle density matrix for nearest-neighbor indices in x direction to be the same for the unperturbed h and for the full H, i.e. evaluated with g_{cc} and with G_{cc}.

One comment about the chemical potential. In principle, when including some of the sites of the leads in h, i. e., when $L_{cx} > \bar{L}_{cx}$, then these additional sites have a chemical potential μ_c which differs from the one they would have if $L_{cx} = \bar{L}_{cx}$ (i. e., μ_l

or μ_r). However, the chemical potential, of these sites does not affect the steady state, as their volume-to-surface ratio is finite. Of course, their on-site energies (ϵ_r and ϵ_l) are important.

Due to translation invariance by a cluster length L_{cy} in the y direction, it is convenient, as in usual VCA, to carry out a Fourier transformation in y direction, with associated momenta q_y. The Green's functions g_{cc} and G_{cc}, as well as T become now functions of two momenta $q_y + Q_y$ and $q_y + Q'_y$, where Q_y and Q'_y are reciprocal superlattice vectors of which there are only L_{cy} inequivalent ones. In order to evaluate the nonequilibrium steady state, one only needs the equilibrium Green's function $g(x_{b\alpha}|q_y|z)$ of the isolated leads at the contact edge to the central region, with x coordinate equal to $x_{b\alpha}$ ($\alpha \in \{l, r\}$), and Fourier transformed in the y directions, where q_y is the corresponding momentum and z the complex frequency. For a semiinfinite nearest-neighbor tight-binding plane with hopping t_L, and on-site energy ϵ_α, this can be expressed as

$$g(x_{b\alpha}|q_y|z) = g_{c,loc}(z - 2t_L \cos q_y - \epsilon_\alpha) \ , \tag{4.1}$$

where $g_{c,loc}(z)$ is the local Green's function of a tight binding chain with open boundary conditions and with zero on-site energy. The latter can be determined analytically along the lines discussed in Ref. [241].

The model studied here, is motivated by the interest in transport across semiconductor heterostructures (see, e.g. [242, 243, 244, 245]). However, it is well known that in this case charging effects are important, also near the boundaries between the leads and the central region. Here, scattering effects produce charge density waves, which, when taking into account the long-range part of the Coulomb interaction, even in mean-field, produce a modification of the single-particle potential. In order to treat realistic structures, these effects should be included at the Hartree-Fock level at least. All these generalizations can be straightforwardly treated with the presented variational cluster method, however, in this work we focus on a first proof of concept study and application containing the essential ingredients for the investigation of the nonequilibrium steady state of strongly correlated many-body systems.

4.2. Results

We have evaluated the steady-state current density j_x of the models discussed in Sec. 4.1 as a function of the bias $V_b \equiv \epsilon_r - \epsilon_l$ between the leads at zero temperature. Simultaneously the chemical potential is adjusted to the on-site energy $\mu_\alpha = \epsilon_\alpha$, which corresponds to a rigid shift of the density of states in both leads in opposite directions.

In Fig. 4.1 we display results for the two-leg ladder ($\bar{L}_{cx} = 2$), for different values of the interaction strength $U = \{0, 2, 4, 6\}$ and lead-to-system hopping $V = \{1.0, 0.75, 0.5, 0.25, 0.1\}$. We use $\hbar = 1$ and $t_L = 1$ which sets the unity of energy. Moreover, we take the lattice constant $a = 1$. The hopping is uniform in the whole system, meaning that t_x, t_y in the correlated region and t_L of the leads are equal. The on-site energy of the correlated region is $\epsilon_c = -U/2$ corresponding to half-filling, whereas the on-site energy of the left (right) lead is equal to its chemical potential μ_l (μ_r). The

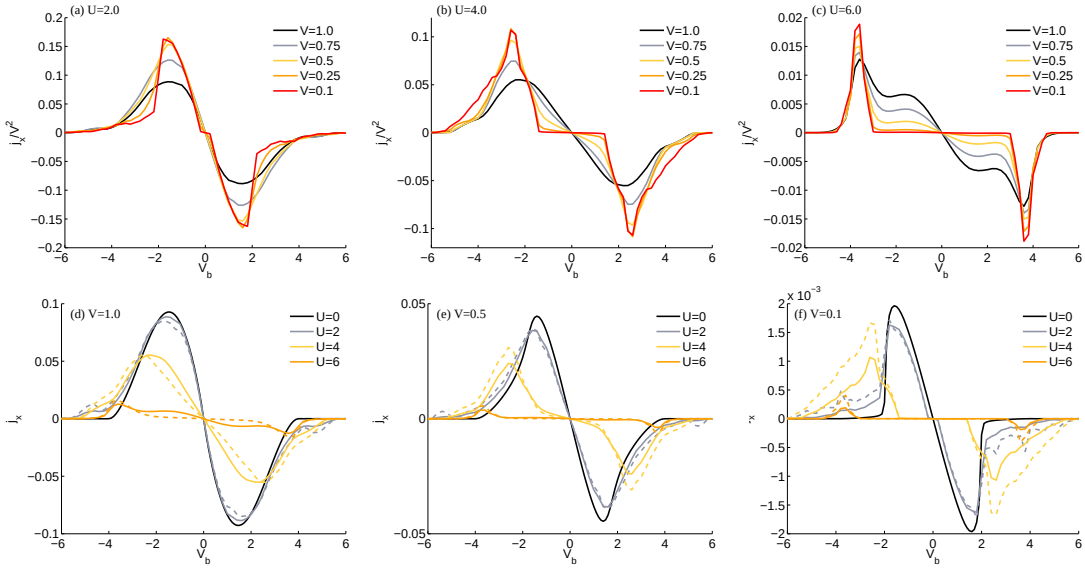

Figure 4.1.: Steady-state current density j_x versus bias voltage V_b for a correlated two-leg ladder ($\bar{L}_{cx} = 2$). First row shows j_x normalized by V^2 as function of V_b evaluated for different values of V and of the interaction (a) $U = 2.0$, (b) $U = 4.0$, and (c) $U = 6.0$. Second row shows the U dependence of the current for different values of the hopping $V = V_{lc} = V_{rc}$ from the leads to the correlated region (d) $V = 1.0$, (e) $V = 0.5$, and (f) $V = 0.1$. Solid (dashed) lines represent results for the current between the left lead and the central region (between two in x direction adjacent sites inside the central region), i. e., evaluated with G^K_{lc} (G^K_{cc}), see text for details. Results are obtained by using a reference Hamiltonian h consisting of disconnected clusters of size $L_c = L_{cx} \times L_{cy} = 2 \times 6$.

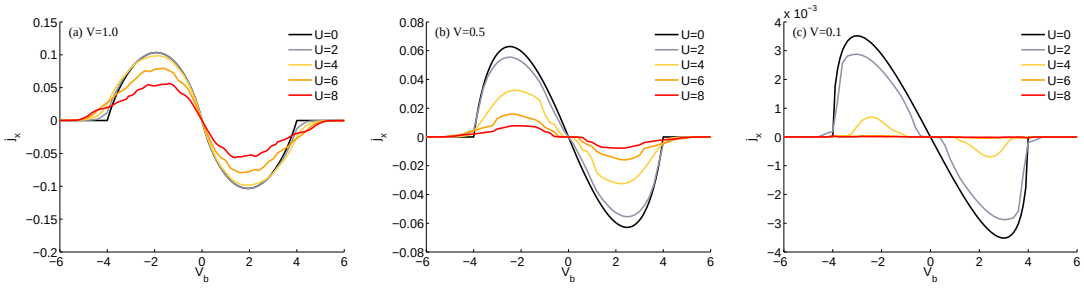

Figure 4.2.: Steady-state current density j_x as in Fig. 4.1 but for the correlated chain ($\bar{L}_{cx} = 1$). The current density is evaluated for different values of the lead to correlated region hopping (a) $V = 1.0$, (b) $V = 0.5$, and (c) $V = 0.1$, and of the interaction U, see legend. Results are obtained for reference clusters of size $L_c = L_{cx} \times L_{cy} = 3 \times 4$.

unperturbed Hamiltonian h describes the central region decomposed into clusters of size $L_c = 2 \times 6$. The corresponding Green's function g_{cc} is determined exactly by Lanczos diagonalization. All results are determined self-consistently using Δt_x as variational parameter, see Sec. 4.1.

Using the Meir-Wingreen expression, Eq. (2.102), the general trend of the results for the steady-state current j_x can be discussed conveniently. At zero temperature there are only contributions to the current for $\min(\mu_l, \mu_r) < \omega < \max(\mu_l, \mu_r)$ due to the difference of the Fermi distribution functions. In particular this leads as expected to zero current for zero bias voltage V_b. With increasing bias voltage V_b the modulus of j_x initially increases. For large values of V_b it decreases again, as the overlap of the local density of states of the two leads enters the expression, which is zero if V_b is greater than the band width of the leads. Hence the local density of states of the leads along with the Fermi function act as a filter that averages the electronic excitations of the central region within a certain energy window.

In the system we are studying, the leads are modeled by semi-infinite tight binding planes. Alternatively, instead of using (4.1) one could simply put a model Green's function "by hand," as for example one which describes a Lorentzian shaped density of states. Such an unbound density of states generally leads to a finite value of the current for arbitrary bias.

The leads have a further effect on the result as they provide an inelastic broadening of the energy spectrum of the central region entering Σ^{eff}, see Eq. (2.101), which smears out details of the excitation spectrum. As far as the lead-correlated region coupling V is concerned, there are two competing effects: on the one hand, the current increases with increasing V due to the stronger coupling between the correlated region and the leads. On the other hand, details of the electronic excitations are smeared out with increasing V leading to a reduced resolution. Therefore, in order to detect the effects of strong correlations, particularly the gap, a small value for V is required.

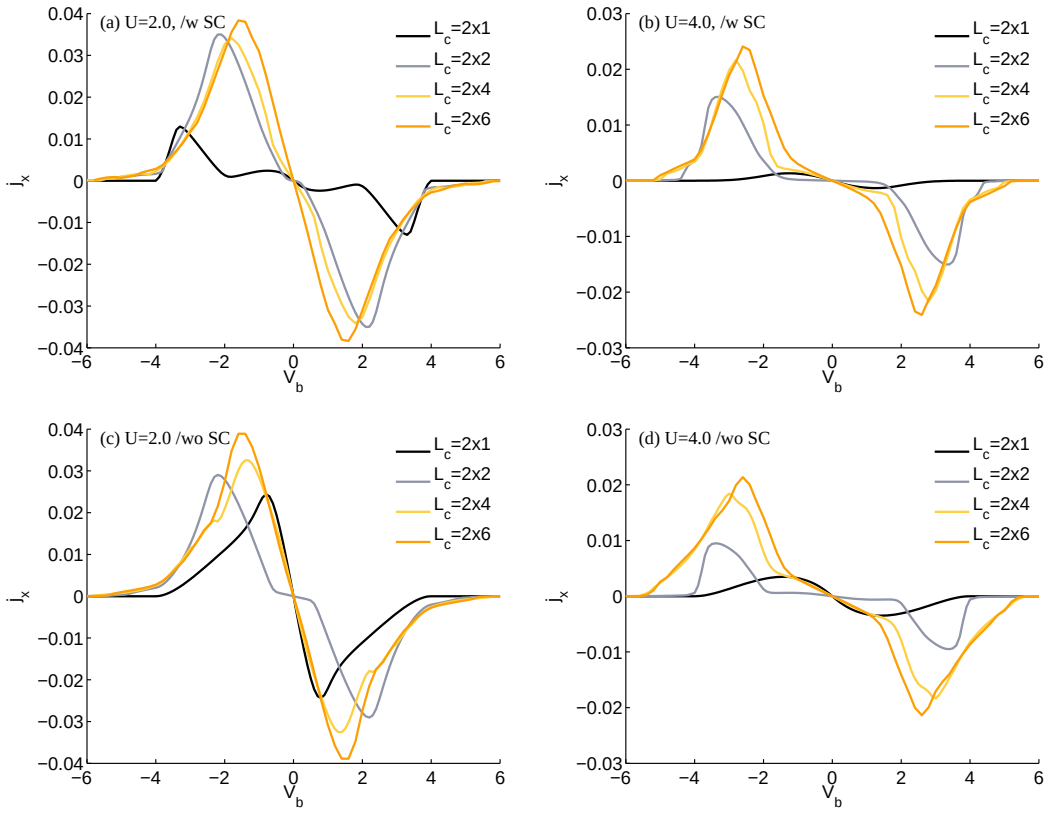

Figure 4.3.: Convergence of the steady-state current density j_x with reference cluster size $L_c = L_{cx} \times L_{cy}$ for the correlated two-leg ladder with $V = 0.5$. Results in (a), (b) are obtained by a variational adjustment of the intra-cluster hopping t_x as discussed in the text, while those of (c), (d) are obtained without modification of t_x. The values for the Hubbard interaction are $U = 2$ in [(a), (c)] and $U = 4$ in [(b), (d)].

The details of the V dependence of j_x for small V can be deduced from (2.102). Here, the expression for the current has a prefactor proportional to V^4 (at least in the $L_{cx} = \bar{L}_{cx}$ case), due to the two Γ terms. On the other hand, for a gapless system, there is a V^2 term in the denominator of $|G^R_{cc}|^2$. For a gapped system, this is cut off by the energy gap E_g, so that in this case $j_x \sim V^4/E_g^2$, while $j_x \sim V^2$ for a gapless spectrum. These aspects are clearly observable in Fig. 4.1 (a)–(c), which shows the scaled current density j_x/V^2 for fixed interaction strength U but varying V. The envelope has a rotated S-like structure due to the combined effects of the lead density of states and of the Fermi functions.

Next we will analyze a bit more in detail the effects of the Hubbard interaction. Increasing the interaction strength U in the correlated region leads to a suppression of the current and the opening of a gap, which is best observed in (f). For $U = 4$ the maximum of the current density is roughly reduced by a factor of two as compared to the noninteracting case, whereas for $U = 6$ the current is almost one order of magnitude smaller as compared to the noninteracting system, see Fig. 4.1 (d)–(f).

Finally, we want to address the the difference between the solid lines and dashed lines in the the panels (d)–(f) of Fig. 4.1, which represent the current density evaluated on a bond connecting the leads to the central region, or on a bond within the two-leg ladder. Due to the stationary condition, the two results should coincide. However, our calculations shows a slight discrepancy between them, which is due to the fact that the method is not completely conserving and, thus, the continuity equation is not completely fulfilled. However, from our results we see that the deviation from the continuity equation is quite small. We expect this discrepancy to be reduced upon improving the optimization with the introduction of additional variational parameters.

In Fig. 4.2 we show the steady-state current density j_x across the correlated chain ($\bar{L}_{cx} = 1$) as a function of the bias voltage. The parameters are the same as in the case of the two-leg ladder, however, the central region is decomposed into clusters of size $L_c = 3 \times 4$, where also sites of the leads are taken into account to improve the results. The half-filled Hubbard chain is gapped as well. As for the two-leg ladder, the gap behavior can be better seen in the current-voltage characteristics for smaller values of V, in our case for $V = 0.1$. In contrast, for strong coupling $V = 1.0$, (a), no gap behavior can be seen in the current due to the strong hybridization with the leads.

For strong values of the coupling V between leads and correlated region ($V = 1.0$), (a), the current is significant for all values of the interaction U. However, with decreasing V, (b)–(c), the current is strongly suppressed for large interaction U. Importantly, for the correlated chain the continuity equation is always strictly fulfilled. In other words, there is no difference between j_x evaluated on a intercluster bond between the leads and the cluster, or on an intracluster bond. This is due to the absence of vertex corrections at the uncorrelated sites.

Next, we study the convergence of our results with the size of the cluster, as well as the effect of the self-consistency condition for the two-leg ladder and $V = 0.5$. Results are depicted in Fig. 4.3 for two different values of the Hubbard interaction, namely $U = 2$ [(a), (c)] and $U = 4$ [(b), (d)]. We do not plot results of the convergence analysis for

$U = 6$, since for this large U the current is already rather small, as can be seen in Fig. 4.1 (d)–(f). Results in (a) and (b), first row, are obtained by adjusting Δt_x self-consistently, as described in Sec. 4.1, whereas (c) and (d), second row, shows results without self-consistency, i. e., with $\Delta t_x = 0$. Results show that the self-consistency procedure improves the results, as the convergence for j_x is faster with increasing cluster size as compared to the case without self-consistency. Generally, we observe pronounced finite size effects for very small clusters up to 2×4, and convergence seems to be reached for the 2×6 cluster.

We now repeat the same analysis for the correlated chain. The corresponding current densities for the parameters $U = 2$ and $V = 0.5$ are shown in Fig. 4.4 for different cluster sizes. Results shown in (a) are with self-consistency procedure (2.104), whereas the results shown in (b) are without. In the present case, where we consider transport across a strongly correlated chain, convergence is achieved very quickly with increasing cluster size. Therefore, there is no sensible difference between results obtained with or without self-consistency, apart for the pathological case $L_c = 3 \times 1$ (see below).

Results obtained for the two-leg ladder and for the chain show that cluster geometries with $L_{cy} = 1$ provide results far from convergence, even with self-consistency. For the chain this is probably due to the degeneracy of the cluster ground state. For the ladder, it seems that using as starting point the 2×1 dimer exaggerates the gap. But besides these data obtained from admittedly very small clusters, results converge quickly as a function of cluster sizes, especially when the hopping in x direction is used as a variational parameter.

Conclusions: In this paper we have presented a novel approach to treat strongly correlated systems in the nonequilibrium steady state. The idea is based on the variational cluster approach extended to the Keldysh formalism. For the present approach the expression for the current resembles the corresponding Meir-Wingreen formulas. As in the original Meir-Wingreen approach, which is also the basis for nonequilibrium density-functional based calculations, we directly address the steady state behavior of a device coupled to infinite leads. The latter is necessary for the system to reach a well-defined steady state.

The present nonequilibrium extension is in a similar spirit to the equilibrium self-energy functional approach, in which one "adds" single-particle terms to the cluster Hamiltonian which is then solved exactly, and "subtract" them perturbatively [66, 57]. The values of the parameters are determined by an appropriate requirement which in the end amounts to optimizing the unperturbed state with respect to the perturbed one.

There is a certain freedom in choosing the most appropriate self-consistency criterion. Here we have required the operators associated with the variational parameters to have the same expectation values in the unperturbed and in perturbed state. Certainly, an interesting alternative would be to generalize the variational criterion provided by the self-energy functional approach [49] to the nonequilibrium case. This will be obtained by a suitable generalization of the Euler equation (Eq. (7) of Ref. [49]) to the Keldysh contour, i. e., by replacing g_{0cc} with the self-energy Σ_h in (2.104) Work along these lines

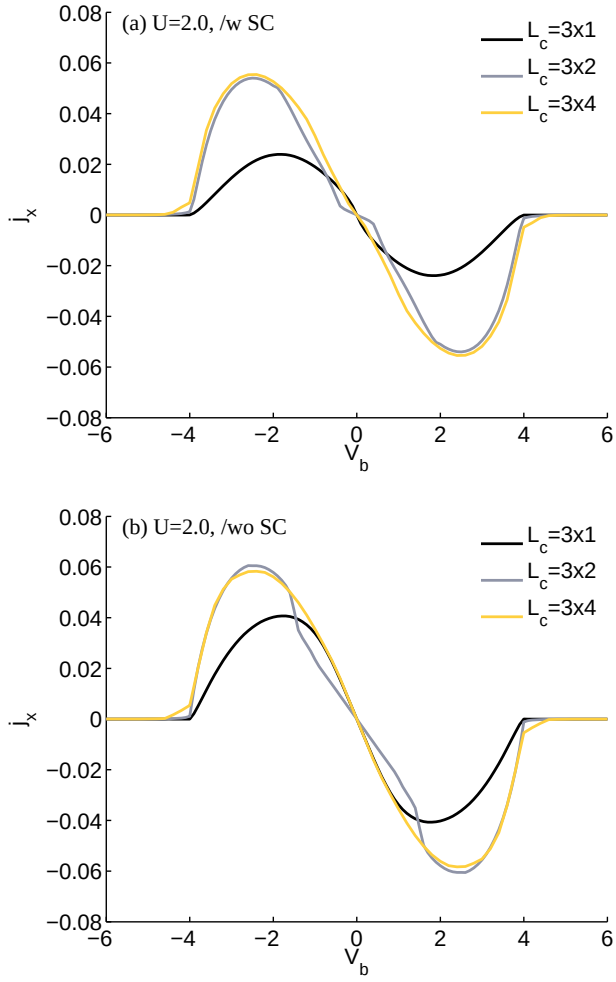

Figure 4.4.: Convergence of the steady-state current density j_x with reference cluster size $L_c = L_{cx} \times L_{cy}$ for the correlated chain. Results in (a) fulfill the self-consistency condition (2.104), whereas results in (b) do not. The parameters are $U = 2$ and $V = 0.5$.

is in progress.

The advantage of the present variational condition (2.104) is that it is computationally less demanding, as one just needs to evaluate cluster single-particle Green's functions. Which one of the two conditions gives more accurate results cannot be stated a priori and should be explicitly checked.

In any case, both methods, the self-energy functional approach and the present one, become equivalent to (cellular) dynamical mean-field theory in the case in which an infinite number of variational parameters is suitably taken (see Appendix C.1).

In general, we expect results to improve when more variational parameters are taken into account. In particular, when evaluating the current across the central region, it would be useful if a current was already flowing in the cluster. This can be achieved by adding a complex variational hopping between the end points of the cluster, and of course remove it perturbatively. The corresponding variational condition would contain the interesting requirement that the current flow in this modified cluster be the same as in steady state.

The model studied here, is motivated by the interest in transport across semiconductor heterostructures (see, e.g. [242, 243, 244, 245]). However, it is well known that in this case charging effects are important, also near the boundaries between the leads and the correlated region. Here, scattering effects produce charge density waves, which, when taking into account the long-range part of the Coulomb interaction, even in mean-field, produce a modification of the single-particle potential. In order to treat realistic structures, these effects should be included at the Hartree-Fock level at least. All these generalizations can be straightforwardly treated with the presented variational cluster method, however, in this work we focus on a first proof of concept study and application containing the essential ingredients for the investigation of the nonequilibrium steady state of strongly correlated many-body systems.

5. Conclusions and Outlook

In this thesis, we explored the collective behavior of many particle systems, and with that the accompanied emergent ordering phenomena and broken symmetries. Strong correlations, resulting from the subtle interplay between the kinetic energy of the particles and their mutual interaction have substantial influence on the observed physics. The contributions of this thesis can be divided into two main points: The first deals with the collective behavior in bosonic manybody systems and the second with the emergent nonequilibrium steady state of strongly correlated manybody systems.

In the recent years the advent of synthetic manybody systems allowed for an extremely accurate and versatile exploration of manybody effects. Among these synthetic systems are systems of ultracold atoms [20, 21, 22], which are handled as promising quantum simulators. Ultracold atom experiments with bosonic constituents are well described by the Bose-Hubbard model. Here, we explored the equilibrium properties of the Bose-Hubbard model in the normal Mott insulating phase and the symmetry broken superfluid phase using the variational cluster approach. Particularly, we calculated dynamical and wavevector dependent single-particle spectral functions, momentum distributions, and mapped out the phase boundaries of the quantum phase transition. In cold atom experiments the momentum distribution is directly accessible in time of flight experiments and dynamical spectral properties using Bragg spectroscopy. In the normal phase we also study the effect of disorder on these quantities, where we focused on disorder distributions which are relevant for cold atom experiments like exponential laser speckle disorder and disorder distributions associated to incommensurable optical lattices.

We studied synthetic light matter systems [23, 24], where nonlinearities result from the strong coupling of light to some form of matter. One possible realization where strong interactions can be achieved are lattice extensions of cavity and circuit quantum electrodynamics setups. Specifically, we focused on two light-matter systems differing in their experimental realization. The first consists of coupled cavities with matter modeled by a single two level system. We study spectral properties and map out the properties of the polaritons, which are superpositions of photons and excitations. We determine the nature of these quasiparticles by extracting the relative contributions of photons and excitations. The second model allows for an arbitrary number of two-level systems per cavity, which could be relevant for experiments, where this quantity might not be well controlled. We explore the quantum phase transition, calculate spectral properties and momentum distributions, and determine the nature of the polariton quasiparticles as a function of the number of two-level systems.

We evaluate the equilibrium properties of these manybody systems by means of the variational cluster approach [28], which has been first applied to bosonic systems by

Koller and Dupuis [51]. In our formulation of the variational cluster approach we employ the Q-matrix formalism for bosonic systems, which allows for an extremely accurate calculation of the momentum distribution and the spectral moments. We also reformulate the variational cluster approach within this Q-matrix formalism for disordered manybody systems. We then extended the variational cluster approach to the symmetry broken superfluid phase of lattice bosons within a pseudoparticle approach and a self-energy functional approach. The pseudoparticle approach, while not as rigorous as the self-energy functional approach, allows for a straight forward extension to the superfluid phase, which in particular amounts to finding the correct expression for the grand potential Ω in the presence of a condensate. To this end, we adopted the Nambu notation. The evaluation of the functional form of the grand potential within the self-energy functional approach puts the pseudoparticle approach results on rigorous grounds and provides additional insight into the functional dependence and structure.

Additionally to equilibrium properties of bosonic systems, we also present a variational cluster approach that allows to compute nonequilibrium steady state properties of strongly correlated manybody systems. The method is embedded in the Keldysh Green's function formalism. We introduce a variational principle which allows for a suitable optimization of the reference state to the nonequilibrium target state. The approach is perturbative in the coupling between the clusters yet is neither perturbative in the manybody interaction nor in the field that drives the system out of equilibrium. As a crucial point the approach allows to study strong perturbations and nonlinear responses of systems in which the correlated region is spatially extended. We apply the presented approach to the nonlinear transport across a strongly correlated quantum wire described by the fermionic Hubbard model, where we observe dielectric breakdown for a strong bias voltage and weak hybridization with the leads. We also illustrate how the method bridges to cellular dynamical mean field theory upon coupling two baths containing an increasing number of uncorrelated bath degrees of freedom.

There are many possible directions for future research. Concerning equilibrium properties of bosonic systems an extension of the disorder calculations to the superfluid phase should give important additional insight into the phase transitions from Mott to Bose glass and from Bose glass to the superfluid phase [30]. Also an extension to finite temperatures might proof interesting not only conceptually but also from the physical point of view. Currently, extremely relevant are also mixtures of two particle species, which could either be Bose-Bose [246, 247], Bose-Fermi [248, 249, 250, 251, 252, 253, 254, 255], or Fermi-Fermi [256, 257, 258, 259, 260, 261] mixtures. The interplay between the various possible interactions gives rise to particularly rich physics. An extension of the study of light-matter systems to the superfluid phase of polaritons and their quasiparticle properties as well as the susceptibility to disorder are other interesting directions. Finally, also in the context of recent cold atom experiments [262, 263] it would be interesting to study the effect of strong magnetic fields giving rise to the Hofstadter problem [264]. Concerning the calculation of the nonequilibrium steady state a whole new direction opens with countless interesting questions including the study of the re-

sponse of a superconducting layer to applied bias voltage [265] and the characteristics of a quantum dot subject to an applied bias voltage [266]. All these diverse fields and many more constitute possible exciting future research directions.

A. Pseudoparticle approach

A.1. Procedure to construct V and S'

Here, we outline how the two conditions on V given in Eqs. (2.41) and (2.42) can be achieved and how S' can be constructed. We start out from the eigenvalue equation for the non-Hermitian matrix M

$$MV = VD \; .$$

As already argued in Sec. 2.1.5, from the physical viewpoint we can only proceed if the eigenvector-matrix V is nonsingular and if all eigenvalues are real, as the system would otherwise be unstable. Hence we can express the Hermitian diagonal matrix of eigenvalues as

$$D = V^{-1}MV \; .$$

The first condition of Eq. (2.41) requires that the Hermitian matrix

$$X \equiv V^\dagger SV$$

be diagonal with diagonal elements $X_{ii} = \pm 1$. Multiplying the two Hermitian matrices and exploiting the Hermiticity of SM results in

$$XD = V^\dagger SMV = (XD)^\dagger = DX \; ; \quad \Rightarrow [X, D] = 0 \; .$$

Commuting Hermitian matrices have a common set of orthonormal eigenvectors. The matrix D is already diagonal. Hence for indices belonging to nondegenerate eigenvalues, X is also diagonal. Within the set of indices belonging to a degenerate eigenvalue, the corresponding Hermitian submatrix of X can be diagonalized by a unitary transformation U. In the following we term the diagonalized matrix as X'. The diagonalization also results in a new matrix $\overline{V} = VU$ of eigenvectors. We still have $\overline{V}^{-1}M\overline{V} = D$, but now

$$\begin{aligned} \overline{V}^\dagger S\overline{V} &= X' = \mathrm{diag}(x'_1, \ldots, x'_L) \\ \overline{V}^\dagger SM\overline{V} &\equiv E' = X'D = \mathrm{diag}(x'_1 d_1, \ldots, x'_{n_s} d_{n_s}) \; . \end{aligned} \tag{A.1}$$

For the condition Eq. (2.41) we still need to ensure that $x'_\alpha = \pm 1$. Provided no x'_α vanishes, which we will show below, this can easily be achieved by a suitable normalization

of the column vector of $\overline{V} \rightarrow \tilde{V} = \overline{V}Z$, with Z being a diagonal matrix, defined as $Z_{\alpha\alpha} \equiv 1/\sqrt{|x'_\alpha|}$. We eventually have

$$\begin{aligned}\tilde{V}^{-1}M\tilde{V} &= D = \mathrm{diag}(d_1, \ldots, d_L) \\ \tilde{V}^\dagger S\tilde{V} &= Z^\dagger X' Z = S' = \mathrm{diag}(s'_1, \ldots, s'_L) \\ \tilde{V}^\dagger SM\tilde{V} &\equiv E = \mathrm{diag}(e_1, \ldots, e_{n_s}) \; .\end{aligned}$$

We are merely left with the proof that

$$x'_\alpha = \bar{\mathbf{v}}^{\alpha\dagger} S \bar{\mathbf{v}}^\alpha \neq 0 \; , \tag{A.2}$$

where $\bar{\mathbf{v}}^\alpha$ stands for the αth column of $\overline{V}$. To this end we assume *ad absurdum* that $\bar{\mathbf{v}}^{\alpha\dagger} S \bar{\mathbf{v}}^\alpha = 0$. In this case, $\bar{\mathbf{v}}^\alpha$ would belong to the (n_s-1)-dimensional space $\mathcal{S}_\alpha$ orthogonal to the vector $S\bar{\mathbf{v}}^\alpha$. According to Eq. (A.1) the vectors $\bar{\mathbf{v}}^1$, … $\bar{\mathbf{v}}^{\alpha-1}$, $\bar{\mathbf{v}}^{\alpha+1}$, … $\bar{\mathbf{v}}^{n_s}$ also belong to $\mathcal{S}_\alpha$ and they are linear independent. Thus they span $\mathcal{S}_\alpha$. Due to the fact that *all* vectors $\bar{\mathbf{v}}^1$, … $\bar{\mathbf{v}}^{n_s}$ are linear independent, $\bar{\mathbf{v}}^\alpha$ cannot belong to $\mathcal{S}_\alpha$, which proves Eq. (A.2).

A.2. Grand potential

In this appendix we derive Eq. (2.59). Starting out from Eq. (2.58) we get

$$\begin{aligned}\Omega &= C - \frac{1}{N_c} \sum_{\mathbf{q}\in \mathrm{BZ}/2} g(D_\mathbf{q}) \\ &= \Omega' + \frac{1}{2}\,\mathrm{tr}\, g(\Lambda) - \frac{1}{N_c} \sum_{\mathbf{q}\in \mathrm{BZ}/2} g(D_\mathbf{q}) + \frac{1}{2}(F^\dagger \Gamma + h.c.) \\ &- \frac{1}{2}\,\mathrm{tr}\, h + \frac{1}{2}\Gamma^\dagger \bar{T}_\mathbf{0} \Gamma + \frac{1}{2}\tilde{F}^\dagger G_{(0)} \tilde{F} \; .\end{aligned} \tag{A.3}$$

We now evaluate the quantity

$$\begin{aligned}W &\equiv \langle A^\dagger \rangle\, G^{-1}_{(0)}\, \langle A \rangle - \langle A^\dagger \rangle'\, G'^{-1}_{(0)}\, \langle A \rangle' \\ &= \Gamma^\dagger G^{-1}_{(0)} \Gamma + \Gamma^\dagger \tilde{F} + \tilde{F}^\dagger \Gamma + \\ &\quad \tilde{F}^\dagger G_{(0)} \tilde{F} - \Gamma^\dagger (G^{-1}_{(0)} + \bar{T}_\mathbf{0}) \Gamma \\ &= (\Gamma^\dagger (F + \bar{T}_\mathbf{0}\Gamma) + h.c.) + \tilde{F}^\dagger G_{(0)} \tilde{F} - \Gamma^\dagger \bar{T}_\mathbf{0} \Gamma \\ &= (\Gamma^\dagger F + h.c.) + \Gamma^\dagger \bar{T}_\mathbf{0} \Gamma + \tilde{F}^\dagger G_{(0)} \tilde{F} \; .\end{aligned}$$

Comparison with (A.3) gives

$$\Omega = \Omega' + \frac{1}{2}\,\mathrm{tr}\, g(\Lambda) - \frac{1}{N_c} \sum_{\mathbf{q}\in \mathrm{BZ}/2} g(D_\mathbf{q}) + \frac{1}{2} W - \frac{1}{2}\,\mathrm{tr}\, h \; ,$$

which is the expression for the grand potential stated in Eq. (2.59).

A.3. Zero-interaction limit

The zero-interaction limit turns out to be a nontrivial check for VCA. For $U = 0$, the BH model can be solved analytically as it reduces to

$$\hat{H} = -t \sum_{\langle i,\, j \rangle} a_i^\dagger \, a_j - \mu \sum_i \hat{n}_i \; .$$

The chemical potential μ has to be smaller than $-2t$ in order to prevent infinitely many particles in the ground state. Taking this into account, the grand potential at zero temperature is $\Omega = 0$. In the zero-interaction limit VCA/CPT yields exact results. Thus the pseudoparticle formalism can be checked by applying this limit. For reference systems $\hat{H}'$ which consist of a single site the calculations can be done analytically. Under these considerations the Hamiltonian $\hat{H}'$ reads

$$\hat{H}' = -\mu' \, a^\dagger \, a \;\; - (a^\dagger \, f + f^* \, a) \; .$$

It can be solved by introducing shifted operators $\tilde{a} \equiv a + x$ and by "completing the square"

$$\begin{aligned} \hat{H}' &= -\mu' \, a^\dagger \, a - (a^\dagger \, f + f^* \, a) \\ &\stackrel{!}{=} \alpha \, \tilde{a}^\dagger \, \tilde{a} \;\; + c = \alpha (a^\dagger + x^*)(a + x) + c \\ &= \alpha \, a^\dagger \, a + \alpha (a^\dagger x + x^* a) + \alpha \, |x|^2 + c \; . \end{aligned}$$

Comparison reveals

$$\begin{aligned} \alpha &= -\mu' \\ x &= -f/\alpha = f/\mu' \\ c &= -\alpha \, |x|^2 = |f|^2/\mu' \; . \end{aligned}$$

The Hamiltonian $\hat{H}'$, rewritten by means of the shifted operators, is given by

$$\hat{H}' = -\mu' \, \tilde{a}^\dagger \, \tilde{a} + |f|^2/\mu' \; .$$

As discussed before we choose $\mu' < 0$. The eigenenergies obtained form the Schrödinger equation are

$$\hat{H}' \, |\tilde{\nu}\rangle = (-\mu' \, \tilde{\nu} + |f|^2/\mu') \, |\tilde{\nu}\rangle = E'_\nu \, |\tilde{\nu}\rangle \;\; .$$

For negative chemical potential μ' the ground state is $|\psi_0\rangle = |\tilde{0}\rangle$ and its energy $E'_0 = |f|^2/\mu'$. The eigenstates of $\hat{H}'$ are number states, therefore the shifted creation and annihilation operators act on them in the usual way

$$\begin{aligned} \tilde{a} \;\; |\tilde{\nu}\rangle &= \sqrt{\tilde{\nu}} \, |\tilde{\nu} - 1\rangle \\ \tilde{a}^\dagger \, |\tilde{\nu}\rangle &= \sqrt{\tilde{\nu} + 1} \, |\tilde{\nu} + 1\rangle \;\; . \end{aligned}$$

To evaluate the Q matrices we apply the original operators a on the eigenstates of $\hat{H}'$

$$a\,|\tilde{\nu}\rangle = (\tilde{a} - f/\mu')\,|\tilde{\nu}\rangle = \sqrt{\tilde{\nu}}\,|\tilde{\nu}-1\rangle - f/\mu'\,|\tilde{\nu}\rangle \ .$$

With that we obtain

$$\begin{aligned}\langle\tilde{0}|\,a\,|\tilde{\nu}\rangle &= 1\\ \langle\tilde{\nu}|\,a\,|\tilde{0}\rangle &= 0\\ \langle\tilde{0}|\,a\,|\tilde{0}\rangle &= -f/\mu' \ .\end{aligned}$$

Writing down the expressions in matrix form yields

$$Q = \begin{pmatrix} 1 & 0 \\ 0 & 1 \end{pmatrix} = \mathbb{1} \quad \Gamma = -1/\mu' \begin{pmatrix} f \\ f^* \end{pmatrix} \quad S = \begin{pmatrix} 1 & 0 \\ 0 & -1 \end{pmatrix}$$

$$\Lambda = S \begin{pmatrix} E_1' - E_0' & 0 \\ 0 & E_1' - E_0' \end{pmatrix} = \begin{pmatrix} -\mu' & 0 \\ 0 & \mu' \end{pmatrix} \ .$$

Using the expressions above and the relation $A = QB + \Gamma$ we obtain for the pseudoparticle operators

$$B = Q^{-1}(A - \Gamma) = \tilde{A} \ .$$

Next, we evaluate the grand potential from Eq. (A.3), where we obtain

$$\Omega = \underbrace{\Omega' + \frac{1}{2}\operatorname{tr} g(\Lambda)}_{\text{A}} - \underbrace{\frac{1}{N_c}\sum_{\mathbf{q}\in \mathrm{BZ}/2} g(D_{\mathbf{q}})}_{\text{B}} + \underbrace{\frac{1}{2}(F^\dagger\Gamma + h.c.)}_{\text{C}}$$
$$\underbrace{-\frac{1}{2}\operatorname{tr} h}_{\text{D}} + \underbrace{\frac{1}{2}\Gamma^\dagger \bar{T}_{\mathbf{0}}\Gamma}_{\text{E}} \underbrace{- \frac{1}{2}\tilde{F}^\dagger Q\ M_{\mathbf{0}}^{-1} S Q^\dagger \tilde{F}}_{\text{F}}$$

by employing Eq. (2.55). We calculate parts A–F of Ω separately

$$\begin{aligned}
&\text{A:} \quad \Omega' + \frac{1}{2}\operatorname{tr} g(\Lambda) = |f|^2/\mu' + \mu'/2\\
&\text{B:} \quad \frac{1}{N_c}\sum_{\mathbf{q}\in \mathrm{BZ}/2} g(D_{\mathbf{q}}) = \mu/2\\
&\text{C:} \quad \frac{1}{2}(F^\dagger\Gamma + h.c.) = -2\,|f|^2/\mu'\\
&\text{D:} \quad \frac{1}{2}\operatorname{tr} h = (\mu' - \mu)/2\\
&\text{E:} \quad \frac{1}{2}\Gamma^\dagger \bar{T}_{\mathbf{0}}\Gamma = |f|^2(\mu' - \mu - 2t)/\mu'^2\\
&\text{F:} \quad \frac{1}{2}\tilde{F}^\dagger Q M_{\mathbf{0}}^{-1} S Q^\dagger \tilde{F} = -|f|^2\,(\mu + 2t)/\mu'^2 \ .
\end{aligned}$$

In order to evaluate part B we need the matrix $M_{\mathbf{q}}$, which is given by

$$M_{\mathbf{q}} = \Lambda + SQ^{\dagger}\,\bar{T}_{\mathbf{q}}\,Q = \begin{pmatrix} -\mu - 2\,t\cos\mathbf{q} & 0 \\ 0 & \mu + 2\,t\cos\mathbf{q} \end{pmatrix} ,$$

where we used that

$$\bar{T}_{\mathbf{q}} = \begin{pmatrix} \bar{t}_{\mathbf{q}} & 0 \\ 0 & \bar{t}^{T}_{-\mathbf{q}} \end{pmatrix}$$

and $\bar{t}_{\mathbf{q}} = \bar{t}^{T}_{-\mathbf{q}} = \mu' - \mu - 2t\cos\mathbf{q}$. Since $M_{\mathbf{q}}$ is already diagonal we can readily evaluate part B as sum over the negative eigenvalues, which is $\mu + 2\,t\cos\mathbf{q}$, since $\mu < -2t$. When summing over half of the $\mathbf{q}$ values the second term of the eigenvalue containing $\cos\mathbf{q}$ is zero. For the calculation of part F we need the inverse of $M_{\mathbf{0}}$, which is simply

$$M_{\mathbf{0}}^{-1} = \begin{pmatrix} -\frac{1}{\mu+2t} & 0 \\ 0 & \frac{1}{\mu+2t} \end{pmatrix} ,$$

and $\tilde{F}$, which reads

$$\tilde{F} = F + \bar{T}_{\mathbf{0}}\,\Gamma = (\mu + 2t)/\mu' \begin{pmatrix} f \\ f^{*} \end{pmatrix} .$$

Collecting all terms yields the grand potential $\Omega = 0$, which is identical to the result obtained from the direct calculation.

B. Notation and conventions for the extended self-energy functional approach

B.1. Matrix notation

B.1.1. General

In order to simplify our notation we omit time arguments, whenever this does not cause ambiguities. Therefore, two-point functions such as Green's functions, self-energies, etc. are interpreted as matrices in Nambu, orbital, and τ space. One-point objects such as $\mathcal{A}$ ($\bar{\mathcal{A}}$) are interpreted as column (row) vectors in the same space. Matrix-matrix and vector-matrix products are understood throughout, whereby internal τ variables are considered to be integrated over. In addition, the transposing operator "^{T}" also acts on time variables. Traces Tr contain an integral over τ and a trace tr over orbital indices, i. e., $\mathrm{Tr}\, M \equiv \beta^{-1}\,\mathrm{tr}\int_0^\beta d\tau M(\tau, \tau + 0^+)$, where the 0^+ leads to the well known convergence factor $e^{i\omega_n 0^+}$ in Matsubara space.

(Functional) derivatives with respect to matrices are defined "transposed":

$$\left(\frac{\delta \hat{X}}{\delta M}\right)_{ij}(\tau, \tau') \equiv \frac{\delta \hat{X}}{\delta M_{ji}(\tau', \tau)} \,.$$

Finally, there are two types of products between row (in the form $\bar{v}$) and column (u) vectors, depending on the order: On the one hand the product $\bar{v}u$ produces a scalar (all indices are summed/integrated over). On the other hand, inverting the order, as in $u\bar{v}$ gives a matrix, as indices are "external" and, thus, not summed over.

B.1.2. Trace in τ and in Matsubara space

In τ space we have

$$\mathrm{Tr}\, M = \beta^{-1}\mathrm{tr}\int_0^\beta d\tau\ M(\tau, \tau + 0^+) \,.$$

The transformation of $M(\tau, \tau')$ to Matsubara space is defined as

$$M(\tau, \tau') \equiv \beta^{-1}\sum_{n,n'} M(\omega_n, \omega'_n) e^{-i\omega_n \tau + i\omega'_n \tau'} \,.$$

The inverse transformation reads

$$M(\omega_n, \omega_n') = \beta^{-1} \int d\tau d\tau' M(\tau, \tau') e^{i\omega_n \tau - i\omega_n' \tau'} \ .$$

Combining the equations above, the trace becomes

$$\begin{aligned} \mathrm{Tr}\, M &= \mathrm{tr} \int_0^\beta d\tau \beta^{-2} \sum_{n,n'} M(\omega_n, \omega_n') e^{-i(\omega_n - \omega_n')\tau + i\omega_n' 0^+} \\ &= \beta^{-1} \sum_n \mathrm{tr} M(\omega_n, \omega_n) e^{i\omega_n 0^+} \ . \end{aligned}$$

B.1.3. Logarithm

There are some subtle points concerning logarithms of two-point functions. Although these issues are immaterial for the final result, we prefer to specify them in detail.

The logarithm of G considered as a matrix in the continuum variable τ is defined up to an infinite constant which depends on the the discretization step δ (see below). In addition, the trace of the logarithm carried out in Matsubara space diverges as well (despite the convergence factor $e^{i\omega_n 0^+}$). The usual result presented in the literature (see, for instance Ref. [71]) implicitly assumes that an infinite constant has been subtracted. In order to avoid these undetermined infinite terms, we subtract them explicitly at the outset with the help of the "infinite energy" Green's function

$$\begin{aligned} G_\infty(\tau, \tau') &= \beta^{-1} \sum_n G_\infty(\omega_n) e^{-i\omega_n(\tau - \tau')} \\ G_\infty(\omega_n) &= \mathbb{1} \frac{1}{i\omega_n - E} \ , \end{aligned}$$

where it is understood that the $E \to +\infty$ limit is taken at the end of the calculation. This choice guarantees, for example, that $\mathrm{Tr} \ln G/G_\infty$, where G is the Green's function in normal (i.e. not Nambu) notation, vanishes in the limit $\mu \to -\infty$, where μ is the chemical potential.

The Fourier transform defined in App. B.1.2 allows to define the logarithm of G in τ space, apart from an infinite multiplicative constant, which originates from the fact that the Fourier transformation is not and cannot be normalized in the continuum limit. In particular,

$$\begin{aligned} [\ln(-G)](\tau, \tau') &= \beta^{-1} \sum_{n,n'} [\ln(-G)](\omega_n, \omega_n') e^{-i\omega_n \tau + i\omega_n' \tau'} \\ &= \beta^{-1} \sum_n \ln\left[-G(\omega_n)\right] e^{-i\omega_n(\tau - \tau')} \ . \end{aligned}$$

B.2. Symmetry of Green's functions and other two-point functions

The action in Eq. (2.66) is invariant under the transformation $G_0 \to (\mathcal{T} G_0^T \mathcal{T})$, where the transposing operator "^{T}" also acts on time variables and $\mathcal{T}$ is defined in Eq. (2.69). This is due to the fact that

$$\bar{A}(\tau') G_0^{-1}(\tau', \tau) A(\tau) \;=\; A(\tau')^T \mathcal{T} G_0^{-1}(\tau', \tau) \mathcal{T} \bar{A}(\tau)^T \;=\; \bar{A}(\tau) (\mathcal{T} G_0^{-1}(\tau', \tau)^T \mathcal{T}) A(\tau') \;.$$

Therefore, we choose G_0 to obey the symmetry

$$G_0 = (\mathcal{T} G_0^T \mathcal{T}) \;. \tag{B.1}$$

The same symmetry is obeyed by other two-point functions, such as the interacting Green's function G, the self-energy Σ, and their inverse.

In principle, this redundancy renders relations such as Eq. (2.76) non invertible. In order to avoid this, we adopt the convention that functional inversions are carried out within the subspace of two-point functions obeying the relation Eq. (B.1). In addition, we adopt the following convention for functional derivatives of an arbitrary functional $\hat{\Xi}$ with respect to a two-point function X:

$$\frac{\delta \hat{\Xi}}{\delta X} \to \frac{1}{2} \left(\frac{\delta \hat{\Xi}}{\delta X} + \frac{\delta \hat{\Xi}}{\delta \mathcal{T} X^T \mathcal{T}} \right) \;.$$

B.3. Continuum limit of the functional integral

In principle, the expression Eq. (2.71) should be understood such that adjoint fields $\bar{a}$ are evaluated at a later imaginary time $\tau + \delta$, whereby δ is the width of the discretization mesh of the interval $(0, \beta)$. The continuum limit $\delta \to 0$ should be taken after having carried out the functional integration, see, e.g. Ref. [267]. Taking this limit at the outset amounts to neglecting the so-called "contribution from infinity". [268, 269] This can be achieved by effectively replacing the normal-ordered Hamiltonian with a "symmetrically ordered" one, which is suitably symmetrized among possible permutation of creation and annihilation operators. [270] In particular, for the noninteracting part, this amounts to replacing the operator expression $a^\dagger a$ by $\frac{1}{2}(a^\dagger a + a a^\dagger) = a^\dagger a + \frac{1}{2}$. Therefore, we should keep in mind that the grand-potential $\widetilde{\Omega}_s$ corresponds to such a symmetrized Hamiltonian.

C. Nonequilibrium Variational Cluster Approach

C.1. Connection to (cellular) Dynamical Mean-Field Theory

Here, we show that the self-consistent condition (2.104) provides a bridge to (cellular) DMFT, when an increasing number of noninteracting bath sites with appropriate parameters and occupations is included in the cluster Hamiltonian. Notice that these are "auxiliary" baths and are not related to the leads. Concretely, this is achieved by introducing into the variational Hamiltonian Δh a coupling of the central region with a set of uncorrelated bath sites with appropriate energies, hybridizations $v_n^{\pm}$, and occupations (see below). The hybridizations $v_n^{\pm}$ and the energies are therefore "included" in h, but "subtracted perturbatively," from the target Hamiltonian H. Their parameters are determined variationally via (2.104).

Now, since g_{0cc} is cluster-local, a solution to (2.104) is obviously given by (2.103). However, this solution can generally not be obtained with a finite number of parameters. As in usual equilibrium (cellular) DMFT [62] (2.103) can thus be solved via an iterative procedure defined by

$$\begin{aligned} g_{0cc,new}^{-1} &= (\mathcal{P}(G_{cc}))^{-1} + \Sigma_h \\ \Sigma_h &= g_{0cc,old}^{-1} - g_{cc}^{-1} \,. \end{aligned} \tag{C.1}$$

It is, thus, sufficient to show that an arbitrary $g_{0cc,new}$ can be obtained by coupling the cluster to a noninteracting bath with suitably chosen bath parameters. For the retarded and advanced Green's functions, the procedure is the same as in equilibrium. The Keldysh part is slightly more complicated. In order to show that an arbitrary $g_{0cc,new}$ can be realized, one introduces the hybridization function

$$\Delta(\omega) = \begin{pmatrix} \Delta^R(\omega) & \Delta^K(\omega) \\ 0 & \Delta^A(\omega) \end{pmatrix} \,, \tag{C.2}$$

where the Δ^R, Δ^A, and Δ^K are matrices in the cluster sites. Similarly to equilibrium DMFT $g_{0cc,new}$ is expressed as

$$g_{0cc,new}^{-1} = g_{0cc,0}^{-1} - \Delta(\omega) \,. \tag{C.3}$$

Here, $g_{0cc,0}^{-1}$ is the "bare" noninteracting cluster Green's function, i. e., the one with neither baths nor variational parameters.

An arbitrary (steady-state) $\Delta(\omega)$ can be produced by coupling the central region to an appropriate bath in the following way. The retarded (and advanced) part are obtained as in equilibrium DMFT [62] by coupling to a bath with spectral function $A_{bath}(\omega)$ given by

$$A_{bath}(\omega) = -\frac{1}{\pi} \operatorname{Im} \Delta^R(\omega) \ , \tag{C.4}$$

($\operatorname{Re} \Delta^R$ is fixed by Kramers-Kronig relations). For cellular DMFT, all spectral functions here $\Delta, A, \cdots$ are matrices in cluster sites. Therefore, Im is understood as the antihermitian part, Re as the hermitian part of such matrices. The $v_n^{\pm}$ are column vectors in cluster sites On the other hand, the Keldysh part is generated by splitting the bath defined by (C.4) into two baths, a full ($\mu = \infty$) and an empty ($\mu = -\infty$) one, respectively. Their spectral functions are denoted by $A^+_{bath}(\omega)$ and $A^-_{bath}(\omega)$, respectively, and should obviously fulfill the condition

$$A_{bath}(\omega) = A^+_{bath} + A^-_{bath} \ . \tag{C.5}$$

Since the Fermi functions of the two baths are 1 and 0, respectively, the Keldysh part $\Delta^K(\omega)$ is given by (Δ^K is anti-hermitian)

$$\Delta^K(\omega) = -2i\pi \ B_{bath}(\omega) \equiv -2i\pi \ \left(A^-_{bath}(\omega) - A^+_{bath}(\omega) \right) \ . \tag{C.6}$$

This fixes the two spectral functions to be

$$A^{\mp}_{bath}(\omega) = \frac{A_{bath}(\omega) \pm B_{bath}(\omega)}{2} \ . \tag{C.7}$$

As usual, the two baths spectral functions $A_{bath,\pm}(\omega)$ are realized by coupling the central region with a set of noninteracting sites with energies $\epsilon_n^{\pm}$ and hybridizations $v_n^{\pm}$, fixed by

$$A^{\pm}_{bath}(\omega) = \sum_n v_n^{\pm} v_n^{\pm\dagger} \delta(\omega - \epsilon_n^{\pm}) \ . \tag{C.8}$$

C.2. The Keldysh formalism

In this section, we review the Keldysh Green's function formalism, which is the basis of the nonequilibrium VCA. To this end, we follow Ref. [87], but provide much more technical details.

The physical system is represented by a time independent Hamiltonian

$$\hat{H} = \hat{H}_0 + \hat{V} \ ,$$

where $\hat{H}_0$ describes the free particles and $\hat{V}$ their mutual interactions. Initially, the physical system is in thermal equilibrium, where it is represented by the density matrix

$$\hat{\rho} = \frac{e^{-\beta \hat{H}}}{\operatorname{tr} e^{-\beta \hat{H}}} \ .$$

The total nonequilibrium Hamiltonian is given by

$$\hat{\mathcal{H}} = \hat{H} + \hat{H}'(t) \ ,$$

where $\hat{H}'(t)$ is switched on at a certain time t_0, i. e., $\hat{H}'(t) = 0$ for $t < t_0$. The goal is to calculate expectation values of an operator $\hat{O}$:

$$\langle \hat{O}_{\mathcal{H}}(t) \rangle = \mathrm{tr}[\rho(H) O_{\mathcal{H}}(t)] \ .$$

Here we adopt the notation that the operator $\hat{O}$ is transformed into the "interaction picture" with respect to the Hamiltonian indicated in the subscript. In particular, we are interested in correlation functions of the form

$$G = \langle \mathrm{T}\, A_{\mathcal{H}}(t) B_{\mathcal{H}}(t') \rangle \ .$$

An extension to a larger number of operators is straight forward.

Let us first assume that the initial state is a pure state $|\phi_0\rangle$, then

$$G = \langle \infty | \,\mathrm{T}\, S(\infty,\, t_0) A_H(t) B_H(t') | \phi_0 \rangle \ ,$$

where we introduced the S-operator $S(\infty,\, t_0) = \exp[-i \int_{t_0}^{\infty} dt'' H'_H(t'')]$ and $|\infty\rangle$ is the state in which the system evolves after an infinite propagation time. More precisely, it is not necessary to propagate to $t = \infty$, rather $t = \max(t, t')$ is sufficient. Since we want to evaluate expectation values as in equilibrium of the form $\langle \phi_0 | \cdots | \phi_0 \rangle$ we insert judiciously an S-operator

$$G = \langle \phi_0 | S(t_0, \infty) \,\mathrm{T}\, S(\infty,\, t_0) A_H(t) B_H(t') | \phi_0 \rangle \ .$$

In order to adopt the time order convention from equilibrium, one introduces a time contour c, which starts and ends at t_0, see Fig. C.1 (a). To lighten notation, we introduce a collective index containing time and position on the contour

$$\tau = (t\, c_a) \ ,$$

where $c_a = c_{\rightarrow}$ ($c_a = c_{\leftarrow}$) corresponds to the upper (lower) contour. With that we can also introduce the contour time ordering operator

$$\mathrm{T}_c(A(\tau), B(\tau')) = \begin{cases} A(\tau) B(\tau') & \text{for} \quad \tau >_c \tau' \\ -\epsilon B(\tau') A(\tau) & \text{for} \quad \tau <_c \tau' \end{cases}$$

where $\tau >_c \tau'$ means that τ appears after τ' when following the contour c and $\epsilon = 1$ ($\epsilon = -1$) for fermion (boson) operators. Using this definition we write

$$\begin{aligned} G &= \langle \phi_0 | \,\mathrm{T}_c\, S(t_0 c_{\leftarrow}, \infty) S(\infty,\, t_0 c_{\rightarrow}) A_H(t c_{\rightarrow}) B_H(t' c_{\rightarrow}) | \phi_0 \rangle \\ &= \langle \phi_0 | \,\mathrm{T}_c\, S(t_0 c_{\leftarrow},\, t_0 c_{\rightarrow}) A_H(t c_{\rightarrow}) B_H(t' c_{\rightarrow}) | \phi_0 \rangle \ . \end{aligned}$$

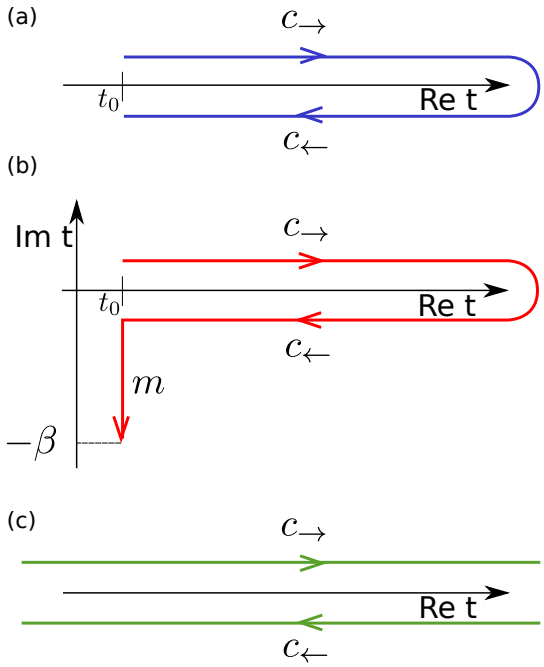

Figure C.1.: (a) Closed path contour, (b) interaction contour, and (c) Keldysh contour, see [87].

Generally, the fields A_H and B_H do not have to be restricted to the upper contour $c_\rightarrow$, and thus in general

$$G = \langle\phi_0|\,\mathrm{T}_c\, S^c A_H(\tau)B_H(\tau')|\phi_0\rangle \ ,$$

where $S^c = S(t_0 c_\leftarrow, t_0 c_\rightarrow)$. Generalizing this expression to a thermal initial state we have

$$\begin{aligned} G &= \frac{\langle \mathrm{T}_c\, S^c A_H(\tau)B_H(\tau')\rangle_H}{\langle \mathrm{T}_c\, S^c\rangle_H} \\ &= \frac{\mathrm{tr}[e^{-\beta H}\,\mathrm{T}_c\, S^c A_H(\tau)B_H(\tau')]}{\mathrm{tr}[e^{-\beta H}\,\mathrm{T}_c\, S^c]} \ . \end{aligned}$$

In order to take advantage of Wick's theorem and with that of the whole Feynman diagram apparatus, we have to transform into the interaction picture with respect to the free Hamiltonian $\hat{H}_0$. Analogously, to the equilibrium case, we assume that the interaction $\hat{V}$ is switched on adiabatically. Formally, one can go through the steps presented above. Using the identity

$$e^{-\beta H} = e^{-\beta H_0}\,\mathrm{T}\, e^{-i\int_{t_0-i\beta}^{t_0} dt' V_{H_0}(t')}$$

one finds

$$G = \frac{\langle \mathrm{T}_c\, S^{c_\beta} S^c A_{H_0}(\tau) B_{H_0}(\tau')\rangle_0}{\langle \mathrm{T}_c\, S^{c_\beta} S^c A_{H_0}(\tau) B_{H_0}(\tau')\rangle_0} = \frac{\mathrm{tr}[e^{-\beta H_0}\, \mathrm{T}_c\, S^{c_\beta} S^c A_{H_0}(\tau) B_{H_0}(\tau')]}{\mathrm{tr}[e^{-\beta H_0}\, \mathrm{T}_c\, S^{c_\beta} S^c]},$$

where

$$S^c = e^{-i\int_c dt'' H'_{H_0}(t'')}$$
$$S^{c_\beta} = e^{-i\int_{c_\beta} dt'' V_{H_0}(t'')}$$

and the contour c_β shown in Fig. C.1 (b) also contains the imaginary Matsubara branch m going from $t_0 - i\beta$ to t_0. Sending $t \to -\infty$ and neglecting the Matsubara branch corresponds to neglecting initial correlations. Extending the contour also to $t \to \infty$ yields the Keldysh contour, see Fig. C.1 (c), which is used in nonequilibrium VCA, where we are mainly interested in evaluating single-particle Green's functions $G(r, r'|\tau, \tau')$ with $A(\tau) = a(r, \tau)$ and $B(\tau') = \bar{a}(r', \tau')$, which are the fields corresponding to single-particle annihilation and creation operators $\hat{a}_r$ and $\hat{a}^\dagger_{r'}$, respectively. The fields $a(r, \tau)$ and $\bar{a}(r', \tau')$ can be associated with the contour $c_\rightarrow$ and $c_\leftarrow$. Therefore, it is convenient to represent the contour ordered Green's function by 2×2 Keldysh matrices, i. e.,

$$G(r, r'|\tau, \tau') \to \hat{G}(r, r'|t, t') = \begin{pmatrix} G_{11} & G_{12} \\ G_{21} & G_{22} \end{pmatrix}$$

with

$$\begin{aligned} G_{11}(t, t') &= \langle \mathrm{T}\, a(r, t)\bar{a}(r', t')\rangle \\ G_{12}(t, t') &= \langle \bar{a}(r', t')a(r, t)\rangle \\ G_{21}(t, t') &= \langle a(r, t)\bar{a}(r', t')\rangle \\ G_{22}(t, t') &= \langle \tilde{\mathrm{T}} a(r, t)\bar{a}(r', t')\rangle \end{aligned} \tag{C.9}$$

where $\tilde{\mathrm{T}}$ is the anti-time-ordering operator. In VCA the Green's functions dressed inter-cluster scattering T, have to be evaluated, which amounts to calculating Feynman diagrams as indicated in Fig. C.2, where the integration over internal times are evaluated over the Keldysh contour c_K. Here, we derive the representation of a single potential scatterer T in Keldysh space. To this end, we explicitly recast the time integration of the first order contribution in matrix form (neglecting for simplicity the trivial spatial

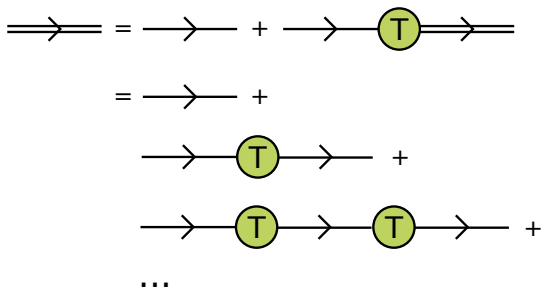

Figure C.2.: Diagrammatic expansion of the renormalization of the Green's function due to a potential scatterer T, green bubble. The single horizontal line represents the bare Green's function and the double horizontal line the dressed Green's function.

dependence)

$$\begin{aligned} G^{(1)} &= \int_{c_K} dt'' G(\tau,\tau'')T(\tau'')G(\tau'',\tau') \\ &= \int_{-\infty}^{\infty} dt'' G(tc,t''c_{\rightarrow})T(t''c_{\rightarrow})G(t''c_{\rightarrow},t'c') \\ &+ \int_{\infty}^{-\infty} dt'' G(tc,t''c_{\leftarrow})T(t''c_{\leftarrow})G(t''c_{\leftarrow},t'c') \\ &= \int_{-\infty}^{\infty} dt'' G(tc,t''c_{\rightarrow})T(t''c_{\rightarrow})G(t''c_{\rightarrow},t'c') \\ &- \int_{-\infty}^{\infty} dt'' G(tc,t''c_{\leftarrow})T(t''c_{\leftarrow})G(t''c_{\leftarrow},t'c') \ . \end{aligned} \tag{C.10}$$

In matrix form this relation is given by

$$\hat{G}^{(1)} = \hat{G}\hat{T}\hat{G} \ , \tag{C.11}$$

where we introduced

$$\hat{T} = \begin{pmatrix} T & 0 \\ 0 & -T \end{pmatrix} \ .$$

This can be checked by explicitly calculating the product

$$\hat{G}^{(1)} = \begin{pmatrix} G_{11}TG_{11} - G_{12}TG_{21} & G_{11}TG_{12} - G_{12}TG_{22} \\ G_{21}TG_{11} - G_{22}TG_{21} & G_{21}TG_{12} - G_{22}TG_{22} \end{pmatrix} \ ,$$

and comparing it to Eq. (C.10).

Only three of the four Green's functions G_{11}, G_{12}, G_{21}, and G_{22} defined in Eq. (C.9), are linear independent. Therefore it is convenient to rotate them, such that they are represented by an upper triangular matrix. This can be achieved by the transformation

$$G(r,r'|t,t') = L\hat{\tau}_3\hat{G}L^{\dagger} \ , \tag{C.12}$$

where $L = (\hat{\tau}_0 - i\hat{\tau}_2)$ and $\hat{\tau}_i$ are the Pauli matrices. Explicitly, one finds

$$G(r, r'|t, t') = \begin{pmatrix} G^R & G^K \\ 0 & G^A \end{pmatrix} ,$$

with the retarded G^R, advanced G^A, and Keldysh $G^K = G_{11} + G_{22}$ Green's functions, see also Eq. (2.95). Having rotated the Green's functions, the potential scatterer $\hat{T}$ has to be evaluated in the rotated Keldysh space. Using the transformation Eq. (C.12), $L^\dagger L = \hat{\tau}_0$, and $\hat{\tau}_3^2 = \hat{\tau}_0$, we rewrite Eq. (C.11)

$$\begin{aligned} \hat{G}^{(1)} &= \hat{G}\hat{T}\hat{G} \\ L\hat{\tau}_3\hat{G}^{(1)}L^\dagger &= L\hat{\tau}_3\hat{G}\ L^\dagger L\ \hat{T}\ \hat{\tau}_3\hat{\tau}_3\ \hat{G}L^\dagger \\ L\hat{\tau}_3\hat{G}^{(1)}L^\dagger &= L\hat{\tau}_3\hat{G}L^\dagger\ L\hat{T}\hat{\tau}_3L^\dagger\ L\hat{\tau}_3\hat{G}L^\dagger \\ G^{(1)} &= G\bar{T}G\ , \end{aligned}$$

where

$$\bar{T} \equiv L\hat{T}\hat{\tau}_3L^\dagger = \begin{pmatrix} T & 0 \\ 0 & T \end{pmatrix}$$

is simply a matrix proportional to the identity.

C.3. Evaluation of observables

Here, we give a brief sketch how observables can be evaluated from the equal time Keldysh Green's function. As an example, we consider the current operator, which is defined as

$$\hat{j} = iV(c_x^\dagger c_y - c_y^\dagger c_x)\ .$$

Its expectation value is obtained from the Keldysh Green's function

$$\begin{aligned} iG^K_{xy}(t=0) &= \langle c_x^\dagger c_y\rangle + \eta\langle c_y c_x^\dagger\rangle = 2\langle c_x^\dagger c_y\rangle + \eta\delta_{xy} \\ \langle c_x^\dagger c_y\rangle &= \frac{i}{2}G^K_{xy}(t=0) - \eta\frac{1}{2}\delta_{xy} \\ \langle c_y^\dagger c_x\rangle &= \langle c_x^\dagger c_y\rangle^* \\ \langle\hat{j}\rangle &= -\frac{V}{2}[G^K_{xy}(t=0) - G^K_{xy}(t=0)^*] \\ &= -V\,\mathrm{Re}\,G^K_{xy}(t=0) \end{aligned}$$

Similarly, the particle density can be evaluated from

$$n(x) = \langle c_x^\dagger c_x\rangle = \frac{i}{2}G^K_{xx}(t=0) - \eta\frac{1}{2}\,.$$

In the steady-state, the $t = 0$ Keldysh Green's function is obtained from the frequency integration

$$G^K_{xy}(t=0) = \int d\omega G^K_{xy}(\omega) \; .$$

C.4. Self-consistency condition

Here, we first indicate that the Pauli matrix $\hat{\tau}_1$ appears quite naturally in the self-consistency condition, Eq. (2.104), from the Keldysh notation and then show that the self-consistency condition is a measure for the difference between cluster and lattice expectation values.

C.4.1. Appearance of the Pauli matrix $\hat{\tau}_1$

Starting with time- and anti-time-ordered Green's functions, the trace in $\tau = (t, c)$ space is positive for both $c = \rightarrow$ and $c = \leftarrow$, see App. C.2. Thus in the self-consistency condition, Eq. (2.104), integrals of the form

$$\int d\tau d\tau' \, \mathrm{sign}\, \tau \, \mathrm{sign}\, \tau' \underbrace{(\tilde{G}_{\alpha\beta}(\tau,\tau') - \tilde{g}_{\alpha\beta}(\tau,\tau'))}_{\tilde{\Delta}(\tau,\tau')} \tag{C.13}$$

appear, where α, β are cluster-orbital indices. $\tilde{G}_{\alpha\beta}$ and $\tilde{g}_{\alpha\beta}$ are matrices in the not yet rotated Keldysh space

$$\tilde{\Delta} = \begin{pmatrix} G^c - g^c & G^> - g^> \\ G^< - g^< & G^c - g^c \end{pmatrix} \; .$$

The integral (C.13) can be cast into the form

$$\int dt dt' \hat{\tau}_3 \hat{\tau}_3 \tilde{\Delta}(t,t') \, .$$

In the convention used in the main text $\tilde{\Delta}(t,t')$ is rotated such that it is of upper triangular form

$$\Delta = L \hat{\tau}_3 \tilde{\Delta} L^\dagger \; ,$$

with

$$\Delta = \begin{pmatrix} G^R - g^R & G^K - g^K \\ 0 & G^A - g^A \end{pmatrix} \; , \tag{C.14}$$

see App. C.2 for details on the rotation L. Employing this relation and writing the integral as a trace gives

$$\mathrm{Tr}\, \hat{\tau}_3 \hat{\tau}_3 \tilde{\Delta}(t,t') = \mathrm{Tr}\, \hat{\tau}_3 \hat{\tau}_3 \tilde{\Delta}(t,t') L^\dagger L = \mathrm{Tr} \underbrace{L \hat{\tau}_3}_{\hat{\tau}_1 L} \hat{\tau}_3 \tilde{\Delta}(t,t') L^\dagger = \mathrm{Tr}\, \hat{\tau}_1 \underbrace{L \hat{\tau}_3 \tilde{\Delta}(t,t') L^\dagger}_{\Delta} = \mathrm{Tr}\, \hat{\tau}_1 \Delta \; ,$$

which indicates that the form of the self-consistency equation (2.104) quite naturally results from Keldysh representation.

C.4.2. Self-consistent calculation of cluster and lattice expectation values

Using Eq. (C.14), we rewrite Eq. (2.104) as

$$\int \frac{d\omega}{2\pi} \operatorname{Tr} \hat{\tau}_1 \Delta \frac{\partial \left(g_{0cc}\right)^{-1}}{\partial \mathbf{p}} = 0 \; .$$

An explicit evaluation of the trace over the Keldysh indices gives

$$\int \frac{d\omega}{2\pi} \operatorname{Tr} \left(g^K_{cc} - G^K_{cc}\right) \frac{\partial \left(g^A_{0cc}\right)^{-1}}{\partial \mathbf{p}} = 0 \; .$$

Here we show that the interpretation of this equation is that $\mathbf{p}$ is a set of variational parameters, whose conjugate operators $\partial h_0 / \partial \mathbf{p}$ are determined self-consistently. The advanced Green's function of the noninteracting central region is

$$(g^A_{0,ij})^{-1} = (\omega + i0^+)\delta_{ij} - h_{0ij} \; ,$$

where h_{0ij} are the single particle terms, which contain both physical parameters and variational parameters. Thus the partial derivative

$$\frac{\partial \left(g^A_{0,ij}\right)^{-1}}{\partial \, p_{\alpha\beta}} = -\delta_{\alpha i}\delta_{\beta j}$$

selects certain contributions from $\left(g^K_{cc} - G^K_{cc}\right)$ labeled by $\alpha\beta$. From the definition of the Keldysh Green's function

$$iG^K_{\alpha\beta} = iG^<_{\alpha\beta} + iG^>_{\alpha\beta} = \langle c_\alpha(t) c^\dagger_\beta(0)\rangle + \eta \langle c^\dagger_\beta(0) c_\alpha(t)\rangle \; ,$$

we obtain the relation between steady-state expectation values of one-particle correlation functions and the equal time Keldysh Green's functions, which for the physical system is given by

$$iG^K_{\alpha\beta} = 2\eta \langle c^\dagger_\beta c_\alpha \rangle_{\mathrm{VCA}} + \delta_{\alpha\beta}$$

and for the reference system by

$$ig^K_{\alpha\beta} = 2\eta \langle c^\dagger_\beta c_\alpha \rangle_{\mathrm{Cl}} + \delta_{\alpha\beta} \; .$$

Thus, the self-consistency condition Eq. (2.104) can be interpreted as a measure for the difference between certain cluster and lattice (VCA) expectation values of the conjugate operators slected by the variational parameters $\mathbf{p}$.

D. Light-Matter systems

D.1. Properties of the VCA Green's function

Here, we will derive some properties of the VCA Green's function for polaritons. To begin with, we define new operators $d^\dagger_{J,r,\tilde{\mathbf{k}}}$ with $d^\dagger_{1,r,\tilde{\mathbf{k}}} \equiv a^\dagger_{r,\tilde{\mathbf{k}}}$ and $d^\dagger_{2,r,\tilde{\mathbf{k}}} \equiv \sigma^+_{r,\tilde{\mathbf{k}}}$, where r stands for the site number within the clusters and $\tilde{\mathbf{k}}$ is the wave vector of the first Brillouin zone of the superlattice. The VCA Green's function will still be diagonal in the latter index due to the periodicity of the clusters. The spectral representation of the cluster Green's function

$$G'_{IJ}(\tilde{\mathbf{k}},\,\omega) \equiv\ll d_{I,r,\tilde{\mathbf{k}}};d^\dagger_{J,s,\tilde{\mathbf{k}}} \gg_\omega$$

can be written in the compact form using the so-called Q-matrices [53, 54]

$$G' = Q\, D'_\omega S\, Q^\dagger \ .$$

Here, Q is a $M \times K$ matrix, where M is twice the number of cluster sites (the factor 2 stems from the two species of operators) and $K = K_p + K_h$, where K_p and K_h is the dimension of the Hilbert space for $N_p + 1$ and $N_p - 1$ particles, respectively. The Q-matrix is defined as follows

$$Q_{I,r;\nu} = \begin{cases} \langle\psi_0|\, d_{I,r,\mathbf{k}}\, |\psi_\nu^{N_p+1}\rangle & \text{for } \nu \le K_p \\ \langle\psi_0|\, d^\dagger_{I,r,\mathbf{k}}\, |\psi_{\nu-K_p}^{N_p-1}\rangle & \text{for } \nu > K_p \end{cases} .$$

The diagonal matrix $D'_\omega = \mathrm{diag}(\omega - \omega'_\nu)^{-1}$ contains the individual poles ω'_ν of the cluster and $S = \mathrm{diag}(s_\nu)$ is a diagonal sign matrix with $s_\nu = +1$ for particle excitations ($\omega'_\nu > 0$) and $s_\nu = -1$ for hole excitations ($\omega'_\nu < 0$). The VCA Green's function in Q-matrix representation for bosons [54] reads

$$G(\tilde{\mathbf{k}},\omega) = Q\, X\, D_\omega\, X^{-1}\, S\, Q^\dagger \ , \tag{D.1}$$

where $D_\omega = \mathrm{diag}(\omega - \omega_\nu)^{-1}$ is the diagonal matrix of the individual poles at the VCA energies. These energies and the corresponding eigenvector matrix X are determined via the generalized eigenvalue problem

$$\underbrace{\left(\mathrm{diag}(s_\nu\, \omega'_\nu) + Q^\dagger\, V\, Q\right)}_{\equiv M} X = S\, X \Delta \ ,$$

where $V = H_0 - H'_0$ is the difference of the matrices of the single-particle part of the Hamiltonian for the original and the reference system (i. e., the cluster).

A general feature of such eigenvalue equations for Hermitian matrices M is that both $X^\dagger M X$ and $X^\dagger S X \equiv \mathrm{diag}(\kappa_\nu^{-1})$ are diagonalized, but X is not unitary. We can exploit this fact as follows

$$G(\tilde{\mathbf{k}}, \omega) = Q X D_\omega \underbrace{X^{-1} S (X^{-1})^\dagger}_{\equiv D_\kappa} X^\dagger Q^\dagger .$$

The matrix $D_\kappa = (X^\dagger S X)^{-1}$ is diagonal as we just discussed and can be combined with D_ω resulting in

$$\begin{aligned} G(\tilde{\mathbf{k}}, \omega) &= Q X \tilde{D}_\omega (Q X)^\dagger \\ (\tilde{D}_\omega)_{\nu\nu'} &= \delta_{\nu,\nu'} \frac{\kappa_\nu}{\omega - \omega_\nu} . \end{aligned}$$

Moreover, the pole strengths κ_ν are real since

$$\begin{aligned} \kappa_\nu^{-1} &= (X^\dagger S X)_{\nu\nu} \\ &= \sum_\mu s_\mu |X_{\nu\mu}|^2 . \end{aligned}$$

When the VCA parameters are determined consistently, the stability of the N_p-particle system requires that the sign of κ_ν coincides with the sign of the excitation energies ω_ν, like in the exact spectral representation.

So far the Green's function still depends on the intra cluster indices r, s. The purely $\mathbf{k}$-dependent Green's function is commonly obtained by Green's function-periodization [64, 73]. Invoking the periodization prescription yields the Green's function matrix merely in the indices I, J for the two particle species

$$G(\mathbf{k}, \omega) = \tilde{Q} X \tilde{D}_\omega X^\dagger \tilde{Q}^\dagger \tag{D.2}$$

$$\text{with} \quad \tilde{Q}_{I,\nu} = \frac{1}{N} \sum_r e^{-i \mathbf{k} \mathbf{x}_r} Q_{I,r;\nu} , \tag{D.3}$$

see also Eq. (3.27). Eq. (D.2) corresponds to the spectral representation of the exact Green's function and it allows to extract the VCA approximation of the many-body eigenstates of the infinite system, which are obviously a linear combination of the cluster eigenstates for both, particle and hole excitations.

As described in the text we need the integrated spectral density, i. e.,

$$\begin{aligned} A_{IJ}(\mathbf{k}, \Omega_\alpha) &= \int_{\Omega_\alpha} (-\frac{1}{\pi} \mathrm{Im}\ G_{IJ}(\mathbf{k}, \omega + i\eta))\, d\omega \\ &= \sum_{\nu,\, \omega_\nu(\mathbf{k}) \in \Omega_\alpha} (\tilde{Q} X)_{I,\nu}\, \kappa_\nu\, (\tilde{Q} X)_{J,\nu} . \end{aligned}$$

We readily recognize, that the integrated spectral density is either positive or negative definite, depending on whether the quasiparticle under consideration is of particle or

hole type. Equivalently, in the original representation

$$A_{IJ}(\mathbf{k},\,\Omega_\alpha) = \sum_{\nu,\,\omega_\nu(\mathbf{k})\in\Omega_\alpha} (\tilde{Q}\,X)_{I,\nu}(X^{-1}S\,\tilde{Q}^\dagger)_{\nu,J}\ .$$

For the polariton discussion it is convenient to suppress the minus sign arising in the hole case and we define the strictly positive integrated spectral densities as

$$\tilde{A}_{IJ}(\mathbf{k},\,\Omega_\alpha) \equiv |A_{IJ}(\mathbf{k},\,\Omega_\alpha)|\ . \tag{D.4}$$

D.2. Solution of the single-site problem

For zero-hopping strength $t = 0$ the JCL model can be solved exactly, as it reduces to a single-site problem, i. e., to the JC model. Including the chemical potential yields the single-site Hamiltonian

$$\hat{H}_S^{JCL} = \hat{H}^{JC} - \mu\,(a^\dagger\,a + \sigma^+\sigma^-)\ , \tag{D.5}$$

where we dropped the site index i. It can be evaluated with respect to the bare states $|n_p,\,s\rangle$, where n_p is the number of photons and $s \in \{\downarrow,\,\uparrow\}$. Next, we sketch the most important steps for solving the single-site JCL model. A detailed discussion can be found for example in Refs. [233] or [271]. As the JC Hamiltonian conserves the particle number the Hamiltonian $\hat{H}_S^{JCL}$ is block diagonal. Each block corresponds to a certain particle number n and thus we use the bare states $|n-1,\,\uparrow\rangle$ and $|n,\,\downarrow\rangle$ to evaluate the block, which yields

$$B_n = \begin{pmatrix} (n-1)\omega_c + \epsilon - \mu\,n & \sqrt{n} \\ \sqrt{n} & n\,\omega_c - \mu\,n \end{pmatrix}\ , \tag{D.6}$$

when using the coupling g as unit of energy. The eigenvalues of the block B_n are

$$E_{|n,\,\alpha\rangle} = n\,\omega_c - \frac{\Delta}{2} + \alpha\,q(n) - \mu\,n\ , \tag{D.7}$$

where $\alpha \in \{-,\,+\}$ and $q(n) = \sqrt{(\Delta/2)^2 + n}$. For a certain particle number n the energy $E_{|n,\,-\rangle}$ is always smaller than $E_{|n,\,+\rangle}$ and thus $E_{|n,\,-\rangle}$ is the ground state energy of the sector with n particles, i. e., of the block B_n. The eigenvectors $|n,\,\alpha\rangle$ of the matrix B_n are termed dressed states and are given by

$$|n,\,\alpha\rangle = u_{n\alpha}\,|n-1,\,\uparrow\rangle + v_{n\alpha}\,|n,\,\downarrow\rangle\ , \tag{D.8}$$

where $n > 0$, $(u_{n+},\,v_{n+}) \equiv (\sin\theta(n),\,\cos\theta(n))$ and $(u_{n-},\,v_{n-}) \equiv (\cos\theta(n),\,-\sin\theta(n))$ with the following relations

$$\sin\theta(n) = \sqrt{(q(n) - \Delta/2)/2q(n)}$$

and

$$\cos\theta(n) = \sqrt{(q(n) + \Delta/2)/2q(n)} \; .$$

An exception is the bare state $|0, \downarrow\rangle$, which forms a 1×1 block of zero particles and has the eigenvalue $E_{|0,\downarrow\rangle} = 0$, independently of the detuning Δ. According to the notation used in Eq. (D.8), we denote this state as $|0, -\rangle$. In order to obtain the phase boundary for zero hopping between two adjacent Mott lobes, the energies $E_{|n,-\rangle}$ and $E_{|n+1,-\rangle}$ have to be set equal. The energies of the states $|m, -\rangle$ are used, as the phase diagram is evaluated for the ground state. The comparison of the energies yields $(\mu - \omega_c) = q(n) - q(n+1)$ for the location of the phase boundary at zero hopping.

D.3. First-order degenerate perturbation theory

In this appendix we evaluate the results of first-order degenerate perturbation theory for the single-particle and single-hole excitation bands of the JCL model. To apply first-order degenerate perturbation theory the matrix elements of the perturbation $\hat{H}_1 = \sum_{ij} t_{ij}\, a_i^\dagger\, a_j$, where t_{ij} is the hopping matrix, have to be evaluated with respect to the degenerate states $|\Psi_p^{\alpha,\,l}\rangle$ and $|\Psi_h^{\alpha,\,l}\rangle$, see Eq. (3.24). As the hopping term $\hat{H}_1$ does not change the total particle number and does not effect the excitation α, the following two matrices have to be evaluated; one for single-particle excitations

$$(M_p^\alpha)_{ll'} \equiv \langle \Psi_p^{\alpha,\,l} | \hat{H}_1 | \Psi_p^{\alpha,\,l'} \rangle \tag{D.9}$$

and one for single-hole excitations

$$(M_h^\alpha)_{ll'} \equiv \langle \Psi_h^{\alpha,\,l} | \hat{H}_1 | \Psi_h^{\alpha,\,l'} \rangle \; . \tag{D.10}$$

Plugging Eq. (3.24a) in Eq. (D.9) yields

$$\begin{aligned}(M_p^\alpha)_{ll'} = \bigotimes_{\substack{\nu=1\\ \nu\neq l}}^{N} \langle n, -|_\nu \, \langle n+1, \, \alpha|_l \sum_{i,\,j} t_{ij}\, a_i^\dagger\, a_j \\ |n+1, \, \alpha\rangle_{l'} \bigotimes_{\substack{\nu'=1\\ \nu\neq l'}}^{N} |n, -\rangle_{\nu'} \; .\end{aligned} \tag{D.11}$$

Due to the orthogonality of the eigenvectors of sectors with different particle number, the conditions $i = l$ and $j = l'$ hold, which reduce the matrix elements to

$$\begin{aligned}(M_p^\alpha)_{ll'} &= t_{ll'} \, \langle n, -|_{l'} \, \langle n+1, \, \alpha|_l \, a_l^\dagger \, a_{l'} \, |n+1, \, \alpha\rangle_{l'} \, |n, -\rangle_l \\ &= t_{ll'} |\, \langle n+1, \, \alpha| \, a^\dagger \, |n, -\rangle \, |^2 \; .\end{aligned} \tag{D.12}$$

In the second step, we dropped the site index as the expectation value does not depend on the specific lattice site. The corrected matrix elements are thus the old ones with

renormalized hopping strength

$$\begin{aligned} -\tilde{t}_p^{\alpha} &\equiv -t|\,\langle n+1,\,\alpha|\,a^{\dagger}\,|n,\,-\rangle\,|^2 \\ &= -t|\sqrt{n}\,u_{n+1\alpha}\,u_{n-} + \sqrt{n+1}\,v_{n+1\alpha}\,v_{n-}|^2\,. \end{aligned} \tag{D.13}$$

Analogously, one obtains

$$(M_h^{\alpha})_{ll'} = t_{l'l}|\,\langle n-1,\,\alpha|\,a\,|n,\,-\rangle\,|^2 \tag{D.14}$$

for the matrix elements defined in Eq. (D.10). From that the renormalized hopping strength for single-hole excitations is evaluated as

$$-\tilde{t}_h^{\alpha} = -t|\sqrt{n-1}\,u_{n-1\alpha}\,u_{n-} + \sqrt{n}\,v_{n-1\alpha}\,v_{n-}|^2\,. \tag{D.15}$$

The eigenvalues of the matrices $M_{p/h}^{\alpha}$ are the first-order corrections and thus the corrected energies $\mathcal{E}_{|n\pm1,\,\alpha\rangle}(k)$ of the one-dimensional JCL model are given by

$$\mathcal{E}_{|n+1,\,\alpha\rangle}(k) = E_{|n+1,\,\alpha\rangle} - 2\,\tilde{t}_p^{\alpha}\cos k \text{ and} \tag{D.16a}$$

$$\mathcal{E}_{|n-1,\,\alpha\rangle}(k) = E_{|n-1,\,\alpha\rangle} - 2\,\tilde{t}_h^{\alpha}\cos k\,, \tag{D.16b}$$

respectively, where k is a wave vector of the first Brillouin zone. Within first-order degenerate perturbation theory we obtain

$$\begin{aligned} \omega_{p,1}^{\alpha} &= \mathcal{E}_{|n+1,\,\alpha\rangle}(k) - E_{|n,\,-\rangle} \\ &= (\omega_c - \mu) + \alpha\,q(n+1) + q(n) - 2\,\tilde{t}_p^{\alpha}\cos k \end{aligned} \tag{D.17}$$

for the single-particle excitation band and

$$\begin{aligned} \omega_{h,1}^{\alpha} &= E_{|n,\,-\rangle} - \mathcal{E}_{|n-1,\,\alpha\rangle}(k) \\ &= (\omega_c - \mu) - \alpha\,q(n-1) - q(n) + 2\,\tilde{t}_h^{\alpha}\cos k\,. \end{aligned} \tag{D.18}$$

for the singe-hole excitation band.

D.4. Polariton operators in the single-site limit

In this appendix, we want to analyze the polaritonic feature in the single-site limit for zero detuning.

In the single-site limit it is exactly possible to construct a polariton operator which, applied to the many-body eigenstate $|n,-\rangle$, generates the eigenstates $|n\pm1,\alpha\rangle$. The polaritonic weights follow from

$$\begin{aligned} &(\beta a^{\dagger} + \gamma\sigma^{+})\,|n,-\rangle = \\ &\quad= \frac{\beta\sqrt{n}-\gamma}{\sqrt{2}}\,|n,\uparrow\rangle - \beta\sqrt{\frac{n+1}{2}}\,|n+1,\downarrow\rangle \\ &\quad\stackrel{!}{=} |n+1,\alpha\rangle \\ &\frac{\beta_{p,n}^{\alpha}}{\gamma_{p,n}^{\alpha}} = \frac{1}{\alpha\sqrt{n+1}+\sqrt{n}} \end{aligned} \tag{D.19}$$

Here, we explicitly include the filling n as index. So the relative weights are $(\sqrt{n+1}+\sqrt{n})^{-1}$ for the upper band ($\alpha=+$) and $-(\sqrt{n+1}+\sqrt{n})$ for the lower band ($\alpha=-$). This means that in the lower band the weights have opposite sign and the polaritons are of predominant photonic character, while the opposite applies to the upper band. The modulus of relative weight is just the inverse, i. e., $|\beta^+/\gamma^+| = |\gamma^-/\beta^-|$.

Next, we study the hole case for $n > 1$

$$\begin{aligned}
&(\beta a + \gamma\sigma^-)\,|n,-\rangle = \\
&\quad = \beta\sqrt{\frac{n-1}{2}}\,|n-2,\uparrow\rangle + \frac{\gamma-\beta\sqrt{n}}{\sqrt{2}}\,|n-1,\downarrow\rangle \\
&\quad \stackrel{!}{=} |n-1,\alpha\rangle \\
&\frac{\beta^\alpha_{h,n}}{\gamma^\alpha_{h,n}} = \frac{1}{\sqrt{n}+\alpha\sqrt{n-1}}\,,
\end{aligned} \tag{D.20}$$

which is positive for both bands $\alpha = \pm$. Again we have the reciprocal property $\beta^+/\gamma^+ = \gamma^-/\beta^-$ and the lower band has predominantly photonic character, while the opposite is the case in the upper band.

Now we want to scrutinize the generalized eigenvalue problem of the Green's function. The single-site Green's function reads

$$\begin{aligned}
G^S_{IJ}(\omega) &= \sum_{\alpha=\pm} \frac{{}^p\mathrm{Q}_{I,\alpha}\,{}^p\mathrm{Q}^\dagger_{\alpha,J}}{\omega-\omega_{p,\alpha}} - \sum_{\alpha=\pm}\frac{{}^h\mathrm{Q}_{I,\alpha}\,{}^h\mathrm{Q}^\dagger_{\alpha,J}}{\omega-\omega_{h,\alpha}} \\
{}^p\mathrm{Q}_{I,\alpha} &= \langle n+1,\alpha|\,d_I^\dagger\,|n,-\rangle^* \\
{}^h\mathrm{Q}_{I,\alpha} &= \langle n-1,\alpha|\,d_I\,|n,-\rangle\ ,
\end{aligned}$$

where we introduced the operators $d_1 \equiv a$ and $d_2 \equiv \sigma^-$. For the single-particle term we obtain

$$\begin{aligned}
{}^p\mathrm{Q}_{1,\alpha} &= \langle n+1,\alpha|\,a^\dagger\,|n,-\rangle^* = \frac{1}{2}(\sqrt{n}-\alpha\sqrt{n+1}) \\
{}^p\mathrm{Q}_{2,\alpha} &= \langle n+1,\alpha|\,\sigma^+\,|n,-\rangle^* = -\frac{1}{2}\,.
\end{aligned}$$

With the definition $\mathbf{x}_\alpha = ({}^p\mathrm{Q}_{1,\alpha}, {}^p\mathrm{Q}_{2,\alpha})^T$ the integrated spectral density for the particle part can be expressed as

$$\tilde{A}_\alpha = \mathbf{x}_\alpha\,\mathbf{x}_\alpha{}^T\,.$$

The overlap matrix $S_p \equiv \langle d_I d_J^\dagger\rangle$ is readily obtained by the spectral theorem

$$S_p = \mathbf{x}_+\,\mathbf{x}_+{}^T + \mathbf{x}_-\,\mathbf{x}_-{}^T\,,$$

and the generalized eigenvalue problem for the polariton weights according to Eq. (3.19) reads

$$(1-\lambda)\,\mathbf{x}_\alpha\,\mathbf{x}_\alpha{}^T\,\tilde{\mathbf{z}}_\alpha = \lambda\,\mathbf{x}_{-\alpha}\,\mathbf{x}_{-\alpha}{}^T\,\tilde{\mathbf{z}}_\alpha\,.$$

The eigenvalues are zero and one. For the polariton weights we are interested in the latter. The corresponding eigenvector is simply given by the vector orthogonal to $\mathbf{x}_{-\alpha}$

$$\tilde{\mathbf{z}}_\alpha = \frac{1}{2}\begin{pmatrix} 1 \\ \sqrt{n} + \alpha\sqrt{n+1} \end{pmatrix} .$$

With that one obtains for the ratio of the weights

$$\frac{\beta^\alpha_{p,n}}{\gamma^\alpha_{p,n}} = \frac{1}{\sqrt{n} + \alpha\sqrt{n+1}} ,$$

which is in agreement with the exact result in Eq. (D.19).

Now we address the hole case, again for $n > 1$,

$$\begin{aligned} {}^h\mathrm{Q}_{1,\alpha} &= \langle n-1, \alpha |\, a \,| n, - \rangle = \frac{1}{2}(\sqrt{n-1} - \alpha\sqrt{n}) \\ {}^h\mathrm{Q}_{2,\alpha} &= \langle n+1, \alpha |\, \sigma^- \,| n, - \rangle = \alpha\frac{1}{2} . \end{aligned}$$

We proceed as in the particle case with the definition of ${\mathbf{x}_\alpha}^T = ({}^h\mathrm{Q}_{1,\alpha}, {}^h\mathrm{Q}_{2,\alpha})$. The remaining steps are the same as before and we end up with

$$\frac{\beta^\alpha_{h,n}}{\gamma^\alpha_{h,n}} = \frac{\alpha}{\sqrt{n-1} + \alpha\sqrt{n}} = \frac{1}{\sqrt{n} + \alpha\sqrt{n-1}} ,$$

which is also in agreement with the exact result, see Eq. (D.20). So we see that the determination of the polaritonic weight via the generalized eigenvalue problem is reasonable. In the single-site limit, the exact many-body eigenstates $|n \pm 1, \alpha\rangle$ can be generated correctly by suitable polariton operators acting on the state $|n, -\rangle$. The operators are, however, not universal, they depend on n and in the lattice case even on $\mathbf{k}$. On top of that, the polariton creation operator for holes is not the adjoint of the corresponding polariton creation operator of the particle type, or in other words its annihilation operator.

Acknowledgements

Studying in Graz over the last years has been a wonderful experience for me. I always enjoyed the stimulating and open-minded scientific environment, and I want to thank a lot of people making this period a success not only physics wise but also in terms of general life experiences.

First of all, I would like to thank my supervisor Prof. Wolfgang von der Linden who gave me the opportunity to continue working on these projects after the completion of my master thesis. I am deeply indebted to him and to Prof. Enrico Arrigoni, who both always have been patient and supportive when guiding me toward the goals of the many projects we accomplished together. Prof. Wolfgang von der Linden and Prof. Enrico Arrigoni sacrificed large amounts of their time for inspiring discussions and have been great leaders throughout. I also would like to thank Prof. Hans Gerd Evertz for several interesting and fruitful discussions during the last years.

I had the opportunity to collaborate with many physicists outside Graz University of Technology over the last years. Especially, I would like to thank Prof. Eugene Demler, who accepted me for a half-year stay in his group at Harvard University, and also Prof. Wolfgang von der Linden for letting me gather this great experience. I am grateful to Prof. Eugene Demler, who provided me a warm welcome to his group and spend a lot of his time with me discussing interesting and challenging topics. I also enjoyed the stimulating and fruitful scientific environment of his group and particularly want to thank Prof. Erez Berg and Prof. Dima Abanin, with whom I had a great time discussing and working together.

I enjoyed very fruitful collaborations with Prof. Jared H. Cole, at that time working at Karlsruhe Institute of Technology (KIT), who now went back home to Australia, joining RMIT University, Melbourne, with Prof. Holger Fehske and Dr. Satoshi Ejima at Ernst-Moritz-Arndt-Universität Greifswald, Germany, and with Prof. Jim K. Freericks at Georgetown University, Washington DC. These collaborations were a great experience to me and exchanging ideas was always a big pleasure. I also would like to thank my colleagues and friends from Austria and from abroad for many discussions, great support and their friendship. Especially, I would like to thank Martin Ganahl, who generously provided me his DMRG program, which I could adapt for the calculations I did during my research stay in the group of Prof. Eugene Demler.

I want to thank Brigitte Schwarz for her help with many administrative and organizational matters occurring over the last years as well as Andreas Hirczy for the organization of the computer cluster at our institute.

I am grateful to Graz University of Technology and to the Austrian Science Fund (FWF) for supporting my research over the last three years as well as several travels to conferences, workshops and meetings. In particular, I obtained funding under the doc-

toral program "Numerical Simulations in Technical Sciences" No. W1208-N18 and the projects P18551-N16, P24081-N16. For my research stay in the group of Prof. Eugene Demler, I acknowledge additional support from the Austrian Marshall Plan Foundation, which helped covering the high living expanses in Boston area and guaranteed a worry-free time also from the financial perspective.

And finally and also most importantly, I could not be where I am now without the enormous support of my wife Sabrina and my parents Maria and Alois. I want to thank them for being the warmest, most supportive, and caring family one could ever have.

Bibliography

[1] Anderson, P. W. More is different. *Science* **177**, 393–396 (1972).

[2] Ginzburg, V. L. & Landau, L. D. *Zh. Eksp. Teor. Fiz.* **20**, 1064 (1950). English translation in: L. D. Landau, Collected papers (Oxford: Pergamon Press, 1965) p. 54.

[3] Wilson, K. G. The renormalization group: Critical phenomena and the Kondo problem. *Rev. Mod. Phys.* **47**, 773–840 (1975).

[4] Orland, H. & Negele, J. W. *Quantum Many Particle Systems* (Perseus Books, 1998).

[5] Giamarchi, T. *Quantum Physics in One Dimension* (Oxford University Press, USA, 2004).

[6] Tomonaga, S. Remarks on Bloch's method of sound waves applied to many-fermion problems. *Prog. Theor. Phys.* **5**, 544–569 (1950).

[7] Luttinger, J. M. An exactly soluble model of a many-fermion system. *J. Math. Phys.* **4**, 1154 (1963).

[8] Mott, N. F. The basis of the electron theory of metals, with special reference to the transition metals. *Proc. Phys. Soc. A* **62**, 416–422 (1949).

[9] Van Santen, J. & Jonker, G. Electrical conductivity of ferromagnetic compounds of manganese with perovskite structure. *Physica* **16**, 599–600 (1950).

[10] Kondo, J. Resistance minimum in dilute magnetic alloys. *Prog. Theor. Phys.* **32**, 37–49 (1964).

[11] Yuval, G. & Anderson, P. W. Exact results for the Kondo problem: One-Body theory and extension to finite temperature. *Phys. Rev. B* **1**, 1522–1528 (1970).

[12] Norman, M. R. The challenge of unconventional superconductivity. *Science* **332**, 196–200 (2011).

[13] Osheroff, D., Richardson, R. & Lee, D. Evidence for a new phase of solid ^{3}He. *Phys. Rev. Lett.* **28**, 885–888 (1972).

[14] Bednorz, J. G. & Müller, K. A. Possible high-T_c superconductivity in the BaLaCuO system. *Z. Phys. B* **64**, 189–193 (1986).

[15] Powell, B. J. & McKenzie, R. H. Strong electronic correlations in superconducting organic charge transfer salts. *Journal of Physics: Condensed Matter* **18**, R827–R866 (2006).

[16] Steglich, F., Aarts, J., Bredl, C. D., Lieke, W., Meschede, D., Franz, W. & Schäfer, H. Superconductivity in the presence of strong Pauli paramagnetism: $CeCu_2Si_2$. *Phys. Rev. Lett.* **43**, 1892–1896 (1979).

[17] Wang, F. & Lee, D. The Electron-Pairing mechanism of Iron-Based superconductors. *Science* **332**, 200–204 (2011).

[18] Hubbard, J. Electron correlations in narrow energy bands. *Proc. R. Soc. A* **276**, 238–257 (1963).

[19] Anderson, P. W. Absence of diffusion in certain random lattices. *Phys. Rev.* **109**, 1492–1505 (1958).

[20] Jaksch, D., Bruder, C., Cirac, J. I., Gardiner, C. W. & Zoller, P. Cold bosonic atoms in optical lattices. *Phys. Rev. Lett.* **81**, 3108 (1998).

[21] Greiner, M., Mandel, O., Esslinger, T., Hänsch, T. W. & Bloch, I. Quantum phase transition from a superfluid to a Mott insulator in a gas of ultracold atoms. *Nature (London)* **415**, 39–44 (2002).

[22] Bloch, I., Dalibard, J. & Zwerger, W. Many-body physics with ultracold gases. *Rev. Mod. Phys.* **80**, 885–80 (2008).

[23] Hartmann, M., Brandão, F. G. & Plenio, M. B. Quantum many-body phenomena in coupled cavity arrays. *Laser Photonics Rev.* **2**, 527–556 (2008).

[24] Tomadin, A. & Fazio, R. Many-body phenomena in QED-cavity arrays. *J. Opt. Soc. Am. B* **27**, A130–A136 (2010).

[25] Schön, G. & Zaikin, A. Quantum coherent effects, phase transitions, and the dissipative dynamics of ultra small tunnel junctions. *Phys. Rep.* **198**, 237–412 (1990).

[26] Fazio, R. & van der Zant, H. Quantum phase transitions and vortex dynamics in superconducting networks. *Phys. Rep.* **355**, 235–334 (2001).

[27] Kippenberg, T. J. & Vahala, K. J. Cavity optomechanics: Back-Action at the mesoscale. *Science* **321**, 1172–1176 (2008).

[28] Potthoff, M., Aichhorn, M. & Dahnken, C. Variational cluster approach to correlated electron systems in low dimensions. *Phys. Rev. Lett.* **91**, 206402 (2003).

[29] Sachdev, S. *Quantum Phase Transitions* (Cambridge University Press, 2011), 2 edn.

[30] Fisher, M. P. A., Weichman, P. B., Grinstein, G. & Fisher, D. S. Boson localization and the superfluid-insulator transition. *Phys. Rev. B* **40**, 546 (1989).

[31] Ritter, S., Nölleke, C., Hahn, C., Reiserer, A., Neuzner, A., Uphoff, M., Mücke, M., Figueroa, E., Bochmann, J. & Rempe, G. An elementary quantum network of single atoms in optical cavities. *Nature* **484**, 195–200 (2012).

[32] Thon, S. M., Kim, H., Bonato, C., Gudat, J., Hagemeier, J., Petroff, P. M. & Bouwmeester, D. Independent electrical tuning of separated quantum dots in coupled photonic crystal cavities. *Appl. Phys. Lett.* **99**, 161102–161102–3 (2011).

[33] Wallraff, A., Schuster, D. I., Blais, A., Frunzio, L., Huang, R.-S., Majer, J., Kumar, S., Girvin, S. M. & Schoelkopf, R. J. Strong coupling of a single photon to a superconducting qubit using circuit quantum electrodynamics. *Nat. (London)* **431**, 162–167 (2004).

[34] Yoshie, T., Scherer, A., Hendrickson, J., Khitrova, G., Gibbs, H. M., Rupper, G., Ell, C., Shchekin, O. B. & Deppe, D. G. Vacuum Rabi splitting with a single quantum dot in a photonic crystal nanocavity. *Nat. (London)* **432**, 200–203 (2004).

[35] Davis, K. B., Mewes, M. O., Andrews, M. R., van Druten, N. J., Durfee, D. S., Kurn, D. M. & Ketterle, W. Bose-Einstein condensation in a gas of sodium atoms. *Phys. Rev. Lett.* **75**, 3969–3973 (1995).

[36] Bakr, W. S., Gillen, J. I., Peng, A., Fölling, S. & Greiner, M. A quantum gas microscope for detecting single atoms in a Hubbard-regime optical lattice. *Nature* **462**, 74–77 (2009).

[37] Sherson, J. F., Weitenberg, C., Endres, M., Cheneau, M., Bloch, I. & Kuhr, S. Single-atom-resolved fluorescence imaging of an atomic Mott insulator. *Nature* **467**, 68–72 (2010).

[38] Stöferle, T., Moritz, H., Schori, C., Köhl, M. & Esslinger, T. Transition from a strongly interacting 1D superfluid to a Mott insulator. *Phys. Rev. Lett.* **92**, 130403 (2004).

[39] Endres, M., Fukuhara, T., Pekker, D., Cheneau, M., SchauÃ, P., Gross, C., Demler, E., Kuhr, S. & Bloch, I. The 'Higgs' amplitude mode at the Two-Dimensional Superfluid-Mott insulator transition. *arXiv:1204.5183* (2012).

[40] Regal, C. A. & Jin, D. S. Measurement of positive and negative scattering lengths in a Fermi gas of atoms. *Phys. Rev. Lett.* **90**, 230404 (2003).

[41] Gupta, S., Hadzibabic, Z., Zwierlein, M. W., Stan, C. A., Dieckmann, K., Schunck, C. H., van Kempen, E. G. M., Verhaar, B. J. & Ketterle, W. Radio-Frequency spectroscopy of ultracold fermions. *Science* **300**, 1723 –1726 (2003).

[42] Clément, D., Fabbri, N., Fallani, L., Fort, C. & Inguscio, M. Exploring correlated 1D Bose gases from the superfluid to the Mott-insulator state by inelastic light scattering. *Phys. Rev. Lett.* **102**, 155301 (2009).

[43] Fabbri, N., Clément, D., Fallani, L., Fort, C., Modugno, M., van der Stam, K. M. R. & Inguscio, M. Excitations of Bose-Einstein condensates in a one-dimensional periodic potential. *Phys. Rev. A* **79**, 043623–4 (2009).

[44] Ernst, P. T., Gotze, S., Krauser, J. S., Pyka, K., Luhmann, D., Pfannkuche, D. & Sengstock, K. Probing superfluids in optical lattices by momentum-resolved Bragg spectroscopy. *Nat Phys* **6**, 56–61 (2010).

[45] Micheli, A., Daley, A. J., Jaksch, D. & Zoller, P. Single atom transistor in a 1D optical lattice. *Phys. Rev. Lett.* **93**, 140408 (2004).

[46] Recati, A., Fedichev, P. O., Zwerger, W., von Delft, J. & Zoller, P. Atomic quantum dots coupled to a reservoir of a superfluid Bose-Einstein condensate. *Phys. Rev. Lett.* **94**, 040404 (2005).

[47] M. Knap, A. Shashi, Y. Nishida, A. Imambekov, D. A. Abanin, E. Demler (in preparation).

[48] Altman, E., Demler, E. & Lukin, M. D. Probing many-body states of ultracold atoms via noise correlations. *Phys. Rev. A* **70**, 013603 (2004).

[49] Potthoff, M. Self-energy-functional approach to systems of correlated electrons. *Eur. Phys. J. B* **32**, 429–436 (2003).

[50] Potthoff, M. Self-energy-functional approach: Analytical results and the Mott-Hubbard transition. *Eur. Phys. J. B* **36**, 335–348 (2003).

[51] Koller, W. & Dupuis, N. Variational cluster perturbation theory for Bose-Hubbard models. *J. Phys.: Condens. Matter* **18**, 9525–9540 (2006).

[52] Zacher, M. G., Eder, R., Arrigoni, E. & Hanke, W. Evolution of the stripe phase as a function of doping from a theoretical analysis of angle-resolved photoemission data. *Phys. Rev. B* **65**, 045109 (2002).

[53] Aichhorn, M., Arrigoni, E., Potthoff, M. & Hanke, W. Variational cluster approach to the Hubbard model: Phase-separation tendency and finite-size effects. *Phys. Rev. B* **74**, 235117–6 (2006).

[54] Knap, M., Arrigoni, E. & von der Linden, W. Spectral properties of strongly correlated bosons in two-dimensional optical lattices. *Phys. Rev. B* **81**, 024301 (2010).

[55] Knap, M. Quantum many body properties of strongly correlated lattice bosons and polaritons. *Master Thesis* (2009).

[56] Knap, M., Arrigoni, E. & von der Linden, W. Excitations in disordered bosonic optical lattices. *Phys. Rev. A* **82**, 053628 (2010).

[57] Knap, M., Arrigoni, E. & von der Linden, W. Variational cluster approach for strongly correlated lattice bosons in the superfluid phase. *Phys. Rev. B* **83**, 134507 (2011).

[58] Arrigoni, E., Knap, M. & von der Linden, W. Extended self-energy functional approach for strongly-correlated lattice bosons in the superfluid phase. *Phys. Rev. B* **84**, 014535 (2011).

[59] Knap, M., von der Linden, W. & Arrigoni, E. Nonequilibrium steady state for strongly-correlated many-body systems: Variational cluster approach. *Phys. Rev. B* **84**, 115145 (2011).

[60] Knap, M., Arrigoni, E. & von der Linden, W. Spectral properties of coupled cavity arrays in one dimension. *Phys. Rev. B* **81**, 104303 (2010).

[61] Knap, M., Arrigoni, E. & von der Linden, W. Quantum phase transition and excitations of the Tavis-Cummings lattice model. *Phys. Rev. B* **82**, 045126 (2010).

[62] Georges, A., Kotliar, G., Krauth, W. & Rozenberg, M. J. The local impurity self consistent approximation (LISA) to strongly correlated fermion systems and the limit of infinite dimensions. *Rev. Mod. Phys.* **68**, 13 (1996).

[63] Gros, C. & Valentí, R. Cluster expansion for the self-energy: A simple many-body method for interpreting the photoemission spectra of correlated Fermi systems. *Phys. Rev. B* **48**, 418 (1993).

[64] Sénéchal, D., Perez, D. & Pioro-Ladrière, M. Spectral weight of the Hubbard model through cluster perturbation theory. *Phys. Rev. Lett.* **84**, 522 (2000).

[65] Sénéchal, D., Perez, D. & Plouffe, D. Cluster perturbation theory for Hubbard models. *Phys. Rev. B* **66**, 075129 (2002).

[66] Dahnken, C., Aichhorn, M., Hanke, W., Arrigoni, E. & Potthoff, M. Variational cluster approach to spontaneous symmetry breaking: The itinerant antiferromagnet in two dimensions. *Phys. Rev. B* **70**, 245110 (2004).

[67] Kotliar, G., Savrasov, S. Y., Pálsson, G. & Biroli, G. Cellular dynamical mean field approach to strongly correlated systems. *Phys. Rev. Lett.* **87**, 186401 (2001).

[68] Hettler, M. H., Tahvildar-Zadeh, A. N., Jarrell, M., Pruschke, T. & Krishnamurthy, H. R. Nonlocal dynamical correlations of strongly interacting electron systems. *Phys. Rev. B* **58**, R7475–R7479 (1998).

[69] Aichhorn, M., Hohenadler, M., Tahan, C. & Littlewood, P. B. Quantum fluctuations, temperature, and detuning effects in Solid-Light systems. *Phys. Rev. Lett.* **100**, 216401–4 (2008).

[70] Ovchinnikov, S. G. & Val'kov, V. V. *Hubbard operators in the theory of strongly correlated electrons* (Imperial College Press, 2004).

[71] Luttinger, J. M. & Ward, J. C. Ground-State energy of a Many-Fermion system. II. *Phys. Rev.* **118**, 1417 (1960).

[72] Freund, R. Band Lanczos method. In Bai, Z., Demmel, J., Dongarra, J., Ruhe, A. & van der Vorst, H. (eds.) *Templates for the Solution of Algebraic Eigenvalue Problems: A Practical Guide*, chap. 4.6, 80–88 (SIAM, Philadelphia, 2000), 1 edn.

[73] Sénéchal, D. An introduction to quantum cluster methods. *arXiv:0806.2690* (2008).

[74] Fetter, A. L. & Walecka, J. D. *Quantum Theory of Many-Particle Systems* (McGraw-Hill, New York, 1971).

[75] Potthoff, M. & Balzer, M. Self-energy-functional theory for systems of interacting electrons with disorder. *Phys. Rev. B* **75**, 125112 (2007).

[76] Haley, S. B. & Erdös, P. Standard-Basis operator method in the Green's-Function technique of Many-Body systems with an application to ferromagnetism. *Phys. Rev. B* **5**, 1106 (1972).

[77] Aichhorn, M. & Arrigoni, E. Weak phase separation and the pseudogap in the electron-doped cuprates. *Europhys. Lett.* **72**, 117–123 (2005).

[78] Aichhorn, M., Arrigoni, E., Potthoff, M. & Hanke, W. Antiferromagnetic to superconducting phase transition in the hole- and electron-doped Hubbard model at zero temperature. *Phys. Rev. B* **74**, 024508–12 (2006).

[79] Potthoff, M. Non-perturbative construction of the Luttinger-Ward functional. *Condens. Matt. Phys.* **9**, 557 (2006).

[80] Balzer, M., Hanke, W. & Potthoff, M. Mott transition in one dimension: Benchmarking dynamical cluster approaches. *Phys. Rev. B* **77**, 045133–18 (2008).

[81] Balzer, M., Hanke, W. & Potthoff, M. Importance of local correlations for the order parameter of high-T_c superconductors. *arXiv:0912.1282* (2009).

[82] Byczuk, K. & Vollhardt, D. Correlated bosons on a lattice: Dynamical mean-field theory for Bose-Einstein condensed and normal phases. *Phys. Rev. B* **77**, 235106 (2008).

[83] Anders, P., Gull, E., Pollet, L., Troyer, M. & Werner, P. Dynamical mean field solution of the Bose-Hubbard model. *Phys. Rev. Lett.* **105**, 096402 (2010).

[84] Sokolowski-Tinten, K., Blome, C., Blums, J., Cavalleri, A., Dietrich, C., Tarasevitch, A., Uschmann, I., Forster, E., Kammler, M., Horn-von Hoegen, M. & von der Linde, D. Femtosecond X-ray measurement of coherent lattice vibrations near the Lindemann stability limit. *Nature* **422**, 287–289 (2003).

[85] Goulielmakis, E., Yakovlev, V. S., Cavalieri, A. L., Uiberacker, M., Pervak, V., Apolonski, A., Kienberger, R., Kleineberg, U. & Krausz, F. Attosecond control and measurement: Lightwave electronics. *Science* **317**, 769–775 (2007).

[86] Haug, H. & Jauho, A.-P. *Quantum Kinetics in Transport and Optics of Semiconductors* (Springer, Heidelberg, 1998).

[87] Rammer, J. & Smith, H. Quantum field-theoretical methods in transport theory of metals. *Rev. Mod. Phys.* **58**, 323 (1986).

[88] Meir, Y. & Wingreen, N. S. Landauer formula for the current through an interacting electron region. *Phys. Rev. Lett.* **68**, 2512–2515 (1992).

[89] Meir, Y., Wingreen, N. S. & Lee, P. A. Low-temperature transport through a quantum dot: The Anderson model out of equilibrium. *Phys. Rev. Lett.* **70**, 2601–2604 (1993).

[90] Ryndyk, D. A., Gutierrez, R., Song, B. & Cuniberti, G. Green function techniques in the treatment of quantum transport at the molecular scale. In Castleman, A. W., Toennies, J. P., Yamanouchi, K., Zinth, W., Burghardt, I., May, V., Micha, D. A. & Bittner, E. R. (eds.) *Energy Transfer Dynamics in Biomaterial Systems*, vol. 93 of *Springer Series in Chemical Physics*, 213–335 (Springer Berlin Heidelberg, 2009).

[91] Schoeller, H. A perturbative nonequilibrium renormalization group method for dissipative quantum mechanics. *Eur. Phys. J. Special Topics* **168**, 179–266 (2009).

[92] Diehl, S., Micheli, A., Kantian, A., Kraus, B., Büchler, H. P. & Zoller, P. Quantum states and phases in driven open quantum systems with cold atoms. *Nat. Phys.* **4**, 878–883 (2008).

[93] Kraus, B., Büchler, H. P., Diehl, S., Kantian, A., Micheli, A. & Zoller, P. Preparation of entangled states by quantum Markov processes. *Phys. Rev. A* **78**, 042307 (2008).

[94] Diehl, S., Tomadin, A., Micheli, A., Fazio, R. & Zoller, P. Dynamical phase transitions and instabilities in open atomic many-body systems. *Phys. Rev. Lett.* **105**, 015702 (2010).

[95] Pichler, H., Daley, A. J. & Zoller, P. Nonequilibrium dynamics of bosonic atoms in optical lattices: Decoherence of many-body states due to spontaneous emission. *Phys. Rev. A* **82**, 063605 (2010).

[96] Tomadin, A., Diehl, S. & Zoller, P. Nonequilibrium phase diagram of a driven and dissipative many-body system. *Phys. Rev. A* **83**, 013611 (2011).

[97] Barmettler, P. & Kollath, C. Controllable manipulation and detection of local densities and bipartite entanglement in a quantum gas by a dissipative defect. *Phys. Rev. A* **84**, 041606 (2011).

[98] Dalla Torre, E. G., Demler, E., Giamarchi, T. & Altman, E. Quantum critical states and phase transitions in the presence of non-equilibrium noise. *Nat. Phys.* **6**, 806–810 (2010).

[99] White, S. R. & Feiguin, A. E. Real-time evolution using the density matrix renormalization group. *Phys. Rev. Lett.* **93**, 076401 (2004).

[100] Daley, A. J., Kollath, C., Schollwöck, U. & Vidal, G. Time-dependent density-matrix renormalization-group using adaptive effective Hilbert spaces. *J. Stat. Mech.* **2004**, P04005 (2004).

[101] Prosen, T. & Žnidarič, M. Matrix product simulations of non-equilibrium steady states of quantum spin chains. *J. Stat. Mech.* **2009**, P02035 (2009).

[102] Benenti, G., Casati, G., Prosen, T., Rossini, D. & Žnidarič, M. Charge and spin transport in strongly correlated one-dimensional quantum systems driven far from equilibrium. *Phys. Rev. B* **80**, 035110 (2009).

[103] Perez-Garcia, D., Verstraete, F., Wolf, M. M. & Cirac, J. I. Matrix product state representations. *Quant. Inf. Comp.* **7**, 401 (2007).

[104] Werner, P., Oka, T. & Millis, A. J. Diagrammatic Monte Carlo simulation of nonequilibrium systems. *Phys. Rev. B* **79**, 035320 (2009).

[105] Anders, F. B. & Schiller, A. Spin precession and real-time dynamics in the Kondo model: Time-dependent numerical renormalization-group study. *Phys. Rev. B* **74**, 245113 (2006).

[106] Jakobs, S. G., Meden, V. & Schoeller, H. Nonequilibrium functional renormalization group for interacting quantum systems. *Phys. Rev. Lett.* **99**, 150603 (2007).

[107] Freericks, J. K., Turkowski, V. M. & Zlatic, V. Nonequilibrium dynamical mean-field theory. *Phys. Rev. Lett.* **97**, 266408 (2006).

[108] Joura, A. V., Freericks, J. K. & Pruschke, T. Steady-state nonequilibrium density of states of driven strongly correlated lattice models in infinite dimensions. *Phys. Rev. Lett.* **101**, 196401 (2008).

[109] Eckstein, M., Kollar, M. & Werner, P. Thermalization after an interaction quench in the Hubbard model. *Phys. Rev. Lett.* **103**, 056403 (2009).

[110] Aron, C., Kotliar, G. & Weber, C. Dimensional crossover driven by an electric field. *Phys. Rev. Lett.* **108**, 086401 (2012).

[111] Mehta, P. & Andrei, N. Nonequilibrium transport in quantum impurity models: The Bethe ansatz for open systems. *Phys. Rev. Lett.* **96**, 216802 (2006).

[112] Gritsev, V., Rostunov, T. & Demler, E. Exact methods in the analysis of the non-equilibrium dynamics of integrable models: application to the study of correlation functions for non-equilibrium 1D Bose gas. *J. Stat. Mech.* **2010**, P05012 (2010).

[113] Jung, C., Lieder, A., Brener, S., Hafermann, H., Baxevanis, B., Chudnovskiy, A., Rubtsov, A., Katsnelson, M. & Lichtenstein, A. Dual-fermion approach to non-equilibrium strongly correlated problems. *Ann. Phys.* **524**, 49–61 (2012).

[114] Balzer, M. & Potthoff, M. Nonequilibrium cluster perturbation theory. *Phys. Rev. B* **83**, 195132 (2011).

[115] Myöhänen, P., Stan, A., Stefanucci, G. & van Leeuwen, R. Kadanoff-Baym approach to quantum transport through interacting nanoscale systems: From the transient to the steady-state regime. *Phys. Rev. B* **80**, 115107 (2009).

[116] Brandbyge, M., Mozos, J., Ordejón, P., Taylor, J. & Stokbro, K. Density-functional method for nonequilibrium electron transport. *Phys. Rev. B* **65**, 165401 (2002).

[117] Fürst, J. A., Brandbyge, M., Jauho, A. & Stokbro, K. Ab initio study of spin-dependent transport in carbon nanotubes with iron and vanadium adatoms. *Phys. Rev. B* **78**, 195405 (2008).

[118] Markussen, T., Jauho, A. & Brandbyge, M. Electron and phonon transport in silicon nanowires: Atomistic approach to thermoelectric properties. *Phys. Rev. B* **79**, 035415 (2009).

[119] Metzner, W. & Vollhardt, D. Correlated lattice fermions in $d = \infty$ dimensions. *Phys. Rev. Lett.* **62**, 324 (1989).

[120] Nevidomskyy, A. H., Sénéchal, D. & Tremblay, A. M. S. Convexity of the self-energy functional in the variational cluster approximation. *Phys. Rev. B* **77**, 075105 (2008).

[121] Kadanoff, L. P. & Baym, G. *Quantum statistical mechanics: Green's function methods in equilibrium and nonequilibrium problems* (Addison-Wesley, Redwood City, Calif., 1962).

[122] Schwinger, J. Brownian motion of a quantum oscillator. *J. Math. Phys.* **2**, 407 (1961).

[123] Keldysh, L. V. Diagram technique for nonequilibrium processes. *Sov. Phys. JETP* **20**, 1018 (1965).

[124] Würtz, P., Langen, T., Gericke, T., Koglbauer, A. & Ott, H. Experimental demonstration of Single-Site addressability in a Two-Dimensional optical lattice. *Phys. Rev. Lett.* **103**, 080404–4 (2009).

[125] Spielman, I. B., Phillips, W. D. & Porto, J. V. Mott-Insulator transition in a two-dimensional atomic bose gas. *Phys. Rev. Lett.* **98**, 080404–4 (2007).

[126] Spielman, I. B., Phillips, W. D. & Porto, J. V. Condensate fraction in a 2D Bose gas measured across the Mott-Insulator transition. *Phys. Rev. Lett.* **100**, 120402–4 (2008).

[127] Bruder, C., Fazio, R. & Schön, G. Superconductor-Mott-insulator transition in Bose systems with finite-range interactions. *Phys. Rev. B* **47**, 342–347 (1993).

[128] Kampf, A. P. & Zimanyi, G. T. Superconductor-insulator phase transition in the boson Hubbard model. *Phys. Rev. B* **47**, 279–286 (1993).

[129] Sheshadri, K., Krishnamurthy, H. R., Pandit, R. & Ramakrishnan, T. V. Superfluid and insulating phases in an Interacting-Boson model: Mean-Field theory and the RPA. *Europhys. Lett.* **22**, 257–263 (1993).

[130] van Oosten, D., van der Straten, P. & Stoof, H. T. C. Quantum phases in an optical lattice. *Phys. Rev. A* **63**, 053601 (2001).

[131] Menotti, C. & Trivedi, N. Spectral weight redistribution in strongly correlated bosons in optical lattices. *Phys. Rev. B* **77**, 235120–13 (2008).

[132] Capogrosso-Sansone, B., Söyler, Ş. G., Prokof'ev, N. & Svistunov, B. Monte Carlo study of the two-dimensional Bose-Hubbard model. *Phys. Rev. A* **77**, 015602–4 (2008).

[133] Rokhsar, D. S. & Kotliar, B. G. Gutzwiller projection for bosons. *Phys. Rev. B* **44**, 10328–10332 (1991).

[134] Capello, M., Becca, F., Fabrizio, M. & Sorella, S. Mott transition in bosonic systems: Insights from the variational approach. *Phys. Rev. B* **77**, 144517 (2008).

[135] Freericks, J. K. & Monien, H. Phase diagram of the Bose-Hubbard model. *Europhys. Lett.* **26**, 545–550 (1994).

[136] Freericks, J. K. & Monien, H. Strong-coupling expansions for the pure and disordered Bose-Hubbard model. *Phys. Rev. B* **53**, 2691 (1996).

[137] Elstner, N. & Monien, H. Dynamics and thermodynamics of the Bose-Hubbard model. *Phys. Rev. B* **59**, 12184 (1999).

[138] Buonsante, P. & Vezzani, A. Cell strong-coupling perturbative approach to the phase diagram of ultracold bosons in optical superlattices. *Phys. Rev. A* **72**, 013614 (2005).

[139] Teichmann, N., Hinrichs, D., Holthaus, M. & Eckardt, A. Bose-Hubbard phase diagram with arbitrary integer filling. *Phys. Rev. B* **79**, 100503–4 (2009).

[140] Teichmann, N., Hinrichs, D., Holthaus, M. & Eckardt, A. Process-chain approach to the Bose-Hubbard model: Ground-state properties and phase diagram. *Phys. Rev. B* **79**, 224515–14 (2009).

[141] Sengupta, K. & Dupuis, N. Mott-insulator-to-superfluid transition in the Bose-Hubbard model: A strong-coupling approach. *Phys. Rev. A* **71**, 033629 (2005).

[142] Huber, S. D., Altman, E., Büchler, H. P. & Blatter, G. Dynamical properties of ultracold bosons in an optical lattice. *Phys. Rev. B* **75**, 085106–12 (2007).

[143] Kühner, T. D., White, S. R. & Monien, H. One-dimensional Bose-Hubbard model with nearest-neighbor interaction. *Phys. Rev. B* **61**, 12474 (2000).

[144] Freericks, J. K., Krishnamurthy, H. R., Kato, Y., Kawashima, N. & Trivedi, N. Strong-coupling expansion for the momentum distribution of the Bose-Hubbard model with benchmarking against exact numerical results. *Phys. Rev. A* **79**, 053631–22 (2009).

[145] Crowell, P. A., Van Keuls, F. W. & Reppy, J. D. Superfluid-insulator transition in ^4He films adsorbed in Vycor glass. *Phys. Rev. Lett.* **75**, 1106–1109 (1995).

[146] Csáthy, G. A., Reppy, J. D. & Chan, M. H. W. Substrate-tuned boson localization in superfluid ^4He films. *Phys. Rev. Lett.* **91**, 235301 (2003).

[147] Haviland, D. B., Liu, Y. & Goldman, A. M. Onset of superconductivity in the two-dimensional limit. *Phys. Rev. Lett.* **62**, 2180–2183 (1989).

[148] van der Zant, H. S. J., Elion, W. J., Geerligs, L. J. & Mooij, J. E. Quantum phase transitions in two dimensions: Experiments in Josephson-junction arrays. *Phys. Rev. B* **54**, 10081–10093 (1996).

[149] Aspect, A. & Inguscio, M. Anderson localization of ultracold atoms. *Physics Today* **62**, 30 (2009).

[150] Fallani, L., Lye, J. E., Guarrera, V., Fort, C. & Inguscio, M. Ultracold atoms in a disordered crystal of light: Towards a Bose glass. *Phys. Rev. Lett.* **98**, 130404 (2007).

[151] Roth, R. & Burnett, K. Phase diagram of bosonic atoms in two-color superlattices. *Phys. Rev. A* **68**, 023604 (2003).

[152] Damski, B., Zakrzewski, J., Santos, L., Zoller, P. & Lewenstein, M. Atomic Bose and Anderson glasses in optical lattices. *Phys. Rev. Lett.* **91**, 080403 (2003).

[153] Hild, M., Schmitt, F. & Roth, R. Response of Bose gases in time-dependent optical superlattices. *J. Phys. B* **39**, 4547 (2006).

[154] Schmitt, F., Hild, M. & Roth, R. Phase diagram of bosons in two-color superlattices from experimental parameters. *Phys. Rev. A* **80**, 023621 (2009).

[155] Pasienski, M., McKay, D., White, M. & DeMarco, B. A disordered insulator in an optical lattice. *Nat Phys* **6**, 677–680 (2010).

[156] White, M., Pasienski, M., McKay, D., Zhou, S. Q., Ceperley, D. & DeMarco, B. Strongly interacting bosons in a disordered optical lattice. *Phys. Rev. Lett.* **102**, 055301 (2009).

[157] Lye, J. E., Fallani, L., Modugno, M., Wiersma, D. S., Fort, C. & Inguscio, M. Bose-Einstein condensate in a random potential. *Phys. Rev. Lett.* **95**, 070401 (2005).

[158] Shrestha, U. & Modugno, M. Correlated bosons in a one-dimensional optical lattice: Effects of the trapping potential and of quasiperiodic disorder. *Physical Review A* **82**, 033604 (2010).

[159] Ospelkaus, S., Ospelkaus, C., Wille, O., Succo, M., Ernst, P., Sengstock, K. & Bongs, K. Localization of bosonic atoms by fermionic impurities in a three-dimensional optical lattice. *Phys. Rev. Lett.* **96**, 180403 (2006).

[160] Scalettar, R. T., Batrouni, G. G. & Zimanyi, G. T. Localization in interacting, disordered, Bose systems. *Phys. Rev. Lett.* **66**, 3144–3147 (1991).

[161] Krauth, W., Trivedi, N. & Ceperley, D. Superfluid-insulator transition in disordered boson systems. *Phys. Rev. Lett.* **67**, 2307–2310 (1991).

[162] Sheshadri, K., Krishnamurthy, H. R., Pandit, R. & Ramakrishnan, T. V. Percolation-enhanced localization in the disordered bosonic hubbard model. *Phys. Rev. Lett.* **75**, 4075–4078 (1995).

[163] Freericks, J. K. & Monien, H. Strong-coupling expansions for the pure and disordered Bose-Hubbard model. *Phys. Rev. B* **53**, 2691–2700 (1996).

[164] Svistunov, B. V. Superfluid–Bose-glass transition in weakly disordered commensurate one-dimensional system. *Phys. Rev. B* **54**, 16131–16134 (1996).

[165] Kisker, J. & Rieger, H. Bose-glass and Mott-insulator phase in the disordered boson Hubbard model. *Phys. Rev. B* **55**, R11981–R11984 (1997).

[166] Herbut, I. F. Dual superfluid–Bose-glass critical point in two dimensions and the universal conductivity. *Phys. Rev. Lett.* **79**, 3502–3505 (1997).

[167] Prokof'ev, N. & Svistunov, B. Superfluid-insulator transition in commensurate disordered bosonic systems: Large-scale worm algorithm simulations. *Phys. Rev. Lett.* **92**, 015703 (2004).

[168] Balabanyan, K. G., Prokof'ev, N. & Svistunov, B. Superfluid-insulator transition in a commensurate one-dimensional bosonic system with off-diagonal disorder. *Phys. Rev. Lett.* **95**, 055701 (2005).

[169] Buonsante, P., Penna, V., Vezzani, A. & Blakie, P. B. Mean-field phase diagram of cold lattice bosons in disordered potentials. *Phys. Rev. A* **76**, 011602 (2007).

[170] Weichman, P. B. & Mukhopadhyay, R. Particle-hole symmetry and the dirty boson problem. *Phys. Rev. B* **77**, 214516 (2008).

[171] Pollet, L., Prokof'ev, N. V., Svistunov, B. V. & Troyer, M. Absence of a direct superfluid to mott insulator transition in disordered Bose systems. *Phys. Rev. Lett.* **103**, 140402 (2009).

[172] Gurarie, V., Pollet, L., Prokof'ev, N. V., Svistunov, B. V. & Troyer, M. Phase diagram of the disordered Bose-Hubbard model. *Phys. Rev. B* **80**, 214519 (2009).

[173] Bissbort, U. & Hofstetter, W. Stochastic mean-field theory for the disordered Bose-Hubbard model. *Europhys. Lett.* **86**, 50007 (2009).

[174] Krüger, F., Wu, J. & Phillips, P. Anomalous suppression of the Bose glass at commensurate fillings in the disordered Bose-Hubbard model. *Physical Review B* **80**, 094526 (2009).

[175] Krüger, F., Hong, S. & Phillips, P. Two distinct mott-insulator to Bose-glass transitions and breakdown of self-averaging in the disordered Bose-Hubbard model. *Phys. Rev. B* **84**, 115118 (2011).

[176] Clément, D., Fabbri, N., Fallani, L., Fort, C. & Inguscio, M. Multi-band spectroscopy of inhomogeneous mott-insulator states of ultracold bosons. *New J. Phys.* **11**, 103030 (2009).

[177] Clément, D., Fabbri, N., Fallani, L., Fort, C. & Inguscio, M. Bragg spectroscopy of strongly correlated bosons in optical lattices. *J. Low Temp. Phys.* **158**, 5–15 (2010).

[178] Zwerger, W. Mott Hubbard transition of cold atoms in optical lattices. *J. Opt. B: Quantum Semiclass. Opt.* **5**, S9–S16 (2003).

[179] Clément, D., Varón, A. F., Retter, J. A., Sanchez-Palencia, L., Aspect, A. & Bouyer, P. Experimental study of the transport of coherent interacting matter-waves in a 1D random potential induced by laser speckle. *New J. Phys.* **8**, 165 (2006).

[180] Zhou, S. Q. & Ceperley, D. M. Construction of localized wave functions for a disordered optical lattice and analysis of the resulting Hubbard model parameters. *Phys. Rev. A* **81**, 013402 (2010).

[181] Knap, M., Arrigoni, E. & von der Linden, W. Benchmarking the variational cluster approach by means of the one-dimensional Bose-Hubbard model. *Phys. Rev. B* **81**, 235122 (2010).

[182] Albuquerque, A. *et al.* The ALPS project release 1.3: Open-source software for strongly correlated systems. *J. Magn. Magn. Mater.* **310**, 1187–1193 (2007).

[183] Alet, F., Wessel, S. & Troyer, M. Generalized directed loop method for quantum monte carlo simulations. *Phys. Rev. E* **71**, 036706 (2005).

[184] P. Pippan, M. Knap and H. G. Evertz (to be published).

[185] Ohashi, Y., Kitaura, M. & Matsumoto, H. Itinerant-localized dual character of a strongly correlated superfluid Bose gas in an optical lattice. *Phys. Rev. A* **73**, 033617 (2006).

[186] Hubener, A., Snoek, M. & Hofstetter, W. Magnetic phases of two-component ultracold bosons in an optical lattice. *Phys. Rev. B* **80**, 245109 (2009).

[187] Hohenberg, P. C. & Martin, P. C. Microscopic theory of superfluid helium. *Ann. Phys.* **34**, 291–359 (1965).

[188] Baym, G. & Kadanoff, L. P. Conservation laws and correlation functions. *Phys. Rev.* **124**, 287–299 (1961).

[189] Baym, G. Self-consistent approximations in many-body systems. *Phys. Rev.* **127**, 1391–1401 (1962).

[190] De Dominicis, C. & Martin, P. C. Stationary entropy principle and renormalization in normal and superfluid systems. I. Algebraic formulation. *J. Math. Phys.* **5**, 14 (1964).

[191] De Dominicis, C. & Martin, P. C. Stationary entropy principle and renormalization in normal and superfluid systems. II. Diagrammatic formulation. *J. Math. Phys.* **5**, 31 (1964).

[192] Ortloff, J., Balzer, M. & Potthoff, M. Non-perturbative conserving approximations and Luttinger's sum rule. *Europ. Phys. J. B,* **58**, 37–49 (2007).

[193] Hugenholtz, N. M. & Pines, D. Ground-State energy and excitation spectrum of a system of interacting bosons. *Phys. Rev.* **116**, 489 (1959).

[194] Kita, T. Self-consistent perturbation expansion for Bose-Einstein condensates satisfying Goldstone's theorem and conservation laws. *Phys. Rev. B* **80**, 214502 (2009).

[195] Strinati, G. C. & Pieri, P. Conserving and gapless approximation for the composite bosons in terms of the constituent fermions. *Europhys. Lett.* **71**, 359–365 (2005).

[196] Yukalov, V. I. & Kleinert, H. Gapless Hartree-Fock-Bogoliubov approximation for Bose gases. *Phys. Rev. A* **73**, 063612 (2006).

[197] Fisher, M. E., Barber, M. N. & Jasnow, D. Helicity modulus, superfluidity, and scaling in isotropic systems. *Phys. Rev. A* **8**, 1111 (1973).

[198] Lieb, E. H., Seiringer, R. & Yngvason, J. Superfluidity in dilute trapped Bose gases. *Phys. Rev. B* **66**, 134529 (2002).

[199] Roth, R. & Burnett, K. Superfluidity and interference pattern of ultracold bosons in optical lattices. *Phys. Rev. A* **67**, 031602 (2003).

[200] Rey, A. M., Burnett, K., Roth, R., Edwards, M., Williams, C. J. & Clark, C. W. Bogoliubov approach to superfluidity of atoms in an optical lattice. *J. Phys. B* **36**, 825–841 (2003).

[201] Poilblanc, D. Twisted boundary conditions in cluster calculations of the optical conductivity in two-dimensional lattice models. *Phys. Rev. B* **44**, 9562 (1991).

[202] Scalapino, D. J., White, S. R. & Zhang, S. C. Insulator, metal, or superconductor: The criteria. *Phys. Rev. B* **47**, 7995 (1993).

[203] Sandvik, A. & Kurkijärvi, J. Quantum Monte Carlo simulation method for spin systems. *Phys. Rev. B* **43**, 5950 (1991).

[204] Evertz, H. G., Lana, G. & Marcu, M. Cluster algorithm for vertex models. *Phys. Rev. Lett.* **70**, 875 (1993).

[205] Syljuåsen, O. F. & Sandvik, A. W. Quantum monte carlo with directed loops. *Phys. Rev. E* **66**, 046701 (2002).

[206] Pollock, E. L. & Ceperley, D. M. Path-integral computation of superfluid densities. *Phys. Rev. B* **36**, 8343 (1987).

[207] Prokof'ev, N. V. & Svistunov, B. V. Two definitions of superfluid density. *Phys. Rev. B* **61**, 11282 (2000).

[208] Rançon, A. & Dupuis, N. Nonperturbative renormalization group approach to the Bose-Hubbard model. *Phys. Rev. B* **83**, 172501 (2011).

[209] Griffin, A. Conserving and gapless approximations for an inhomogeneous Bose gas at finite temperatures. *Phys. Rev. B* **53**, 9341 (1996).

[210] Shi, H. & Griffin, A. Finite-temperature excitations in a dilute Bose-condensed gas. *Phys. Rep.* **304**, 1–87 (1998).

[211] Barnett, R., Petrov, D., Lukin, M. & Demler, E. Quantum magnetism with multicomponent dipolar molecules in an optical lattice. *Phys. Rev. Lett.* **96**, 190401 (2006).

[212] Micheli, A., Brennen, G. K. & Zoller, P. A toolbox for lattice-spin models with polar molecules. *Nat. Phys.* **2**, 341–347 (2006).

[213] Aichhorn, M., Evertz, H. G., von der Linden, W. & Potthoff, M. Charge ordering in extended Hubbard models: Variational cluster approach. *Phys. Rev. B* **70**, 235107 (2004).

[214] Kollath, C., Schollwöck, U., von Delft, J. & Zwerger, W. Spatial correlations of trapped one-dimensional bosons in an optical lattice. *Phys. Rev. A* **69**, 031601 (2004).

[215] Greentree, A. D., Tahan, C., Cole, J. H. & Hollenberg, L. C. L. Quantum phase transitions of light. *Nat. Phys.* **2**, 856–861 (2006).

[216] Hartmann, M. J., Brandão, F. G. S. L. & Plenio, M. B. Strongly interacting polaritons in coupled arrays of cavities. *Nat. Phys.* **2**, 849–855 (2006).

[217] Illuminati, F. Quantum optics: Light does matter. *Nat. Phys.* **2**, 803–804 (2006).

[218] Hartmann, M. J. & Plenio, M. B. Strong photon nonlinearities and photonic mott insulators. *Phys. Rev. Lett.* **99**, 103601–4 (2007).

[219] Angelakis, D. G., Santos, M. F. & Bose, S. Photon-blockade-induced mott transitions and XY spin models in coupled cavity arrays. *Phys. Rev. A* **76**, 031805(R)–4 (2007).

[220] Makin, M. I., Cole, J. H., Tahan, C., Hollenberg, L. C. L. & Greentree, A. D. Quantum phase transitions in photonic cavities with two-level systems. *Phys. Rev. A* **77**, 053819–10 (2008).

[221] Irish, E. K., Ogden, C. D. & Kim, M. S. Polaritonic characteristics of insulator and superfluid states in a coupled-cavity array. *Phys. Rev. A* **77**, 033801–7 (2008).

[222] Koch, J. & Le Hur, K. Superfluid–Mott-insulator transition of light in the Jaynes-Cummings lattice. *Phys. Rev. A* **80**, 023811–13 (2009).

[223] Lei, S. & Lee, R. Quantum phase transitions of light in the Dicke-Bose-Hubbard model. *Phys. Rev. A* **77**, 033827–8 (2008).

[224] Na, N., Utsunomiya, S., Tian, L. & Yamamoto, Y. Strongly correlated polaritons in a two-dimensional array of photonic crystal microcavities. *Phys. Rev. A* **77**, 031803(R)–4 (2008).

[225] Schmidt, S. & Blatter, G. Strong coupling theory for the Jaynes-Cummings-Hubbard model. *Phys. Rev. Lett.* **103**, 086403–4 (2009).

[226] Rossini, D. & Fazio, R. Mott-Insulating and glassy phases of polaritons in 1D arrays of coupled cavities. *Phys. Rev. Lett.* **99**, 186401–4 (2007).

[227] Rossini, D., Fazio, R. & Santoro, G. Photon and polariton fluctuations in arrays of QED-cavities. *Europhys. Lett.* **83**, 47011 (2008).

[228] Zhao, J., Sandvik, A. W. & Ueda, K. Insulator to superfluid transition in coupled photonic cavities in two dimensions. *arXiv:0806.3603* (2008).

[229] Pippan, P., Evertz, H. G. & Hohenadler, M. Excitation spectra of strongly correlated lattice bosons and polaritons. *Phys. Rev. A* **80**, 033612–16 (2009).

[230] Brandão, F. G. S. L., Hartmann, M. J. & Plenio, M. B. Light-shift-induced photonic nonlinearities. *New J. Phys.* **10**, 043010 (2008).

[231] Ji, A., Xie, X. C. & Liu, W. M. Quantum magnetic dynamics of polarized light in arrays of microcavities. *Phys. Rev. Lett.* **99**, 183602–4 (2007).

[232] Jaynes, E. & Cummings, F. Comparison of quantum and semiclassical radiation theories with application to the beam maser. *Proc. IEEE* **51**, 89–109 (1963).

[233] Haroche, S. & Raimond, J. *Exploring the Quantum: Atoms, Cavities, and Photons* (Oxford University Press, 2006).

[234] Kiffner, M. & Hartmann, M. J. Dissipation-induced Tonks-Girardeau gas of polaritons. *Phys. Rev. A* **81**, 021806 (2010).

[235] Boyd, R. W. & Gauthier, D. J. Photonics: Transparency on an optical chip. *Nature* **441**, 701–702 (2006).

[236] Birnbaum, K. M., Boca, A., Miller, R., Boozer, A. D., Northup, T. E. & Kimble, H. J. Photon blockade in an optical cavity with one trapped atom. *Nat. (London)* **436**, 87–90 (2005).

[237] Tavis, M. & Cummings, F. W. Exact solution for an N-molecule–radiation-field Hamiltonian. *Phys. Rev.* **170**, 379–384 (1968).

[238] Tavis, M. & Cummings, F. W. Approximate solutions for an N-molecule–radiation-field Hamiltonian. *Phys. Rev.* **188**, 692–695 (1969).

[239] Bogoliubov, N. M., Bullough, R. K. & Timonen, J. Exact solution of generalized Tavis-Cummings models in quantum optics. *J. Phys. A* **29**, 6305 (1996).

[240] Yamamoto, Y. & Imamoglu, A. *Mesoscopic Quantum Optics* (John Wiley & Sons, 1999).

[241] Economou, E. N. *Green's Functions in Quantum Physics* (Springer, Heidelberg, 2006).

[242] Pérez-Merchancano, S., Gutiérrez, H. P. & Marques, G. E. Spin transport properties in double-barrier systems with diluted magnetic semiconductor doped layers. *Microelectronics Journal* **39**, 1339 – 1340 (2008). Papers CLACSA XIII, Colombia 2007.

[243] Ertler, C., Pötz, W. & Fabian, J. Proposal for a ferromagnetic multiwell spin oscillator. *Appl. Phys. Lett.* **97**, 042104 (2010).

[244] Ertler, C., Senekowitsch, P., Fabian, J. & Pötz, W. Self-consistent study of transport in Mn-doped semiconductor heterostructures. In *Computational Electronics (IWCE), 2010 14th International Workshop on*, 1–4 (2010).

[245] Chioncel, L., Leonov, I., Allmaier, H., Beiuseanu, F., Arrigoni, E., Jurcut, T. & Pötz, W. Electronic correlations in short period $(CrAs)_n/(GaAs)_n$ ferromagnetic heterostructures. *Phys. Rev. B* **83**, 035307 (2011).

[246] Bloch, I., Greiner, M., Mandel, O., Hänsch, T. W. & Esslinger, T. Sympathetic cooling of ^{85}Rb and ^{87}Rb. *Phys. Rev. A* **64**, 021402(R) (2001).

[247] Modugno, G., Ferrari, G., Roati, G., Brecha, R. J., Simoni, A. & Inguscio, M. Bose-Einstein condensation of potassium atoms by sympathetic cooling. *Science* **294**, 1320–1322 (2001).

[248] Schreck, F., Khaykovich, L., Corwin, K. L., Ferrari, G., Bourdel, T., Cubizolles, J. & Salomon, C. Quasipure Bose-Einstein condensate immersed in a Fermi sea. *Phys. Rev. Lett.* **87**, 080403 (2001).

[249] Ospelkaus, S., Ospelkaus, C., Wille, O., Succo, M., Ernst, P., Sengstock, K. & Bongs, K. Localization of bosonic atoms by fermionic impurities in a three-dimensional optical lattice. *Phys. Rev. Lett.* **96**, 180403 (2006).

[250] Günter, K., Stöferle, T., Moritz, H., Köhl, M. & Esslinger, T. Bose-Fermi mixtures in a three-dimensional optical lattice. *Phys. Rev. Lett.* **96**, 180402 (2006).

[251] Zaccanti, M., DâErrico, C., Ferlaino, F., Roati, G., Inguscio, M. & Modugno, G. Control of the interaction in a Fermi-Bose mixture. *Phys. Rev. A* **74**, 041605 (2006).

[252] Best, T., Will, S., Schneider, U., Hackermüller, L., van Oosten, D., Bloch, I. & Lühmann, D. Role of interactions in ^{87}Rb-^{40}K Bose-Fermi mixtures in a 3D optical lattice. *Phys. Rev. Lett.* **102**, 030408 (2009).

[253] Fukuhara, T., Sugawa, S., Takasu, Y. & Takahashi, Y. All-optical formation of quantum degenerate mixtures. *Phys. Rev. A* **79**, 021601 (2009).

[254] Tey, M. K., Stellmer, S., Grimm, R. & Schreck, F. Double-degenerate Bose-Fermi mixture of strontium. *Phys. Rev. A* **82**, 011608 (2010).

[255] Wu, C., Santiago, I., Park, J. W., Ahmadi, P. & Zwierlein, M. W. Strongly interacting isotopic Bose-Fermi mixture immersed in a Fermi sea. *Phys. Rev. A* **84**, 011601 (2011).

[256] Zwierlein, M. W., Schirotzek, A., Schunck, C. H. & Ketterle, W. Fermionic superfluidity with imbalanced spin populations. *Science* **311**, 492–496 (2006).

[257] Taglieber, M., Voigt, A., Aoki, T., Hänsch, T. W. & Dieckmann, K. Quantum degenerate two-species Fermi-Fermi mixture coexisting with a Bose-Einstein condensate. *Phys. Rev. Lett.* **100**, 010401 (2008).

[258] Wille, E., Spiegelhalder, F. M., Kerner, G., Naik, D., Trenkwalder, A., Hendl, G., Schreck, F., Grimm, R., Tiecke, T. G., Walraven, J. T. M., Kokkelmans, S. J. J. M. F., Tiesinga, E. & Julienne, P. S. Exploring an ultracold Fermi-Fermi mixture: Interspecies Feshbach resonances and scattering properties of ^{6}Li and ^{40}K. *Phys. Rev. Lett.* **100**, 053201 (2008).

[259] Tiecke, T. G., Goosen, M. R., Ludewig, A., Gensemer, S. D., Kraft, S., Kokkelmans, S. J. J. M. F. & Walraven, J. T. M. Broad feshbach resonance in the ^{6}Li-^{40}K mixture. *Phys. Rev. Lett.* **104**, 053202 (2010).

[260] Trenkwalder, A., Kohstall, C., Zaccanti, M., Naik, D., Sidorov, A. I., Schreck, F. & Grimm, R. Hydrodynamic expansion of a strongly interacting Fermi-Fermi mixture. *Phys. Rev. Lett.* **106**, 115304 (2011).

[261] Hara, H., Takasu, Y., Yamaoka, Y., Doyle, J. M. & Takahashi, Y. Quantum degenerate mixtures of alkali and alkaline-earth-like atoms. *Phys. Rev. Lett.* **106**, 205304 (2011).

[262] Lin, Y., Compton, R. L., Jiménez-García, K., Porto, J. V. & Spielman, I. B. Synthetic magnetic fields for ultracold neutral atoms. *Nature* **462**, 628–632 (2009).

[263] Aidelsburger, M., Atala, M., Nascimbène, S., Trotzky, S., Chen, Y. & Bloch, I. Experimental realization of strong effective magnetic fields in an optical lattice. *Phys. Rev. Lett.* **107**, 255301 (2011).

[264] Hofstadter, D. R. Energy levels and wave functions of Bloch electrons in rational and irrational magnetic fields. *Phys. Rev. B* **14**, 2239–2249 (1976).

[265] A. Fulterer, *et al.* (in preparation).

[266] M. Nuss, *et al.* (in preparation).

[267] Schulman, L. S. *Techniques and Applications of Path Integration* (Wiley, New York, 1981).

[268] Arrigoni, E., Castellani, C., Grilli, M., Raimondi, R. & Strinati, G. C. Functional–integral formulation of the slave–boson approach: Beyond the mean–field treatment with the correct continuum limit. *Phys. Rep.* **241**, 291–371 (1994).

[269] Arrigoni, E. & Strinati, G. C. Beyond the Gutzwiller approximation in the slave–boson approach: Inclusion of fluctuations with the correct continuum limit of the functional integral. *Phys. Rev. Lett.* **71**, 3178–3181 (1993).

[270] Arrigoni, E. & Strinati, G. C. Correct continuum limit of the functional–integral representation for the four–slave–boson approach to the Hubbard model: Paramagnetic phase. *Phys. Rev. B* **52**, 2428–2462 (1995).

[271] Hussin, V. & Nieto, L. M. Ladder operators and coherent states for the Jaynes-Cummings model in the rotating-wave approximation. *J. Math. Phys.* **46**, 122102–21 (2005).

List of publications and preprints

[1] **Michael Knap**, Enrico Arrigoni, Wolfgang von der Linden, Spectral properties of strongly correlated bosons in two-dimensional optical lattices. *Phys. Rev. B* **81**, 024301 (2010).
Selected for the Virtual Journal of Quantum Fluids, January 2010, edited by Prof. Wolfgang Ketterle (MIT), Prof. Markus Greiner (Harvard), and Prof. Peter Zoller (Innsbruck).

[2] **Michael Knap**, Enrico Arrigoni, Wolfgang von der Linden, Spectral properties of coupled cavity arrays in one dimension. *Phys. Rev. B* **81**, 104303 (2010).

[3] **Michael Knap**, Enrico Arrigoni, Wolfgang von der Linden, Benchmarking the variational cluster approach by means of the one-dimensional Bose-Hubbard model. *Phys. Rev. B* **81**, 235122 (2010).
Selected for the Virtual Journal of Quantum Fluids, July 2010, edited by Prof. Wolfgang Ketterle (MIT), Prof. Markus Greiner (Harvard), and Prof. Peter Zoller (Innsbruck).

[4] **Michael Knap**, Enrico Arrigoni, Wolfgang von der Linden, Quantum phase transition and excitations of the Tavis-Cummings lattice model. *Phys. Rev. B* **82**, 045126 (2010).
Selected for the Virtual Journal of Quantum Fluids, August 2010, edited by Prof. Wolfgang Ketterle (MIT), Prof. Markus Greiner (Harvard), and Prof. Peter Zoller (Innsbruck).

[5] **Michael Knap**, Enrico Arrigoni, Wolfgang von der Linden, Excitations in disordered bosonic optical lattices. *Phys. Rev. A* **82**, 053628 (2010).

[6] **Michael Knap**, Enrico Arrigoni, Wolfgang von der Linden, Jared H. Cole, Emission characteristics of laser-driven dissipative coupled-cavity systems. *Phys. Rev. A* **83**, 023821 (2011). Selected for the Phys. Rev. A Kaleidoscope Images in February 2011.

[7] **Michael Knap**, Enrico Arrigoni, Wolfgang von der Linden, Polaritonic properties of the Jaynes-Cummings lattice model in two dimensions. *Comp. Phys. Comm.* **182**, 2036 (2011).

[8] **Michael Knap**, Enrico Arrigoni, Wolfgang von der Linden, Variational cluster approach for strongly-correlated lattice bosons in the superfluid phase. *Phys. Rev. B* **83**, 134507 (2011).

[9] Enrico Arrigoni, **Michael Knap**, Wolfgang von der Linden, Extended self-energy functional approach for strongly correlated lattice bosons in the superfluid phase. *Phys. Rev. B* **84**, 014535 (2011).

[10] **Michael Knap**, Enrico Arrigoni, Wolfgang von der Linden, Nonequilibrium steady state for strongly-correlated many-body systems: Variational cluster approach. *Phys. Rev. B* **84**, 115145 (2011).

[11] Satoshi Ejima, Holger Fehske, Florian Gebhard, Kevin zu Münster, **Michael Knap**, Enrico Arrigoni, Wolfgang von der Linden, Characterization of Mott-insulating and superfluid phases in the one-dimensional Bose–Hubbard model. *Phys. Rev. A* **85**, 053644 (2012).

[12] **Michael Knap**, Erez Berg, Martin Ganahl, Eugene Demler, Clustered Wigner crystal phases of cold polar molecules in arrays of one-dimensional tubes. Preprint: arXiv:1112.5662 (2011).

List of abbreviations and symbols

BH	Bose-Hubbard
(C)-DMFT	(cellular) dynamical mean-field theory
CPT	cluster perturbation theory
DMRG	density matrix renormalization group
JC	Jaynes-Cummings
JCL	Jaynes-Cummings lattice
MF	mean-field
QPT	quantum phase transition
QMC	quantum Monte-Carlo
RPA	random phase approximation
SFA	self energy functional approach
TCL	Tavis-Cummings lattice
VCA	variational cluster approach

t	hopping strength
U	on-site repulsion
ϵ_i	on-site energy
μ	chemical potential
ω_c	cavity resonance frequency
ϵ	energy spacing of the two-level system
g	dipole coupling constant
T	temperature
β	inverse temperature
N	number of lattice sites of the total lattice
N_c	number of clusters
L	number of sites within a cluster
N_p	number of particles
A	vector potential
ρ_s	superfluid density
ρ_c	condensate density
j_α	current density in α-direction
V_b	bias voltage
V	hybridization between leads and correlated region